UiT The Arctic University of Norway

Faculty of Science and Technology
Department of Physics and Technology

Super-Resolution Histology
Towards the Adoption of Tissue Super-Resolution Microscopy in Research and Clinical Practice

Luis E. Villegas-Hernández
A dissertation for the degree of Philosophiae Doctor – September 2023

Cover image: the phenomenon of total internal reflection illustrated on a glass rod.

By: Luis E. Villegas-Hernández.

Super-Resolution Histology

Towards the Adoption of Tissue Super-Resolution Microscopy in Research and Clinical Practice

Luis E. Villegas-Hernández

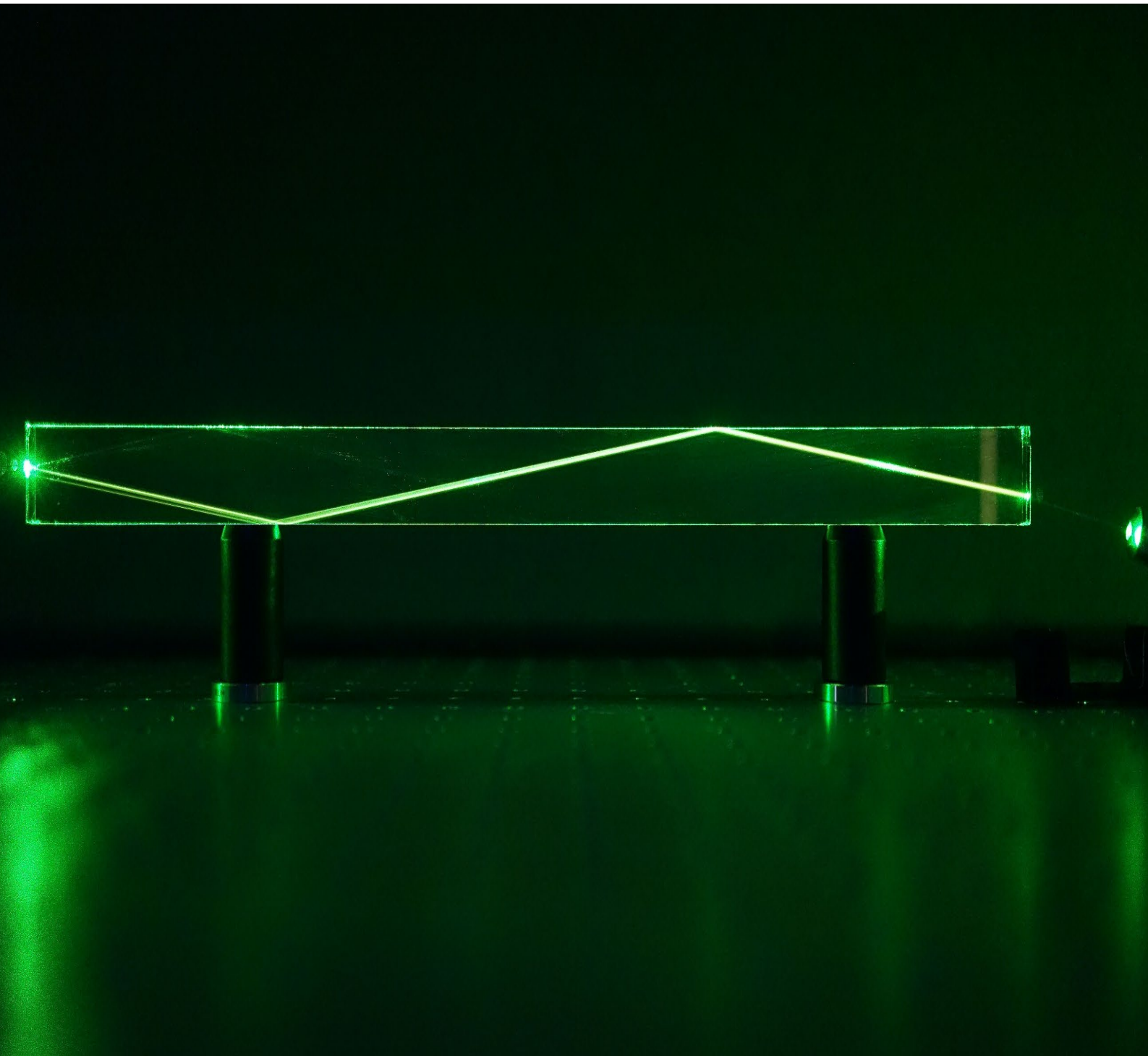A dissertation submitted for the degree of Philosophiae Doctor

September 2023

UiT The Arctic University of Norway
Faculty of Science and Technology
Department of Physics and Technology

Abstract

Super-resolution optical microscopy (SRM) holds great promise for the advancement of life sciences, unlocking the secrets of the minute machinery composing living organisms. While broadly accepted in cell biology, the existing SRM methods haven't effectively breached relevant fields such as histological practice, mainly due to the complexity, elevated costs, limited throughput, and incompatibility with conventional sample preparation workflows posed by these novel imaging methods.

This thesis contributes to the adoption of super-resolution histology both in research and clinical settings by shedding light on the practical aspects of tissue super-resolution. Here, two SRM microscopy platforms with good prospects for high throughput imaging of tissues are evaluated: **a)** a state-of-the-art commercially-available DeltaVision OMX V4 Blaze microscope, supporting multi-color 3D structured illumination microscopy (3D-SIM); and **b)** a custom-built photonic chip-based microscope, offering a series of high-contrast waveguide-based microscopy modalities including total internal reflection fluorescence (chip-TIRF), and SRM imaging via single-molecule localization microscopy (on-chip SMLM), fluorescence fluctuations-based super-resolution microscopy (on-chip FF-SRM), and correlative light-electron microscopy (on-chip CLEM). Accordingly, to evaluate the SRM imaging capabilities of such microscopy platforms, two distinct histological methods are explored, namely **1)** the Tokuyasu cryopreservation; and **2)** the formalin-fixation paraffin-embedding (FFPE). These include tissue sections of human and animal origin.

The research results are presented in three original scientific papers. Paper I deals with the implementation of 3D-SIM on human placental sections. Particularly, the use of the 3D-SIM method allowed for a high-contrast visualization of individual microvilli on cryo-preserved sections, a structural feature not visible in conventional optical microscopy methods. This, to our knowledge, is the first observation of this kind using optical microscopy. A major limitation of the explored 3D-SIM configuration, however, was the limited field-of-view (FOV) supported by the OMX microscope. In Paper II, a photonic chip-based microscopy approach for the screening of Tokuyasu tissue sections is proposed, allowing for high-contrast large FOV screening of histological samples through diverse on-chip imaging modalities including TIRF, SLML, FF-SRM, and CLEM. This work is, to our understanding, the first experimental demonstration of chip-based histology. Lastly, continuing with the photonic chip approach, Paper III proposes a novel methodology for super-resolution histology of conventional FFPE sections. Here, the photonic chip not only proved compatible with the standard FFPE preparation protocols but also showed unprecedented optical sectioning capabilities that, together with its multimode interference illumination pattern, enabled superior observation of clinically-relevant samples via the on-chip FF-SRM method.

The practical challenges of both imaging acquisition and sample preparation are thoughtfully discussed throughout this dissertation, providing a holistic perspective for their practical implementations. Overall, the adoption of SRM methods in histology will require further advancements in aspects such as sample preparation, imaging acquisition, storage, and data post-processing, directed towards their integration into existing laboratory routines, enabling a simple, repeatable, and low-cost operational workflow.

Acknowledgments

This Ph.D. thesis has been possible thanks to the support of multiple people, for which I am deeply grateful. First and foremost, I would like to thank my Ph.D. supervisor, Professor Balpreet Singh Ahluwalia, for showing me the path to becoming a scientist, and for supporting my ideas through my Ph.D. journey. Next, I would like to thank my co-supervisor, Dr. Florian Ströhl, for his continuous support and clever advice during the experimental and conceptual making of this work.

I am grateful to my colleagues at the Optical Nanoscopy Research Group at UiT – The Arctic University of Norway, for the stimulating discussions and troubleshooting support during the experimental work. I am also thankful to all the collaborators who endeavor with me in the exploration of tissue super-resolution, including the excellent people from the University of Zurich, the Karolinska Institute, the University Hospital of North Norway, the Medical Faculty at UiT, Radium Hospital, the Institute of Nuclear Physics in Krakow, and other sporadic collaborators from the USA, Europe, and India, who contributed in different aspects of this Ph.D. dissertation.

Of particular mention, I would like to thank all the histo-technicians and researchers who patiently helped me understand the intricate world of histology and guided me in finding the preservation methods presented in this work. This includes the personnel from different departments at the UiT, including the Advanced Microscopy Core Facility, the Translational Cancer Research Group, the RNA and Molecular Pathology Research Group at UiT, the Vascular Biology Research Group, the Department of Arctic and Marine Biology, and the Aquaculture and Environment Research Group, as well as collaborators from external institutions including the Institute for Cancer Genetics and Informatics at Radium Hospital, and the Center for Microscopy and Image Analysis at the University of Zurich.

Last but not least, I am profoundly grateful to my family for supporting me through my Ph.D. studies. Specifically, I am grateful to my wife, for encouraging me to pursue this academic venture. To my son, for giving me the daily sparkling to conduct my research, and to my mother, for stimulating my curiosity in the fields of medicine, microscopy, and histopathology at the early stages of my life.

Table of Contents

List of figures

List of abbreviations

BF	brightfield microscopy
chip-TIRF	chip-based total internal reflection fluorescence microscopy
DV	deconvolution microscopy
FFPE	formalin-fixation paraffin-embedding
FF-SRM	fluorescence fluctuations-based super-resolution microscopy (same as IFON)
FOV	field of view
FWHM	full width at half maximum
H&E	hematoxylin and eosin
IHC	immunohistochemistry
IF	immunofluorescence
IFON	intensity fluctuations-based optical nanoscopy (same as FF-SRM)
MMI	multimode interference
MTF	modulation transfer function
MUSICAL	multiple signal classification algorithm
MVBB	microvilli brush border
NA	numerical aperture
OMX	DeltaVision OMX V4 Blaze microscope
OTF	optical transfer function
PBS	phosphate-buffered saline
PDMS	polydimethylsiloxane
PIC	photonic integrated circuit
PSF	point spread function
SBR	signal-to-background ratio
SEM	scanning electron microscopy
SIM	structured illumination microscopy
SMLM	single-molecule localization microscopy
SRM	super-resolution microscopy
STED	stimulated emission depletion microscopy
TIR	total internal reflection
TIRF	total internal reflection fluorescence

Introduction

This section offers a contextual view of the research work carried out by the Ph.D. candidate during his doctoral studies. This includes an introduction to super-resolution optical microscopy and its relevance to the field of histology, the scope and structure of the thesis, and the materials and methods employed throughout the presented research. A brief description of the scientific articles is presented, together with an overview of the research framework in which the doctoral studies were conducted. Finally, a summary of the main findings of this thesis is offered.

Background

The microscope is one of the most important inventions of humanity. Since its creation in the 1590s, the microscope has allowed the visualization of the miniature world around and within us, enabling the understanding of physical and biological phenomena otherwise not perceptible to our eyes. From the rudimentary observations of Antonie van Leeuwenhoek to the cellular organization described by Robert Hooke[1], the microscope has revealed to us the intricate details of nature, enabling leap steps in all aspects of science.

Nowadays, microscopes are an essential tool in many scientific domains including genetics, invitro fertilization, bacterial screening, and physiology research. In histology, microscopes allow for the study of the microanatomy of biological tissues, providing insights into their functional role in plants and animals. In histopathology, microscopes are used for the identification of structural changes in tissues associated with the onset and progression of diseases. Moreover, with the aid of microscopes, histopathologists can guide medical treatment and predict clinical outcomes. In general, histological workflows involve several steps including a) sample collection; b) fixation and preservation; c) sectioning and labeling; d) microscopy imaging and postprocessing; and e) image interpretation and conclusion. Although there exist multiple strategies for carrying out each of these steps, the underlying objective in all of them is the same: to maintain the tissue architecture as close as possible to its native state while enhancing its contrast for microscope visualization. In this interplay, the chosen preparation technique and the microscope imaging method have a significant effect on the level of structural detail observable in the tissue samples.

Since the early days of histology, developments in sample preservation and labeling methods have brought several advantages to the microstructural visualization of tissues. For example, through the utilization of chemical fixatives and subsequent wax infiltration, histologists can preserve tissue sections at room temperature for decades, avoiding biological denaturation inherent to enzymatic reactions, autolysis, and putrefaction after surgical excision from the body. This method, referred to as formalin-fixation paraffin-embedding or *FFPE*, in short, is the most employed preservation procedure in histological analyses [2], for its affordability, reproducibility, and seamless compatibility with multiple labeling strategies including hematoxylin and eosin (H&E), immunohistochemistry (IHC) and immunofluorescence (IF). However, the FFPE method has drawbacks. By inducing chemical cross-linking on the samples and subsequent paraffin infiltration, the FFPE method limits the availability of binding sites required for immunolabeling and, to some extent, compromises the ultrastructural preservation of the samples. To circumvent these problems, alternative preservation methods have been

proposed, including sample storage at cryogenic temperatures. In particular, the cryo-preservation method developed by Kiyoteru Tokuyasu in the 1970s allows for superior labeling specificity and ultrastructural preservation as compared to FFPE samples. However, this method also has limitations. Designed for the visualization of tissue samples in transmission electron microscopy [3], the so-called *Tokuyasu* method requires advanced and costly sectioning devices and special cooling conditions that make the technique inaccessible to most histological laboratories. Also, the cross-sectional areas attainable with this method (roughly, 500 μm × 500 μm) are insufficient for screening large histological samples, as required in histopathological analyses.

When it comes to microscopy observations of tissues, two techniques are generally employed, namely, optical microscopy (also referred to as light microscopy) and electron microscopy. Optical microscopes offer relatively simple and affordable sample preparation, high specificity (e.g., in fluorescence microscopy), and fast acquisition rates. However, due to the phenomenon of diffraction, their resolution is limited to around 250 nm, making it difficult to observe subcellular structures beyond that scale [4]. On the other hand, electron microscopes allow for ultrastructural observation of tissue samples, identifying small features like microvesicles and tight junctions. However, they require time-consuming and expensive sample preparation and have low imaging throughput, limited specificity, and high operating costs. The choice between light and electron microscopy for tissue analysis depends on the level of structural detail required for research or clinical diagnosis. While optical microscopy is sufficient for most pathologies, certain disorders like minimal change disease [5], primary ciliary dyskinesia [6], and amyloidosis [7] require high-resolution power for accurate diagnosis.

Between the late 1990s and early 2000s, a new microscopy field emerged, bridging the resolution gap existing between light and electron microscopy [8]. This new field, coined as fluorescence-based super-resolution optical microscopy (SRM), or optical nanoscopy, encompasses a series of optical microscopy techniques that cleverly exploit the photochemical and photokinetic properties of fluorescent markers [9] to resolve biological structures beyond the limits of diffraction. These include single-molecule localization microscopy (SMLM) [10], stimulated emission depletion microscopy (STED) [11], structured illumination microscopy (SIM) [12], fluorescence fluctuations-based super-resolution microscopy (FF-SRM) [13], and expansion microscopy[1] (ExM) [14]. Despite their relatively short presence, the SRM methods have revolutionized the microscopy arena, offering several advantages for life sciences such as high contrast, high specificity, and unprecedented resolution. Moreover, current developments are pushing the SRM methods towards life-cell imaging, allowing the observation of sub-cellular dynamics otherwise not conceivable via conventional microscopy methods. Lastly, the SRM techniques, in general, allow for relatively easy and short sample preparation as compared to electron microscopy, which greatly simplifies the imaging workflow and alleviates the operational costs, enabling its adoption by laboratories around the world. Since the early days, the scientific community acknowledged the potential benefits of SRM methods, and their inventors were awarded in 2014 with the Nobel Prize in Chemistry for "the development of super-resolved fluorescence microscopy" [8].

---

[1] Expansion microscopy (ExM) is a particular SRM method in which the sample is physically enlarged, allowing for an enhanced resolution according to the expansion factor of the sample [14].

The field of SRM has been widely adopted in cell biology, becoming a routine method for the interrogation of biological mechanisms of interest in multiple domains ranging from genomic research to drug development. Although STED [15], SMLM [16, 17], and particularly SIM [18, 19], have been successfully implemented for the visualization of subcellular features in tissue sections, the integration of these novel techniques in routine histology and histopathology is still far from reality, limiting the potential benefits the SRM methods could bring to research and clinical practice. This fact can be attributed to the following challenges: 1) the high cost of SRM systems, which is still unaffordable for most histology laboratories; 2) the incompatibility of the SRM methods, in terms of sample preparation, with routine histological workflows, and 3) the limited imaging throughput of present-day SRM techniques, which is insufficient to meet the screening requirements for large tissue samples in a fast basis.

Over the last decade, a new microscopy platform based on photonic integrated circuits (PIC) has been proposed as an alternative to achieving high-throughput super-resolution imaging of biological samples [20-26]. The technique, successfully demonstrated in cells yet unexplored in tissues, features a flat silicon chip that serves the dual purpose of providing the sample with physical support while delivering the illumination necessary for super-resolution microscopy. By exploiting the evanescent field excitation, the so-called photonic chip provides several advantages for bio-imaging including a) total internal reflection fluorescence (TIRF) imaging over large fields of view [21, 22]; b) sample observations at scalable magnifications employing conventional objectives [22]; c) compatibility with multiple imaging modalities including label-free optical methods [27] and scanning electron microscopy [28]; d) reduction of system footprint and operational complexity compared to SRM methods based on free-space optics; and e) possibilities for cost-reduction of the photonic chip via mass-fabrication using standard semiconductor processes.

Scope of the thesis

This doctoral thesis aims to facilitate the adoption of fluorescence-based super-resolution optical microscopy in histology both in research and clinical settings. To this end, two imaging systems with promising potential for high throughput super-resolution histology are covered. Specifically, the commercial DeltaVision OMX V4 Blaze microscope (General Electric Healthcare), hereafter referred to as the OMX microscope, and the photonic chip-based microscope developed at UiT – The Arctic University of Norway.

The main objectives of this work are 1) to identify and optimize the histological processing methods for super-resolution imaging of tissue sections using the OMX microscope; 2) to explore and validate the feasibility of the photonic chip-based microscopy platform for high-contrast and high-throughput super-resolution histology.

Other aspects outlined in this thesis such as the photonic chip fabrication and the development of SRM reconstruction algorithms fall outside the scope of this work. Particularly, the fabrication of the photonic chips was outsourced to different foundries, while the FF-SRM algorithms used in this thesis were either publicly available from published papers or obtained via collaborators.

Materials and methods

Two histological preservation methods are studied along the course of this work, namely, formalin-fixation paraffin-embedding (FFPE), and cryo-preservation via the Tokuyasu method. Tissue sections from diverse origins were used in the experiments, including pig heart, mouse kidney, fisheye retina, and human tissues of placenta, colon, and prostate.

The imaging modalities explored in the OMX microscope include deconvolution microscopy (DV), and 3D structured illumination microscopy (3D-SIM). The chip-based imaging modalities explored in this work include total internal reflection fluorescence microscopy (chip-TIRF), single-molecule localization microscopy (on-chip SMLM), fluorescence fluctuations-based super-resolution microscopy (on-chip FF-SRM), and correlative light-electron microscopy (on-chip CLEM). Figure A offers an overview of the imaging modalities explored in this thesis.

Setting for the thesis

The work presented here is framed within two research lines carried out at the Optical Nanoscopy Research Group, Department of Physics and Technology at UiT – The Arctic University of Norway. The first research line focuses on the application of SRM methods using the OMX microscope. The second and major research line focuses on the development of a photonic chip-based microscopy platform that aims at facilitating the broad adoption of super-resolution microscopy by improving the imaging throughput and compatibility with FFPE samples, and in the long run, reducing the operational cost of these techniques.

This thesis contributed toward two externally funded research projects with a common objective of developing a photonic chip-based microscopy platform for high-throughput super-resolution histopathology applications. These include the projects NANO2021–288565 and BIOTEK2021–285571 funded by the Research Council of Norway. This work was possible thanks to the collaborative effort of several research institutions including the University Hospital of North Norway (Tromsø, Norway), Oslo University Hospital (Oslo, Norway), Karolinska Institute (Stockholm, Sweden), and UiT - The Arctic University of Norway (Tromsø, Norway).

The research presented in this thesis was conducted between August 2018 to June 2023. The thesis was supervised by Prof. Balpreet Singh Ahluwalia and co-supervised by Dr. Florian Ströhl.

Publications

This thesis is comprised of three original research articles, referred to as *Papers*, produced by *the Ph.D. candidate*, namely Luis E. Villegas-Hernández, in collaboration with other researchers during his doctoral studies. At the time of submission of this thesis, two of the papers have been published in peer-review journals, and one is self-archived in a public repository while being considered for publication in a peer-review journal. The Ph.D. candidate has made a leading contribution to the research articles hereby presented. The complete list of papers includes:

Paper I

Title: *Visualizing ultrastructural details of placental tissue with super-resolution structured illumination microscopy.*

Status: Published in Placenta (2020).

Authors: <u>Luis E. Villegas-Hernández</u>, Mona Nystad, Florian Ströhl, Purusotam Basnet, Ganesh Acharya, Balpreet S. Ahluwalia.

Description A methodology for multicolor 3D-SIM imaging of placental tissue sections is presented. This includes the preparation steps and the acquisition parameters for a successful structured illumination microscopy of placental samples preserved under two different approaches, namely the FFPE method and the Tokuyasu method.

Contribution: LEVH prepared the tissue samples, performed the imaging experiments and subsequent image analysis. LEVH wrote the first draft of the manuscript and finished the paper. All authors contributed to writing and revising selected sections of the article.

Paper II

Title: *Chip-based multimodal super-resolution microscopy for histological investigations of cryopreserved tissue sections.*

Status: Published in Light: Science & Applications (2022).

Authors: <u>Luis E. Villegas-Hernández</u>*, Vishesh Dubey*, Mona Nystad, Jean-Claude Tinguely, David A. Coucheron, Firehun T. Dullo, Anish Priyadarshi, Sebastian Acuña, Azeem Ahmad, José M. Mateos, Gery Barmettler, Urs Ziegler, Åsa Birna Birgisdottir, Aud-Malin Karlsson Hovd, Kristin Andreassen Fenton, Ganesh Acharya, Krishna Agarwal, Balpreet Singh Ahluwalia.

Description Photonic chip-based microscopy is validated as a multimodal imaging platform for cryopreserved Tokuyasu sections. The proposed methodology offers multicolor high-contrast visualizations of histological samples over large fields of view, together with tissue super-resolution imaging SMLM, FF-SRM, and CLEM methods.

Contribution: LEVH planned and coordinated the experiments, performed sample preparation, image acquisition, and subsequent image analysis. LEVH wrote the first draft of the manuscript and finished the paper. All authors contributed to writing and revising selected sections of the article. *These two authors contributed equally to this work.

Paper III

Title: *Super-resolution histology of paraffin-embedded samples via photonic chip-based microscopy.*

Status: Self-archived in bioRxiv:2023-06 (2023). Under peer review in Nature Communications.

Authors:	<u>Luis E. Villegas-Hernández</u>, Vishesh K. Dubey, Hong Mao, Manohar Pradhan, Jean-Claude Tinguely, Daniel H. Hansen, Sebastián Acuña, Bartłomiej Zapotoczny, Krishna Agarwal, Mona Nystad, Ganesh Acharya, Kristin A. Fenton, Håvard E. Danielsen, Balpreet Singh Ahluwalia.
Description	Photonic chip-based microscopy is proposed as a high-throughput super-resolution imaging platform for the observation of commonly available FFPE samples. The high-intensity variance supported by the chip is harnessed by the MUSICAL algorithm to obtain large FOV super-resolution images using an FF-SRM approach. The photonic chip is proven compatible with existing preparation steps of FFPE samples, enabling seamless integration into routine histological workflows.
Contribution:	LEVH planned and coordinated the experiments, performed sample preparation, image acquisition, and subsequent image analysis. LEVH wrote the first draft of the manuscript and finished the paper. All authors contributed to writing and revising selected sections of the article.

In addition to Papers I, II, and III, there are other research articles that, although not included for consideration in this dissertation, have contributed to the academic advancement of the field by offering alternative perspectives and methodologies that have enriched the understanding of super-resolution methods in histology. These include:

Paper IV

Title:	Fluorescence fluctuations-based super-resolution microscopy techniques: an experimental comparative study.
Status:	Self-archived in arXiv:2008.09195 (2020).
Authors:	Ida S. Opstad, Sebastian Acuña, <u>Luis E. Villegas- Hernández</u>, Jennifer Cauzzo, Nataša Škalko-Basnet, Balpreet S. Ahluwalia, Krishna Agarwal
Description	An experimental comparison of diverse FF-SRM methods is presented, highlighting their strengths and weaknesses on a wide variety of fluorescence data ranging from computational simulations to nanoparticles, cells, and tissues.
Contribution:	LEVH prepared the tissue samples, performed the tissue imaging experiments and subsequent tissue image analysis. All authors contributed to writing and revising selected sections of the article.

Paper V

Title:	Deriving high contrast fluorescence microscopy images through low contrast noisy image stacks.
Status:	Published in Biomedical Optics Express (2021).
Authors:	Sebastian Acuña, Mayank Roy, <u>Luis E. Villegas-Hernández</u>, Vishesh K. Dubey, Balpreet Singh Ahluwalia, Krishna Agarwal.

Description: A contrast enhancement approach using a modified version of MUSICAL is presented, highlighting the potential of this FF-SRM algorithm to improve the visualization of biological samples without necessarily improving lateral resolution.

Contribution: LEVH prepared the tissue samples, performed the tissue imaging experiments and subsequent SIM image reconstructions. All authors contributed to writing and revising selected sections of the article.

Paper VI

Title: Label-free incoherent super-resolution optical microscopy

Status: Self-archived in arXiv (2023).

Authors: Nikhil Jayakumar, <u>Luis E. Villegas-Hernández</u>, Weisong Zhao, Hong Mao, Firehun T. Dullo, Jean-Claude Tinguely, Krizia Sagini, Alicia Llorente, Balpreet Singh Ahluwalia.

Description: A label-free super-resolution photonic chip-based microscopy method is proposed. By exploiting the photoluminescence and scattering properties of the waveguide materials, the photokinetics and nanosize of fluorescent markers are mimicked, allowing for a label-free incoherent system compatible with fluorescence-based optical super-resolution methods such as SIM and FF-SRM.

Contribution: LEVH prepared the tissue samples, performed the tissue imaging experiments and subsequent tissue image analysis. All authors contributed to writing and revising selected sections of the article.

Structure of the thesis

This thesis is divided into five chapters. *Chapter 1* offers a theoretical framework covering relevant concepts to appropriately follow the research work here presented. *Chapter 2* deals with the implementation of 3D-SIM for super-resolution histology employing the commercial OMX microscope. This includes the findings and conclusions of Paper I. The main contribution of this doctoral thesis, namely *Chapter 3,* covers the advantages and drawbacks of chip-based microscopy for the visualization of tissue sections, summarized in Papers II and III, respectively. *Chapter 4* offers a global conclusion to this work and provides insights into future perspectives of chip-based super-resolution histology. Finally, *Chapter 5* provides an overview of additional scientific contributions made during the doctoral studies of the Ph.D. candidate that are not directly covered in this thesis. The complete versions of research Papers I, II, and III are presented in appendices A, B, and C, respectively. The layout of Chapters II and III is outlined in Figure A below.
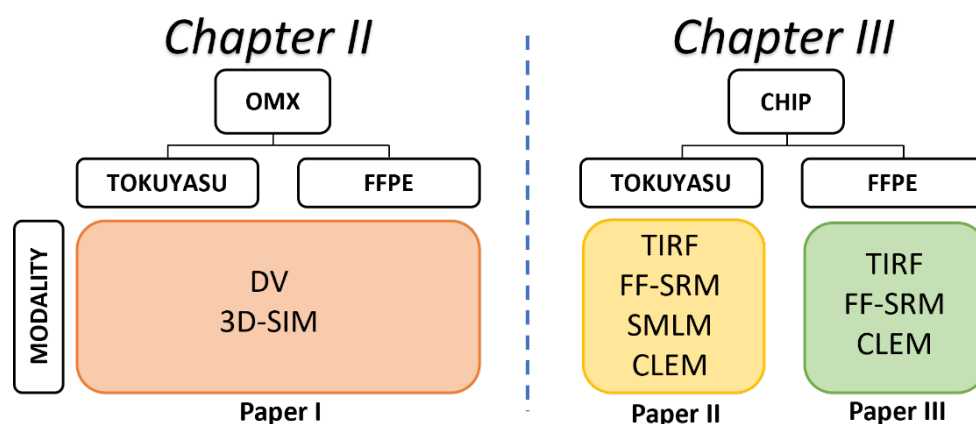
Figure A. Layout of Chapters II and III. Legend: CLEM: correlative light-electron microscopy / DV: deconvolution microscopy / FF-SRM: fluorescence fluctuations-based super-resolution microscopy / 3D-SIM: 3D structured illumination microscopy / SMLM: single-molecule localization microscopy / TIRF: total internal reflection microscopy.

Results

In *Paper I*, the implementation of SIM allowed the identification of microvilli features in the human placenta that were otherwise not visible via diffraction-limited optical microscopy methods. The Tokuyasu cryosections were found to be a good fit for SIM. However, the cryopreserved samples often exhibited artifacts in the form of folds and knife marks that limited the use of this histological method. The FFPE samples, on the other hand, were easily accessible but exhibited high autofluorescence and refractive index heterogeneity that posed great challenges for the reconstruction algorithm, requiring several preparation and acquisition optimizations for successful SIM imaging. The FOV supported by the commercial SIM microscope used in this part of the study was found limited for the observation of large histological samples, needing tile mosaic stitching to screen tissue sections.

In *Paper II*, the principle of photonic chip-based histology was for the first time proposed on Tokuyasu cryosections, demonstrating the feasibility of this imaging platform for histological investigations across scalable fields of view. Here, multiple histological imaging modalities were presented, including on-chip TIRF, SMLM, FF-SRM, and CLEM. Finally, in *Paper III*, the photonic chip platform was found compatible with the preparation protocols of common FFPE samples, enabling seamless integration of the chip-based method into routine histological workflows. Moreover, the combination of a high signal variability and ultrathin optical sectioning supported by the on-chip illumination was successfully harnessed by the MUSICAL algorithm to enable high-resolution images of clinically relevant paraffin-embedded samples over large FOVs.

Super-resolution optical microscopy offers several advantages to histology, allowing the observation of structural changes beyond the physical limits of conventional optical microscopes. This doctoral thesis contributes to the adoption of super-resolution microscopy in histology by shedding light on the application aspects of novel SRM methods in tissue samples. Particularly, the on-chip histology method presented here is an attractive route for high-resolution screening of tissue samples, allowing for sharp visualization of organ tissues

over large areas. Future developments in super-resolution histology can potentially assist in the identification of morphological variations at the molecular level associated with the onset and progression of diseases.

INTRODUCTION

Chapter 1   Theoretical framework

This chapter, divided into four parts, offers an introduction to concepts associated with super-resolution imaging of organ tissues. The first part covers general concepts of optics and microscopy. The second and third parts, respectively, offer an overview of various diffraction-limited and SRM fluorescence-based microscopy techniques used in this work. The fourth part provides a brief description of histology and outlines the sample preparation steps used in this thesis.

1.1 General concepts in optical microscopy

Optical microscopy makes use of light and a lens system to examine objects that are too small to be observed by the naked eye. Microscopes must satisfy three criteria: a) the subject under investigation, such as a biological sample, needs to be visually enlarged beyond the resolving limit of the eyes (approximately, 175 μm [29]); b) the augmented features must be distinguishable from each other; and c) the magnified image must possess sufficient clarity for interpretation and analysis. These three aspects, referred to as *magnification*, *resolution*, and *contrast*, respectively, are key aspects of microscopy. This section covers the fundamental notions that lead to the understanding of these concepts.

1.1.1 Light-matter interactions

Light interacts with matter in multiple ways, leading to physical phenomena including *refraction, diffraction, transmission, absorption, emission*, and *scattering*. These phenomena determine how matter around us is perceived (e.g., the colors of the rainbow, the shadow of a tree), and can be exploited to retrieve information from nature. The field of microscopy relies on many of these phenomena to visualize the miniature world. The principle of refraction is presented hereby. The other light-matter interaction phenomena will be appropriately covered in different sections of this document.

Refraction and Snell's law

Light propagates in a straight direction and at a constant velocity through a uniform medium. In a vacuum, light travels at an approximate speed of $3\text{x}10^8$ m/s. However, in different media such as water or glass, light travels at a slower pace. The refractive index n of a given medium is defined as the ratio between the speed of light in a vacuum c_0 and the speed of light in that medium c, also referred to as phase velocity. Equation (1.1-1) provides the general expression for the refractive index of a given medium [30].

$$n = \frac{c_0}{c} \qquad (1.1\text{-}1)$$

In general, each material exhibits a particular refractive index. For example, air has a refractive index of $n_{air} \approx 1.0003$, while water has a refractive index of $n_{water} \approx 1.333$. Microscopy glass slides, usually made of borosilicate glass, have a refractive index of $n_{glass} \approx 1.52$. The refractive index is also a function of the wavelength of light. This phenomenon is known as dispersion. Due to dispersion, different wavelengths of light experience different degrees of bending when passing through a medium, leading to a variation in its refractive index. While this effect can be useful for splitting white light into its constituent colors through a prism, it can also introduce chromatic aberrations in optical systems that might require further corrections.
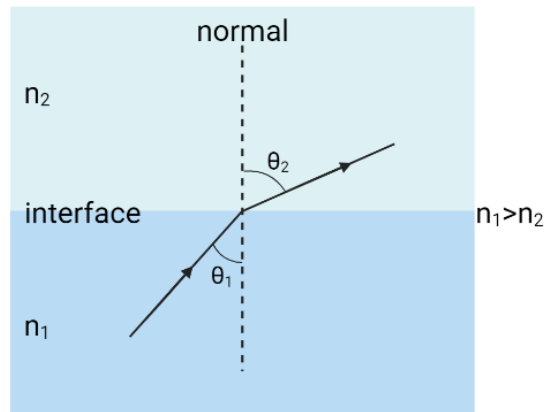
Figure 1.1-1.   Schematic representation of Snell's law. A light beam transitioning from a medium with a refractive index n_1 to another medium with a lower index n_2, will experience a change in the direction of propagation relative to the normal of the interface where the transition takes place[2]. The relation between the incident and the refracted angles is given by Snell's law, presented in Equation (1.1-2).

When light transitions from a medium with a refractive index n_1 to another with a different refractive index n_2, e.g. from water to air, it experiences refraction, resulting in a change in the direction relative to the normal of the interface where the transition takes place (see Figure 1.1-1). The relation between the incident and the refracted angles θ_1 and θ_2, respectively, is given by Snell's law, detailed in Equation (1.1-2).

$$n_1 sin\theta_1 = n_2 sin\theta_2 \qquad\qquad (1.1\text{-}2)$$

Snell's law has important implications for another physical phenomenon called total internal reflection. This concept is fundamental to Chapter 3 of this thesis, and it is further discussed in section 1.2.3.

1.1.2 Image formation in a compound microscope

Compound microscopes are optical systems made of several optical components that harness the phenomenon of refraction to enable the visualization of small samples that cannot be identified with the naked eye. An example of this configuration is the brightfield microscope illustrated in Figure 1.1-2a. In this microscopy modality, a light source is projected towards a condenser lens that redirects the light to provide uniform illumination to a thin specimen resting in a glass slide and covered with a coverslip. Upon transmission through the sample, the objective lens collects the light stemming from the specimen plane and magnifies it. Further magnification by the eyepiece reveals an image with larger dimensions than the object under study. Modern microscopes are equipped with additional instrumentation to facilitate sample visualization under different imaging modalities. Figure 1.1-2b offers a schematic representation of a fluorescence microscope in an upright configuration, with a camera on the top, and a light source on the back.

---

[2] The schematic representations presented in this thesis were made in Biorender.com.
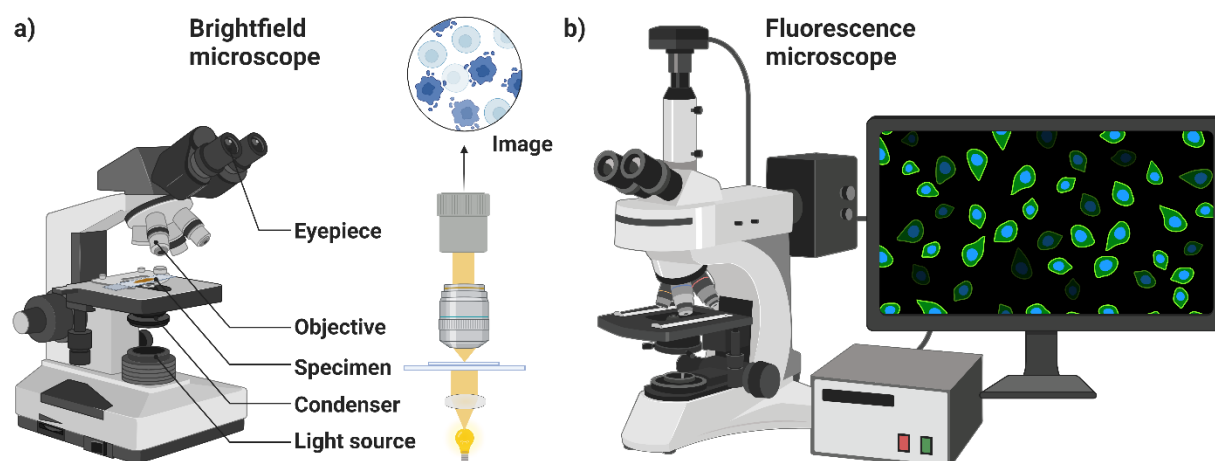
Figure 1.1-2.   Schematic representation of a compound microscope.a) Components of a conventional brightfield microscope. b) Fluorescence microscope in an upright configuration.

Magnification

Magnification is a ratio that indicates the enlargement of an object relative to its original size. In optical microscopy, magnification refers to the apparent enlargement of the sample image by using lenses. As seen in Figure 1.1-2, the term *apparent* denotes that, indeed, what is enlarged is the visual projection of the object rather than its physical dimensions[3].

The magnification of a microscope is the product of the various magnification values along its optical path. In a conventional compound microscope such as in Figure 1.1-2, the total magnification M is given by the multiplication of the objective lens magnification M_o and the eyepiece magnification M_e. Equation (1.1-3) provides a mathematical expression for the calculation of the total magnification of a compound microscope.

$$M = M_o \times M_e \qquad\qquad (1.1\text{-}3)$$

Higher magnification allows for the visualization of finer details and structures that otherwise would be indiscernible to the human eye. However, as will be explained in the next section, magnification alone is not sufficient for visualization in microscopy. While magnification allows for the object to be seen at a larger scale, it does not inherently improve the resolution or sharpness of the image. Thus, visualization in microscopy requires a combination of magnification, contrast, and resolution.

Field of view

The field of view, or FOV, is a measure of the area captured in an image field. In an optical microscope, the FOV takes the form of a circle. However, in modern microscopes employing

---

[3] Novel microscopy approaches such as expansion microscopy (ExM) make use of chemical compounds to also enlarge the physical dimensions of biological samples to enhance their visualization [14]. In this thesis, the concept of magnification is used solely to describe the apparent enlargement of the sample by the microscope lenses.

a camera for imaging, the FOV is ultimately limited by the sensor size and it is commonly specified in rectangular dimensions (height and width) in square millimeters. Figure 1.1-3 offers a schematic representation of a microscope FOV.
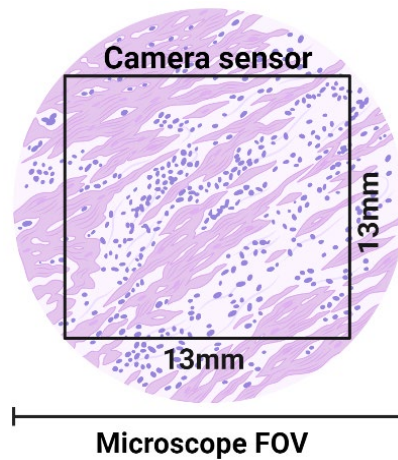
Figure 1.1-3.   Schematic representation of a microscope FOV. In an optical microscope, the FOV takes the form of a circle. However, in modern microscopes employing digital cameras for image acquisition, the FOV is determined by the width and height of the sensor.

The FOV is inversely proportional to the magnification. Thus, higher magnification entails a smaller FOV and vice versa. To give an example, let us consider an optical microscope employing a 13 mm × 13 mm camera sensor composed of 2000 × 2000 pixels (each one with physical dimensions of 6.5 μm × 6.5 μm), such as in Figure 1.1-3. Assuming a 60X magnification, the resulting FOV in this configuration is approximately 216 μm × 216 μm. However, as will be illustrated in section 1.2.1, the illumination strategy used in the imaging method can also affect the FOV, further reducing the effective imaging area. This fact has an important implication in the imaging throughput of SRM methods requiring high NA (and consequently high magnification) objectives, leading to FOVs between 40 μm × 40 μm [31] and 100 μm × 100 μm [32]. Also, when aiming for better (higher) resolution, one has to fulfill the Nyquist criteria, e.g. in 3D-SIM, where the use of a higher magnification objective lens results in a smaller FOV.

1.1.3 Optical resolution

The term resolution is a broad concept used in microscopy. It entails the distinction between two events, either in space or in time. Particularly, spatial resolution refers to the ability of a system to distinguish closely spaced structures within the object of study. In other words, spatial resolution is a parameter that defines the minimum distance between two adjacent points at which they can be distinguished as individual entities rather than merged elements. On the other hand, temporal resolution refers to the system's ability to differentiate between two events occurring at different instances in time. The spatial resolution is a measure of how small details can be seen in a static frame, whereas the temporal resolution gives information about how fast the optical system can collect and process dynamic events.

Within the spatial resolution, two distinct concepts exist. When measured along the image plane, it is termed lateral resolution, whereas, in the direction of the light propagation, it is called axial resolution[4].

A physical phenomenon, known as diffraction, sets the spatial resolution limit of optical systems, including microscopes. Such systems are called *diffraction-limited*. The phenomenon of diffraction is explained hereby.

Diffraction and the Airy pattern

Just like sound waves or water surface waves, light exhibits a wave-like behavior. When light encounters an edge or interacts with an obstacle with dimensions comparable to its wavelength, the phenomenon of diffraction occurs, causing it to change direction or spread out. In microscopy, the energy redistribution caused by diffraction leads to the blurring and spreading of tiny features of the specimen at the image plane, effectively limiting the resolving capabilities of the system.
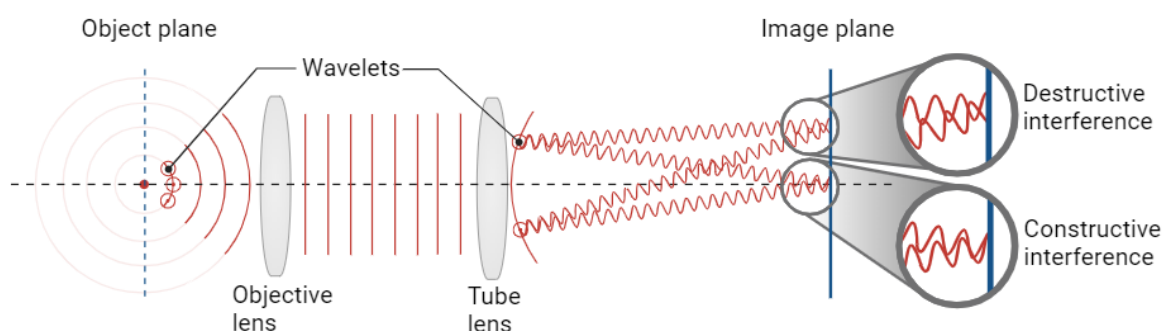
Figure 1.1-4.   The phenomenon of diffraction in a compound microscope. From left to right, an infinitesimally small point source such as a fluorescent molecule emits light in the form of diverging spherical waves. These waves, per Huygens' principle, contain wavelets emitting synchronized light. The objective lens captures a portion of these waves, before further propagation to the tube lens as plane waves. This lens then refracts them as converging spherical waves toward an imaging detector. As a result of the destructive and constructive interference of these waves, a bright spot with surrounding concentric fringes emerges on the image plane.

To explain this phenomenon, let us describe the process of image formation in a compound microscope via wave optics representation. In the schematic representation given by Figure 1.1-4, an infinitesimally small light-emitting source, such as a fluorescent molecule, is the object under study. Here, the emitted light propagates in diverging spherical waves. According to Huygens' principle [33], at the front of each light wave, there are infinitesimally small sources known as wavelets that emit light at a synchronous pace. An angular sector of the propagating wavefronts is intercepted by the objective lens and further propagated towards the tube lens, this time as plane waves. Finally, the tube lens collects the incoming wavefronts and refracts them as converging spherical waves to the imaging detector (e.g., camera chip). Due to constructive and destructive interference of the converging wavefronts, a bright spot emerges

---

[4] Unless otherwise stated, the term *resolution* used in this work refers to spatial resolution.

at the image plane, surrounded by concentric fringes of varying intensities, as illustrated in Figure 1.1-5. This diffraction pattern is known as the Airy pattern, and its central spot is referred to as the Airy disk.
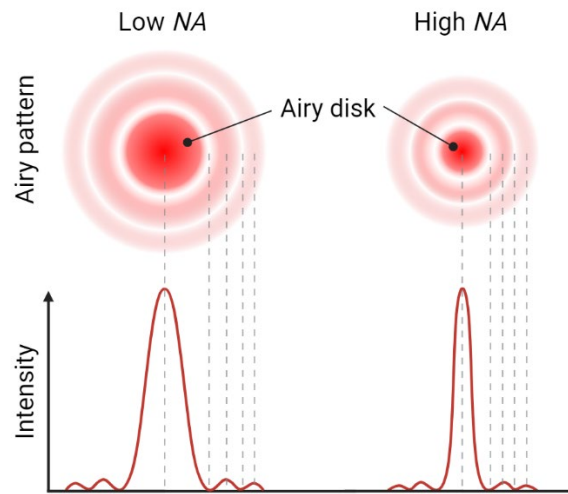
Figure 1.1-5.   Airy pattern of an infinitesimally small light-emitting source. The size and shape of the Airy pattern depend on factors such as the numerical aperture (*NA*) of the objective lens and the light wavelength.

The Airy pattern is a key parameter for the estimation of resolution in a microscope and it has several characteristics worth mentioning: a) the central spot concentrates most of the energy reaching the image plane; b) the size and shape of the Airy disk, as well as the spacing of the rings, are determined by various factors such as the numerical aperture (*NA*) of the objective lens and the wavelength of light (see below); c) the size and shape of the Airy pattern is larger than the point source being imaged, and remains unchanged for any emitter significantly smaller than the Airy disk; d) the intensity profile of the Airy pattern approximates a two-dimensional Gaussian distribution (bottom panel in Figure 1.1-5); e) the bright rings exhibit radially decaying intensities; and f) the dark rings, match the locations of destructive interference, reaching down to zero intensities.

The point spread function

The point spread function, in short PSF, is a broader concept in microscopy that is also related to diffraction and, as such, to the Airy pattern. It is defined as the impulse response of an optical system to a point source emitting light uniformly in all directions. Following the rationale of wave optics in Figure 1.1-4, the converging wavefronts exiting the tube lens interfere with each other in multiple locations of the three-dimensional image space, giving rise to a symmetrical pattern resembling an hourglass along the optical axis of the microscope. This pattern in three-dimensional space is the impulse response, or PSF, of the microscope to an emitting point source. Experimentally, in fluorescence microscopy (see section 1.2), the PSF can be observed by acquiring multiple images through discrete camera steps along the optical axis of the microscope system, followed by orthogonal projections (see Figure 1.1-6). The shape and symmetry of the PSF can be influenced by multiple factors including diffraction, light wavelength, optical aberrations, system misalignment, and refractive index heterogeneities in the sample.
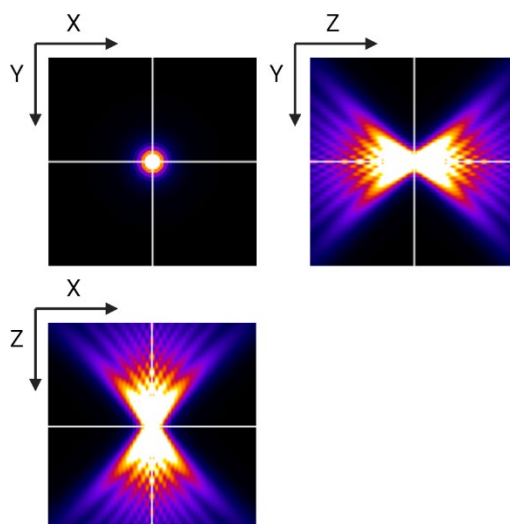
Figure 1.1-6.   Orthogonal views of a three-dimensional point spread function. The top-left panel illustrates the Airy pattern formed at the image plane. The XZ and YZ panels represent the orthogonal views of the point spread function, where the Z direction corresponds to the optical axis of the microscope. Simulated with PSF Generator in FIJI [34].

The Airy pattern and the PSF are closely related to each other, and these terms are often interchanged. In microscopy, the term PSF often refers to the intensity distribution across the image plane (i.e., the Airy pattern), rather than in the three-dimensional space[5].

An important aspect of the PSF theory is that the image formation of a point source object can be mathematically expressed as its convolution with the microscope's PSF. In fluorescence microscopy, it is given by Equation (1.1-4):

$$i(r) = o(r) * psf(r) \qquad\qquad (1.1\text{-}4)$$

Where $i(r)$ represents the microscopy image at a location r, $o(r)$ is the point source object, and $psf(r)$ is the PSF of the system.

In the case of a real sample (e.g., biological cell), each infinitesimally small element on it is considered a point source. Thus, for an ideal microscope system fulfilling the condition of incoherent emission and assuming linearity and shift-invariance, each point source is convolved with the PSF of the imaging system, rendering an independent Airy pattern at the image plane. Then, the final image results from superimposing all these convolutions together.

Understanding the shape and characteristics of the PSF is crucial for image processing, deconvolution algorithms (see section 1.2.2), and for analyzing image quality in optical microscopy. By knowing the factors that influence the PSF, it is possible to optimize system design, correct aberrations, and improve imaging performance. These aspects will be brought

---

[5] In this thesis, unless otherwise specified, the term PSF will be used to describe the intensity distribution across the image plane, i.e., the Airy pattern.

to attention in section 1.3.1, where the optimization of the PSF is fundamental for super-resolution imaging via structured illumination microscopy (SIM).

The numerical aperture

The size of the Airy pattern is dependent on the wavelength of light λ and the ability of the objective lens to collect the incoming light emanating from the sample. The latter is coined as numerical aperture, or *NA*, and is an important parameter for improving the sharpness of microscopy images. The numerical aperture, illustrated in Figure 1.1-7, is the product of the imaging medium's index n (i.e., between the sample and the objective), and the angle α of the half cone of light collected by the objective lens, which is given by Equation (1.1-5)

$$NA = n\ sin\alpha \tag{1.1-5}$$

In essence, the broader the cone of light accepted by the objective, the narrower the diffraction pattern that originates at the image plane, and therefore, the better the resolution. Hence, in microscopy, higher resolution is often achieved by the collection of a wide cone of light. As depicted in Figure 1.1-7, this usually entails reducing the distance between the specimen and the front face of the objective (i.e., short working distance), and using high refractive index media such as water or oil for imaging. In practice, there exist multiple objective lens configurations offering numerical apertures ranging from NA 0.1 - 0.95 in air to NA 0.30 - 1.27 in water, and NA 1 - 1.7 in oil.
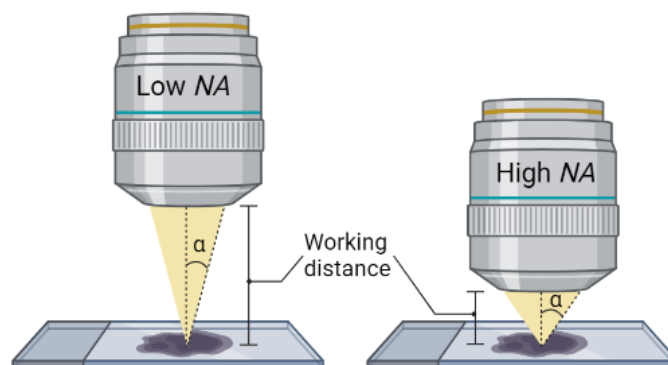
Figure 1.1-7.   Schematic representation of the numerical aperture. The low NA objective exhibits a long working distance and a narrow half-cone of light. In contrast, the high NA objective exhibits a short working distance and a broad half-cone of light.

Lateral resolution

The size and shape of the Airy pattern define the lateral resolution of an optical system. To explain this relation, let us now consider two adjacent emitting point sources located at the sample plane. When the distance between them is larger than the size of their corresponding Airy disks, the two spots can be distinguished as individual sources (left panel in Figure 1.1-8). However, when the distance is reduced, the overlap of the two Airy disks makes it difficult to discern the two sources as individual entities (right panel in Figure 1.1-8). Hence, one approach to improve the microscope's resolution consists of narrowing the size of the Airy disks, such

that the two emitters can be distinguished at a shorter separation distance. As discussed in the previous section, one way to achieve this is by increasing the numerical aperture.
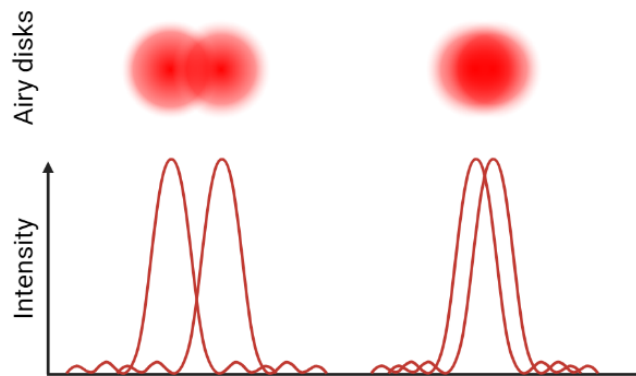
Figure 1.1-8.   Diffraction limit and resolution. The left panel illustrates two emitting sources separated by a resolvable distance. The right panel shows two emitting sources not resolved.

Resolution limit criteria

There are three popular criteria to estimate the lateral resolution of an optical microscope, namely, the Rayleigh, the Sparrow, and the Abbe criteria [35]. The difference between them is based on their conceptualization of what it meant for two objects to be resolvable. However, in all cases, the three criteria are linearly dependent on the wavelength of light and inversely proportional to the numerical aperture of the objective lens used for imaging. The Rayleigh criterion, frequently employed in spectroscopy and astronomy, establishes the resolution limit $R_{RAYLEIGH}$ of an optical microscope as the distance between two emitters when the maximum of one Airy disk overlaps with the first minimum of the second. Mathematically, it is expressed by Equation (1.1-6):

$$R_{RAYLEIGH} = \frac{0.61\lambda}{NA} \tag{1.1-6}$$

The Abbe criterion, commonly used in microscopy, is derived from Abbe's theory of image formation [36], which considers the diffraction orders intercepted by the microscope objective. The resolution limit R_{ABBE} is given by Equation (1.1-7):

$$R_{ABBE} = \frac{0.5\lambda}{NA} \tag{1.1-7}$$

Finally, the Sparrow criterion estimates the resolution $R_{SPARROW}$ by the distance at which a flat intensity profile between two maxima occurs. Equation (1.1-8) offers the mathematical notation for this criterion.

$$R_{SPARROW} = \frac{0.47\lambda}{NA} \tag{1.1-8}$$

The difference between these three criteria is small, and they all provide an approximation for the best possible resolution based on the full width at half-maximum (FWHM) of an ideal Airy disk. For example, using Abbe's criterion, the resolution limit of an ideal optical microscope becomes ~200 nm when using a high numerical aperture objective ($NA = 1.4$) and green light ($\lambda = 550$ nm). In reality, there exist other factors such as noise, optical aberrations, and sample imperfections that further degrade the resolution of the captured image below the theoretical diffraction limit, to around 250 nm – 300 nm. While using shorter wavelengths could also increase the resolution, these bring other challenges into the picture. First, short wavelengths carry more energy and, therefore, are incompatible with life cell imaging. Second, common optical elements have limited transmission of light in, for example, the ultra-violet spectra.

Since 1873, when the German physicist Erns Abbe [4] postulated the resolution was limited by diffraction, it was regarded as impossible to resolve sub-200 nm features by far-field optical microscopy methods. However, since the late 1990s, a new set of optical methods came into the microscopy arena, enabling sub-diffraction visualization of structures by cleverly manipulating the properties of light using fluorescent markers. The working principle of these methods, coined as super-resolution microscopy or optical nanoscopy, is discussed in section 1.3.

Axial resolution

The spreading caused by diffraction and interference of the light not only limits the lateral resolution at the image plane but also in the axial domain. In fact, the blur experienced by the light is more elongated along the optical axis of the microscope system. Consequently, the axial resolution of an optical microscope is worse than its lateral resolution. The axial resolution R_{AXIAL} of an optical microscope is approximated by Equation (1.1-9):

$$R_{AXIAL} = \frac{2\lambda}{NA^2} \qquad (1.1\text{-}9)$$

To give an example, considering the same parameters as before ($\lambda = 550$ nm, $NA = 1.4$), two emitters in the axial domain can only be distinguished if their separation is greater than 561 nm, as opposed to the ~200 nm in the lateral domain.

1.1.4 Frequency domain representation

The Fourier representation is a robust concept in optics and a useful tool to deal with mathematical operations related to image processing. As will become evident in further sections, the Fourier transform plays a crucial role in mathematical-driven microscopy methods such as deconvolution (DV) and structured illumination microscopy (SIM). To explain the Fourier theory, one needs to refer to two concepts: the real space domain (what our senses perceive), and the frequency domain (its mathematical representation). According to this theory, any single variable, continuous function $f(t) = A\cos(\omega t + \varphi)$ oscillating in real space (e.g., a periodic sound pressure wave) carries information in the form of an amplitude A, an angular frequency ω, and a phase φ that can be mapped in the frequency domain by a Fourier pair $F(\omega)$, stemming from the Fourier transformation. Moreover, the process is reciprocal, meaning that for a given Fourier pair in the frequency domain, there is a periodic signal in the

real space domain. Equation (1.1-10) shows the mathematical reciprocity of a single variable signal $f(t)$ and its representation in the Fourier domain $F(\omega)$:

$$f(t) = A\cos(\omega t + \varphi) \xoverleftrightarrow{Fourier} F(\omega) = \left\{\left(\frac{A}{2}e^{-j\varphi}\delta(-\omega)\right), \left(\frac{A}{2}e^{j\varphi}\delta(\omega)\right)\right\} \quad (1.1\text{-}10)$$

In this expression, the corresponding Fourier pairs are represented as two delta functions $\delta(\omega)$ located at angular frequencies $-\omega$ and ω, with complex amplitudes $\frac{A}{2}e^{-j\varphi}$ and $\frac{A}{2}e^{-j\varphi}$, respectively. The Fourier transform can be expanded from this one-dimensional case to multidimensional (e.g., 2D, 3D) periodic signals. Moreover, any oscillating signal in the real space domain can be represented in the frequency domain as the superposition of multiple sinusoidal waves, including the case of microscopy images. Here, the variations in brightness across the image field encode information in terms of spatial frequency (i.e., lines per unit distance), amplitude, orientation, and phase, all of which can be represented in the frequency domain by performing a Fourier transform.
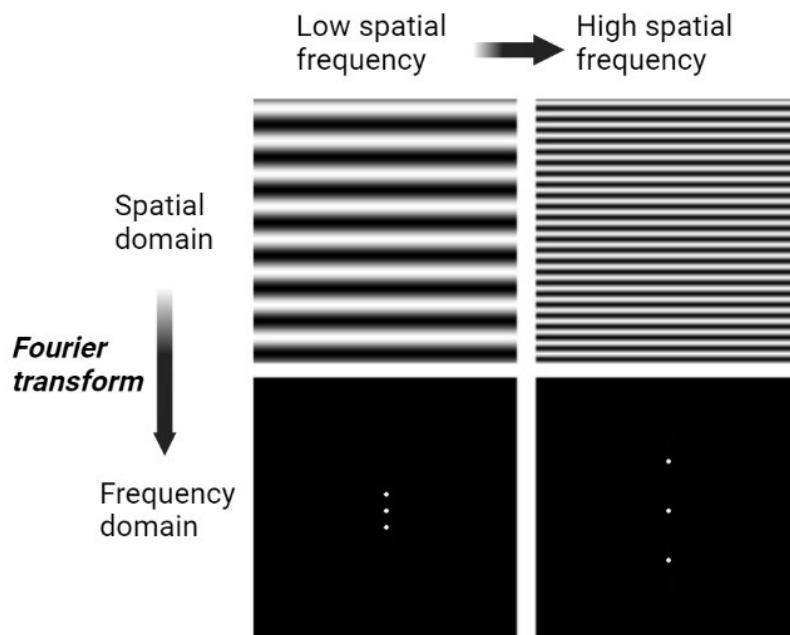
Figure 1.1-9. Frequency domain representation. Top panel: sinusoidal stripe patterns in the spatial domain. Bottom panel: reciprocal images in the frequency domain. Note that the spacing between the Fourier pairs (e.g. white dots) scales with the spatial frequencies.

To illustrate this, let us consider two different images containing straight fringe patterns of different periodicities, as shown in Figure 1.1-9. In the upper panel, the spatial frequency relates to the rate at which the dark and bright features repeat along the image field. Consequently, the coarsely spaced image on the top left carries a low spatial frequency, while the more finely spaced image on the upper right panel carries a higher spatial frequency. In the frequency domain, the Fourier pairs appear as three dots encoding the information carried by their corresponding images in the spatial domain. More specifically: a) the orientation of the Fourier pairs matches the orientation at which the intensity variations propagate in the image

field; b) the spread of the Fourier pairs, i.e., the distance from the origin, scales with the spatial frequency of the image field; and c) the intensity and phase values are encoded in the complex amplitudes of the two bright spots.

The optical transfer function

A key advantage of the Fourier theory is the convolution theorem, which allows turning complicated operations in the spatial domain, such as convolution, into a simple multiplication in the frequency domain. Therefore, the image function described in Equation (1.1-4) can be Fourier transformed as follows:

$$I(k) = O(k).OTF(k) \tag{1.1-11}$$

Where $I(k)$ is the Fourier value at a frequency k, $O(k)$ is the Fourier transform of the object, and $OTF(k)$ is the Fourier transform of the PSF, namely the optical transfer function (OTF) of the system[6]. Figure 1.1-10 provides an example of the reciprocity between the space and the frequency domain. In the top panel, the object is convolved with the microscope's PSF in the real space domain, rendering an image that lacks high-frequency information. Equivalently, in the frequency space, the object is multiplied by a bandwidth-limited OTF, resulting in a diffraction-limited image.
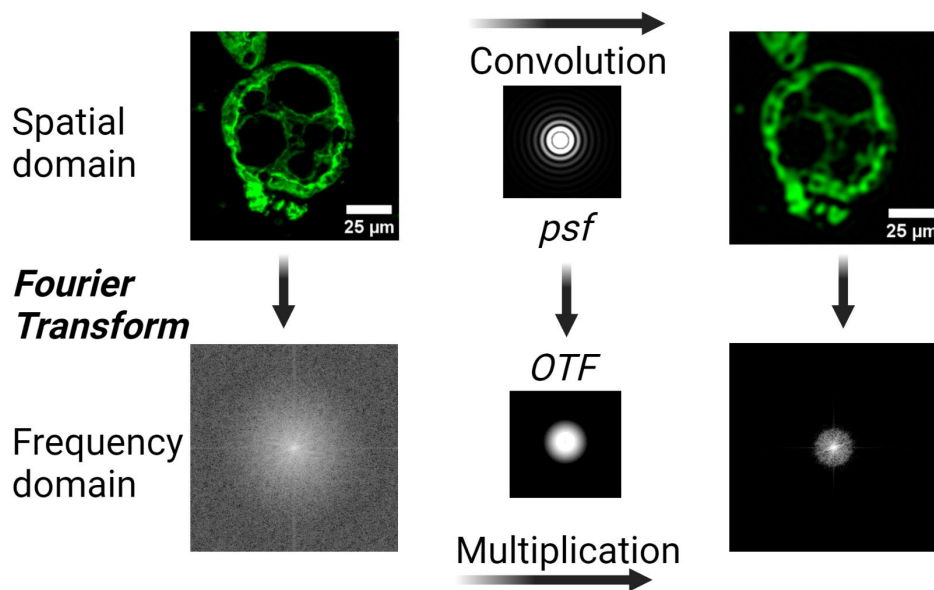
Figure 1.1-10.   Correspondence between the spatial and the frequency domain. The top-left panel illustrates a tissue sample being imaged on a microscope. In the spatial domain, the object is convolved with the microscope's PSF to render a microscopy image. Equivalently, in the frequency domain, the Fourier transform of the object is multiplied by the microscope's OTF, which effectively acts as a low-pass filter. In this example, all the grayscale images have been saturated for illustration purposes.

---

[6] As a convention in this document, capital letters sybolize the Fourier transform of the a given signal.

In microscopy, the modulus of the OTF, namely the modulation transfer function (MTF), provides valuable information such as the amplitude modulation and the cutoff frequency. The first relates to the decay of intensity, resulting from diffraction and interference, experienced by the different spatial frequencies at the image plane. The second relates to the highest spatial frequency supported by the objective lens, and consequently, to its resolution limit. Effectively, the OTF functions as a low-pass filter positioned at the origin of the frequency spectrum, which gradually reduces the signal strength away from the center. Consequently, as the objective lens sets the spatial frequency limit collected by a microscope, from the Fourier domain perspective this optical element is commonly acknowledged as a low-pass filter.

1.1.5 Contrast

Our visual system works by distinguishing the elements present across the field of view. Contrast, defined as the difference in intensity or color between an object and its surroundings, is an essential factor for visual perception. In essence, the higher the contrast, the sharper we see, and the lower the contrast, the poorer we see.

Contrast is not an inherent property of the specimen, but it is subject to the interaction of the specimen with light. A wide range of biological specimens such as cells and tissues are either transparent or translucent, requiring a contrast enhancement mechanism to become visible under the microscope. These mechanisms can be categorized into two groups: label-free methods and label-based methods. Label-free methods utilize physical phenomena such as [37]: a) light interference (e.g., phase-contrast microscopy, differential interference contrast microscopy); b) light scattering (e.g., Raman spectroscopy, darkfield microscopy, optical coherence tomography); or c) nonlinear effects (e.g., second harmonic generation). On the other hand, label-based methods rely on the application of chemical compounds that either absorb or emit light to stain specific areas of the tissues, thereby improving their visualization under a microscope. A useful implementation of this principle is fluorescence microscopy, further detailed in section 1.2.

The distribution of contrast is not uniform across the different spatial frequencies in a microscopy image. The MTF enables high contrast for lower spatial frequencies (e.g., larger sample features), and low contrast for higher spatial frequencies (e.g., smaller sample features) [35]. As a result, the level of contrast ultimately governs the extent of detail that can be observed within the physical limits of the microscope. In addition, the presence of background signals and system noise adds complexity to the identification of small sample features.

This thesis explores diverse strategies for improving contrast in histology. These include the use of fluorescent dyes and a combination of various optical and analytical methods to minimize the background signals. Sections 1.2 and 1.3 offer an overview of such methods.

1.1.6 Imaging throughput

In microscopy, imaging throughput is defined as the rate at which a microscope technique can acquire and process images. It represents the efficiency of the method in capturing and handling images within a given timeframe. The throughput is typically measured in terms of the number of images acquired or processed per unit of time.

As illustrated in Figure 1.1-11, several factors contribute to the imaging throughput of a microscope method. These include [38]:

Sample preparation: most samples require a certain degree of manipulation before visualization in a microscope. In the case of biological tissues, for example, this encompasses several steps including organ sampling, fixation, preservation, sectioning, and labeling. As will be detailed in 1.4.2, the complexity of such steps varies dramatically depending on the chosen microscopy method, therefore affecting the overall throughput of the methodology.

Acquisition speed: the speed at which the microscope can capture images depends on factors such as the sensor readout speed, exposure time, number of frames, and the exploitable field of view. All these parameters are relevant for super-resolution imaging (see section 1.4.1). For example, while some super-resolution techniques (e.g., SIM and FF-SRM) require a relatively low number of frames, other SRM methods such as SMLM, demand thousands of frames, therefore limiting the imaging throughput.

Data transfer and storage: the throughput also depends on how efficiently the system can transfer and store the acquired images. This includes considerations such as data transfer rates, storage capacity, and the performance of the storage medium.

Processing capabilities: once the images are acquired and stored, the processing speed determines how quickly the system can handle and analyze the captured data. This includes tasks like image denoising, resolution and/or contrast enhancement, feature extraction, mosaic stitching, or any other image processing task. The efficiency of the software algorithms used for image processing and analysis also affects the throughput.
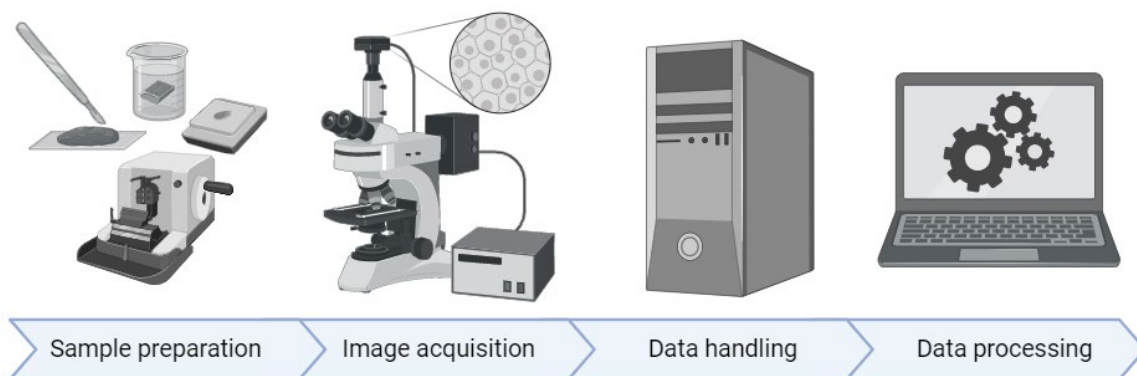
Figure 1.1-11. Imaging throughput in microscopy. Several factors contribute to the rate at which microscopy images can be obtained. These include sample preparation, image acquisition, data storage and handling, and data processing.

Imaging throughput is a critical factor for the adoption of SRM methods in life sciences and, particularly, in histology. In medical practice, higher throughput enables faster image acquisition and analysis, which contributes to cost reductions, improved productivity, and more accurate diagnosis. Diverse methodologies have been proposed for different SRM methods to increase the imaging throughput in super-resolution microscopy, including automated acquisition over multiple regions of interest [39], reduction in the number of frames [13], or expansion of the image FOV [32, 40]. The last two strategies are explored in this thesis through the photonic chip-based microscopy methodology (see Chapter 3).

1.2 Fluorescence microscopy

Fluorescence microscopy encompasses a wide variety of optical methods that exploit the properties of fluorescence. Fluorescence is a natural phenomenon in which a substance absorbs light at a particular wavelength and then re-emits light at a longer wavelength, typically in the visible or near-infrared spectrum. It is a type of photoluminescence, which involves the emission of light by a material after the absorption of photons.

To describe the process of fluorescence, let us revisit the concept of photons. Light can be described not only as a wave but also as a collection of particles known as photons. Photons carry discrete amounts of energy, which are inversely proportional to the wavelength of light according to the Planck-Einstein equation:

$$E = hf = \frac{hc}{\lambda} \tag{1.2-1}$$

Where E corresponds to the photon energy, h is the Planck constant, c is the speed of light, and λ is the wavelength of light.

The fluorescence process is composed of three phenomena, namely, absorption, relaxation, and emission, which are schematically represented in the simplified Jablonski diagram of Figure 1.2-1. When a substance is exposed to light, it can absorb photons if the energy of the photons matches the energy levels of the substance's electrons. The absorbed photons elevate the electrons from the ground state (S_0) to a higher energy level (S_2), creating an excited state (i.e., blue arrow). Thereafter, in a short time (called fluorescence lifetime), the molecules transition to a lower excitation energy level S_1, losing some energy in the form of vibration and heat. Finally, the molecules transition back to the ground state level by releasing energy in the form of a photon, in a process called radiative relaxation, (i.e., green arrow). The fluorescence lifetime spans a short timescale, typically on the order of picoseconds to nanoseconds depending on the fluorescent molecule.
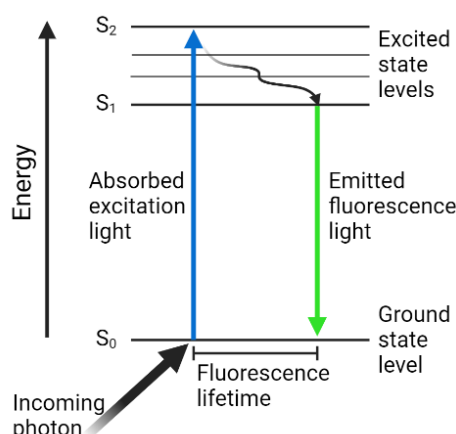
Figure 1.2-1.   Simplified Jablonski diagram. Upon excitation by a photon, the fluorescent molecule transitions from the ground state level to an excited state. After a short relaxation time of combined vibrational and heat losses, the molecule transitions back to the ground state emitting light with a less energetic wavelength compared to the excitation light. Adapted from ref. [41].

Due to the principle of energy conservation, the emitted photon carries less energy than the absorbed excitation photon. Therefore, evaluating the photon energy in Equation (1.2-1), we obtain that - for the case of single-photon excitation - the wavelength of the emitted light is larger than the wavelength of the excitation light. The difference between absorption and emission wavelengths is known as the Stokes' shift, and each fluorophore type exhibits characteristic absorption-emission spectra.

Advantages and limitations of fluorescence microscopy

In fluorescence microscopy, fluorophores are used to label specific structures of interest within the specimen, allowing for superior contrast imaging compared to brightfield methods (Figure 1.2-2a). Moreover, by employing highly selective labeling strategies, a high degree of specificity is also achieved. Fluorescence microscopy has a competitive advantage over traditional low-contrast microscopy methods, e.g. brightfield microscopy, where both the sample and the background are visualized. Particularly, fluorescence microscopy restricts the visualization of the background signal, which shows dark, in favor of the fluorescently labeled structures, which show bright (see Figure 1.1-2b). To achieve this, the sample is illuminated with a specific wavelength that matches the excitation spectra of the fluorescent marker. Then, by using a specific set of bandpass optical filters, the excitation light is blocked while the emitted fluorescence light is captured by a camera detector.
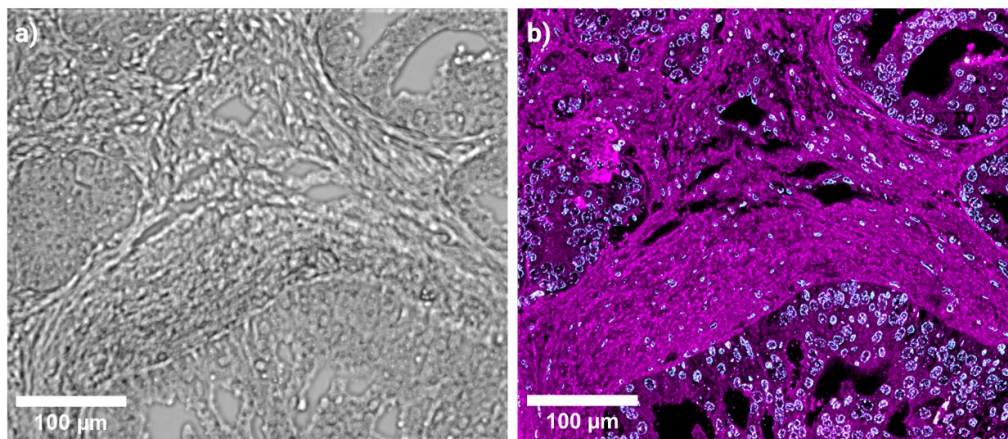
Figure 1.2-2.   Comparison between brightfield and fluorescence microscopy. a) A human prostate tissue section imaged in brightfield modality. The low contrast between the sample and the background makes it difficult to appreciate the morphological information of the tissue. b) The same sample was imaged in fluorescence modality. Here, the high specificity and superior contrast supported by the fluorescent markers allow for the identification of nuclei in cyan, and the membranes in magenta. Adapted from Paper III.

Despite its multiple advantages compared to, for example, brightfield microscopy, fluorescence microscopy also exhibits limitations: a) Upon illumination, the fluorophores can undergo a chemical change that regards them as non-fluorescent, in a process referred to as photobleaching [42]. Photobleaching limits the imaging duration and the quality of the fluorescent data; b) In addition, the interaction between fluorophores, living biological samples, and light (particularly for shorter wavelengths), can induce the formation of reactive oxygen species (ROS) that disturb the natural conditions of the specimens, in a process known

as phototoxicity; c) Moreover, some cellular components may be autofluorescent to specific wavelengths used in the experiment, potentially increasing the background signal and therefore reducing the image contrast. As will be illustrated in Chapter 2, tissue autofluorescence can be detrimental to imaging techniques such as structured illumination microscopy.

Like in any other optical method, the spatial resolution of fluorescence-based microscopy is limited by diffraction. However, there is a good amount of information within the resolution boundaries of fluorescence microscopes that can be visually enhanced by improving the contrast. The next section covers the diffraction-limited fluorescence-based methods used in this study[7], namely epifluorescence (EPI), total internal reflection fluorescence (TIRF), and deconvolution (DV) microscopy. Their advantages and tradeoffs are hereby discussed.

1.2.1 Widefield epifluorescence microscopy

The most employed fluorescence-based microscopy configuration makes use of a single objective both for the illumination (e.g., fluorophore excitation), and the signal collection (e.g., capturing the fluorescence emission). This configuration, known as widefield epifluorescence, or EPI, is schematically represented in Figure 1.2-3a. In an EPI microscope, a light beam originating at a light source (e.g., laser, light-emitting diode LED, or halogen lamp), passes through an excitation filter and is then redirected by a dichroic mirror to the microscope objective. Then, the incoming light excites the fluorescent molecules in the specimen, which undergo fluorescence. Both the emitted light and part of the excitation light are collected by the objective lens and further propagated through the optical system. Thereafter, an emission filter blocks the remanent excitation light and allows propagation of the emission signal. Finally, the fluorescent signal is refracted by the tube lens to a camera sensor that records it.

The general EPI configuration described here is relatively simple to build and affordable. Moreover, being a widefield technique, it allows for single-shot acquisition over the entire FOV, which is a desired feature for high-throughput imaging. However, this method exhibits two known tradeoffs, namely, out-of-focus blur and anisotropic image field illumination. The former is depicted in Figure 1.2-3b. Here, the excitation light illuminates the whole sample volume and records the fluorescent emission occurring along the axial direction of the microscope. Consequently, an out-of-focus blur is introduced, reducing the contrast of the features in the focal plane and, therefore, hampering the interpretability of the image. The latter, illustrated in Figure 1.2-3c, relates to the illumination profile of the excitation beam. In this case, the characteristic Gaussian distribution of EPI illumination renders non-uniform intensities across the image field, with the central part exhibiting a brighter signal compared to the borders of the image. This compromises the exploitable FOV to a portion of the image field, therefore reducing the throughput capabilities of the method and introducing stitching artifacts that affect the overall visualization of large samples (Figure 1.2-3d).

---

[7] The list of fluorescence-based microscopy methods is extensive, and detailing them is beyond the scope of this work.
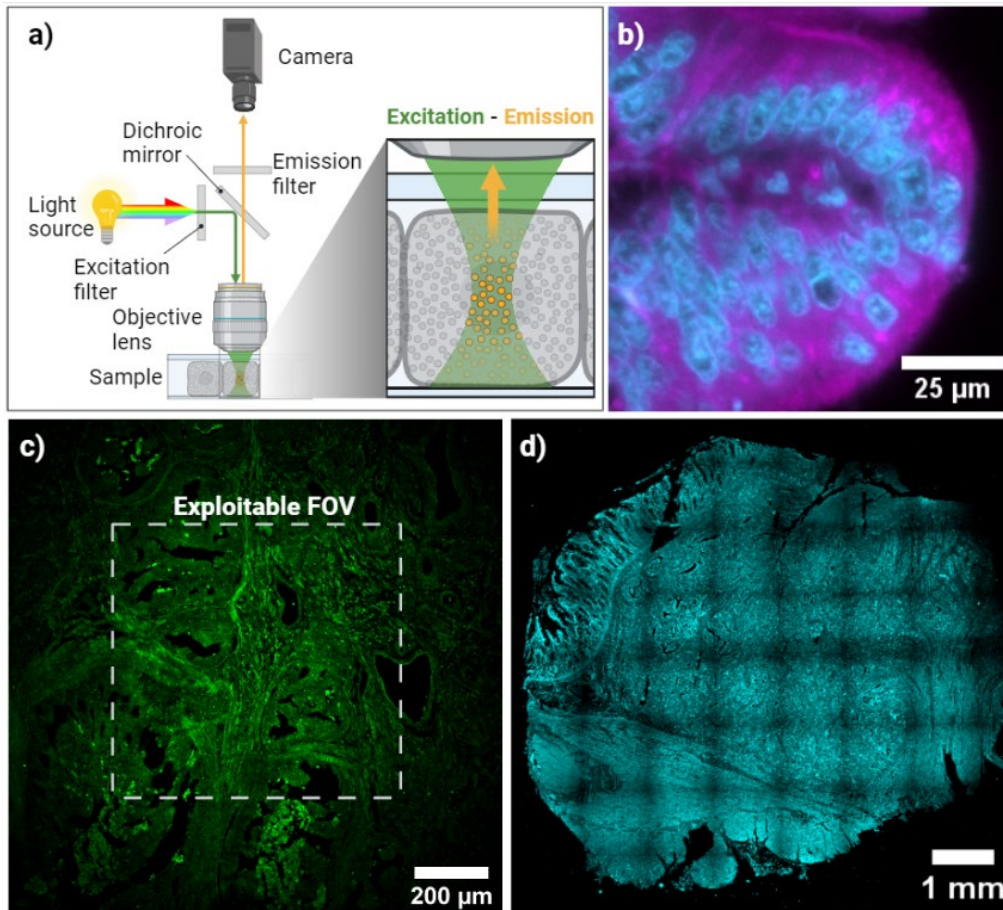
Figure 1.2-3. Epifluorescence microscopy. a) Schematic representation of an epifluorescence microscope setup. b) Multicolor EPI image of a colorectal tissue section. Membranes in magenta and nuclei in cyan. The out-of-focus light introduces blur and limits the image contrast. c) EPI image of a prostate tissue section. The white-dotted box denotes the exploitable FOV. The vignetting effect along the periphery of the image is caused by the Gaussian profile illumination. d) Large FOV image of a colorectal tissue sample. The grid-like dark bands are stitching artifacts stemming from the non-uniform illumination on the constituent EPI images. Adapted from Paper III.

There are diverse strategies for improving the image contrast and for enhancing the exploitable FOV in epifluorescence-based microscopy. The contrast enhancement approaches seek to remove the off-focus signal, while the FOV improvements aim for a uniform distribution of the illumination intensities across the image field, such as the use of dynamic speckle illumination strategies [32]. A brief description of these methods is presented hereby.

Contrast enhancement approaches for EPI-based microscopy:

Removing the off-focus information is essential for an accurate interpretation of the fluorescent data. Within the field of concern for this thesis, namely histology, this can be achieved in three ways:

By physical sectioning. A simple yet useful method to increase the contrast in EPI-based microscopy is by employing thin samples. By reducing the thickness of the samples, less out-of-focus contribution is captured and, therefore, less blur is perceived in the fluorescence image. The thickness of histological samples depends highly on the chosen

preservation and sectioning methods. In the case of paraffin-embedded formalin-fixed (FFPE) samples, for example, the thinnest possible thickness varies between 2-4 μm [17]. Alternative methods such as the Tokuyasu technique or resin embedding can achieve thinner sections, down to 70 nm [43], which dramatically improves the contrast compared to the FFPE method. Both the FFPE and the Tokuyasu methods are studied in this doctoral thesis. Further information about these histological methods is presented in section 1.4.

By optical sectioning. This strategy consists of manipulating the excitation and/or emission light paths to selectively illuminate and collect information from specific planes of the sample. By performing optical sectioning, the out-of-focus information can be minimized and, therefore, the image contrast be enhanced. There exist various EPI-based microscopy methods performing optical sectioning. These include confocal microscopy [44], multi-photon excitation microscopy [45], oblique-plane illumination microscopy [46], and total internal reflection fluorescence (TIRF) microscopy [47]. The latter, TIRF, is an essential element of this doctoral thesis and is further addressed in sections 1.2.3 and Chapter 3.

By image post-processing. An alternative route for out-of-focus light removal is by using computational methods. These include mathematical-based algorithms such as deconvolution microscopy (DV) [48], structured illumination microscopy (SIM) [12], fluorescence fluctuations-based microscopy (FF-SRM) [13], and machine learning [49, 50]. The DV, SIM, and FF-SRM methods are explored in this thesis. Detailed information for such methods is provided in sections 1.2.2, 1.3.1, and 1.3.3, respectively.

1.2.2 Deconvolution microscopy

Deconvolution, in short DV, is a computational technique used to improve image quality by removing the out-of-focus blur caused by diffraction. It enhances the latent fine details present in raw images, making it easier to interpret the underlying structures in the specimen. The DV method is commonly used in fluorescence microscopy to enhance the image contrast by reassigning the off-focus light to its original plane location. The method involves the acquisition of multiple images along the optical axis of the microscope (e.g., z-stack), which are computationally enhanced by a post-processing algorithm [48].

Mathematically, the concept behind the DV method is simple and can be derived from Equation (1.1-11) in section 1.1.4. Here, as outlined below in Equation (1.2-2), the Fourier values of the object $O(k)$ can be calculated by dividing each point in the Fourier image, $I(k)$, by its corresponding point in the optical transfer function $OTF(k)$. Subsequently, the original object, $o(r)$ in the spatial domain is obtained by the inverse Fourier transform F^{-1}.

$$O(k) = \frac{I(k)}{OTF(k)} \xrightarrow{F^{-1}} o(r) \qquad (1.2\text{-}2)$$

In practice, the high-frequency noise values $n(k)$ carried by the image $I(k)$ become amplified in the division by the low $OTF(k)$ amplitude values near the cutoff frequency of the microscope, transforming this simple idea into a complicated operation. To circumvent this issue, in the DV method, the object $\hat{O}(k)$ is estimated. Nowadays, there exists a wide variety of reconstruction algorithms under the umbrella of deconvolution, some of them requiring specific parameters and thresholds to achieve the best results. Among them, the Wiener

deconvolution and the Richardson-Lucy deconvolution are well-known in fluorescence microscopy [48], yet there are many other approaches, including artificial intelligence-based deconvolution [51].

While deconvolution offers high-contrast fluorescence images with a resolution near the diffraction limit of the microscope, it is susceptible to imaging artifacts such as noise amplification and ringing pseudo-structures around bright sample features. Therefore, the selection of adequate parameters is key for successful image reconstruction. Additionally, for accurate results, the experimental PSF should match that of the expected PSF used by the reconstruction algorithm, as deviations from it may lead to unrealistic reconstructions.

Advanced deconvolution theory is commonly used by super-resolution methods such as the fluorescence fluctuations-based SRM (FF-SRM), further detailed in section 1.3.3.

1.2.3 Total internal reflection fluorescence microscopy

Total internal reflection fluorescence (TIRF) microscopy is an optical imaging technique that allows for thin optical sectioning at the interface between the sample media and its supporting substrate, enabling high-contrast visualization of sample features over a single plane. The technique builds upon the principle of total internal reflection (TIR), discussed hereby.

Total internal reflection

Total internal reflection (TIR) is a phenomenon that occurs when light traveling within a medium encounters the interface of another medium and, instead of transmitting through the interface, it is reflected back entirely into the original medium.
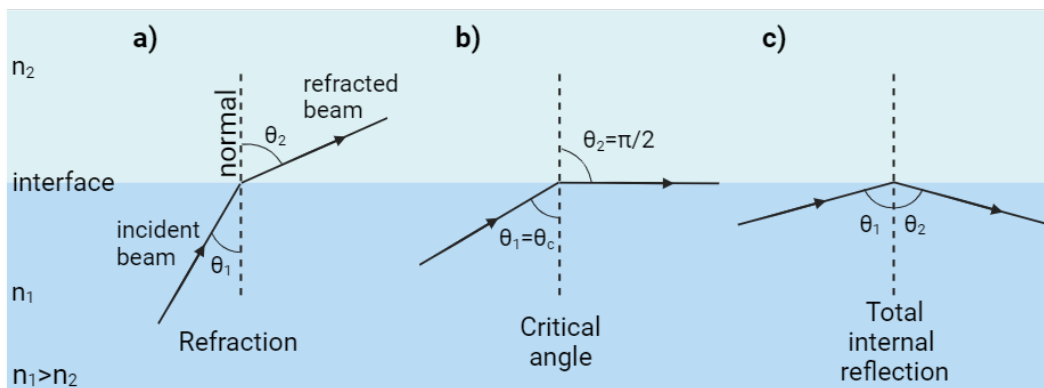
Figure 1.2-4.   Principle of total internal reflection. a) an incident ray at an angle θ_1 passes from a medium with a refractive index n_1 to a medium with a refractive index n_2 (where $n_1 > n_2$), and is refracted at an angle θ_2 according to Snell's law. b) at a critical angle $\theta_1 = \theta_c$ the refracted angle θ_2 reaches $\pi/2$. c) by increasing the incident angle beyond the critical angle ($\theta_1 > \theta_c$), the boundary of the two media acts as a mirror, reflecting the light inside the medium n_1.

To explain this principle, let us consider a scenario where a light ray transitions from a medium n_1 to a medium n_2, where $n_1 > n_2$ (Figure 1.2-4a). In this condition, according to Snell's law, the refracted ray will exhibit a larger angle θ_2 compared to the incident angle θ_1. Upon increasing the angle of incidence, the angle of refraction also increases, until the condition of

the critical angle $\theta_1 = \theta_c$ is met, and $\theta_2 = \pi/2$ (Figure 1.2-4b). Thereafter, for an incident angle $\theta_1 > \theta_c$, the boundary of the two media acts as a perfect mirror, reflecting the ray into the medium n_1 (Figure 1.2-4c). Accordingly, TIR occurs when the condition $\theta_1 > \theta_c$ is satisfied.

Total internal reflection (TIR) is the basis for several optical applications such as optical fibers, reflecting prisms, and total internal reflection fluorescence microscopy.

Evanescent field excitation

When the TIR condition is satisfied, an evanescent field originates at the boundary of the two media (Figure 1.2-5a), with an exponentially decaying profile extending a short distance ($\sim$20 nm to $\sim$200 nm) from the interface according to the expression [47, 52]:

$$I(z) = I_0 e^{-\frac{z}{d}} \tag{1.2-3}$$

Where $I(z)$ is the intensity at a distance z away from the medium with a higher refractive index (i.e., n_1), I_0 is the intensity at the interface, and d is the depth of penetration of the evanescent field. As a convention, the penetration depth of the evanescent field is defined as the distance z at which the intensity approximates $I(z) = I_0/e$, and its mathematical formulation is given by:

$$d = \frac{\lambda}{4\pi\sqrt{n_1^2 sin^2\theta_1 - n_2^2}} \tag{1.2-4}$$

As outlined in Equation (1.2-4), the extent of the evanescent field depends on several parameters including the wavelength λ of the light beam being reflected, the refractive index of the two media n_1 and n_2, and the angle of incidence θ_1.

In biological applications of TIR, such as in fluorescence microscopy and biosensing [53], a short penetration depth is beneficial both for a selective interrogation of the sample and for an increased signal-to-background (SBR) ratio. In such applications, the extent of the evanescent field can be confined by: a) using short excitation wavelengths; b) increasing the illumination angle; and c) enhancing the refractive index contrast between the sample medium and the supporting TIR substrate. Particularly, biological samples exhibit heterogeneous refractive indices [54], ranging from 1.36 to 1.6. Therefore, the selection of the supporting TIR substrate material is fundamental for achieving high refractive index contrast and, consequently, a confined penetration depth. The graph in Figure 1.2-5b illustrates the penetration depth of a TIR system as a function of the refractive index contrast between the core material (e.g., sample substrate) and the sample media. In this particular example, parameters such as the illumination wavelength and the angle of incidence are kept to fixed values of $\lambda = 561$ nm and $\theta_1 = 75$ degrees, respectively.
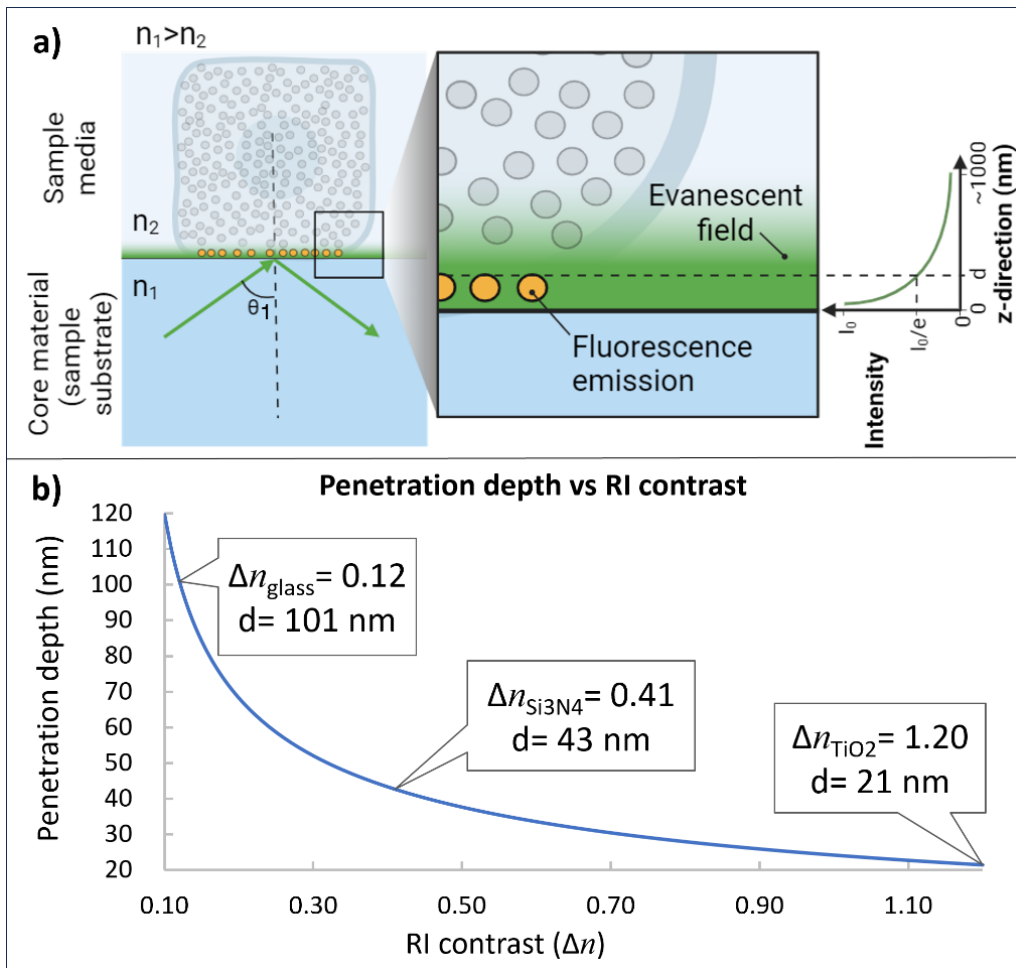
Figure 1.2-5. Evanescent field excitation. a) Schematic representation of the evanescent field and its use in total internal reflection fluorescence microscopy. The dark-dotted line illustrates its penetration depth. b) Penetration depth as a function of the refractive index (RI) contrast between the core material and the sample media. The penetration depths attainable with three different core materials are presented, including glass, silicon nitride (Si_3N_4), and titanium dioxide (TiO_2). Higher RI contrast allows for shorter evanescent field depths. Adapted from Paper III.

TIR-based fluorescence microscopy

The high intensity of the evanescent field produced by TIR can be harnessed to induce spontaneous emission of fluorescent molecules on its reach. This is the working principle of total internal reflection fluorescence (TIRF) microscopy. In this method, illustrated in Figure 1.2-5a, the fluorescently labeled sample and its surrounding medium, denoted with refractive index n_2, are placed over a substrate with a higher refractive index n_1. Upon TIR illumination, the fluorophores located at the sample-substrate interface are excited by the evanescent field. The emitted fluorescence is then collected by an objective lens and further recorded by a camera sensor. Since only fluorophores in close proximity to the interface are effectively excited, TIRF microscopy selectively captures the information at or near the sample-substrate interface, resulting in ultrathin optical sectioning that renders a high-contrast image of the specimen.

TIRF microscopy is an established method in cell biology for the study of cellular processes occurring near the plasma membrane, such as cell signaling, membrane dynamics, and protein interactions [55]. However, in recent years, there has been an increasing interest in this method for the visualization of tissues since it offers high sensitivity, reduced background noise, and the ability to visualize single-molecule fluorescence events, all valuable features for super-resolution microscopy [56, 57].

There are multiple TIRF microscope configurations nowadays. These are broadly divided into two categories including glass-based TIRF and waveguide-based TIRF.

1.2.3.1 Glass-based TIRF microscopy

As the name suggests, glass-based TIRF approaches use glass substrates for the realization of TIR. Typical examples are glass coverslips and microscope glass slides made of borosilicate ($n \approx 1.52$). There are two approaches within this category, namely objective-based TIRF microscopy and prism-based TIRF microscopy [52].
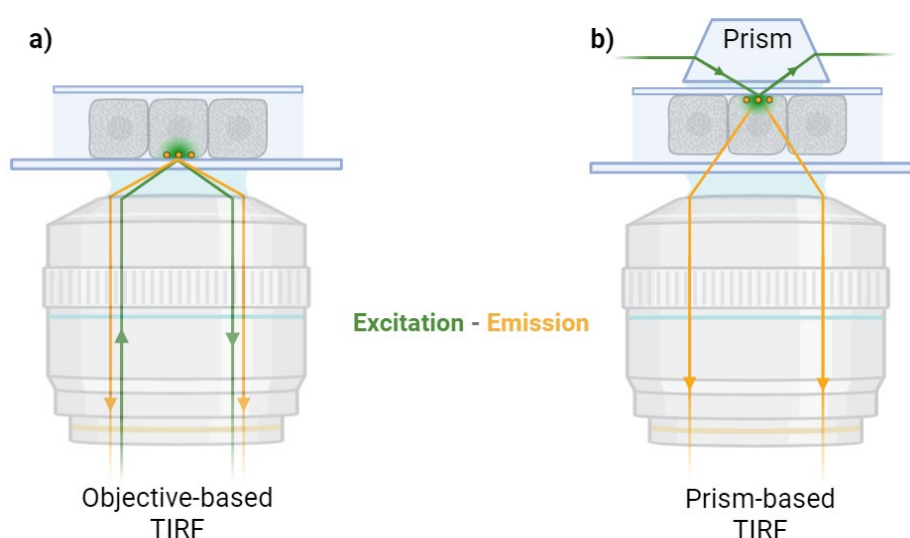
Figure 1.2-6.   Glass-based TIRF microscopy configurations. a) In the objective-based TIRF configuration, an objective lens is used both for the illumination and collection of the fluorescent signal. To achieve the high angles for TIR, a high NA is required. This also entails high magnification and, as such, a limited FOV. b) In the prism-based TIRF configuration the illumination and collection paths are decoupled, such that the excitation is achieved via a prism element, and the fluorescent signal is captured with an arbitrary objective lens.

Objective-based TIRF microscopy. The most commonly employed glass-based TIRF configuration consists of an EPI-based scheme where a single objective is used both for high-angle illumination and subsequent collection of fluorescence (Figure 1.2-6a). To achieve the TIR angles, a high numerical aperture is required and, consequently, high magnification objectives are used [47]. Typical TIRF objectives range from 60X/1.45NA to 100X/1.7NA. As discussed in section 1.1.2, a practical consequence of using high magnification objectives for imaging is the restricted FOV these offer. In typical objective-based TIRF configurations, the FOV usually spans 50 µm × 50 µm [21], which in many cases is insufficient for high-content screening such as in large cultured cell populations or

tissue sections. There are several objective-based TIRF solutions commercially available for microscopy under the umbrella of renowned brands such as Olympus, Zeiss, Leica, and Nikon.

Prism-based TIRF microscopy. An alternative glass-based TIRF approach uses a prism element to achieve the inclined angles required for TIR [58]. As illustrated in Figure 1.2-6b, in this configuration, the illumination and the collection light paths are decoupled, enabling the collection of the fluorescent emission with an arbitrary objective lens regardless of its numerical aperture and magnification. However, the prism-based TIRF method has gained attention over recent years in the research community due to its affordability and relatively low fabrication complexity, enabling unprecedented results in terms of both FOV [59] and lateral resolution [56]. To the best of our knowledge, there is only one commercial supplier of prism-based TRIF microscopy called TIRF Labs, based in North Carolina, USA.

Despite the simplicity, affordability, and commercial availability of these methods, the glass-based TIRF microscopy approach faces some limitations including: a) low refractive index contrast between the sample medium and the substrate, leading to extended penetration depths (Figure 1.2-5b); b) the need for free-space optomechanical elements along the excitation light path to control the illumination angles; and c) in the case of objective-based TIRF, a limited FOV. To alleviate these limitations, a waveguide-based TIRF microscopy has been proposed. The working principle of this method is discussed hereby.

1.2.3.2 Waveguide-based TIRF microscopy

An alternative route to harness evanescent field excitation for fluorescence is via waveguide propagation. The waveguide-based TIRF method is similar to that of glass-based TIRF described in the previous section, except that in this case the excitation light is tightly confined to a light-guiding structure. The guiding structure, commonly referred to as the waveguide core, consists of a thin-film geometry made of a high refractive index material deposited over a planar substrate for mechanical support. To perform TIRF microscopy, a light beam is coupled to the guiding structure, allowing for light propagation via the principle of total internal reflection. Thereafter, the evanescent field excites the part of the sample in the vicinity of the waveguide core surface, promoting fluorescence emission that is independently collected by a microscope objective, and finally recorded by a camera sensor. Figure 1.2-7a offers a schematic representation of waveguide-TIRF microscopy.

Since the pioneering report of evanescent field excitation using a Ta_2O_5 waveguide, published in 2005 [60], the field of waveguide-based fluorescence has gained increasing attention, enabling applications in microscopy [61-64] and biosensing [61]. Initial reports, however, revealed challenges with non-uniform illumination, which hampered the technique's widespread adoption. One decade later, advancements in waveguide fabrication using semiconductor photolithography processes [65, 66], led to the first report of photonic chip-based TIRF microscopy showcasing uniform illumination on liver endothelial cells [67]. Since then, the field of photonic chip-based TIRF microscopy has experienced rapid growth, facilitating high-resolution observations of cellular organisms in both fixed [20-22, 28] and living conditions [68, 69], over large FOVs. Figure 1.2-7b shows a laser beam propagating along a photonic chip. In this configuration, the objective lens on the left side of the image is

used for light coupling into the waveguide geometry, while the top objective is used for the collection of the fluorescent signal.
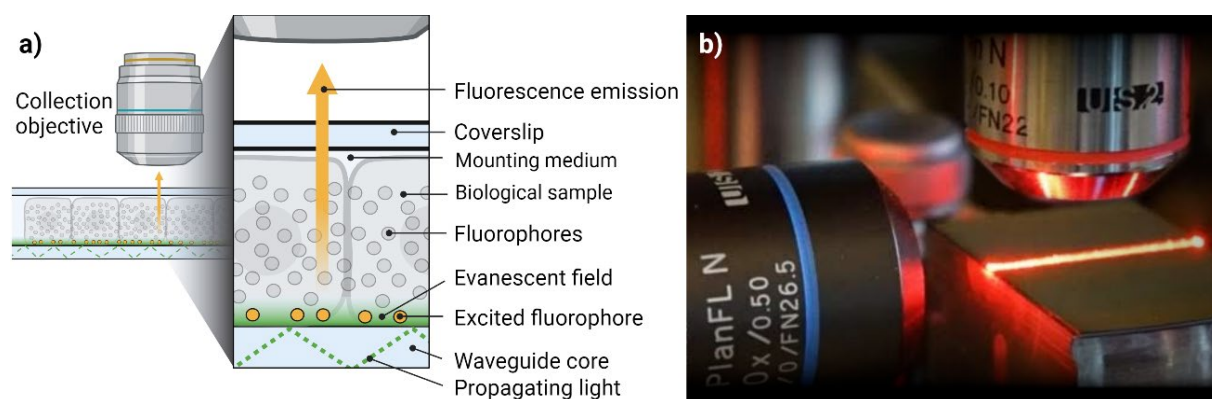
Figure 1.2-7.   Waveguide-based TIRF microscopy. a) The waveguide-based TIRF principle is similar to that of glass-based TIRF, except that in this case the excitation light propagates through a light-guiding structure commonly referred to as the waveguide core. b) A red laser beam propagating in a photonic waveguide-based chip. The objective lens on the left side is used for light coupling, while the objective on the top is used for the collection of the fluorescent signal.

There are multiple waveguide-based TIRF configurations, depending on the materials used, the fabrication method, the coupling and collection strategies, the waveguide geometry, and the excitation light distribution. More specifically:

Materials and fabrication. There are two waveguide-based TIRF platform variants, one using opaque and another using transparent substrates (Figure 1.2-8). The first version, known as a photonic chip, or photonic integrated circuit (PIC), owes its opacity to the use of materials from the semiconductor industry. The photonic chips are typically made of three layers. The bottom layer consists of an opaque material, namely silicon (Si, $n \approx 4$), followed by a cladding layer of silicon dioxide (SiO_2, $n \approx 1.46$), and a top layer, namely the waveguide core, made of higher refractive index material. As will be further detailed in Chapter 3, in this thesis, we used either silicon nitride (Si_3N_4, $n \approx 2$) or tantalum pentoxide (Ta_2O_5, $n \approx 2.14$) as waveguide core materials. The transparent version, on the other hand, consists of two combined layers either of a) fused silica ($n \approx 1.46$) for the substrate and tantalum pentaoxide for the waveguides [23]; or b) borosilicate glass for the substrate ($n \approx 1.52$) and a photoresist polymer (EpoCore, $n \approx 1.59$) for the waveguides [70]. Photonic chips containing silicon nitride or tantalum pentaoxide waveguides can be mass-produced at high-end foundries following matured semiconductor fabrication processes such as complementary metal-oxide semiconductor (CMOS) [22, 23]. The polymer waveguide platforms, although comparatively less developed than the semiconductor approach, hold good promise for mass fabrication, requiring simpler and accessible laboratory tools such as spin-coaters, ablation lasers, and UV light [70]. A critical aspect of the fabrication process is the imperfections. Fabrication imperfections can alter the light-guiding properties of the waveguide by introducing impurities (e.g., dust particles or debris) and/or by altering the geometry of the waveguides (e.g., side-wall roughness). Therefore, regardless of the chosen fabrication method, several optimization steps are necessary to achieve the desired light-guiding behavior of the waveguides.
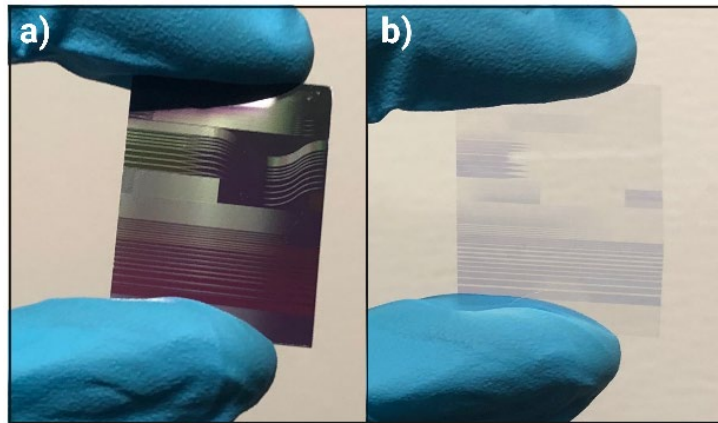
Figure 1.2-8.   Waveguide-based TIRF in opaque and transparent configurations. a) Photonic waveguide-based chip in opaque configuration. b) Photonic waveguide-based chip in transparent configuration. Adapted from ref. [23].

Objective lens orientation. In fluorescence microscopy, two common strategies are used for collecting the emitted light, namely the *upright* and the *inverted* configurations. In the upright configuration, the objective lens is positioned on top of the sample, whereas in the inverted configuration, it is positioned underneath. In waveguide-based TIRF, opaque chips allow only for upright collection [68], whereas transparent chips allow for either upright or inverted collection [23, 70] (Figure 1.2-9).
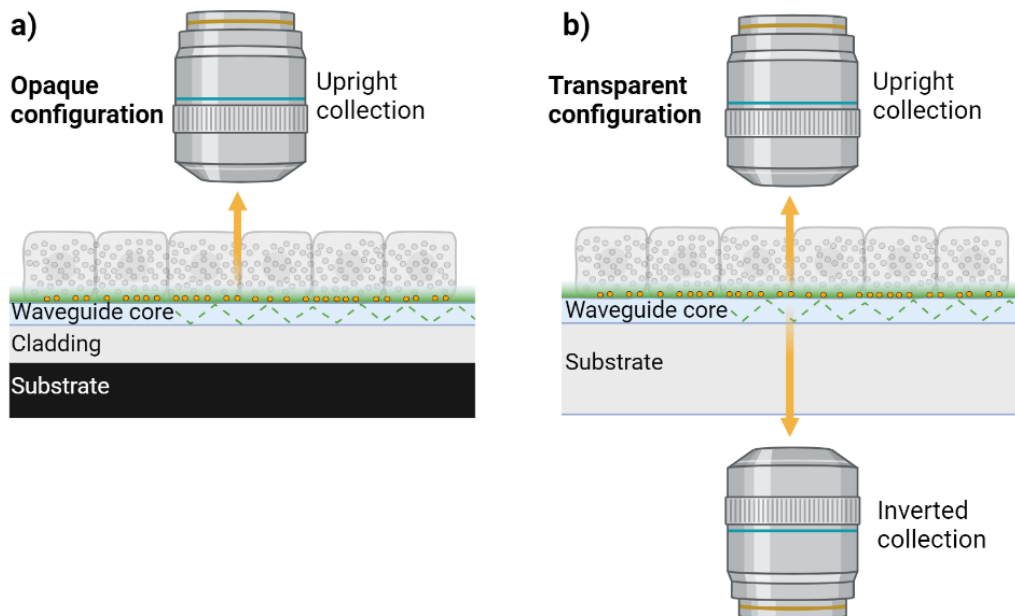
Figure 1.2-9.   Collection modalities in waveguide-based TIRF microscopy. a) Opaque waveguide-based configuration allows for upright collection. b) Transparent waveguide-based configuration allows both for upright and inverted collection.

Coupling method. There are diverse strategies for coupling the excitation light onto the waveguides [71] (Figure 1.2-10). These include a) end-fire coupling, where the light beam is aligned parallel to the end face of the waveguide; b) prism coupling, where the light beam is directed into a prism with a high refractive n_{prism}, resulting in an evanescent field that ultimately couples into a waveguide core with a refractive index n_{core} satisfying the

condition $n_{core} < n_{prism}$; and c) grating coupling, where the incident light beam is directed onto a grating that, due to its structure's periodicity, diffracts the light beam and couples it into the waveguide. Within these three approaches, the end-fire coupling provides the highest coupling efficiency but requires both a precise alignment of the beam and a clean waveguide facet with minimal roughness.

a) b) c)
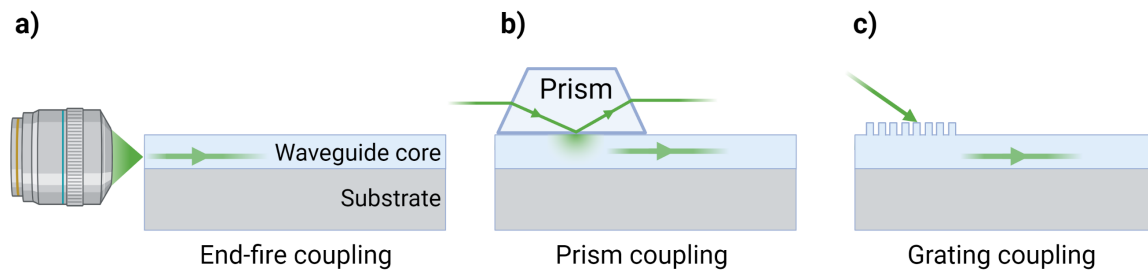
Figure 1.2-10. Waveguide coupling strategies. a) End-fire coupling. b) Prism coupling. c) Grating coupling.

Waveguide geometry. The photonic chips used in waveguide-based TIRF applications can be manufactured in different geometries according to the desired light behavior for a particular application. Some of the geometries explored in photonic chip-based microscopy include the slab, rib, and strip configurations, as depicted in Figure 1.2-11.
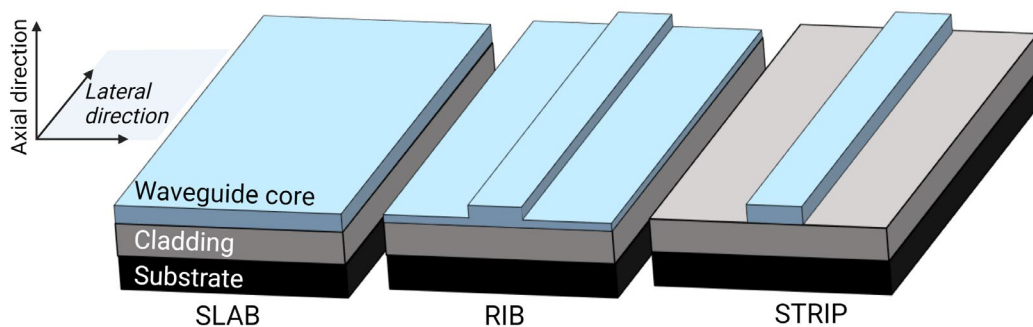
Figure 1.2-11. Photonic waveguide-based geometries. From left to right: slab, rib, and strip waveguides. Adapted from ref. [22]. The slab configuration allows light confinement only along the axial direction while allowing arbitrary divergence along the lateral direction. The rib geometry allows for lateral and axial confinement of the light and low propagation losses, yet it is susceptible to bending losses. The strip waveguides support better lateral confinement of the light as compared to the rib geometry, at the cost of higher propagation losses stemming from the sidewall roughness.

The specific characteristics of these configurations are hereby presented:

a) The s*lab* waveguides confine the light only along the axial direction, allowing for light divergence along the lateral dimensions. While this configuration provides sample illumination over arbitrarily large FOVs, the light divergence limits the control of the mode profiles (see below and section 3.2.3), leading to anisotropic excitation and low power density across the image field.

b) The *rib* waveguides are slab geometries with a partially etched channel. The limited height of the rib structure, e.g. 4 nm, allows for lateral confinement of the light with relatively low propagation losses, due to reduced sidewall interactions. While this configuration is interesting for single-mode propagation, e.g. using waveguide widths of 1 μm, the rib geometries are susceptible to bending losses.

c) The *strip* waveguides are rib geometries where the sidewalls are fully etched. This configuration allows for a better lateral confinement of the light as compared to the rib waveguides, at the cost of a higher propagation loss due to the sidewall roughness. As will be further detailed in Chapter 3, strip waveguide configurations were explored in this thesis for tissue imaging.

Mode distribution. To propagate throughout the length of an optical waveguide, a light wave must fulfill the so-called self-consistency condition (also known as the transverse resonance condition) [30], in which it must reflect from the boundaries and reproduce itself through constructive interference. The light waves that meet this requirement are known as modes or eigenfunctions of the waveguide. These modes maintain a consistent transverse distribution and polarization throughout the entire length of the waveguide axis, provided that the geometry of the waveguide remains unchanged. In other words, their patterns remain unchanged as they propagate along the waveguide. For planar waveguides undergoing end-fire coupling, the number of propagating modes M on a given direction (e.g., lateral or axial directions), depends on the wavelength λ and the polarization of the incident light, the refractive indices of core n_1 and cladding n_2, and the waveguide dimensions d, either in height or width, along each direction. For transverse electric propagation, for example, the number of modes is given by Equation (1.2-5), where the symbol $\doteq$ denotes the nearest integer [30]. When $M = 1$, the waveguide is called single-moded. When $M > 1$, it is referred to as multimoded. The mode distribution is determined by the waveguide's design. For instance, a waveguide might have a single mode based on its height (axial direction) but multiple modes based on its width (lateral direction), and vice versa. It's also possible for both directions to either be multimoded or just single-moded. An accurate determination of the transverse electric and transverse magnetic propagating modes can be done by electromagnetic wave theory solving Maxwell equations. However, this task might be difficult for certain geometries and boundary conditions. In practice, the propagating modes are approximated via computational simulations. These approximations might differ from the actual number of modes observed in the experiments, due to fabrication imperfections.

$$M \doteq \frac{2d}{\lambda} \sqrt{n_1^2 - n_2^2} \qquad (1.2\text{-}5)$$

The principle of waveguide-based TIRF microscopy is proposed in this doctoral work as a potential method for histological examinations. Chapter 3 provides further details about the waveguide-based TIRF configuration and imaging acquisition steps used in this work for histological observations.

Advantages and limitations of photonic waveguide-based TIRF microscopy

Waveguide-based TIRF microscopy provides several advantages to the analysis of biological specimens, both living and fixed, including tissue sections. These advantages are hereby outlined:

Large FOV TIRF. The light-guided propagation of this method provides the sample with a large and uniform evanescent illumination along the length and width of the waveguides, enabling fluorescent signals over large areas [21, 68, 69, 72, 73]. The decoupled excitation and collection light paths allow for the acquisition of TIRF images using any arbitrary magnification objective lens, e.g. 4-100X, enabling high-contrast images over large FOVs (Figure 1.2-12), thus overcoming the limitations of common objective-based TIRF systems, typically restricted to approx. 50 µm × 50 µm, due to the use of high magnification lenses of 60-100X.
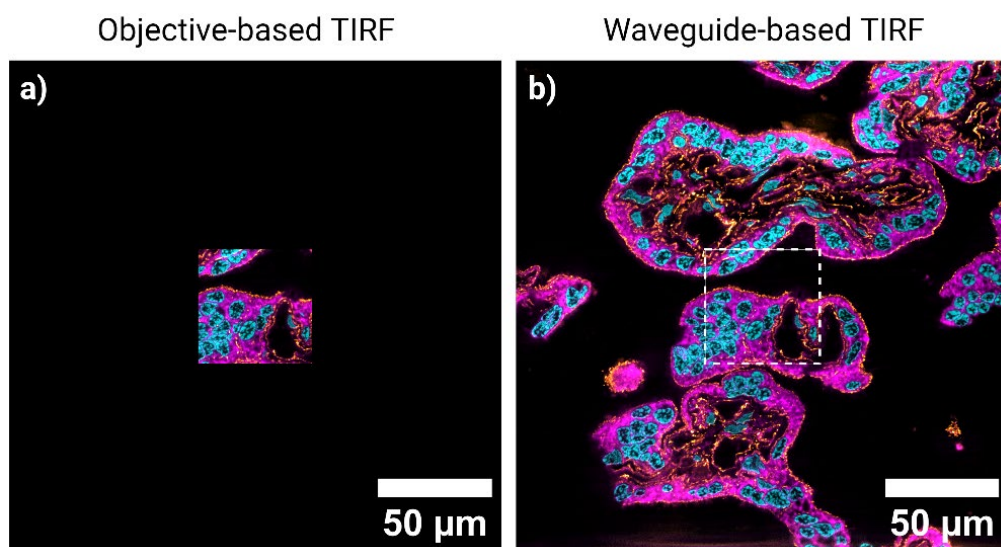
Figure 1.2-12. Field of view of different TIRF microscopes. a) In objective-based TIRF microscopy, the objective lens is used both for the illumination and collection of the fluorescent signal. To satisfy the high illumination angles required for TIRF, a high NA and high magnification objective is used. In this configuration, the exploitable FOV is limited to approx. 50 µm × 50 µm. b) In waveguide-based TIRF microscopy, the illumination and collection light paths are decoupled. Therefore, the FOV can be arbitrarily changed according to the magnification of the microscope objective. The white-dotted square represents the FOV attainable via conventional objective-based TIRF on the left panel. Adapted from Paper I.

High-intensity signal. By using an optical waveguide made of high refractive index material such as Si_3N_4 and Ta_2O_5, the light can be tightly confined into a smaller waveguide dimension. Next, by designing thin waveguide geometries, e.g. 100-150 nm in thickness, a large portion of the guided light can be made available in the evanescent field and thus enhances the intensity. The use of high refractive index contrast material also assists in reducing the evanescent field penetration as compared to the glass-based TIRF approaches [68, 74]. The high-intensity field near the sample-substrate interface not only increases the sensitivity of the system by enhancing the SBR but also favors the conditions for the

accurate localization of single-molecule fluorescence events [20, 22], a feature highly-valued in super-resolution microscopy (see section 1.3.2) and in biosensing applications [53, 75].

Biocompatibility. The materials used in waveguide-based TIRF approaches have proven compatible with standard cell culture methods, including cell plating and growing, enabling the study of both fixed [20, 21] and live specimens, including the imaging of delicate living neurons [69]. A more thorough investigation would be beneficial and is being carried out by others in the group.

Multimodal super-resolution imaging. The waveguide-based TIRF approach, like any other optical system, is limited by diffraction. However, the method is complementary to TIRF-based super-resolution imaging modalities such as FF-SRM, SMLM, and SIM [20, 22, 25, 26] (further details in Chapter 3). Also, in the case of photonic chips, the fabrication process supports the inclusion of landmarks that can further aid in the identification of specific regions of interest across different microscopy methods including scanning electron microscopy (SEM), thus allowing for correlative studies such as CLEM [28].

Compact size. The integration of the excitation light path into a miniaturized fixed structure alleviates the need for optical alignments, thus reducing the TIRF system footprint and the imaging workflow complexity compared to conventional free-space optics approaches such as glass-based TIRF.

Design. The waveguide design offers virtually unlimited light-propagating configurations, which open possibilities for expanding the method's capabilities that are not even considered today using free-space optical beam shaping.

Integrability. Leveraging the decoupled collection and miniature size, the waveguide-based TIRF method has a potential advantage for its integration in conventional microscopy setups with minimum interventions.

Mass production. Particularly, photonic chips can be mass manufactured by conventional photolithography processes employed in the semiconductor industry [22, 68], therefore benefiting from large-scale low-cost fabrication.

On the other side of the coin, the waveguide-based TIRF method has the following technical limitations:

2D imaging. The main limitation of current waveguide-based TIRF methods is their inability to extend the illumination beyond the reach of the evanescent field, which makes it impossible, for example, to achieve volumetric visualization (e.g., 3D) of the specimens. Current efforts, however, are addressing this limitation by projecting the guided beam out of the waveguide core, opening avenues for volumetric imaging [76, 77].

Autofluorescence. Certain waveguide materials such as silicon nitride (Si_3N_4), exhibit autofluorescence at shorter wavelengths from the visible spectrum, which may hamper the overall SBR of the image [78]. This issue, however, can be minimized by manufacturing optimizations Interestingly, the autofluorescence of the waveguide can also be harnessed for label-free imaging [79].

Losses. Similarly, certain waveguide materials such as Si_3N_4 exhibit losses along the direction of propagation [68], especially for shorter excitation wavelengths (e.g., 405 nm),

therefore affecting the intensity distribution throughout the waveguides. Consequently, the exploitable waveguide imaging length is usually compromised for shorter wavelengths. Optimization of the high-refractive index materials aiming for low propagation losses at the shorter waveguides, down to 405 nm, would be beneficial for waveguide-based TIRF microscopy. Promising materials include aluminum oxide and aluminum nitride.

1.3 Super-resolution optical microscopy

Fluorescence optical microscopy techniques have greatly contributed to the understanding of biological processes at the cellular and subcellular levels. However, the resolution capabilities of these techniques are limited by diffraction, meaning that several processes taking place at the nano-scale regime could not be resolved under these microscopes.

Nearly two decades ago, a new set of fluorescence-based optical microscopy methods was born under the name of super-resolution microscopy (SRM), allowing the visualization of subcellular features beyond the limits of diffraction. Due to the sub-100 nm resolution capabilities of some of these methods, this new discipline was also coined as optical nanoscopy. The SRM methods include a) structured illumination microscopy (SIM), a widefield method that uses a modulated excitation pattern to effectively down-convert high spatial frequencies of the sample into the observable regime of the objective lens [12]; b) stimulated emission depletion microscopy (STED), a point-scanning method that uses a combination of two lasers, one for excitation and one for depletion, to effectively reduce the size of the fluorescence spot [11]; c) single-molecule localization microscopy (SMLM), a widefield method that achieves sub-diffraction resolution through temporal sparsity of the fluorescent emission [10]; and more recently, d) fluorescence fluctuations-based super-resolution microscopy (FF-SRM), a widefield method that performs statistical analysis over a fluorescence image stack to reconstruct sub-diffraction features [13]; and e) expansion microscopy[8] (ExM), a chemical method used to increase the fluorescence labeling sparsity by physically expanding the samples using swelling compounds [14]. Although these methods are intrinsically different from each other, the common feature between them is the clever exploitation of the photochemical and photokinetic properties of fluorescent molecules to extract sub-diffraction information from fluorescent images collected with diffraction-limited microscopes.

In this thesis, two fluorescence-based microscopy platforms supporting super-resolution were explored for the contrast and resolution enhancement of tissue sections, namely the DeltaVision OMX V4 Blaze microscope, in short OMX, and the photonic chip-based optical microscope. The selection of such microscopy systems was based on their potential performance for relatively high-throughput super-resolution imaging and their availability in the group. The OMX microscope was employed to harness the fast-imaging capabilities of the SIM method, while the photonic chip-based microscope was used to realize super-resolution over large fields of view using SMLM and FF-SRM. A brief description of the super-resolution methods used in this thesis is given in the following sections.

---

[8] Expansion microscopy is a particular SRM method composed of two steps. First, the spatial sparsity of the fluorophores is enhanced by swelling the sample, and then, a complementary microscopy method is used to achieve super-resolution.

1.3.1 Structured Illumination Microscopy (SIM)

Structured illumination microscopy (SIM) enhances spatial resolution by projecting a structured excitation light pattern onto the specimen (Figure 1.3-1a) and analyzing the resulting images. Specifically, the patterned illumination (Figure 1.3-1b) creates high-frequency moiré fringes in the image field that effectively down-converts higher spatial frequencies in the sample into the frequency support of the microscope objective (Figure 1.3-1c). By collecting multiple images with different moiré patterns and applying a computational reconstruction process, the high-frequency information contained in the moiré patterns is used to extract high-resolution details that were previously inaccessible via conventional widefield microscopy (Figure 1.3-1d).
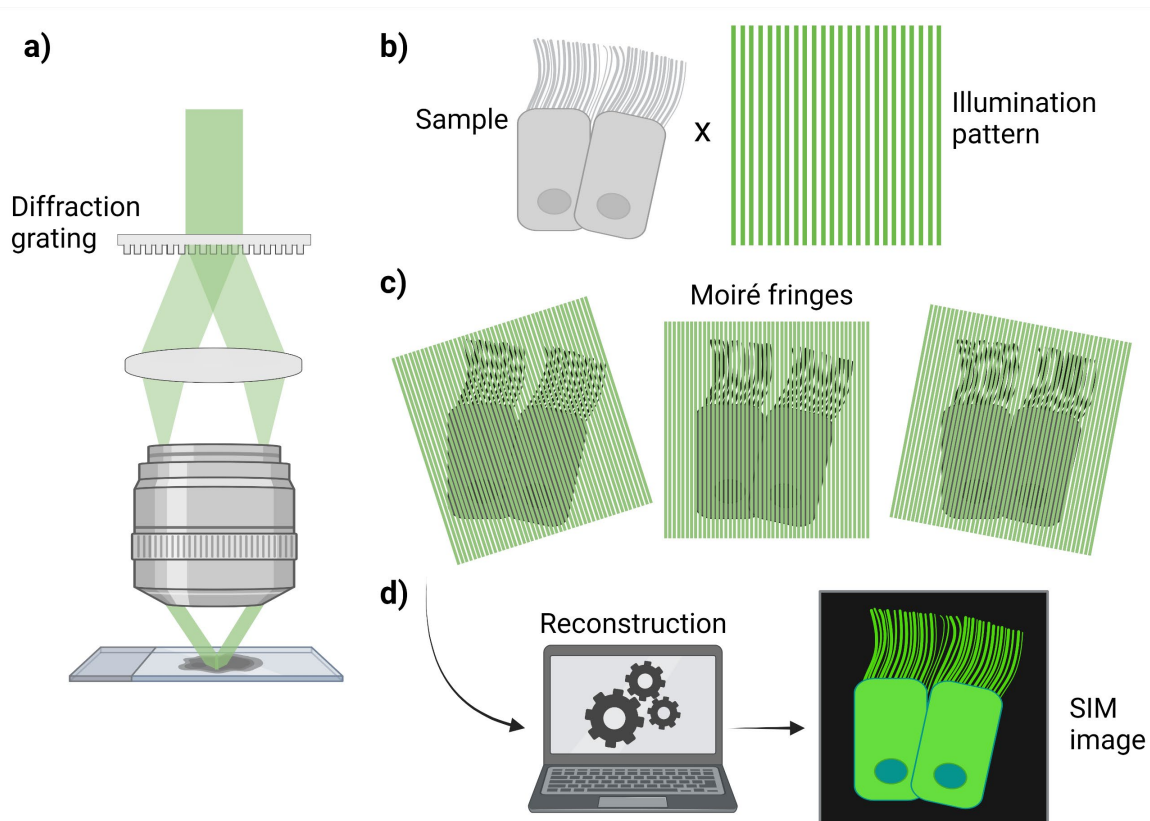
Figure 1.3-1.   Working principle of 2D-SIM. a) The illumination pattern consists of sinusoidal stripes produced by the interference of two beams exiting a diffraction grating. b) The sample is excited with the illumination pattern. Note the high spatial frequency of the sample and the illumination pattern. c) Diverse coarse Moiré fringes are generated upon rotation and phase-shifting of the illumination pattern. In 2D-SIM, 3 rotation angles and 3 phase shifts per rotation are typically performed. Individual images are acquired for each Moiré fringe. d) The 9 images are processed by a computational algorithm to reconstruct the SIM image of the sample.

A common method to achieve structured illumination is by splitting the excitation laser beam using a diffraction grating and then making the diffracted beams interfere with each other at the sample plane by focusing through a microscope objective. The process is mathematically

described hereby. In the 2D interference approach[9] shown in Figure 1.3-1a, the excitation light $e(r)$ takes the form of a periodic pattern whose intensity can be represented by Equation (1.3-1) [80]:

$$e(r) = A(1 + cos(k_r r + \varphi))$$ (1.3-1)

Where A is the modulation factor of the excitation pattern, k_r is the spatial frequency, φ is the phase and r is the location. Consequently, the fluorescent emission $f(r)$ can be described as the product of the excitation pattern and the object:

$$f(r) = o(r)e(r) = A[o(r)(1 + cos(k_r r + \varphi))]$$ (1.3-2)

Now, expanding from Equation (1.1-4), the image function i(r) becomes the convolution of the fluorescent emission $f(r)$ and the PSF of the microscope:

$$i(r) = f(r) * psf(r) = A[o(r)(1 + cos(k_r r + \varphi))] * psf(r)$$ (1.3-3)

Which can be rewritten in the frequency domain via Fourier transform as:

$$I(k) = A\left[O(k) * \left(\delta(k) + \frac{e^{j\varphi}}{2}\delta(k - k_r) + \frac{e^{-j\varphi}}{2}\delta(k + k_r)\right)\right]OTF(k)$$ (1.3-4)

After performing the convolution operation inside the square brackets, three copies of the object function O(k) appear, located at k, $k - k_r$, and $k + k_r$, respectively:

$$I(k) = A\left[O(k) + \frac{e^{j\varphi}}{2}O(k - k_r) + \frac{e^{j\varphi}}{2}O(k + k_r)\right]OTF(k)$$ (1.3-5)

Equation (1.3-5) tells us that the acquired image $I(k)$ is actually limited by the cut-off frequency of the OTF. However, the object functions $O(k - k_r)$ and $O(k + k_r)$ carry high spatial frequency information from the object, which is down-converted by the structured illumination. Thus, by solving Equation (1.3-5), the down-converted values can be reassigned back to their corresponding positions in Fourier space, effectively increasing the spatial frequency support of the system. To solve Equation (1.3-5), three-phase shifted images over the same orientation are needed. To obtain isotropic coverage of the Fourier space, the process is repeated for two more orientations (i.e., $\pm\pi/3$), until a total of 9 images are collected. Finally, the extended Fourier image is reconstructed in the spatial domain via inverse Fourier

---

[9] In practical applications of SIM, two interfering approaches exist: a) the 2D illumination approach, illustrated here, where only the first order diffracted beams interfere with each other; and b) the 3D illumination approach, in which the zero order is also allowed to interfere with the first order diffracted beams. The 2D example is shown here for simplicity of the mathematical explanation.

transform, allowing the visualization of structures beyond the resolution limit of the microscope.

The 3D interference approach follows the same rationale covered here for the 2D approach. However, the mathematical derivation in the 3D case results in 5 unknowns. Consequently, in this case, a total of 15 images (i.e., 5 phase-shifted images x 3 orientations) are required for optimal SIM reconstruction. A schematic representation of the 2D-SIM process in Fourier space is presented in Figure 1.3-2.
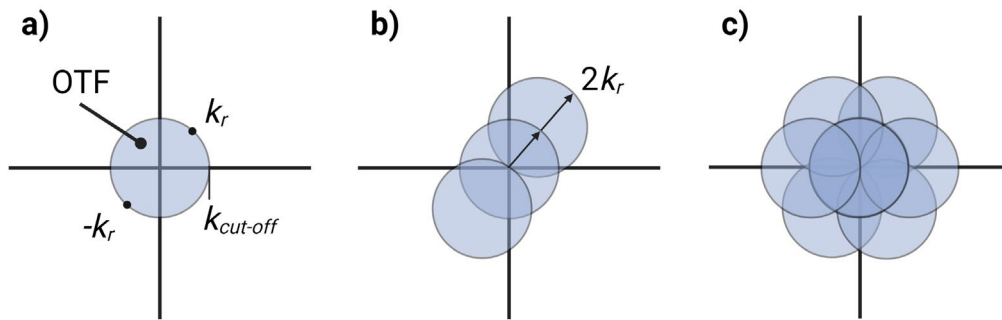
Figure 1.3-2.   Schematic representation of SIM in Fourier space. a) In optical microscopy, the highest spatial frequency k_r observable on the image field is determined by the cutoff frequency of the objective $k_{cut-off}$ of the system's OTF. b) The structured illumination projected on the sample effectively increases the frequency support of the microscope objective, reaching up to 2-fold in the case of objective-based SIM. c) To obtain isotropic frequency support, several SIM raw frames are acquired along different orientations and phase shifts. In the case of 2D-SIM, three phase-shifted images are collected for each of the three orientations of the illumination pattern. The nine raw frames are then used for SIM reconstruction.

The maximum spatial frequency supported by SIM is given by $k_{SIM} = k + k_r$, where the maximum k is given by the cut-off frequency $k_{cut-off}$ of the objective, and k_r is given by the highest spatial frequency of the illumination pattern. For an EPI-based SIM setup, where the same objective is used both for illumination and collection of the fluorescent signal, the illumination pattern is also limited by diffraction, giving $k_{SIM} = 2k_{cut-off}$. This means a maximum resolution improvement of 2X. Figure 1.3-3 provides a 3D-SIM image example of actin filaments in a mammalian cell.

In principle, by decoupling the illumination and the collection light paths, the maximum illumination fringe frequency can be increased, and therefore, new possibilities arise for enhancing SIM resolution. Relevant examples of these approaches include the use of surface plasmonics [81] and standing waves generated by counterpropagating beams [26, 82].
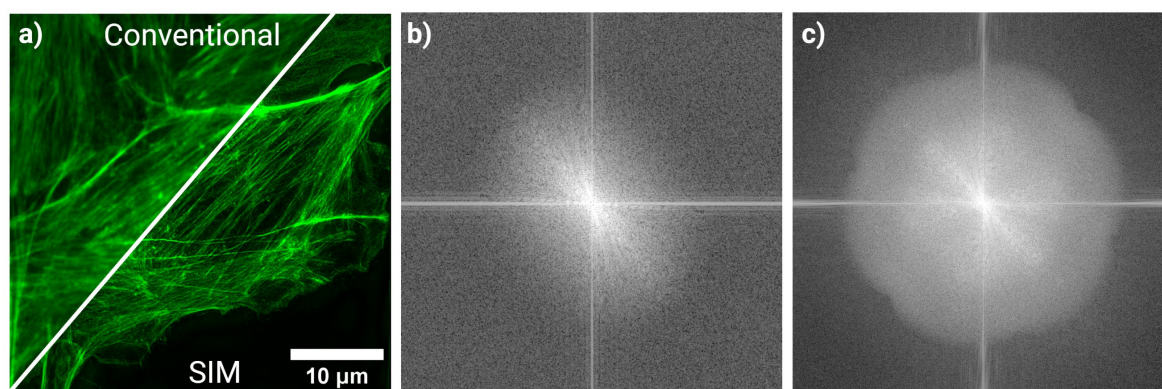
Figure 1.3-3.   3D-SIM image example. a) Actin filaments in a mammalian cell. The top panel shows a conventional microscopy image. The bottom panel shows the enhanced contrast and resolution achieved by the 3D-SIM method. b) Fourier representation of the conventional image. c) Fourier representation of the 3D-SIM image. Note the extended frequency support as compared to b).

Practical considerations for SIM implementation

Structured illumination microscopy is a robust method that stands out for its speed [83], making it an attractive option for applications requiring high throughput, such as live-cell imaging [84] and intraoperative histopathological diagnosis [85]. Moreover, the 3D illumination approach (supported by the OMX microscope), enables three-dimensional super-resolution visualization of biological samples by repeating the SIM imaging process at finely-spaced steps along the optical axis of the microscope. Also, the method is compatible with commonly available dyes, which simplifies its operability.

Despite these advantages, the SIM method is prone to imaging artifacts derived from inappropriate imaging settings and sample imperfections [86]. Particularly, the SIM algorithms are susceptible to:

PSF symmetry. The SIM algorithms use a pre-calibrated PSF with perfect symmetry as shown in Figure 1.1-6. Therefore, experiments with asymmetrical PSF will render artifact reconstructions. The PSF symmetry depends on the refractive index matching between the sample and the imaging media and is evaluated by collecting an image stack of single emitters in the sample and observing their orthogonal views. If an asymmetric PSF is observed (Figure 1.3-4a), an optimization step is performed until a symmetrical PSF is achieved (Figure 1.3-4b). The PSF optimization is, in practice, an iterative process where either the objective's collar (if available) is adjusted, or the imaging medium (typically oil) is replaced by another medium with a different refractive index, a method known as oil-matching. As the refractive index changes with temperature, it is important to maintain thermal stability during the PSF optimization and subsequent SIM acquisition. Moreover, with an increase in specimen thickness, the PSF gets asymmetric and often distorted for scattering samples such as tissues. Therefore, the SIM method is often used on thin samples.
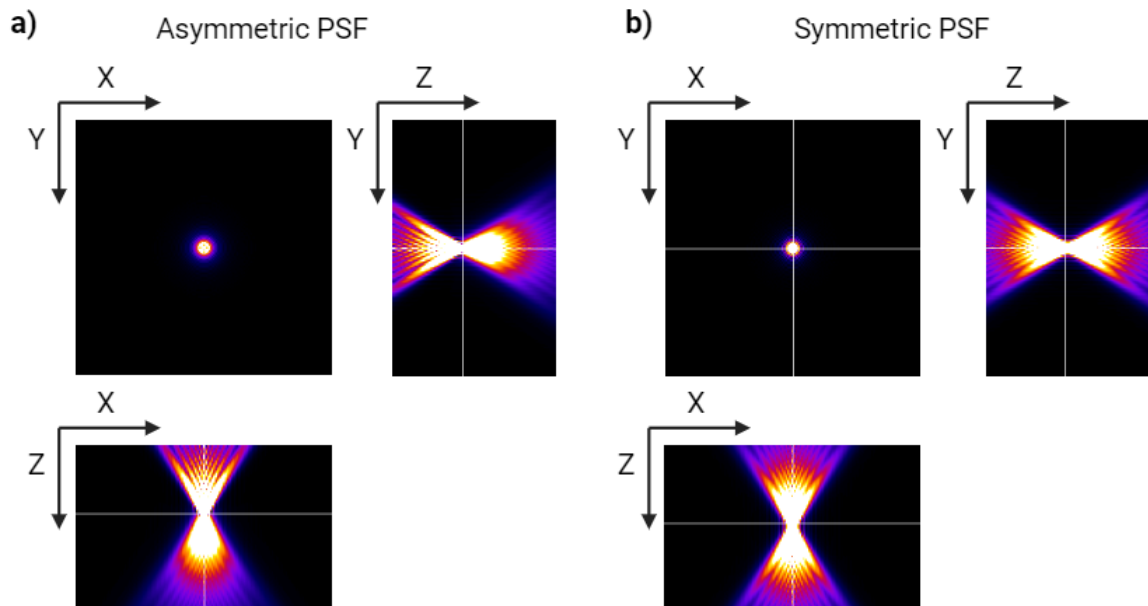
Figure 1.3-4. PSF optimization. a) The orthogonal views of a point source reveal an asymmetric PSF distribution. b) After oil matching, a symmetrical visualization of the PSF is achieved. Simulated with PSF generator in FIJI [34].

Uniform emission and sample beaching. The amplitude of the fluorescent signal is also important for the SIM method. Particularly, the reconstruction algorithms assume a uniform intensity of the fluorescence emission, which in practice is not always achievable due to photobleaching of the fluorophores, especially for 3D-SIM imaging, where a considerable amount of frames are required to reconstruct a projected SIM image. For example, to obtain a 3D-SIM image over a 2 μm sample volume, a total of 16 planes must be imaged at axial steps of 125 nm. Considering that 15 images must be taken per plane, this equals 240 raw frames with a good SBR.

Optical imperfections. The SIM method is susceptible to optical imperfections such as autofluorescence and to refractive index mismatch between the sample and the imaging media that, respectively, lead to unwanted background signals that reduce the fringe contrast and ultimately affect the SIM reconstruction, or introduce optical aberrations that produce pseudo structures in the reconstructed SIM image.

There is plenty of literature offering guidelines for optimal SIM imaging and reconstruction [86]. However, the practical use of this method requires several iterations until the sample preparation and imaging conditions render the desired results.

Lastly, it should be noted that the current commercial SIM setups, such as the OMX microscope, use an episcope approach to achieve both illumination and collection through high magnification and high numerical aperture objective lenses, which in practice limits their visualization to a FOV of approximately 40 μm × 40 μm [87]. Recent research approaches such as transmission-SIM [88] and fiber-SIM [87], however, have demonstrated extended fields of view over 150 μm × 150 μm and more, at two-fold resolution improvement.

1.3.2 Single-molecule localization microscopy (SMLM)

Single-molecule localization microscopy (SMLM) comprises a series of optical microscopy techniques that achieve super-resolution by mapping the location of individual fluorescent events over time. To illustrate this concept, let us consider an object sample with several closely spaced fluorescent emitters located at distances smaller than the resolution limit of the imaging microscope, as represented in Figure 1.3-5. To visualize them, the SMLM method involves fluorescence intermittency of these point sources, such that the probability of simultaneous emission at a given time point is low. This enables the acquisition of a time series image stack of sparsely separated single-molecule fluorescence events, in which the positions of individual emitters can be subsequently estimated by fitting their diffraction spots into a 2D-Gaussian profile. Through this process, the coordinates of the center of each Gaussian curve are determined, and the precise localization of these points is mapped into a super-resolved reconstructed image.
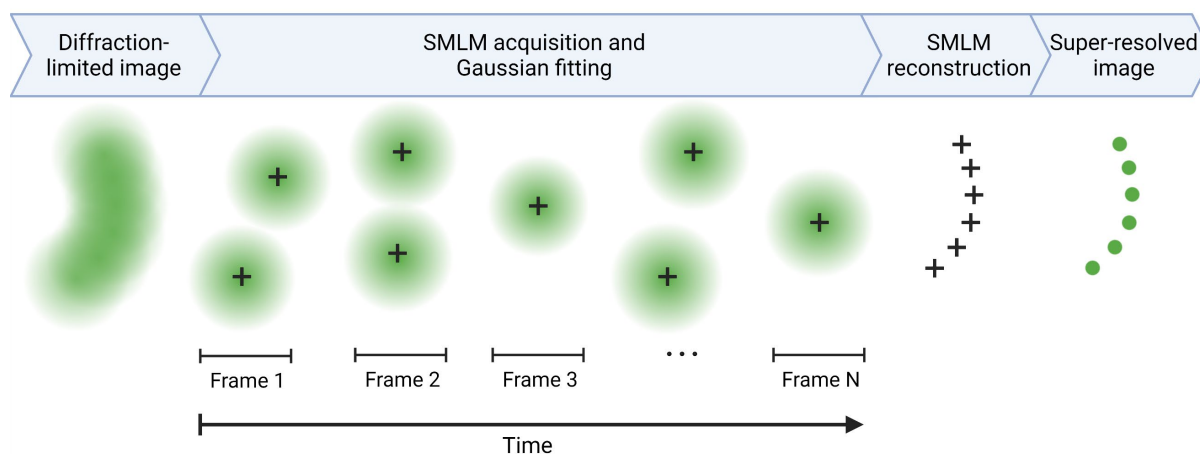
Figure 1.3-5. Working principle of SMLM method. By manipulating the photophysical properties of the fluorescent markers, it is possible to induce a long-lived dark state, where most molecules remain OFF, while only a small amount of them emit light (ON). By repeating this strategy over several acquisition cycles, the individual fluorescence events from a single molecule can be accurately localized in the image field, allowing the reconstruction of a super-resolved image of the sample.

For successful emitter localization, the SMLM method must ensure emission sparsity throughout the timelapse acquisition process. This means that, for any given frame, most of the fluorophores must remain inactive (e.g., off) while a relatively small subset emits light (e.g., on). To this end, various methods have been developed to manipulate the fluorescence response of the fluorophores to achieve the desired on/off blinking behavior. A great deal of these methods achieve blinking by harnessing the photophysical properties of the energy level transitions experienced by the fluorescent molecules during the imaging cycle [10]. Particularly, the inter-system crossing process, schematically represented in Figure 1.3-6, is exploited by these SMLM methods. Briefly, expanding from the Jablonski diagram in section 1.2, upon photon absorption by the fluorescent molecule, an electron is promoted from the ground state S_0 to a higher energy level, resulting in an excited singlet state S_1. Thereafter, the fluorophore can undergo fluorescence (typically within nanoseconds), and repeat this process several times. However, some fluorophores can undergo intersystem crossing, where the

excited singlet state S_1 transitions to a longer-lived triplet state T_1, in a process governed by spin selection rules from quantum mechanics. Fluorophores populating the triplet state become more stable, non-fluorescent, and longer-lived excited state compared to the singlet state, enabling long-lasting photophysical processes such as:

a) Phosphorescence, where the fluorophores emit light when transitioning back from the triplet state T_1 to the ground state S_0 (with a lifetime ranging from milliseconds to minutes);

b) Irreversible photobleaching, where the fluorophores lose their fluorescence permanently due to chemical reactions or structural changes, rendering them unable to return to the fluorescent state; and

c) Reversible photoswitching, where the fluorophores lose their fluorescence temporarily due to transient interactions or changes in their local environment, which can be afterward recovered, becoming fluorescent again over time. The latter, reversible photoswitching, is precisely the feature exploited by most SMLM methods.
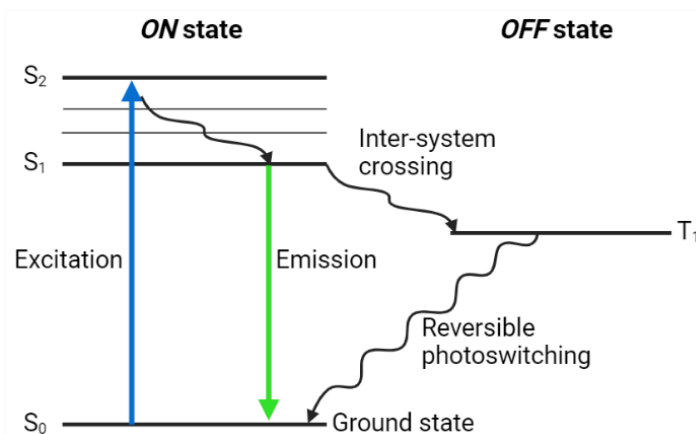
Figure 1.3-6.   Schematic representation of the inter-system crossing. In most SMLM imaging methods, a few fluorophore molecules undergo fluorescence while most others transition to a long-lived triplet state (T_1) via inter-system crossing. At the T_1 state, the molecules remain non-fluorescent, i.e. *OFF* state, allowing the precise localization of individual emitters in the *ON* state. The molecules in the *OFF* state transition back to the ground state stochasticly, where the cycle repeats.

Relevant SMLM methods exploiting the long-lived excited state include[10]:

a) Stochastic optical reconstruction microscopy (STORM), which utilizes an activator-reporter pair of organic fluorophores (e.g., cyanine dyes Cy3 and Cy5), to enable single-molecule on/off photo-switching by alternating between two light sources of different wavelengths [89];

b) *d*irect stochastic optical reconstruction microscopy (*d*STORM), where a high-intensity excitation laser and a dedicated imaging buffer are employed to induce long-lived triplet states in commonly available fluorophores (e.g., Alexa Fluor and ATTO) [42, 90];

---

[10] The list of SMLM methods is extensively long and detailing them is beyond the scope of this work. The SMLM methods described here are the most representative.

c) Ground state depletion followed by individual molecule return (GSDIM), where intense illumination is utilized to accelerate the transition of molecules into the triplet state, surpassing the rate of their return to the ground state[91]; and

d) Photo-activated localization microscopy (PALM), which employs photo-activatable proteins (e.g., genetically encodable fluorescent proteins such as the green fluorescent protein, GFP) that become active upon illumination with a 405 nm laser, and relies on photobleaching for the off-state [92].

There is, however, an alternative SMLM method that achieves fluorophore blinking differently, the so-called DNA points accumulation for imaging in nanoscale topography (DNA-PAINT). This method utilizes conventional fluorophores conjugated to complementary DNA strands to enable stochastic on/off events via reversible binding [93, 94].

Arguably, *d*STORM and DNA-PAINT are the most versatile and user-friendly methods among the SMLM family, and therefore heavily used in super-resolution studies. However, the DNA-PAINT method requires specifically designed fluorophores, as opposed to *d*STORM which harnesses the photokinetic behavior of virtually any dye upon the use of the appropriate blinking buffer. Therefore, in this work, *d*STORM was the chosen method for the assessment of SMLM-based histology on a photonic chip (see Paper II).

Practical considerations for SMLM implementation

While the SMLM is considered one of the most robust SRM imaging methods, there are several parameters to be considered for its successful application. For example:

Localization precision. Despite the differences in the SMLM methods, these share the same analysis principle, which consists of mapping the locations of each one of the fluorescent events at high precision to enable computational reconstruction of the imaged sample. Thus, the localization precision Δx of a single-molecule fluorescence event is given by [10, 95]:

$$\Delta x = \sqrt{\left(\frac{\sigma^2 + a^2/12}{N}\right)\left(\frac{16}{9} + \frac{8\pi(\sigma^2 + a^2/12)b^2}{Na^2}\right)} \qquad (1.3\text{-}6)$$

Where σ represents the standard deviation of the 2D-Gaussian fit, a is the pixel size of the camera, N is the number of photons collected by the camera, and b is the background signal (including background fluorescence and detector noise). To achieve high localization precision, both a high photon count and a low background signal are necessary. Increasing the photon count can be achieved through camera integration times matching the on-state lifetime, which can vary between 5 ms and 500 ms depending on the laser intensity and the chemical formulation of the blinking buffer [10]. On the other hand, background signal suppression is typically accomplished using high-contrast optical sectioning methods, like the TIRF technique.

Resolution. An important aspect of Equation (1.3-6) is that it refers to localization precision and not to resolution. In SMLM methods, the resolution is directly proportional to the localization precision, but these two are not the same. While a smaller Δx value allows for finer discrimination between two emitters, the optical resolution of the SMLM reconstruction is also dependent on other variables, including drift (e.g., sample drift and/or

instrumentation drift), motion blur, labeling density, sub-optimal sample preparation (e.g., fluorophore aggregates), selection of appropriate fitting parameters, and post-processing analysis. In practice, the expected lateral resolution for optimal SMLM imaging experiments involving cells typically ranges from 20 nm to 50 nm [10].

Blinking sparsity. The blinking density is also relevant to SMLM imaging and needs to be taken care of to avoid the superimposed emission of fluorophores. At the beginning of a typical *d*STORM experiment, for example, most fluorophores undergo continuous cycles of fluorescence. This can be helpful to, for example, visualize the sample and bring it into focus. To allow single-molecule localization, most fluorophores are turned off by using high excitation intensities of ~10–50 kW/cm^2 at an adequate excitation wavelength for a few seconds to populate the triplet state with photo-reduced molecules. Thereafter, the excitation intensity can be decreased to ~1–10 kW/cm^2 to allow sparse and stochastic single-molecule fluorescence [10]. Common *d*STORM buffers include a mixture of thiols that act as reducing agents providing fluorophores with electrons, and an oxygen scavenging system to minimize oxidation with molecular oxygen and thus avoid rapid transitions to the ground state.

Limited throughput. It should be noted that SMLM methods have an inherent limitation in terms of throughput, as they require a large number of datasets (typically ranging from 30,000 to 70,000 frames) to reconstruct a single super-resolved image. Depending on factors like image size, acquisition rate, fitting parameters, and image analysis, the whole process can take several minutes to hours with modern computers. Moreover, in SMLM applications using objective-based TIRF setups, the field of view (FOV) is limited to around 50 µm × 50 µm. This poses challenges in imaging large specimens, like histological samples, where multiple rounds of SMLM are needed to visualize the entire context. To alleviate this issue, there are however potential approaches, such as using multi-emitter fitting algorithms to identify partially overlapping fluorescence emission profiles, albeit with a trade-off of slightly reduced localization precision and increased computational cost [96]. Additionally, waveguide-based SMLM can help increase throughput by increasing the FOV [20, 21, 56, 73, 97].

SMLM methods offer an unprecedented lateral resolution, albeit a low temporal resolution. Moreover, the need for large datasets, complex imaging buffers, and specialized sample preparation protocols limits the widespread adoption of SMLM methods in, for example, medical settings. Over the last decade, however, a novel SRM field known as fluorescence fluctuations-based super-resolution microscopy (FF-SRM) has made significant inroads by addressing these hurdles, greatly simplifying the super-resolution workflow process. A brief description of the FF-SRM method is presented in the next section.

1.3.3 Fluorescence fluctuations-based SRM (FF-SRM)

Fluorescence fluctuations-based super-resolution microscopy (FF-SRM), or intensity fluctuations-based optical nanoscopy[11] (IFON), comprises a series of computational methods

---

[11] Both FF-SRM and IFON terms denote the same principle of fluorescence-based intensity fluctuation analysis. Both terms are commonly found in the literature, existing no consensus on their use. The term IFON was used in Paper II, while FF-SRM was used in subsequent Paper III in this thesis.

that achieve sub-diffraction optical resolution by analyzing pixel-wise intensity changes in a fluorescence dataset. The idea behind the FF-SRM methodology involves the acquisition of a timelapse image stack and capitalizes on the stochastic behavior of fluorescence (Figure 1.3-7). Briefly, throughout the image sequence, each fluorophore has a random fluorescence pattern, uncorrelated from other emitters. By analyzing these patterns over time, the FF-SRM algorithms can estimate the location of the emitters in a final super-resolution image.
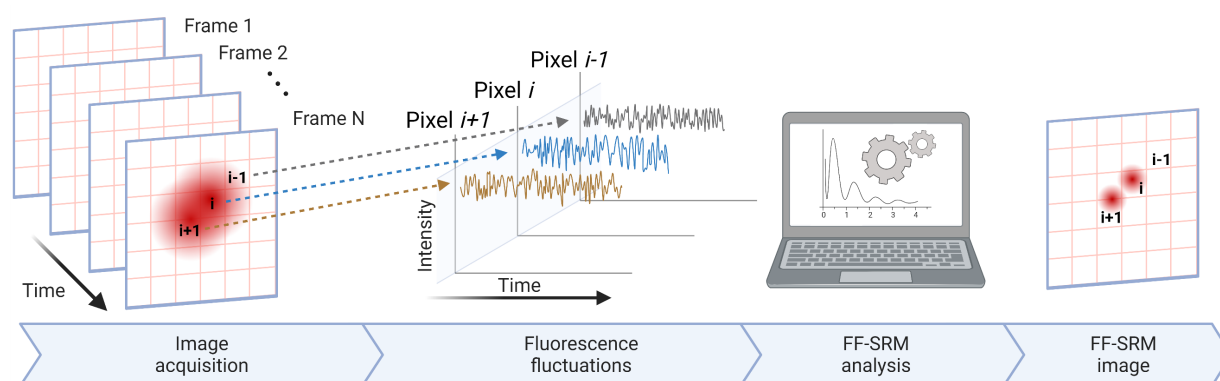
Figure 1.3-7.   Schematic representation of FF-SRM methodology. Upon acquisition of an image stack, the intensity fluctuations registered on each pixel over time are statistically analyzed by an FF-SRM algorithm, allowing for the identification of sub-diffraction limit information of the sample. Adapted from ref. [98].

While FF-SRM methods require an image timelapse, they differ from SMLM methods by allowing spatial signal overlap of fluorophores within a diffraction-limited spot. This provides several advantages over SMLM methods, including a) fast imaging acquisition, requiring as few as 20-100 frames for optimal reconstruction [99]; b) simplified sample preparation, i.e. by not requiring blinking buffers; c) compatibility with common dyes; d) easy implementation, since the imaging can be performed on conventional epifluorescence microscopes; and e) compatibility with live cell imaging, due to its high temporal resolution and compatibility with low illumination intensities.

Since the publication of the FF-SRM idea in 2009 [98], there has been an avalanche of FF-SRM methods in the optical community [99], each one addressing the statistical analysis differently to achieve super-resolution. Representative examples include[12]: a) super-resolution optical fluctuation imaging (SOFI) [98], which utilizes higher order cross-cumulants to analyze the temporal fluctuations of blinking emitters; b) entropy-based super-resolution imaging (ESI) [100], where the emitter presence is estimated by calculating the local and cross-pixel entropy across an image timelapse; c) multiple signal classification algorithm (MUSICAL) [101], which calculates higher resolution by differentiating between signal and noise sub-spaces through singular value decomposition; d) super-resolution radial fluctuations [102], where in addition to SOFI, assumes radiality of emitters; e) super-resolution imaging based on autocorrelation with two-step deconvolution (SACD) [103], which in addition to the signal autocorrelation approach from SOFI, includes a (Lucy-Richardson) deconvolution step before and after the autocorrelation analysis; and e) haar wavelet kernel (HAWK) [104], which serves

---

[12] The complete list of FF-SRM is extensive and including all these methods is beyond the scope of this work. A comprehensive literature review can be found in references [13, 99].

as a data pre-processing technique that can be used to increase the temporal sparsity by distributing the data over more frames.

The FF-SRM concept was initially designed to statistically analyze intermittent and independent emissions of fluorophores under continuous illumination. However, later implementations of the SOFI method have shown promising results using speckled illumination [105] and structured illumination [106, 107], suggesting that the FF-SRM methods could be employed not only with intrinsic but also with extrinsic illumination fluctuations. Recently, this has been further demonstrated on waveguide-based TIRF datasets obtained with multimode illumination patterns using ESI [22], SRRF [23], MUSICAL [25], and a combination of balanced-SOFI with HAWK wavelet kernel [24].

Practical considerations for FF-SRM applications

While the FF-SRM methods offer promising advantages to the field of super-resolution microscopy, the use of these computational methods requires an understanding of their limitations:

Reconstruction parameters. Most FF-SRM algorithms require user input by either introducing experimental information such as emission wavelength, numerical aperture, and pixel size; or by selecting reconstruction parameters that require a lot of expertise [13] and, in many cases, lack comprehensive user guidance in the published methods. The latter leads to a subjective selection of parameters, affecting the scientific validity of the reconstructions. This is fortunately changing, with new strategies evolving towards subjective-free reconstructions [103, 108, 109].

Resolution. The resolution of FF-SRM is generally lower than for example SMLM methods and is strongly influenced both by the variability of the intensity fluctuation and by the chosen reconstruction parameters [110]. The lateral resolution of these methods is often estimated with simulation data, resulting in ideal values of 40-100 nm that often deviate from experimental results.

Imaging artifacts. The FF-SRM methods assume a stationary behavior of fluorophores, making them susceptible to reconstruction artifacts derived from sample and/or system drift. Moreover, the reconstruction fidelity of the FF-SRM methods can be affected by the level of variations in the fluorescence fluctuations [110]. For example, SOFI and MUSICAL perform well with high-intensity fluctuations but exhibit artifacts when this condition is not fulfilled.

Non-linearity. The FF-SRM reconstructions are a non-linear representation of the fluorescent signal, therefore introducing non-uniform fluorescence intensity amplification of the sample features. This could hinder, for example, the quantitative analysis of biological mechanisms and make these methods more prone to reconstruction artifacts.

Labeling density. The FF-SRM algorithms are often benchmarked in fiber-like subcellular structures such as tubulin and actin filaments [99]. While these serve the purpose of demonstrating the methods, future development of the imaging protocols for dense structures such for example, the plasma membrane, Golgi apparatus, or densely labeled tissue sections would be beneficial for the field.

1.3.4 Correlative light-electron microscopy (CLEM)

While fluorescence microscopy provides excellent structural specificity, it lacks contextual information about the surrounding features in the field of view. On the other hand, electron microscopy allows for high-resolution visualization of ultrastructural features on the samples, at the cost of limited specificity. Therefore, the combination of these two methods is beneficial for the visualization and understanding of several aspects of the organization of biological specimens. Correlative light and electron microscopy (CLEM) is a method that combines the advantages of both fluorescence microscopy and electron microscopy to enable the visualization of specific structures over a high-resolution context. CLEM is a powerful technique often employed in life science fields such as neuroscience, cell biology, and histological research [111].

Apart from the biological applications, the CLEM methodology is also a useful tool to benchmark the advances in super-resolution microscopy. By imaging a fixed sample over the same region of interest using separate instruments, it is possible to verify the findings of a given SRM method by overlaying the fluorescence SRM image over the corresponding electron micrograph. In such cases, substrate landmarks are beneficial both for easy navigation over the sample and for an accurate and unbiased image alignment for the CLEM overlay, as demonstrated recently for on-chip CLEM [28]. Figure 1.3-8 illustrates a CLEM image on a photonic chip.
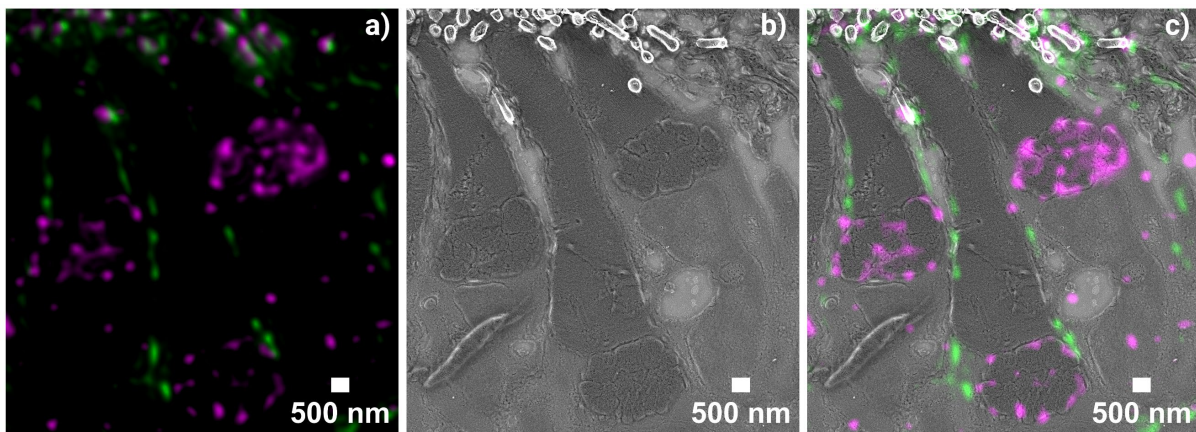

Figure 1.3-8.   Example of a CLEM image. a) Fluorescence image of a zebrafish eye retina. Mitochondrial membranes are shown in magenta and actin filaments are in green. b) SEM image of the same sample region. c) CLEM image illustrating the correlation between images in a) and b). Adapted from Paper II.

1.4 Histology

Cells are the basic building blocks of living organisms, responsible for vital processes such as metabolism, movement, and reproduction. The human body is made of approximately 200 distinct types of cells, characterized by their structure and size, ranging between 7-120 µm depending on the cell type [112]. Inside the cell, organelles and molecules vary in size from a couple of nanometers to a few microns. To accomplish the vital activities of the organism, cells with a similar structure and function group together in specific mesh-alike arrays, namely tissues, and work jointly as a unit. All organs, such for example the kidney in Figure 1.4-1, are composed of various tissue layers. Diverse organs form an organ system, which collectively builds up living organisms.
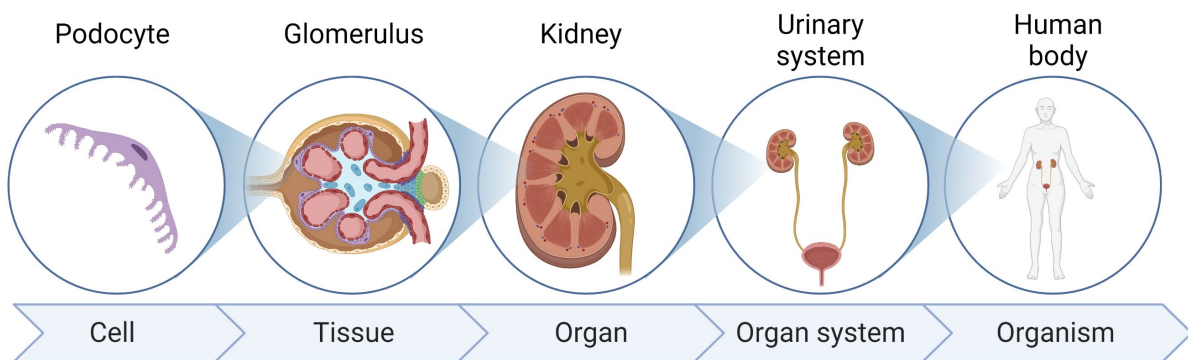
Figure 1.4-1.　Levels of organization in a multicellular organism. From left to right, specialized cells compose a tissue. Diverse tissues form an organ, which becomes part of an organ system. Organ systems, collectively, build up living organisms.

The composition and arrangement of each tissue play a physiological role in the body. Morphological changes in tissues are often related to the development and progression of diseases. Therefore, good knowledge of the microanatomy of tissues is beneficial both for the understanding of their functional contribution in a healthy organism and for the identification of changes related to pathologies. The field that studies the structure and organization of tissues using microscopes is called *histology* and, within it, *histopathology* is the discipline that analyzes morphological and molecular changes associated with the onset and progression of diseases.

Histological examination involves the extraction of a small portion of the organ under study. To perform the microscopic analysis, the sample is fixed, sectioned, and stained following a preparation protocol (more on this in section 1.4.2) and then observed under the microscope. The histological assessment usually involves hierarchical visualizations to navigate through different levels of detail within the sample. This is accomplished by alternating between low and high magnification according to the desired level of information. Typically, the tissue section is first scanned at low magnification (e.g., 10X/0.25NA) to identify the different regions of interest for analysis. Depending on the specimen size, the imaging area spans from a few mm^2 to several cm^2 [85]. Thereafter, higher magnification and resolution powers are used to visualize finer morphological details within the sample (e.g., 40X/0.6NA). The process is commonly repeated over several slides until sufficient information is visually collected to render a research conclusion or, in the case of histopathology, a clinical diagnosis. Particularly, a routine histopathological workflow involves the visualization and analysis of tens of

microscopy slides by a single histopathologist physician every day. Therefore, the combination of high imaging throughput, high contrast, and high resolution is beneficial to meet the demands of routine histological studies.

While a vast amount of histopathological conditions can be nowadays assessed via high-throughput whole-slide microscope scanners [113], the resolution power of such optical devices is bounded by diffraction, making them inviable for the identification of certain pathologies that require sub-diffraction resolution power for diagnosis. Examples of these are minimal change disease [5], primary ciliary dyskinesia [6], and amyloidosis [114]. Traditionally, such cases required the high-resolution capabilities of electron microscopy, at the expense of low imaging throughput and elevated costs. The new field of fluorescence-based super-resolution optical microscopy has the potential to bridge the resolution-throughput gap between conventional brightfield microscopy and electron microscopy, enabling a faster, sharper, and more cost-effective approach for the visualization of sub-diffraction features in tissues relevant both for research and for clinical practice.

1.4.1 Practical considerations for super-resolution histology

To date, nearly all SRM methods have been demonstrated in tissues, giving the scientific community a glimpse of its potential benefits. These include a) the identification of morphological changes in renal samples using SIM [18, 19]; b) the visualization of cancer-specific intracellular protein distribution in colorectal samples by STED [15]; and c) the observation of higher-order chromatin folding and other sub-diffraction features associated with cancer development via SMLM [16, 17]. However, the adoption of super-resolution optical microscopy in the field of histology is still far from reality, due to several aspects:

Limited throughput. Most optical SRM methods have intrinsically low imaging throughput, rendering them impractical for the assessment of large histological samples. For example, despite recent efforts to increase the FOV of SMLM methods over 100 μm × 100 μm [32], these techniques require the acquisition of thousands of frames for a single super-resolved FOV, which severely slows down their imaging throughput and poses a technical challenge for the storage and postprocessing of the fluorescence data. On the other hand, STED microscopes are point-scanning systems that make them impractical for analyzing centimeter-scale tissue sections commonly used in histology. Next, although the SIM method is known for its fast acquisition capabilities, requiring as little as 9 or 15 frames per 2D-SIM or 3D-SIM reconstruction, respectively, commercial SIM implementations are limited to a FOV up to 50 μm × 50 μm, implying sequential acquisition of adjacent areas followed by tile-mosaic stitching to obtain large FOVs [85]. Recent SIM developments, however, have surpassed imaging areas of 150 μm × 150 μm [87, 88], offering good prospects for the advancement of high-throughput super-resolution histopathology. Finally, while the combination of the ExM method [115] and multi-focus light-sheet microscopy imaging [46] hold good promise for tissue super-resolution microscopy, further advancements in the sample preparation protocols are necessary for its adoption in histological settings.

Light scattering. SRM methods are susceptible to light scattering induced by refractive index heterogeneities of tissue sections. Particularly in formalin-fixed paraffin-embedded (FFPE) sections, the refractive index mismatch between the imaging and the sample media

leads to spherical aberrations that produce reconstruction artifacts in the SIM method [86]. Also, index variations within the sample lead to light scattering and subsequent distortion of the illumination patterns, rendering failed SIM reconstructions. Similarly, in the case of STED, the light scattering experienced by the depletion laser affects the shape and size of the depletion doughnut, therefore compromising the lateral resolution of the method [116]. As for SMLM, the light scattering aberrations limit the localization precision of the fluorescence events, also affecting the lateral resolution of the method [10].

Autofluorescent signal. Common histological reagents such as paraformaldehyde and glutaraldehyde, used for the fixation of biological samples, induce autofluorescence [117, 118]. The autofluorescence increases the background signal, affecting the resolution capabilities of SRM methods in different ways. In SIM, for example, the background signal reduces the contrast of the illumination pattern, posing a technical demand on the algorithm's task to recognize and decode the moire fringes, and subsequently, reconstruct the super-resolved SIM image. In SMLM, on the other hand, an elevated background signal is detrimental to the localization precision, and therefore, unfavorable to the lateral resolution of the method.

High labeling densities. Super-resolution optical methods like SMLM and FF-SRM are particularly sensitive to fluorophore density. While these methods successfully resolve fine cellular features like cytoskeletal filaments, they tend to underperform on densely labeled structures, requiring labeling optimization steps to meet the method's demands in terms of temporal and spatial sparsity [10, 110].

Special preparations. The susceptibility of the SRM methods to light scattering, autofluorescence, and labeling density, particularly on FFPE samples, sometimes requires the adoption of special preparation steps that deviate from standard histological methods. These include a) employing optical clearing reagents to homogenize the index of refraction of the sample [119]; b) using ultra-thin tissue sections to reduce the background signal and to minimize the light scattering issues [10]; and c) reducing the autofluorescence through chemical quenching and/or photobleaching [117]. These strategies often require special tools, equipment, reagents, and manual handling, which effectively increases the sample preparation time, cost, and complexity, making them unattractive for standard histological laboratories.

System complexity. Besides sample preparation, commercial SRM systems require advanced expertise in fluorescence microscopy to handle tasks related to image acquisition, post-processing, and troubleshooting. While all these aspects require close attention to accomplish the desired level of contrast and resolution, this particular skill set is not commonly available in routine histological laboratories.

High costs. The instrumentation and operational costs of commercial SRM methods are still unaffordable for most histological laboratories around the world. To name a few examples, a multimodal imaging system (e.g., multicolor DV, TIRF, SMLM, and 3D-SIM) such as the OMX microscope used in this doctoral thesis is expensive and in the order of EUR 500,000. Single modality imaging systems such as benchtop SMLM microscopes have an average price tag of EUR 250,000. In addition to the microscope's cost, the service and scheduled maintenance of SRM systems are also high, with fees typically exceeding EUR 5,000 per intervention.

1.4.2 Sample preparation for histology

Equally important to the invention of new microscopy methods, the development of sample preparation methods has been fundamental for advancements in all fields of life sciences, including histology. There exist multiple strategies for preserving the chemical composition and the micro-architecture of the specimens as close as possible to their native state. However, it should be noted that all preparation methods introduce some degree of distortion in the sample, which can be detrimental to the quality of the imaging system. Therefore, an adaptation of the preparation method is often necessary, particularly in SRM methods, to allow for optimal sample observations.

There are several approaches for preserving histological samples but, in essence, these consist of removing, fixing, infiltrating, embedding, and sectioning part of an organ for observation in a microscope. The fixation step usually involves the use of chemical reagents (e.g., formaldehyde and/or glutaraldehyde derivatives) that stop the enzymatic activity of the sample by inducing chemical cross-linking. The chemical fixation prevents the autolysis and putrefaction of the specimen while preserving its structural characteristics. Next, the infiltration and embedding step provide mechanical strength for sectioning, allowing for thin tissue slices beneficial for microscopic observations[13]. Particularly, as discussed in section 1.2.1, thin tissue sections are advantageous in epifluorescence-based microscopy approaches for reducing the off-focus contribution, and therefore, enhancing the image contrast and resolution.

After the preservation and sectioning steps, the sample is further prepared for labeling and subsequent microscope imaging. Here, the sample preparation steps vary depending on the histological method and the imaging modality, but they usually consist of removing the protectant materials used for infiltration, followed by rehydration before labeling. Conventionally, chemical markers are used to add contrast to the sample, allowing for optimal identification of microanatomical structures relevant to the histological analysis. As discussed in section 1.1.5, there exist different labeling strategies for tissue sections, one of them being fluorescence labeling.

The histological methods can be broadly divided into two groups, one group utilizing resin or wax embedding to allow smooth sectioning at room temperature, and another group utilizing cryogenic temperatures both for preservation and sectioning. Among these[14], the formalin-fixation paraffin-embedding (FFPE) [120] and the Tokuyasu cryopreservation method [111] are well-established approaches for histological analysis in light and electron microscopy, respectively.

    FFPE method. The FFPE preservation method consists of a series of steps in which the specimens are infiltrated with a paraffin wax-based agent that, once solidified, provides the mechanical support necessary for thin sectioning. The process, illustrated in Figure 1.4-2,

---

[13] Conventionally, thin tissue samples (2-4 μm) are employed for the transmission of the light in brightfield microscopy. Similarly, ultrathin secitons (70-100 nm) are used in transmisison electron microscopy. However, other approaches such as multiphoton microscopy and light-sheet microscopy allow for visualization of thick (i.e., hundreds of microns) specimens.

[14] The complete list of histological preservation methods is extensive and a detailed coverage of them is beyond the scope of this thesis. The two methods presented here, namely, the FFPE and the Tokuyasu cryo-preservation, are common preservation methods used in light and electron microscopy, respectively.

covers fixation, grossing, dehydration, paraffin infiltration, embedding, sectioning (usually, 2-4 μm), deparaffinization, rehydration, and labeling of the specimen[15]. A great deal of these steps are fully automated by tissue processors, taking approximately 12 hours from dehydration to paraffin infiltration, depending on the sample size and composition. Paraffin-embedded specimens benefit from high stability, allowing for several years of storage at room temperature [120].

Due to its simplicity, repeatability, reliability, low cost, and large section areas (ranging from the square millimeter to the square centimeter scale), the FFPE method is nowadays the most common histological preservation method, with hundreds of millions of samples stored in biobanks around the world [17, 122]. All these features make FFPE a valuable source of biological material for a wide variety of studies to aid in the diagnosis [120] and prognosis [123, 124] of diseases.

The main disadvantages of the FFPE method are the notorious autofluorescence [117] and the epitope masking induced by the fixative cross-linking and subsequent paraffin infiltration [125]. While these issues are less noticeable for histological workflows based on absorbent dyes such as hematoxylin and eosin (H&E), they pose a challenge for fluorescence-based studies by increasing the background signal and the unspecific labeling, therefore necessitating additional preparation steps such as bleaching and antigen retrieval for optimal results.
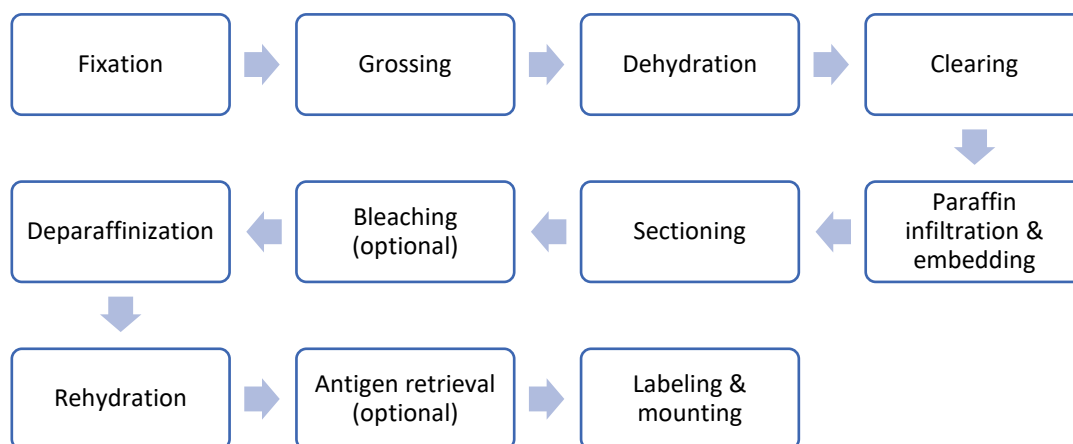
Figure 1.4-2.   Preparation steps for FFPE samples. A conventional sample preparation protocol for paraffin-embedded sections includes fixation, grossing, dehydration, clearing, paraffin infiltration, embedding, sectioning, deparaffinization, rehydration, labeling, and mounting of the specimen. Additional steps such as bleaching and antigen retrieval can be introduced to, respectively, reduce the autofluorescence and improve the antibody binding specificity.

Tokuyasu method. In the early days of electron microscopy, the preferred method for preserving and sectioning thin biological samples was resin embedding. Similarly to the FFPE method, the main drawback of this approach was the limited epitope accessibility for immunolabeling. To solve this problem, in the 1970s, a Japanese scientist named Kiyoteru

---

[15] A complete description of these steps can be found in specialized histological literature, for example, in ref. [121].

Tokuyasu developed an alternative technique based on cryogenic preservation and sectioning that allowed both for superior antigenicity and ultrathin sectioning (e.g., 70-100 nm) for transmission electron microscopy (TEM) [3]. Since then, the so-called Tokuyasu method has become the gold standard preservation strategy for high-specificity observations in electron microscopy, and more recently, in correlative light-electron microscopy [111].

The Tokuyasu workflow, illustrated in Figure 1.4-3, comprises distinct steps including rinsing, fixation, grossing, sucrose infiltration, cryogenic storage, cryosectioning, labeling, and mounting.
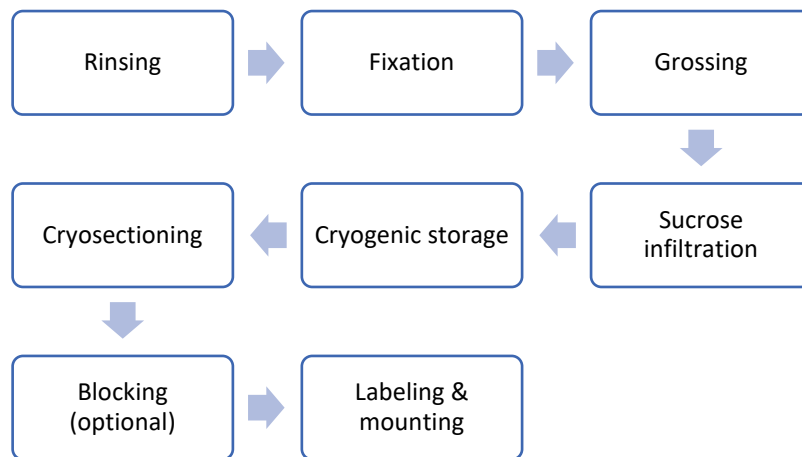
Figure 1.4-3.   Preparation steps for Tokuyasu cryosections. The Tokuyasu method comprises distinct steps including rinsing, fixation, grossing, sucrose infiltration, cryogenic storage, cryosectioning, labeling, and mounting. An additional blocking step can be introduced to reduce the unspecific binding of the antibodies to the sample substrate and/or non-targeted sample components.

Despite its multiple advantages in terms of ultrastructural preservation and antigenicity, the Tokuyasu method presents several limitations for routine histology. For example: a) contrary to the FFPE method, where many of the steps are fully automated by tissue processors and tissue stainers, the Tokuyasu cryopreservation method requires manual intervention in practically all the processing steps; b) the method requires special tools (e.g., a diamond knife), reagents (e.g., liquid nitrogen), storage (e.g., nitrogen tank), and sectioning equipment (e.g., a cryo-ultramicrotome) to work at cryogenic temperatures; c) the ultrathin cryosectioning requires a highly skilled histo-technician; and d) the section area is usually limited to a maximum of 500 μm × 500 μm that is insufficient for the analysis of large tissue samples.

Chapter 2   Histology on a commercial SIM setup

This chapter explores the use of a commercial 3D-SIM microscope for the visualization of placenta sections prepared by the FFPE and Tokuyasu methods, respectively. The advantages and tradeoffs of using 3D-SIM for histological studies are hereby discussed. The chapter covers the scientific contributions of Paper I, whose complete version is presented in Appendix A.

Paper I

Title:	**Visualizing ultrastructural details of placental tissue with super-resolution structured illumination microscopy**
Status:	Published in Placenta (2020).
Authors:	<u>Luis E. Villegas-Hernández</u>, Mona Nystad, Florian Ströhl, Purusotam Basnet, Ganesh Acharya, Balpreet S. Ahluwalia.
Description	A methodology for multicolor SIM imaging of placental tissue sections is presented. This includes the preparation steps and the acquisition parameters for a successful structured illumination microscopy of placental samples preserved under two different approaches, namely the FFPE method and the Tokuyasu method.
Contribution:	LEVH optimized the sample preparation and acquisition steps for 3D-SIM imaging of placental tissue. LEVH performed the imaging experiments and subsequent image analysis. LEVH wrote the first draft of the manuscript and finished the paper. All authors contributed to writing and revising selected sections of the article.

2.1 Background and objectives

The placenta is a pregnancy-related organ responsible for the exchange of gases, waste, and nutrients between the mother and the fetus [126]. The placental tissue is divided into two components, the maternal and the fetal sides. The maternal side provides blood from which the fetus takes in the nutrients and discards the fetal waste (Figure 2.1-1). To maximize the surface area in contact with the maternal blood, the fetal tissue takes the form of tree-like protrusions known as chorionic villi. All the biochemical exchange between mother and fetus takes place at the apical side of the chorionic villi, in a fine interface called microvilli brush border (MVBB). Placental dynamics not only play a critical role in fetus development and pregnancy health by protecting the fetus against external pathogens [127] but also in the post-partum well-being of individuals. Scientific evidence suggests that placental pathologies are associated with post-birth diseases both for the mother and her offspring [128], such as in the case of pre-eclampsia [129].

Previous electron microscopy studies have identified morphological changes in pre-eclamptic placentas occurring at a sub-diffraction scale including, among others, alterations in the placental microvilli brush border (MVBB) [130]. This makes the placenta a relevant case study for the exploration of super-resolution imaging on tissue samples. Having no precedent literature covering SRM of placental samples, this technical paper aimed to shed light on the sample preparation steps and imaging parameters necessary for successful SRM imaging of chorionic villi tissues via the SIM method. Moreover, both due to the placental sample availability and the existing co-operation between the research groups at the UiT, made the choice of placental tissue adequate for this investigation.
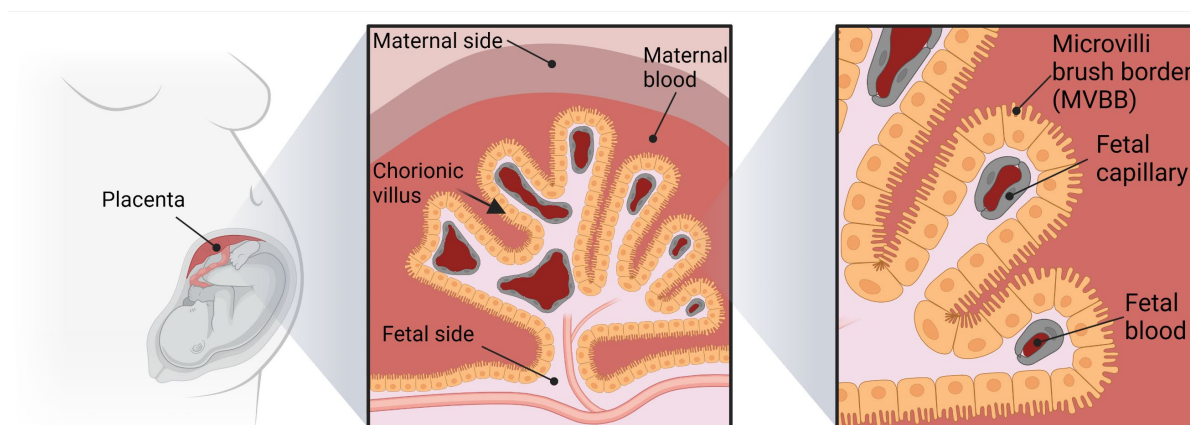
Figure 2.1-1.   Schematic representation of a human placental tissue. The placenta is divided into the maternal side and the fetal side. The food and waste exchange between the fetus and the mother occurs at tiny ultrastructural protrusions collectively called microvilli brush border (MVBB), not resolvable in conventional optical microscopy methods.

2.2 Materials and methods

The microscopy imaging was performed on a commercial DeltaVision OMX V4 Blaze imaging system (GE Healthcare), equipped with a 60X/1.42NA oil-immersion objective. To qualitatively compare the results, two imaging modalities available on the OMX microscope were implemented: deconvolution microscopy (DV) and 3D structured illumination microscopy (3D-SIM). The DV method was used as a high-resolution benchmark near the diffraction limit of the microscope, whereas the SIM method was used to visualize ultrastructural features beyond the reach of the DV method.

To assess the performance of 3D-SIM on different histological preparations, placental sections preserved under the FFPE and the Tokuyasu methods were used. The samples were previously collected and preserved by Dr. Mona Nystad and Prof. Ganesh Acharya, both co-authors of this study. Histological slices of both FFPE and Tokuyasu samples were sectioned by experienced histo-technicians and deposited on #1.5 coverslips in their native states (e.g., unlabeled and unprocessed) for further preparation steps inherent to this study. Each type of sample (e.g., FFPE and Tokuyasu) required several preparation iterations to achieve the optimal labeling characteristics for 3D-SIM. These included, among others, selecting and adjusting the dye concentrations, optimizing the incubations and washing times, and choosing the appropriate sample thickness. Thereafter, additional optimization steps were carried out to find the best imaging parameters for 3D-SIM. These included, for example, adjusting the acquisition time and illumination intensity, selecting the number of z-planes for optimal DV and 3D-SIM reconstructions, identifying the oil index, and selecting the appropriate overlap for tile-mosaic stitching. The resulting preparation and SIM imaging workflows are summarized in Figure 2.2-1.
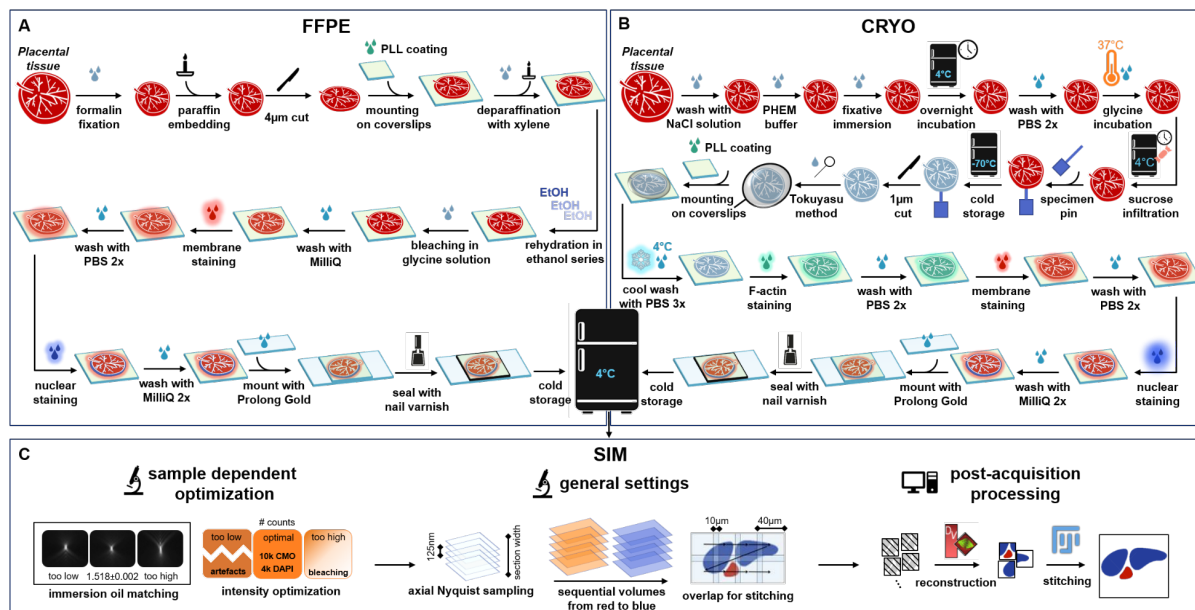
Figure 2.2-1.　Preparation workflow for 3D-SIM imaging. A) Sample preparation protocol for FFPE placental sections. B) Sample preparation protocol for Tokuyasu cryosections. C) Acquisition parameters for 3D-SIM imaging. Adapted from Paper I.

2.3 Scientific contribution

Paper I provides a step-by-step protocol for successful 3D-SIM imaging of tissue sections prepared under two different histological procedures, namely FFPE and Tokuyasu methods. The presented work was the realization, for the first time, of super-resolution optical microscopy of placental chorionic villi sections. Both in the FFPE and the Tokuyasu sections, the 3D-SIM method allowed for a contrast and resolution improvement compared to the conventional DV method (Figure 2.3-1). In the FFPE samples, for example, the SIM method enabled the distinction of features like the plasma membrane separation between adjacent cells and other structural details in the sample not visible with the DV method (Figure 2.3-1a1 and Figure 2.3-1a2). Remarkably, the 3D-SIM method allowed the visualization of the MVBB in the Tokuyasu sample (Figure 2.3-1b1), a structural feature relevant for placental studies that, previously, was only attainable via electron microscopy. Apart from the sample preparation challenges (discussed below), the Tokuyasu cryosections allowed for a shorter and simpler sample preparation protocol compared to the FFPE samples, requiring fewer steps than the FFPE method.
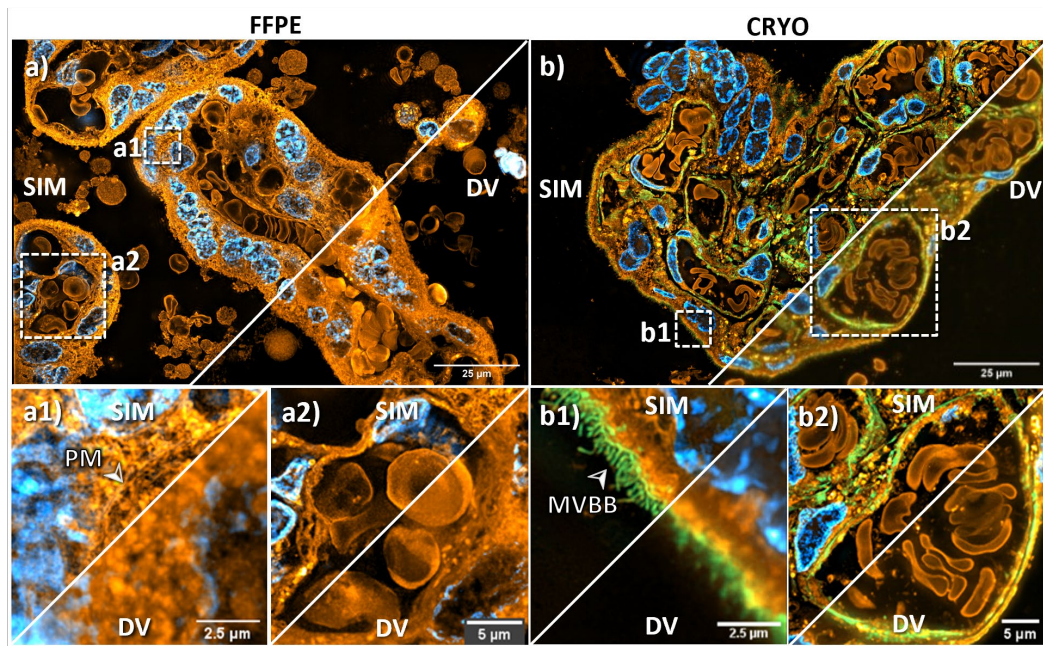
Figure 2.3-1.   Representative results from Paper I. a) The SIM method allowed for higher contrast and resolution on the FFPE placental section compared to the DV method. This enabled the identification of a plasma membrane component between two adjacent cells in (a1), as well as a sharper visualization of subcellular features around a fetal capillary in (a2). b) In the Tokuyasu cryosection, the SIM method enabled, for the first time using optical methods, the visualization of the microvilli brush border along the apical side of a chorionic villus, as shown in (b1). Moreover, a zoomed-in view of the (b2) region in SIM revealed fine details of a pericyte supporting an endothelial cell lining a fetal capillary. Adapted from Paper I.

2.4 Limitations, challenges, and opportunities

In this work, two limitations to the application of 3D-SIM in histology were recognized:

Limited FOV. A common limitation encountered in the study was that, for the 3D-SIM configuration supported by the OMX microscope, the imaging area was limited to a maximum FOV of 40 μm × 40 μm, which was insufficient to image large sample areas. To address this issue, several SIM images were acquired over adjacent sample regions and subsequently put together in a tile-mosaic format (Figure 2.4-1). To allow for optimal stitching, an image-to-image overlap of 10 μm was introduced during the imaging acquisition. Despite enabling the visualization of large sample areas, the stitching approach was somewhat slow for routine histological analysis. For example, to obtain an assembled 3D-SIM FOV of 220 μm × 220 μm, a tile-mosaic of 7 × 7 images would be required. This, considering 15 raw frames for a single z-plane, and the 8 z-planes required for a single 3D-SIM image, means a total of 5880 SIM raw frames (15 raw frames/z-plane × 8 z-planes/3D-SIM × 49 3D-SIM = 5880 raw frames). As further discussed in Supplementary Information S12 in Paper II, the processing time of such a dataset would account for approximately 2.5 hours. We acknowledge that, potentially, the 2D-SIM method could alleviate the imaging demands for histology, since only 9 frames are required per 2D-SIM image. Unfortunately,

we could not benchmark this premise, since the 2D-SIM modality was not available at our laboratories.
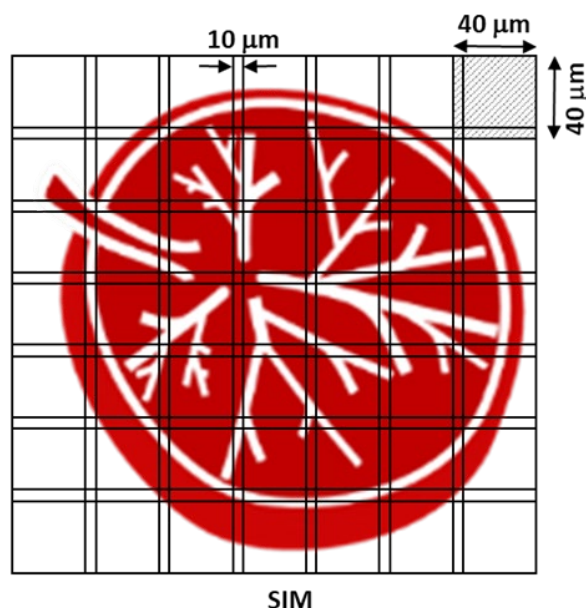
Figure 2.4-1.   Tile-mosaic imaging acquisition for large FOV 3D-SIM imaging. The limited FOV supported by the 3D-SIM method explored in this work (roughly, 40 μm × 40 μm), made it necessary to acquire multiple images across adjacent regions, and subsequently stitch them together in a tile-mosaic format to obtain a large SIM image. In this particular example, to obtain a 220 μm × 220 μm FOV, a total of 49 SIM images would be required. This, considering the z-planes, phase shifts, and pattern orientations, meant a total of nearly 5880 raw frames. Adapted from Paper II.

Manual handling. The second limitation, also related to the OMX microscope configuration, was the requirement for a #1.5 glass coverslip as a sample substrate. Since the automated tissue stainers are designed for conventional microscope slides and not for coverslips, we could not integrate these devices along the processing workflow, and instead, we were constrained to manual handling of the samples throughout the whole preparation process, therefore limiting the overall throughput of the 3D-SIM imaging method. We acknowledge that this limitation can potentially be alleviated by the use of custom-made adapters such that the coverslip substrates can be fitted into existing histological devices. This approach, however, was not explored in this thesis, and therefore, is left for future studies.

When it comes to the histological methods, each one presented unique challenges both in the preparation and imaging acquisition steps:

FFPE sections. The paraffin-embedded samples exhibited high levels of autofluorescence, particularly at 488 nm excitation, which contributed to artifacts in the reconstructed SIM images. This issue was partially minimized by using a bleaching solution and by avoiding the 488/520 nm excitation/collection channel in the experiments. Another challenge with the FFPE samples was the refractive index heterogeneity between the sample and the imaging media that induced reconstruction artifacts in the 3D-SIM algorithm. Although a simple PSF optimization would have solved this issue, the high sample density and thickness

made it difficult for the observation of single emitters in the orthogonal views, to successfully achieve the oil-matching (see section 1.3.1). To tackle this issue, instead of characterizing the symmetry of the PSF via orthogonal views, the oil was iteratively changed until optimal SIM reconstructions were obtained. We acknowledge that, despite providing a solution to the problem, this method might not suit routine SIM imaging of FFPE samples, and future works should address this topic by, for example, introducing fluorescent beads near the sample environment, such that they can be used as single emitters for PSF optimization. Lastly, in the FFPE sections, we could not identify individual microvilli in the MVBB as in the Tokuyasu sections. We initially hypothesized that, due to the aforementioned challenges of this preparation method, the 3D-SIM method failed in reconstructing such features, but a later visualization of FFPE placental sections through a scanning electron microscope suggested that, in this preservation method, the ultrastructural morphology of the MVBB might have been altered by clustering of adjacent microvilli (see Fig. 5 in Paper III), therefore limiting the visualization of these structural features in 3D-SIM.

Tokuyasu sections. The main limitation experienced with the cryopreserved samples was the need for a highly-skilled histo-technician and a specialized sectioning device (i.e., a cryo ultramicrotome) associated with the Tokuyasu method, which increased the operational costs compared to the FFPE sections. On the handling aspect, the transparency of the ultrathin cryosections posed a challenge through the labeling process, as they tended to detach from the coverslip during the washing steps, without noticing it. In addition, the placental cryosections exhibited several structural artifacts in the form of folds and tearing upon cryosectioning that severely limited the contextual visualization of the samples. This issue was partially remediated by sectioning thicker slices of 400-1000 nm, which allowed for significantly fewer folds, but often led to other issues, such as structural damage on the sectioning blade. Consequently, sectioning artifacts were often observed in the sample in the form of knife marks, which hindered the visualization of the sample. Relevant examples of the folding and sectioning artifacts are presented in Supplementary Information S5 of Paper II.

Chapter 3   Histology on a photonic chip setup

This chapter explores the use of the photonic chip-based imaging platform for histological examinations. The chapter is comprised of Paper II and Paper III, respectively. In Paper II, the photonic chip is validated as a feasible method for multimodal super-resolution optical microscopy of cryopreserved tissue sections by the Tokuyasu method. Next, in Paper III, the photonic chip is proposed for high-contrast and high-resolution imaging of FFPE samples over scalable fields of view. The working principle of photonic chip-based histology is herewith presented, along with a discussion of the strengths and weaknesses of the method.

Paper II

Title: **Chip-based multimodal super-resolution microscopy for histological investigations of cryopreserved tissue sections.**

Status: Published in Light: Science & Applications (2022).

Authors: <u>Luis E. Villegas-Hernández</u>*, Vishesh Dubey*, Mona Nystad, Jean-Claude Tinguely, David A. Coucheron, Firehun T. Dullo, Anish Priyadarshi, Sebastian Acuña, Azeem Ahmad, José M. Mateos, Gery Barmettler, Urs Ziegler, Åsa Birna Birgisdottir, Aud-Malin Karlsson Hovd, Kristin Andreassen Fenton, Ganesh Acharya, Krishna Agarwal, Balpreet Singh Ahluwalia.

Description: Photonic chip-based microscopy is validated as a multimodal imaging platform for cryopreserved Tokuyasu sections. The proposed methodology offers multicolor high-contrast visualizations of histological samples over large fields of view, together with tissue super-resolution imaging SMLM, FF-SRM, and CLEM methods.

Contribution: LEVH planned and coordinated the experiments, performed sample preparation, image acquisition, and subsequent image analysis. LEVH wrote the first draft of the manuscript and finished the paper. All authors contributed to writing and revising selected sections of the article. *These two authors contributed equally to this work.

Paper III

Title: **Super-resolution histology of paraffin-embedded samples via photonic chip-based microscopy.**

Status: Self-archived in bioRxiv:2023-06 (2023). Under peer review in Nature Communications.

Authors: <u>Luis E. Villegas-Hernández</u>, Vishesh K. Dubey, Hong Mao, Manohar Pradhan, Jean-Claude Tinguely, Daniel H. Hansen, Sebastián Acuña, Bartłomiej Zapotoczny, Krishna Agarwal, Mona Nystad, Ganesh Acharya, Kristin A. Fenton, Håvard E. Danielsen, Balpreet Singh Ahluwalia.

Description: Photonic chip-based microscopy is proposed as a high-throughput super-resolution imaging platform for the observation of commonly available FFPE samples. The high-intensity variance supported by the chip is harnessed by the MUSICAL algorithm to obtain large FOV super-resolution images using an FF-SRM approach. The photonic chip is proven compatible with existing preparation steps of FFPE samples, enabling seamless integration into routine histological workflows.

Contribution: LEVH planned and coordinated the experiments, performed sample preparation, image acquisition, and subsequent image analysis. LEVH wrote the first draft of the manuscript and finished the paper. All authors contributed to writing and revising selected sections of the article.

3.1 Background and objectives

Morphological changes associated with diseases are heterogeneous, often showing an uneven distribution across affected organs. A tissue suspected of pathological damage might show diseased features in certain regions of the slide while exhibiting healthy signs in others. Therefore, histological investigations require the inspection of large tissue areas, typically on the square-millimeter or square-centimeter scale, for the identification of relevant regions to the tissue analysis. In some conditions, high magnification and high resolution are also required to render a diagnosis or a research conclusion (see section 1.4). While super-resolution optical microscopy methods can achieve detailed visualizations of pathologies beyond the resolution limit of conventional microscopes, the small imaging FOV supported by many of these novel SRM methods might be inadequate to meet the fast-imaging demands of routine histological analysis.

Waveguide-based TIRF microscopy is an appealing approach for histological investigations, due to its high contrast, high sensitivity, and large-scale visualization of fluorescently labeled specimens. Despite its successful applicability in cellular studies [20-22, 25, 60-62, 68, 69], the use of waveguide-based microscopy for histological evaluations remained largely unexplored. Hence, this research work aimed to explore, for the first time, the capabilities of the photonic chip for super-resolution imaging of histological sections over large fields of view. To achieve this, the following research questions were addressed:

a) Can the photonic chip withstand the sample preparation steps related to histological samples?

b) What type of histological method is most appropriate for on-chip tissue imaging?

c) Which on-chip imaging modalities can be exploited for histological evaluations?, and

d) How can photonic chip-based microscopy assist in super-resolution histology?

The on-chip work was initially planned for a single manuscript covering both the Tokuyasu and the FFPE sections. However, soon after the start of the experimental work, we recognized the need for addressing each histological method separately, to properly address each one of the above questions. Consequently, we decided to split the work into two parts, one for the on-chip histology of Tokuyasu samples, and another for the on-chip histology of FFPE samples. In both works, namely Paper II and Paper III, diverse tissue samples from human and non-human origin were tested. These include human samples of placenta, colon, and prostate, as well as animal samples of mouse kidney, fish retina, and pig heart. Efforts were made to screen different tissue samples to obtain a better overview of the proposed technology.

3.2 Materials and methods

Similarly to Chapter 2, the work presented here required several iterations and optimization steps to fine-tune the sample preparation and imaging acquisition steps to realize the different on-chip histology imaging modalities.

3.2.1 Sample preparation

Leveraging on the acquired knowledge from Paper I, we further optimized the sample preparation steps for on-chip imaging of the Tokuyasu and FFPE samples. These included, among others, the selection of the appropriate fluorescent dyes, the identification of the optimal section thickness, the exploration of different labeling concentrations and incubation times, and the surface functionalization of the chips for sample adhesion. In both cases, the histological material was previously preserved by other article co-authors.

Two distinct sample preparation approaches were followed, depending on the histological method. Briefly:

> **Tokuyasu sections**. After sectioning in a cryo ultramicrotome device, the samples were collected with a loop wire filled up with a cryoprotectant droplet, and carefully deposited over the surface of photonic chip waveguides. Thereafter, the cryoprotectant was dissolved by incubating the sample in phosphate-buffered saline (PBS) and further removed with an aspiration pump. The sample was then labeled with fluorescent markers according to the experimental plan. Here, diverse labeling strategies were implemented including:
>
> a) Direct labeling of membranes, actin filaments, and nuclei; and
>
> b) Indirect immunolabeling, by using primary and secondary antibodies, to visualize mitochondrial structures in the fish eye retina and renal features in the mouse kidney.
>
> After labeling, the samples were washed and impregnated with mounting media before covering them with a #1.5 coverslip and sealing them with picodent twinsil dental glue. A detailed description of the preparation steps for on-chip Tokuyasu sections is offered in Supplementary Information S2 of Paper II.
>
> **FFPE sections**. After microtome sectioning, the paraffin-embedded slices were floated in suspension on a warm water bath and further scooped with a photonic chip. After air drying on a flat surface, the samples were incubated in a 60 °C oven to melt the paraffin excess. Thereafter, the samples were incubated in a series of chemical reagents for deparaffinization and rehydration. These included, for example, the submersion of the chip into harsh solvents like xylene and ethanol. After this point, the samples were fluorescently labeled according to the experimental plan, followed by washing, mounting, and sealing, similar to the steps described for the Tokuyasu samples. Here, both direct and indirect labeling approaches were explored and documented. A detailed description of the preparation steps for on-chip FFPE sections is offered in Supplementary Information S5 of Paper III.

In addition to fluorescence-based imaging on the chip, scanning electron microscopy (SEM) was also explored in this chapter for the dual purpose of validating the on-chip results and obtaining a contextual visualization of the tissue samples. In these cases, the tissue sample required a few additional sample preparation steps. Specifically, after the on-chip imaging, the coverslips were removed from the chips, and the samples were subsequently dried and coated with heavy metals before transferring them to an electron microscope device for SEM imaging.

3.2.2 Photonic chip configuration

The chosen waveguide-based TIRF configuration for this thesis consisted of opaque photonic chips comprised of three distinct layers (Figure 3.2-1a). At the bottom, a ~1 mm substrate layer

of silicon (Si), in the middle, a ~2.5 μm intermediate cladding layer of silicon dioxide (SiO$_2$), and at the top, a waveguide core layer of a high refractive index material that transmits light in the visible spectrum [68]. Two waveguide materials were explored, namely tantalum pentoxide (Ta$_2$O$_5$, $n \approx 2.14$) and silicon nitride (Si$_3$N$_4$, $n \approx 2.0$). The choice of these waveguides were based on its availability in the research group. To ensure maximum sample coverage, several strip waveguide geometries were designed and manufactured in parallel at spacing distances of approximately 25 μm (Figure 3.2-1b). In previous works carried out by other group members [21, 22, 68], the photonic chips were optimized to have a high intensity in the evanescent field, resulting in waveguide heights of 140-250 nm. To enable large FOV imaging of the tissue sections, in this thesis, diverse waveguide widths of 100-1000 μm were explored. The chosen waveguide configurations allowed for single-mode propagation in the vertical direction and multimode propagation in the horizontal direction, respectively (see section 1.2.3.2). Figure 3.2-1c provides a representative example of a photonic chip during the sample preparation of an FFPE tissue sample.
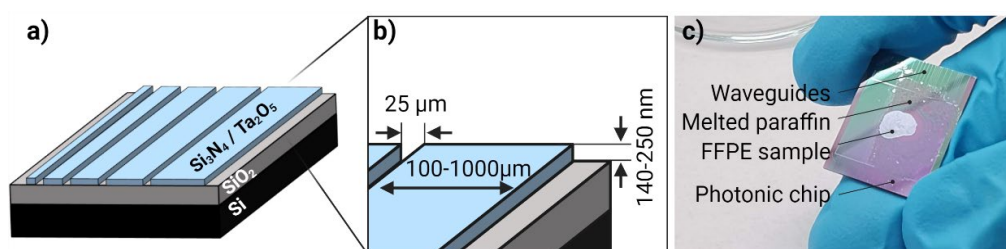
Figure 3.2-1.   Photonic chip configuration used in this thesis. a) The photonic chips are made of three layers consisting of a bottom substrate of silicon (Si), followed by an intermediate cladding layer of silicon dioxide (SiO$_2$), and a top waveguide layer of either silicon nitride (Si$_3$N$_4$) or tantalum pentoxide (Ta$_2$O$_5$). b) Strip waveguide geometries were explored in this work, with varying widths between 100-1000 μm and heights of 140-250 nm. The spacing between adjacent waveguides was set to 25 μm. c) Example of a photonic chip with an FFPE tissue sample after overnight incubation at 60 °C for paraffin melting. Adapted from Paper III.

3.2.3 Chip-based TIRF histology

In Papers II and III, the image acquisition was carried out on a photonic chip-based setup comprised of two modules (Figure 3.2-2): at the top, a collection module consisting of a commercial upright modular microscope (BXFM, Olympus); and at the bottom, a custom-built photonic chip module composed of several translation stages for precise coupling and modulation of the multimode interference (MMI) patterns (details below). Notably, while we followed the same chip-TIRF imaging approach in Papers II and III, in the last study we modified the collection module, to allow an epifluorescence visualization of the FFPE samples (Figure 3.2-2a).

To perform photonic chip-based image acquisition, a laser light beam was coupled to a selected waveguide via the end-fire coupling method with the aid of a microscope objective (0.5 NA) mounted on a precision stage (Figure 3.2-2c). The coupled light propagated through the waveguide core due to total internal reflection, giving rise to a thin evanescent field of ~50-100 nm penetration depth on the surface of the waveguide (Figure 1.2-9a). The evanescent field generated on top of the waveguide surface excited the part of the sample in close proximity to

the chip, enabling TIRF microscopy. The MMI patterns in the horizontal direction provided a semi-stochastic, non-uniform illumination to the tissue sample [22, 24, 25]. To achieve uniform illumination, the MMI patterns were averaged via stepwise coordination of the illumination and the collection light paths (see details below). The fluorescent signal and part of the excitation light were then collected by an objective lens at the top. The excitation light was further blocked by an emission filter and the fluorescent signal was imaged by a scientific CMOS camera (Figure 3.2-2 b). For multicolor imaging, the process was repeated using a specific excitation wavelength for each fluorescent marker. Finally, the acquired image stacks were computationally averaged, pseudo-colored, and merged to obtain a photonic chip-based TIRF (chip-TIRF) image.
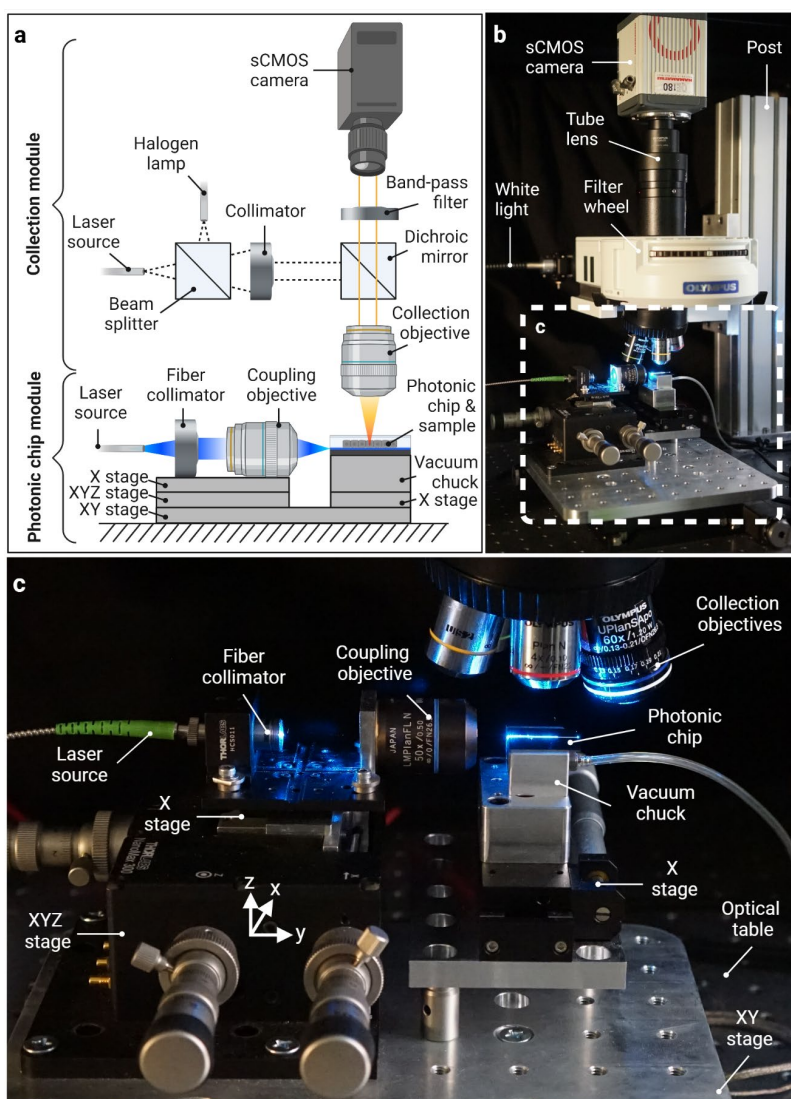
Figure 3.2-2.   Photonic chip-based microscopy setup. a) Schematic representation of the setup used in Paper III. At the bottom is a photonic chip module composed of translation stages, a laser fiber, and a coupling objective for precise modulation of the chip-TIRF illumination. At the top is a collection module comprising the collection objectives, and other optical elements both for EPI illumination and for image acquisition. b) A picture of the photonic chip setup. The white-dotted box denotes the area magnified in c). c) A close view of the photonic chip module. Adapted from Paper III.

Mode averaging

For multimoded waveguides, such as in the photonic chips used in this chapter, the MMI pattern resulting after coupling exhibited a non-uniform intensity distribution along the image field that changed as a function of the illumination source position (Figure 3.2-3a). To obtain uniform intensity distribution across the waveguide, the illumination light was averaged. This was achieved by step-wise coordination of the illumination and the collection paths with the assistance of a motorized stage [22, 24]. In this approach, for each position of the illumination source, an individual chip-TIRF image was collected. By performing this operation in discrete steps over the width of the waveguide facet, an image stack was obtained, where each frame exhibited a unique MMI pattern distribution (Figure 3.2-3b). The collected image stack (typically 200-500 frames) served a dual purpose. On one hand, it enabled a uniform chip-TIRF image (Figure 3.2-3c) via computational averaging in FIJI, and on the other hand, it allowed super-resolution reconstructions via FF-SRM methods.
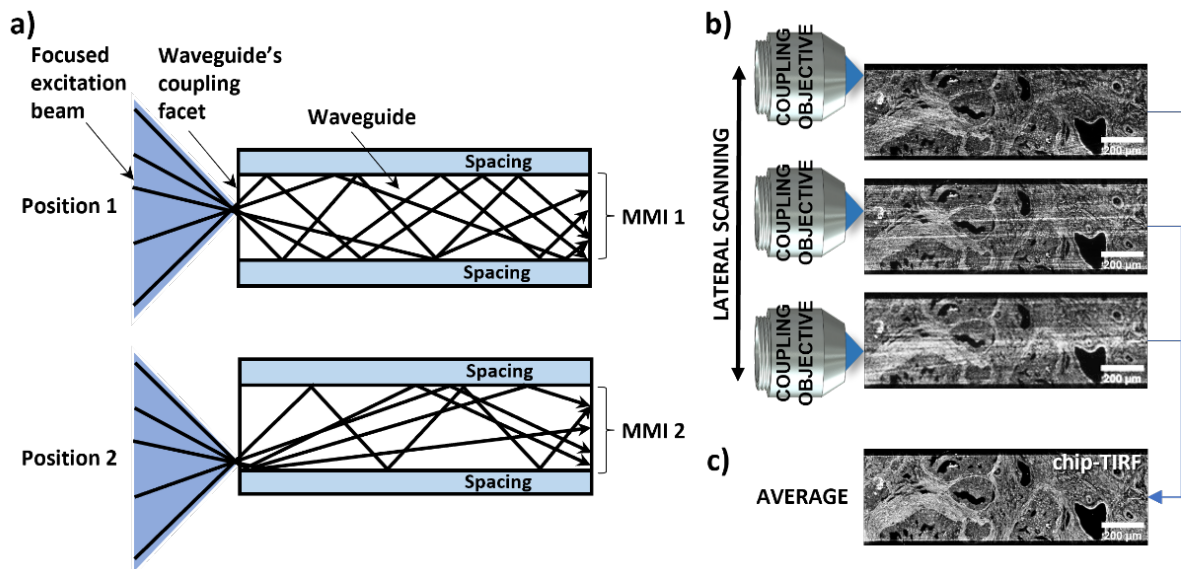
Figure 3.2-3.   Mode averaging in photonic chip-based microscopy. a) Upon end-fire coupling, the excitation light propagates along the waveguide material via total internal reflection. The multi-mode interference (MMI) patterns can be modulated by scanning the coupling objective along the input facet of the chip. b) For each position of the coupling objective, an individual frame is collected. c) The image stack is computationally averaged to obtain a chip-TIRF image. Further analysis of the image stack also allows for FF-SRM reconstructions. Adapted from Paper III.

3.2.4 Chip-based super-resolution histology

Throughout Papers II and III, the photonic chip platform was validated as a feasible imaging platform for fluorescence-based super-resolution histology. Out of the existing on-chip SRM developments, namely SMLM [20, 21], FF-SRM [23-25], and SIM [26], the first two methods were chosen due to their promising capabilities for super-resolution imaging over large

FOVs[16]. While the chosen methods followed the principle of chip-TIRF imaging described above, each of them presented unique acquisition requirements:

On-chip SMLM. The evanescent field excitation delivered by the photonic chip allowed for ultrathin optical sectioning, beneficial both for suppressing the background signal and for ensuring a high illumination intensity. Specifically, the on-chip *d*STORM explored in Paper II involved a high-power laser (e.g., ~100-250 mW), and a thiol-based imaging buffer with an oxygen scavenging system for fluorophore blinking [22]. To enable the dark state, the laser power was initially increased until a low-density blinking was observed on the screen. In addition, in the on-chip *d*STORM approach, there was no step-wise coordination between the illumination and the collection light paths. Instead, the laser beam was arbitrarily scanned along the input facet of the chosen waveguide while multiple blinking events were collected over time. After the collection of several thousand images, these were reconstructed using the ThunderSTORM plugin in FIJI to obtain a super-resolved on-chip *d*STORM image.

On-chip FF-SRM. The properties of the MMI pattern were capitalized by on-chip FF-SRM to achieve sub-diffraction lateral resolution of both Tokuyasu and FFPE sections by acquiring image stacks of 200-500 frames identically as described above for chip-TIRF imaging. The difference, in this case, was that the image reconstruction step was carried out through an FF-SRM algorithm instead of pixel-wise averaging. In particular, the time-modulated high spatial frequencies delivered by the MMI pattern[17], together with the ultrathin optical sectioning provided by the evanescent field, contributed to a finely spaced illumination of adjacent fluorophores that proved advantageous for super-resolution image reconstructions of tissue samples via the MUSICAL algorithm.

3.3 Scientific contributions

Super-resolution histology of cryopreserved tissue specimens

The proposed photonic chip-based method opens new avenues for the application of optical super-resolution microscopy to the field of histology, allowing for high-contrast and high-resolution visualization of tissue sections over large fields of view. Particularly, Paper II experimentally demonstrated, for the first time, the idea of waveguide-based imaging of tissue sections under diverse modalities, including diffraction-limited chip-TIRF, and on-chip super-resolution techniques including SMLM, FF-SRM, and CLEM. Chip-TIRF illustrated the FOV scalability of the photonic chip-based microscopy method (Figure 3.3-1a). On-chip *d*STORM enabled the identification of morphological features in a mouse kidney with a separation of ~100 nm, which were in agreement with the dimensions of the glomerular basement membrane Figure 3.3-1b). Next, the on-chip FF-SRM method allowed the identification of individual microvilli along the apical side of the chorionic villi tissue of placental samples, over a field of view of 220 μm × 220 μm with just 500 frames (Figure 3.3-1c). Arguably, with nearly 10 min

---

[16] Despite achieving sub 100 nm resolution, the on-chip SIM approach developed in ref. [26] provides a limited window imaging area of a few hundreds of microns, thus limiting the applicability this method for large FOV examination of tissue sections.

[17] A previous on-chip study demonstrated a fine speckle size of the MMI illumination patterns, with individual mode widths ~140 nm, measured by FWHM [22].

of combined collection and processing time, the on-chip MUSICAL approach of placental tissue proposed in Paper II provided a higher imaging throughput compared to the 3D-SIM method explored on the OMX microscope in Paper I (see section 2.4). The on-chip CLEM image (Figure 3.3-1d) enabled a good correlation between the fluorescent signals of mitochondria and actin filaments reconstructed by MUSICAL and the SEM image over the entire fish eye retina cryosection, thus validating the photonic chip as a suitable platform for histological CLEM evaluations.
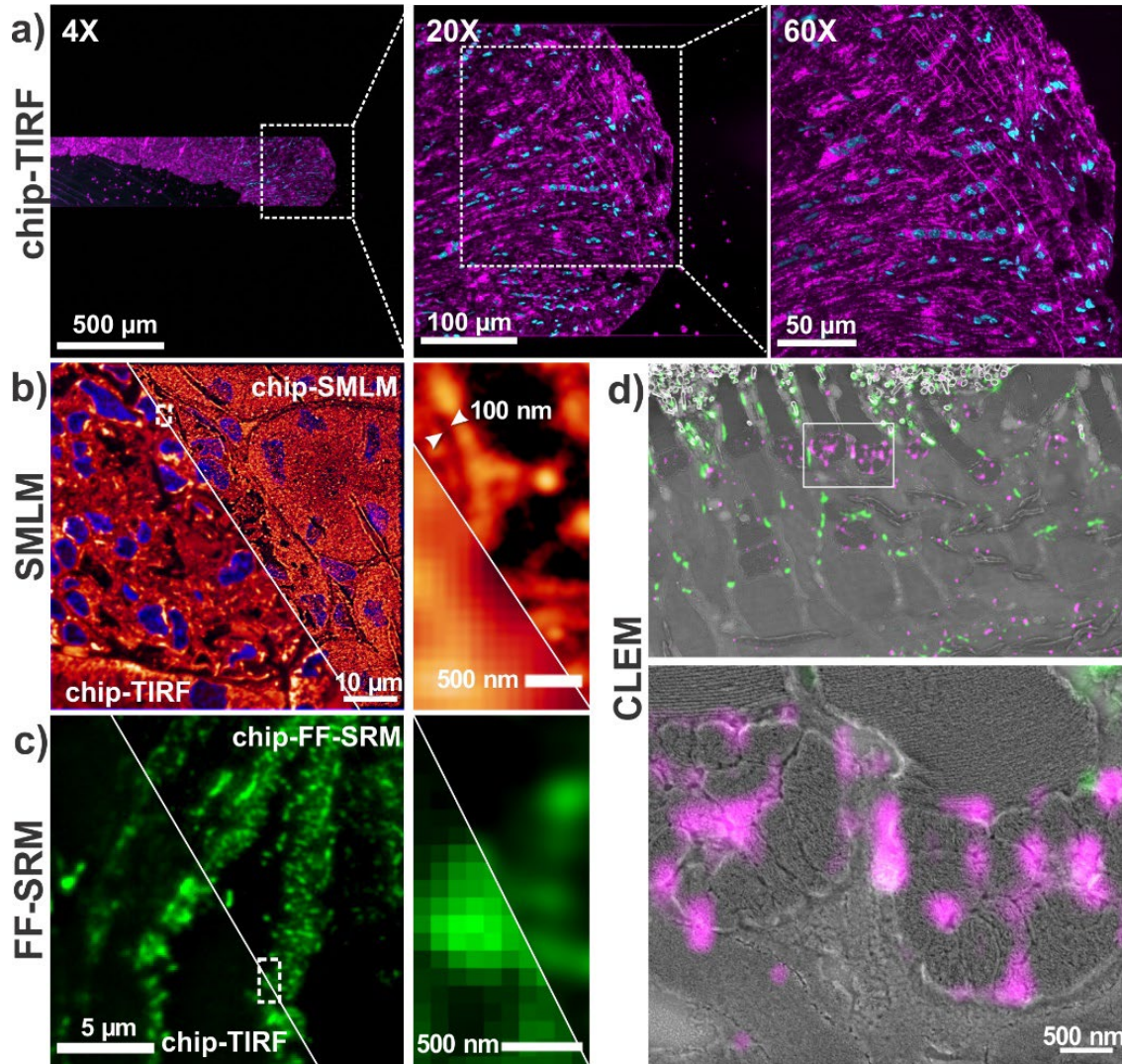
Figure 3.3-1.   Representative results from Paper II. a) The scalable FOV attainable with the chip-TIRF method allowed for high-contrast visualization of a pig heart tissue cryosection at different levels of magnification. b) The on-chip SMLM method allowed the identification of ultrastructural features of 100 nm separation, in agreement with the glomerular basement membrane in a mouse kidney cryosection. c) The on-chip FF-SRM method allowed the identification of individual microvilli along the brush border of a human placental cryosection. d) The on-chip CLEM method enabled an excellent correlation of the mitochondrial and actin signals across the scanning electron microscopy and the chip-TIRF images in a zebrafish eye retina cryosection. Adapted from Paper II.

Super-resolution histology of FFPE tissue specimens

While photonic chip-based histology was successfully demonstrated in Paper II, the Tokuyasu sample availability represented a minority compared to other histological preservation methods. Therefore, to explore the integration of the photonic chip-based microscopy method into routine histology, standard histological samples must be used. This meant exploring the imaging capabilities of the photonic chip on FFPE samples. Consequently, Paper III revealed the advantages of photonic chip-based microscopy for the analysis of FFPE sections. Here, a direct comparison over the same FOV of a placental section showed significant differences in the fluorescence fluctuations upon two distinct illumination approaches. As suggested in the paper (Figure 3.3-2), the combination of the MMI patterns and short penetration depth provided by the chip-based excitation allowed for a superior contrast and resolution visualization of the tissue sample compared to the conventional epifluorescence approach, an imaging modality often used for acquisition of FF-SRM stacks. This work was, to the best of our knowledge, the first demonstration of the MUSICAL method on paraffin-embedded samples.
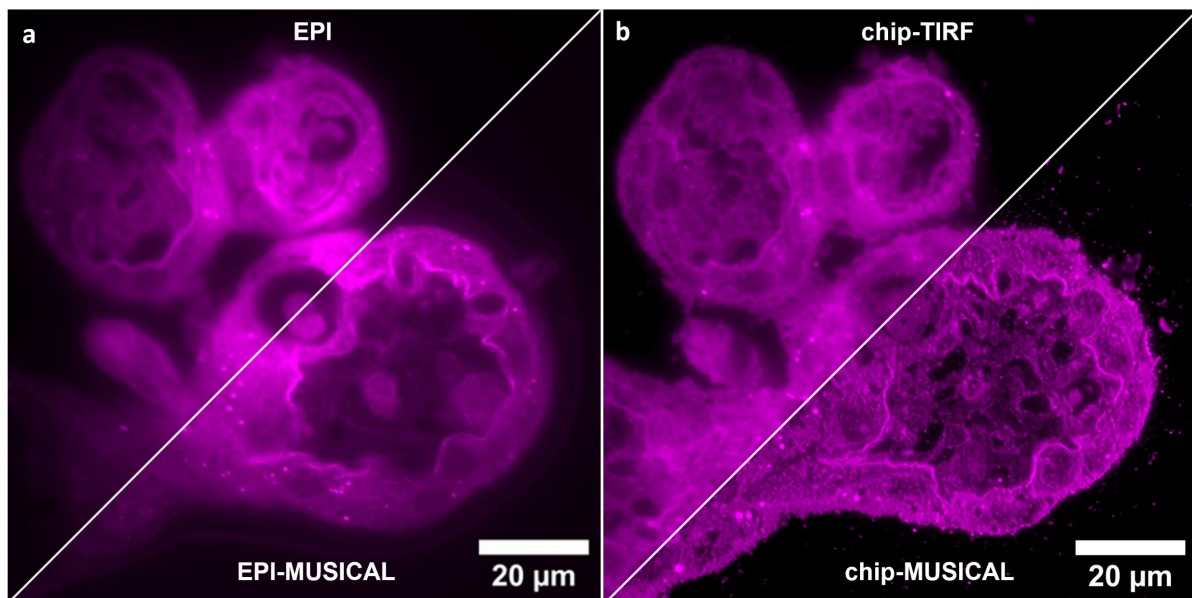
Figure 3.3-2.   On-chip FF-SRM of FFPE sections. a) An FFPE human placental tissue section imaged in epifluorescence (EPI) modality. The top panel illustrates a single-frame EPI acquisition, while the bottom panel illustrates the FF-SRM reconstruction via the MUSICAL algorithm. b) The same sample was imaged via the chip-TIRF method. The top panel illustrates the chip-TIRF image, while the bottom panel illustrates the on-chip FF-SRM reconstruction via the MUSICAL algorithm. Note the enhanced contrast and resolution provided by the on-chip FF-SRM as compared to the conventional EPI-based FF-SRM approach in a). Adapted from Paper III.

The photonic chip-based histology method revealed additional benefits for the evaluation of FFPE samples, such as:

a) An ultrathin optical sectioning that allowed for a high-contrast identification of features not achievable by EPI-based approaches (Figure 3.3-3a); and

b) A uniform illumination over scalable FOVs that significantly expanded the exploitable FOV compared to conventional epifluorescence illumination (Figure 3.3-3b).
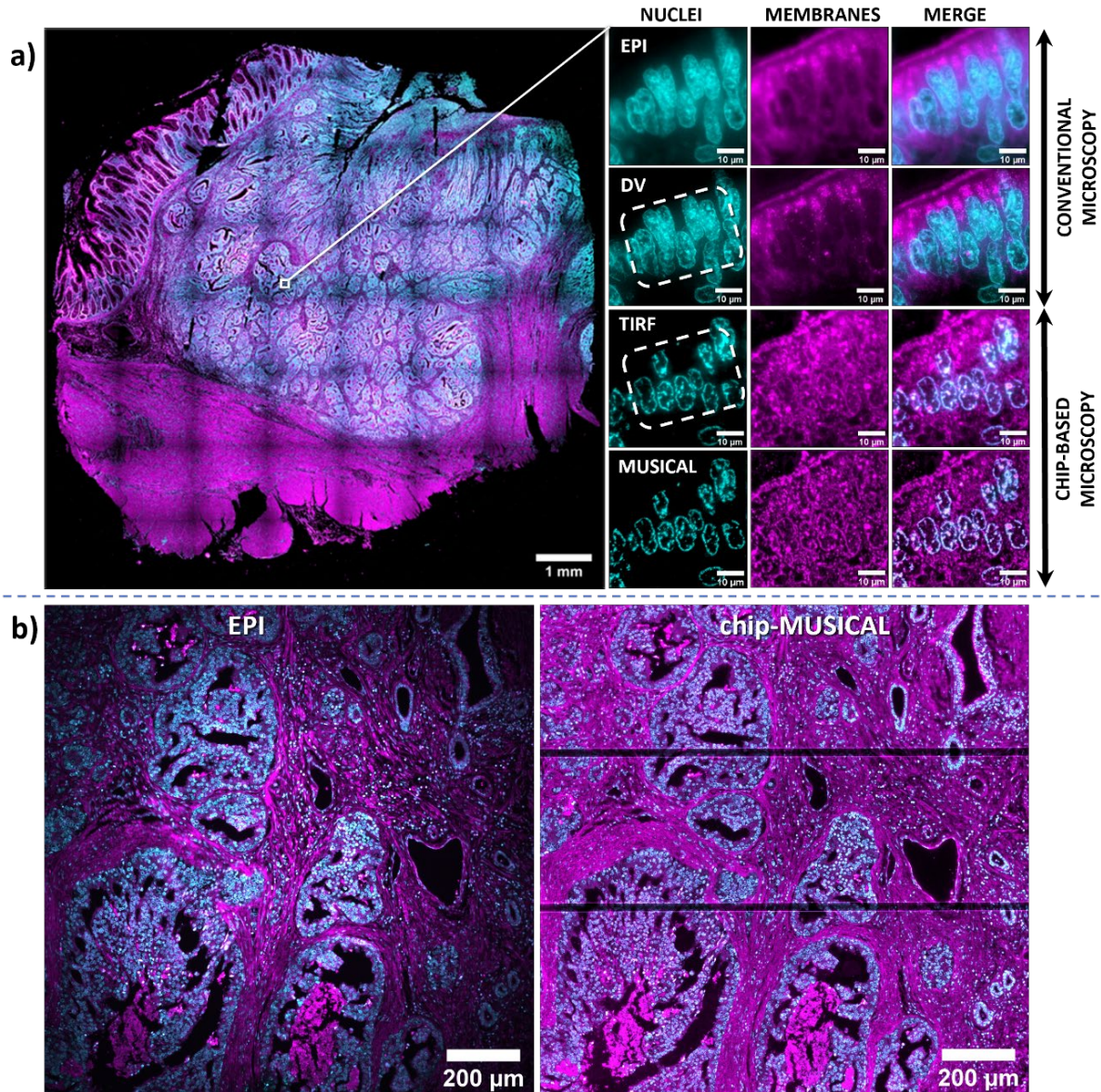
Figure 3.3-3.   Representative results from Paper III. a) An FFPE human colorectal tissue sample visualized in different fluorescence microscopy modalities. The chip-TIRF and on-chip MUSICAL allowed the identification of individual nuclei that were otherwise difficult to distinguish via EPI-based methods. b) An FFPE human prostate sample imaged over a large FOV using a 10X objective. The on-chip MUSICAL image allows uniform illumination across the entire image field, dramatically increasing the exploitable FOV compared to the conventional EPI-based approach. Adapted from Paper III.

Lastly, the CLEM experiment on the FFPE placental sample not only demonstrated the convenience of land-marked chips for easy navigation across different imaging instruments but also allowed for a 1:1 match of structural features corresponding to the microvilli brush border in direct contact with the chip surface.
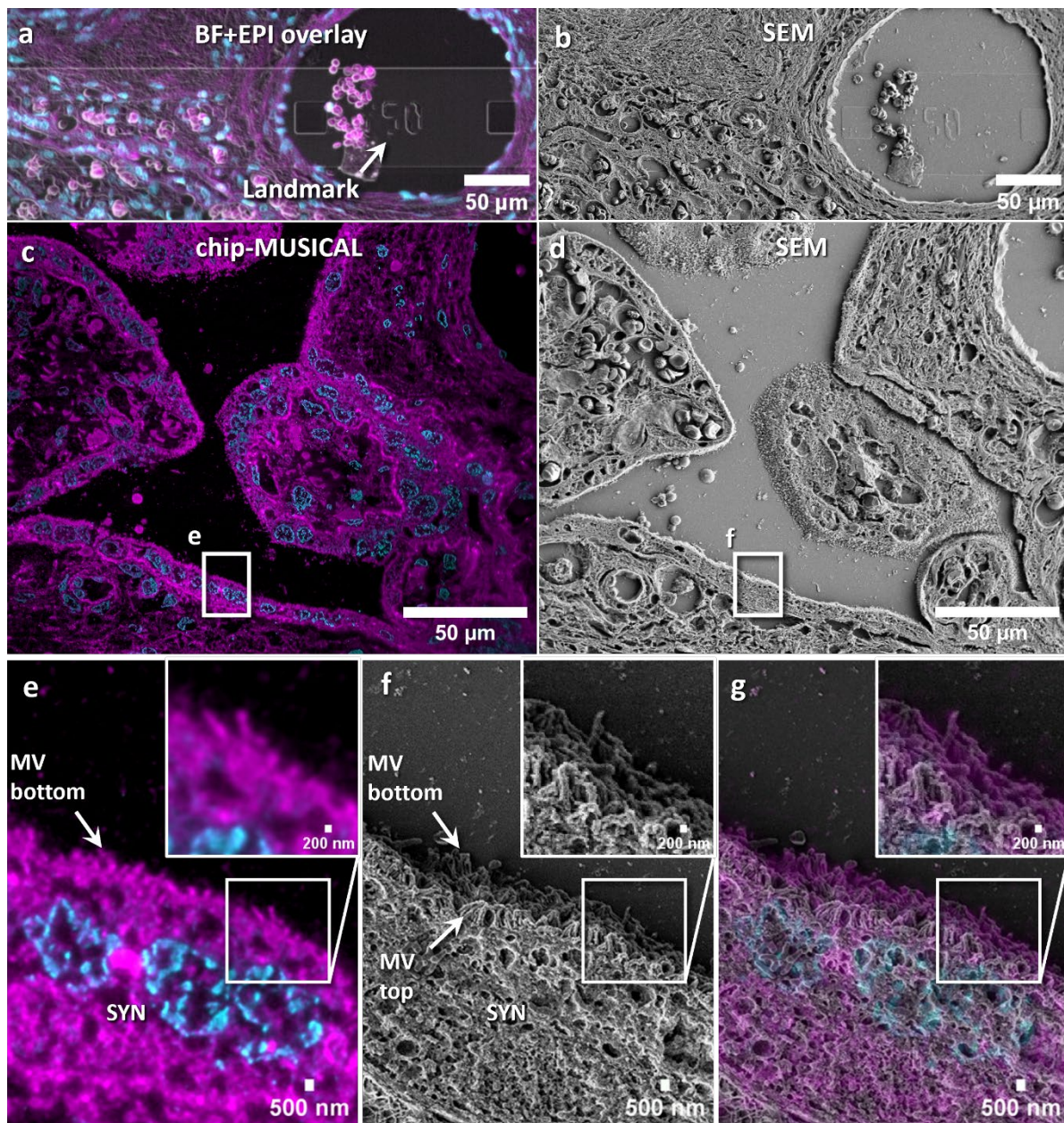
Figure 3.3-4.   CLEM imaging of an FFPE placental section. **a)** Brightfield and EPI overlay illustrating a chip landmark. These landmarks allow for fast and simple identification of the regions of interest across different imaging systems. **b)** The same landmark spotted in an SEM microscope. **c)** Large FOV super-resolution image of the placental section via on-chip FF-SRM, reconstructed by the MUSICAL algorithm. Membranes are shown in magenta and nuclei in cyan. **d)** Corresponding SEM view of the FOV shown in panel c). **e)** The zoomed-in view of the chip-MUSICAL image reveals the presence of microvilli protrusions (MV) along the apical side of the syncytiotrophoblast cells (SYN). **f)** An SEM observation of the same sample region confirms the presence of MV features. In this case, the topographical view of the SEM method allows for the identification of MV elements across the sample volume, with distinctive features at the top and the bottom of the tissue. **g)** An overlay CLEM visualization confirms that the observed features in panel e) match the location of the MV protrusions in direct contact with the chip waveguide, i.e. MV bottom in panel f).

3.4 Limitations, challenges, and opportunities

In general, the implementation of the photonic chip platform for the visualization of histological samples poses some limitations and challenges. These include:

High-speed chip-TIRF. The motorized-assisted illumination approach explored in this thesis, while allowing for the collection of the MMI patterns beneficial for FF-SRM reconstructions, was somehow slow for obtaining diffraction-limited chip-TIRF images. To enhance the imaging speed in such cases, an alternative scanning illumination method via galvanometric (i.e. galvo) mirror can be easily implemented. In this approach, the galvo mirror is used to steer the excitation light along the back aperture of the coupling objective at high speed, such that the focus spot rapidly scans the waveguide facet while a single (uniformly illuminated) image is acquired. The galvo scanning approach allows for relatively short acquisition times, e.g. 10 ms, in comparison with the 10-50 s required for the motorized-assisted approach. In this thesis, however, most of the work was performed by acquiring a stack of MMI pattern images, such that it could be used both for uniform chip-TIRF images and FF-SRM reconstructions.

Fabrication imperfections. The manufacturing process plays a crucial role in determining the performance of photonic chips. Imperfections, such as inhomogeneities in waveguide deposition, might result in scattering spots that can interfere with mode propagation and arbitrarily amplify the collected signal, leading to the appearance of hot spots that, consequently, might hamper the visualization and assessment of the fluorescence image. Additionally, the waveguide walls should be smooth, as side roughness can affect the mode distribution and subsequently lead to the formation of uneven stripe patterns in the averaged chip-TIRF image. In practice, multiple fabrication and characterization cycles are necessary to refine the manufacturing process and produce high-quality chips. Despite these challenges, the fabrication process of these optical waveguides is similar to the CMOS foundries and is a heavily researched field, thus once the process is optimized, a large portion of the fabricated photonic-chips are estimated to be of high quality.

Unguided light. The end-fire coupling strategy is favorable for delivering high illumination intensities to the sample. For efficient coupling, the waveguide facet must be flat, smooth, and clean. Facet imperfections, like cracks, lead to reduced or uncoupled light, resulting in an inhomogeneous mode distribution throughout the image field. Such imperfections can also lead to unguided light in free space, contributing to the background signal by either interacting with the sample (e.g., side illumination) or by coupling into the glass coverslip. Addressing these challenges requires precision cutting of the photonic chips after wafer manufacturing using specialized dicing and cleaving technology. If required, the chips must be further polished with specialized grinding mats until the facet is smooth. Careful chip handling is also necessary to avoid damage to the coupling facet. A simple yet practical way to reduce unwanted side illuminations is by placing a light-absorbing element, such as black polydimethylsiloxane (PDMS), near the input coupling of the photonic chip, such that the stray light is effectively blocked [20].

Waveguide imperfections. Previous research has shown that certain waveguide materials such as Si_3N_4 exhibit autofluorescence and propagation losses at short wavelengths [78]. While these issues can be potentially addressed both by using longer excitation wavelengths and by optimizing the fabrication steps, it is important to consider them when designing

sensitive SRM experiments. For example, in on-chip *d*STORM, the waveguide autofluorescence can increase the background signal, therefore reducing the localization precision, while the propagation losses can attenuate the intensity of the excitation light, making it difficult to induce long-lived dark states. These challenges can be addressed by opting for different material waveguide chips, such as Ta_2O_5 or Al_2O_3, which exhibit both a high refractive index and a low autofluorescence at shorter wavelengths.

2D imaging. In histological analysis, particularly, a three-dimensional visualization of the specimen is beneficial for analysis. However, in the chip configuration explored in this thesis, the short extent of the evanescent field makes it impossible to achieve a volumetric view of the samples, therefore limiting the visualization to a single 2D plane. Recent developments in the field, however, have proposed the projection of the guided light away from the chip, enabling super-resolution imaging in free space [76, 77].

Waveguide width. The waveguide widths explored in this thesis (100-1000 µm), were in some instances insufficient to illuminate the complete sample area. While sequential illumination of adjacent waveguides provides a holistic view in such cases, the separation gap between them introduces imaging stripes (see Fig. 4b in Paper III) that might be detrimental to the histological analysis. This, in theory, could be fixed by different waveguide configurations. These include a) the design of wider waveguide geometries, for example, of 5 mm width, and b) reducing the separation gap between waveguides from its current 25 µm to, for instance, 1 µm. Alternatively, it is also possible to use a slab waveguide configuration and scan the different parts of the waveguide for uniform illumination.

Sample detachment. Due to the short penetration depth of the evanescent field, the sample must be perfectly attached to the waveguide surface for fluorescence emission to occur. While this condition was normally fulfilled in the case of the Tokuyasu samples, we often experienced sample micro-detachments on the FFPE samples that led to non-uniform sample visualization (see Supplementary Information S12 in Paper III). Admittedly, though we tried to improve the adherence of the FFPE samples through diverse coating strategies (see Supplementary Information S15 in Paper III), no significant differences between the tested methods were observed. Instead, an atomic force microscopy (AFM) analysis of a paraffin-embedded colorectal section (see Supplementary Information S14 in Paper III), suggested that the re-hydration involved in the sample preparation steps of FFPE samples introduced physical transformations in the form of swelling that, presumably, induced sample detachment. This particular aspect of sample preparation deserves further attention in future on-chip FFPE imaging studies.

Light scattering. The opaque photonic chips employed in this demanded an upright microscope configuration for the collection of the fluorescent signal. This means that, since the sample illumination takes place at the waveguide surface, the emitted light must have traveled through the sample volume and part of the mounting media, before passing the coverslip and reaching the microscope objective. Consequently, refractive index heterogeneities within the sample environment might lead to light scattering, introducing optical aberrations in the image [23]. While we did not observe light scattering issues in the tissue samples used in this study, this might be a limiting factor in histological applications of tissue sections exceeding, for example, 10 µm thickness. In such cases, two alternatives could be proposed to alleviate the scattering issues: a) use clearing reagents to homogenize the refractive index of the tissue [119], or b) use transparent chips in combination with an

inverted microscope setup, such that the emitted light experiences a more uniform collection pathway to the camera sensor [23, 73].

Collection limitations. While the photonic chip-based TIRF approach provides sample illumination over arbitrarily large areas along the width and length of the coupled waveguides, the imaging field is still limited by the FOV of the collection objective. Here, the use of alternative collection approaches such as microlens arrays [131] or mesoscopic objectives [59] could dramatically improve the imaging FOV, therefore increasing the system's throughput.

Unspecific binding. Unspecific binding is a common challenge to all fluorescence microscopy techniques, in which the fluorophores attach to the sample substrate, or non-specific structures in the sample, therefore increasing the background signal and hampering the visualization of the features of interest for microscopic analysis. To prevent this issue, a blocking agent is used. Typical blocking agents are composed of bovine serum albumin (BSA), goat serum, or other complementary serums [132]. While blocking agents proved successful for immunofluorescence labeling approaches on the chip [22], we experienced high-affinity fluorophore binding of the lipophilic membrane dyes, irrespective of the blocking method we used (see section *Optimization steps for successful on-chip tissue imaging* in Paper II). We attributed this phenomenon to the amphipathic characteristics of the membrane dyes, which resulted in high-affinity labeling of the waveguide surface for nearly all the surface functionalization tested (e.g., chemical etching, plasma treatment, and surface coating). We found two ways of remediating this issue. In the case of Tokuyasu samples, we increased the laser power to induce dye photobleaching on the chip surface (see Supplementary Information S4 in Paper II). In the case of FFPE samples, we replaced the membrane dye with a less waveguide-affinity marker such as the MitoTracker. We acknowledge that this marker was designed to label mitochondrial activity in live cells, however in practice, as further validated in the CLEM experiments (see Fig. 5 in Paper III), the MitoTracker served the purpose of contextual visualization of membrane structures in the sample.

On-chip *d*STORM. The experimental demonstration of on-chip *d*STORM for Tokuyasu samples (see Fig. 3 in Paper II) also presented some complications. Specifically, despite increasing the laser power to its maximum, the background signal could not be fully mitigated, therefore affecting the localization precision and subsequent image reconstruction. We hypothesized that this issue stemmed from the weak intensity at the tail of the evanescent field, which did not carry enough energy to induce the dark state at sample regions away from the chip surface. Subsequent experiments (not included in this thesis), suggested that this issue could be alleviated by initial high-power illumination of the sample via epifluorescence approach. Additionally, like in any other SMLM approach, the proposed on-chip *d*STORM method requires a strategy for proper management of the microscopy data. For example, a typical on-chip *d*STORM experiment consisting of 50,000 frames covering a FOV of 2048 × 2048 pixels entails hundreds of gigabytes of data to obtain a single super-resolved image. This not only puts pressure on the storing capacity of the imaging system but also on the processing software, which can take several hours to localize the emission events and output the reconstructed image.

Manual handling. Similar to our experience in Paper I, the sample preparation steps on the chip also required manual handling throughout the whole process, therefore limiting the

overall throughput of the method. Although the current dimensions of the chip are approximately 2.5 mm × 2.5 mm, these could be either fabricated in larger size or incorporated into mechanical adapters to match the physical dimensions of conventional microscopy glass slides, therefore benefitting from the use of automated histological processors and stainers.

Chapter 4   Conclusion and Future Perspectives

4.1 Conclusions

The objective of this thesis was to explore new approaches to facilitate the adoption of tissue super-resolution microscopy (SRM) in routine histological practice, both in research and clinical settings. In this work, two SRM platforms with high imaging throughput prospects were explored: **a)** a state-of-the-art DeltaVision OMX V4 Blaze microscope, supporting multi-color 3D structured illumination microscopy (3D-SIM); and **b)** a custom-built photonic chip-based microscope, delivering a series of chip-based imaging modalities including total internal reflection microscopy (chip-TIRF), single-molecule localization microscopy (on-chip SMLM), fluorescence fluctuations-based SRM (on-chip FF-SRM), and correlative light-electron microscopy (on-chip CLEM). To evaluate these two microscopy systems, two distinct histological preservation methods were employed, namely, the Tokuyasu cryopreservation and the formalin-fixation paraffin-embedding (FFPE). Within these preservation approaches, diverse tissue sections of human and animal origin were evaluated. The research results were presented in three original scientific papers, all of which were summarized and further discussed in this dissertation.

In terms of imaging capabilities, the two microscope systems performed differently. On one hand, the 3D-SIM method presented in Paper I, despite offering sharp visualizations of placental tissue beyond diffraction, was found too slow for imaging large sample areas. Here, the field of view (FOV) supported by the OMX microscope of roughly 40 μm × 40 μm was insufficient to obtain a contextual visualization of the tissue sections, therefore requiring a lengthy tile-mosaic imaging approach to screen the samples. On the other hand, using waveguides, the chip-based histology method presented in Paper II enabled sample illumination over arbitrarily large sample areas. This feature was advantageous for the screening of cryopreserved tissue sections. By decoupling the illumination and the collection pathways, the chip-TIRF method not only allowed for high-contrast 2D TIRF images of the sample throughout diverse levels of magnification and FOVs, but also assisted in the realization of on-chip tissue SRM via SMLM, FF-SRM, and CLEM methods. To the best of our knowledge, Paper II was the first SRM imaging demonstration of histological samples in the field of photonic chip-based microscopy.

The work presented in Paper III, particularly, highlighted the twofold advantages of the photonic chip-based methodology for the integration of SRM in routine histological settings. Firstly, the photonic chip demonstrated full compatibility with the harsh processing steps associated with the preparation of FFPE sections. Secondly, the implementation of the on-chip FF-SRM approach via the multiple signal classification algorithm (MUSICAL) enabled unprecedented high-contrast SRM images of clinically relevant FFPE samples over FOVs spanning up to the millimeter scale, in a staggering acquisition-processing time of around 10 min. The chip-based FFPE histology method was, to our knowledge, the first report of paraffin-embedded samples using a waveguide-based approach, and the first successful implementation of MUSICAL in FFPE sections.

From an application viewpoint, the chosen preservation methods showed distinct advantages and pitfalls, requiring the optimization of sample preparation and/or acquisition steps for successful tissue SRM imaging:

> **Tokuyasu**. This cryopreservation method was found to be a short, simple, and effective approach for imaging samples both in the OMX microscope and in the photonic chip,

allowing for high-detail observations of ultrastructural features not attainable via diffraction-limited approaches. A relevant example of this was the visualization of the individual microvilli along the brush border of human placental sections, identified here for the first time using optical methods via 3D-SIM (Paper I), and further visualized via on-chip FF-SRM (Paper II). However, the Tokuyasu samples exhibited major challenges such as frequent folds, tearing, and knife marks arising from the cryosectioning steps, in addition to a maximum section area of roughly 500 μm × 500 μm, which posed an intrinsic limitation for the screening, for example, of large histopathological sections. Lastly, the need for specialized cryo ultramicrotome equipment and a highly skilled histo-technician to assist in various steps of the preservation and sectioning process, rendered the Tokuyasu as a costly method, potentially restricting its applicability for histological research rather than for routine histological analysis.

FFPE. In this work, the main advantage of using FFPE samples was their compatibility with common histological workflows. Contrary to the Tokuyasu method, the FFPE samples were widely available, allowing for simple and repeatable sectioning procedures through accessible microtome equipment in standard histological laboratories. Moreover, the FFPE method allowed for large and flat section areas without noticeable slicing artifacts, which was beneficial for SRM imaging both on the OMX (Paper I) and on the photonic chip-based (Paper III) microscopes. However, the FFPE preservation posed diverse challenges to the tested SRM methods, hence complicating the image analysis. In the experimental making of Paper I, for example, the 3D-SIM visualization of paraffin-embedded sections of human placenta was hampered by the imaging artifacts stemming from the sample autofluorescence and the refractive index mismatch between the sample and the imaging media. In the case of the chip-based FFPE histology method, the most relevant issue was the sample micro-detachments experienced by the paraffin-embedded sections, which led to discontinuities in the image field. This issue remained upon submission of this thesis unsolved, thus deserving further attention.

By exploring distinct factors contributing to the imaging workflow, such as sample preparation and microscopy instrumentation, this Ph.D. thesis offered a multidisciplinary perspective to the practical implementation of super-resolution histology in research and clinical settings. Overall, the Tokuyasu cryopreservation method, while providing excellent compatibility with the tested SRM techniques, proved impractical for routine analysis, yet it can be regarded as a useful approach for histological research. The FFPE preservation, while posing challenges to the tested SRM techniques, showed promising results, suggesting a pathway for future efforts in the field of super-resolution histology. While the 3D-SIM method proved useful for detailed visualization of sub-diffraction features, it showed too slow for screening histological samples. The photonic chip-based method, despite being restricted to 2D visualizations, offered large FOV multimodal imaging capabilities that, in addition to its compatibility with standard FFPE protocols, hold good promise for the advancement of tissue SRM imaging in routine histopathological settings. Further steps toward the adoption of SRM methods in histology will require a holistic approach where sample preparation, imaging acquisition, storage, and processing steps are seamlessly integrated into the existing laboratory routines, enabling a simple, repeatable, and low-cost operational workflow.

4.2 Future perspectives

From a generalistic standpoint, diverse strategies can be proposed for further advancements in the field of super-resolution histology. To name a few:

SIM imaging. While the 3D-SIM configuration studied here proved slow, the implementation of alternative SIM schemes might significantly improve the imaging throughput on histological sections. To this end, approaches such as 2D fiber SIM [87], transmission SIM [88] (provided it can demonstrate sub-200 nm resolution), and on-chip SIM [26] (upon increasing the window imaging area), are potential candidates for increasing the imaging throughput of histological analysis. Particularly, photonic chip-based SIM schemes such as far-field UV SIM [76] could not only assist in increasing the imaging speed but potentially allow for volumetric tissue imaging, a feature not available in the chip-based configuration used in this thesis.

AI-assisted imaging. A current bottleneck for high throughput super-resolution imaging is the limited availability of computational resources for data handling and storage. Especially in the case of SMLM schemes, large datasets surpassing hundreds of gigabytes are generated. Moreover, sub-diffraction visualizations of the whole samples might be redundant, rendering them not necessary. To alleviate this, an artificial intelligence model might become handy to identify the areas of interest before conducting SRM imaging. Following hierarchical imaging, just like histopathologists do, the algorithm would first identify the regions of interest for analysis by screening the sample at low resolution. By merely restricting the SRM imaging to the previously identified regions of interest, smaller datasets can be generated, and therefore a higher throughput could be accomplished. This AI-assisted imaging approach could be integrated into nearly all SRM methods, including SIM and chip-based SRM. The conceptual idea and preliminary findings of this AI-assisted imaging method were recently presented at Focus On Microscopy (Porto, 2023) under the title "Transformers Can Decide Where to Image at What Resolution" (poster ref. P2-B / 7).

Particularly, within the field of chip-based microscopy, the following research lines might significantly contribute to the progress of super-resolution histology:

Resin embedding. While the FFPE histological method is by far the most widely used strategy for preserving biological samples, this technique was optimized for microscopic analysis rather than for nanoscopic observations. Particularly, within the field of electron microscopy, alternative embedding approaches have been developed to enable ultrastructural observation of tissues. One such approach is resin embedding, which covers diverse types of polymeric compounds such as Epon, LR White, and polyethylene glycol (PEG) [133, 134]. Notably, some resin-embedding approaches are compatible with fluorescence labeling, allowing complementary visualizations via fluorescence microscopy and, ultimately, assisting in CLEM studies [135]. Preliminary chip-based imaging of PEG-embedded tissue samples has shown promising results, exhibiting superior flatness and more uniform attachment to the waveguide surface, promising an attractive solution to the micro-detachment challenge observed on the FFPE samples. Figure 4.2-1 shows a PEG-embedded hamster brain tissue section imaged on a photonic chip.
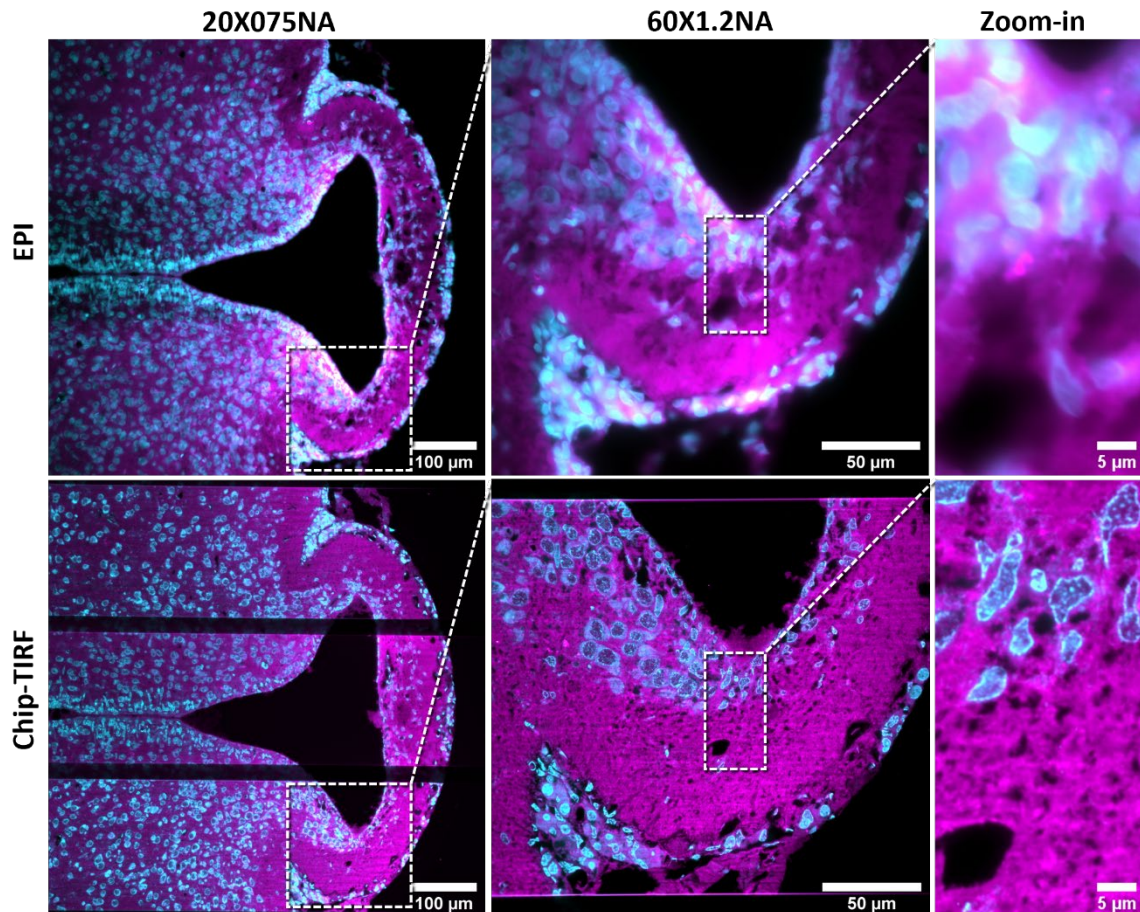
Figure 4.2-1.   Example of resin embedding histology. A 10 µm thick PEG-embedded hamster brain section imaged in EPI (top row) and in chip-TIRF (bottom row) modalities. Membranes are shown in magenta and nuclei in cyan. In this example, the chip-TIRF method offers superior contrast and resolution of the histological sample compared to the EPI method. Note the uniform sample attachment provided by the PEG embedding.

Clinical applications. Future progress of the tissue on-chip methodology presented in this thesis could potentially assist in the diagnosis of diseases that, to date, require electron microscopy. For example, the photonic chip could aid in the identification of morphological changes in kidney diseases (e.g. minimal change disease), where both a contextual (large FOV) visualization of the sample and a detailed observation of structural features such as podocyte foot processes and glomerular basement membrane are critical for clinical diagnosis [136]. Preliminary findings of on-chip FFPE human kidney samples suggest that the optical sectioning provided by the photonic chip-based microscopy method might allow the identification of such features, as illustrated in Figure 4.2-2.
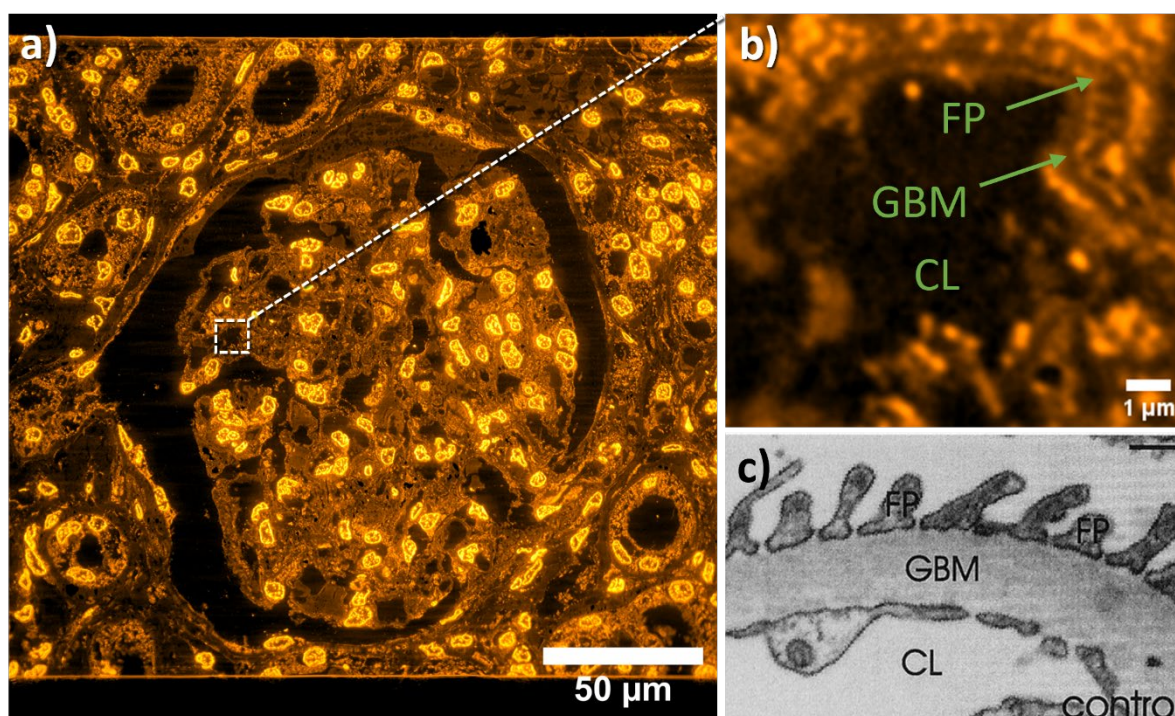
Figure 4.2-2. On-chip histology for clinical diagnosis. **a)** In the central portion of the image, an FFPE human kidney glomerulus tissue imaged on a photonic chip. **b)** A magnified view of the white-dotted box in a) allows for the visualization of kidney structures like podocyte foot processes (FP), glomerular basement membrane (GBM), and the capillary lumen (CL). **c)** A representative transmission electron microscope image showing similar structures as in b) at higher resolution. Scale bar 100 nm. Adapted from ref. [136]

DNA-PAINT. The realization of on-chip *d*STORM of Tokuyasu samples proved somehow challenging due to the presence of background signal, and due to the need for high laser power combined with a special imaging buffer. In contrast, the alternative waveguide-PAINT method, successfully demonstrated in cells [20], holds good promise for accomplishing SMLM on tissue sections, requiring low laser power and no special imaging buffers. This method not only could improve the resolution capabilities of the on-chip SMLM method but also allow for quantitative super-resolution histological analyses.

Label-free. Fluorescence labeling, while assisting in increasing sample contrast, entails a lengthy, and sometimes costly, sample preparation. On the other hand, certain histological preservation methods such as FFPE exhibit high levels of autofluorescence. Hence, by cleverly exploiting the sample autofluorescence properties, SRM imaging could be in principle achievable [76, 137].

Transparent photonic chip. Although no relevant optical aberrations were observed in this work, the opaque chip configuration used for the screening of tissue samples could, in principle, lead to light scattering issues in thick specimens for the current upright microscope setup. A practical solution in such cases would be to use a transparent chip configuration [23, 70], such that the emitted light could be collected in an inverted microscope setup, with minimal distortion. This scheme, in addition, could be assisted by a microfluidics approach, to enable DNA-PAINT [56].

Extended collection. Despite illuminating the sample over large areas, the imaging area of the photonic chip-based histology method presented in this thesis is currently limited by the pupil dimensions of the objective lens used for signal collection. Thus, complementary collection methods such as microlens arrays [131] or mesoscopic objectives [59] could dramatically improve the imaging FOV, therefore increasing the photonic chip-based system throughput.

System complexity and cost. The photonic chip-based microscopy method presented in this work, while relatively simple to learn and operate, exhibited a few operational complexities stemming from manual light coupling, such as side illumination, and low coupling efficiency. Future developments in automatic coupling could potentially facilitate an easier user experience, making this method an attractive option for the microscopy market. Similarly, the photonic chip-based microscopy setup presented in this work carried an elevated cost of peripheral equipment like lasers, scientific cameras, and motorized stages, which made this microscopy method expensive. Future integration of industrial-grade components might contribute to reducing the photonic chip-based system's cost.

Slab waveguide configuration. A particular disadvantage of the strip waveguide configuration explored in this thesis was the spacing gap between adjacent waveguides. A potential solution for this issue is by using a slab waveguide geometry, such that the sample can be uniformly illuminated via the chip-TIRF method. At the time of writing this thesis, this approach is being explored.

Optical waveguides. In this thesis, optimization of the waveguide chips was not carried out. However, future improvements in optical waveguides are desirable for histology applications. In particular, the use of waveguide materials such as Al_2O_3 supporting shorter wavelengths [76], e.g. 405 nm and also for 377 nm, could not only allow for expanding the photonic chip's compatibility with commonly used markers such as DAPI and Hoechst but also assist in the exploitation of the autofluorescent signal in label-free methods [79]. In addition, the use of lower refractive index waveguide core materials could be useful for extending the evanescent field stretch, as reported in previous studies [62].

Chapter 5   Additional contributions

5.1 International conference participation

- *Optical Nanoscopy In Histopathology*. Oral presentation at Focus on Microscopy 2019, London, UK.

- *Photonic-chip: a multimodal imaging tool for histopathology*. Oral presentation at Biophotonics Congress: Optics in the Life Sciences 2021, Online.

- *Photonic chip: a versatile nanoscopy platform for histopathology*. Poster presentation at the European Light Microscopy Initiative 2022, Turku, Finland.

- *Photonic chip: a versatile nanoscopy platform for histopathology*. Oral presentation at Focus on Microscopy 2023, Porto, Portugal.

5.2 Master thesis supervision

- Optimization of biomarkers for morphological analysis of healthy and preeclamptic term human placental tissue sections using advanced fluorescence microscopy methods. By Maddhusja Nalliah. 2021, UiT – The Arctic University of Norway. https://hdl.handle.net/10037/22666

References Chapters 1-5

1. Gest, H., *The discovery of microorganisms by Robert Hooke and Antoni Van Leeuwenhoek, fellows of the Royal Society.* Notes and records of the Royal Society of London, 2004. **58**(2): p. 187-201.

2. Donczo, B. and A. Guttman, *Biomedical analysis of formalin-fixed, paraffin-embedded tissue samples: The Holy Grail for molecular diagnostics.* Journal of pharmaceutical and biomedical analysis, 2018. **155**: p. 125-134.

3. Griffiths, G., J.-W. Slot, and P. Webster, *Kiyoteru Tokuyasu: a pioneer of cryo-ultramicrotomy.* 2015, The Japanese Society of Microscopy.

4. Abbe, E., *Beiträge zur Theorie des Mikroskops und der mikroskopischen Wahrnehmung.* Archiv für mikroskopische Anatomie, 1873. **9**(1): p. 413-468.

5. Kopp, J.B., et al., *Podocytopathies.* Nature Reviews Disease Primers, 2020. **6**(1): p. 68.

6. Werner, C., J.G. Onnebrink, and H. Omran, *Diagnosis and management of primary ciliary dyskinesia.* Cilia, 2015. **4**: p. 1-9.

7. Fernández de Larrea, C., et al., *A practical approach to the diagnosis of systemic amyloidoses.* Blood, The Journal of the American Society of Hematology, 2015. **125**(14): p. 2239-2244.

8. Möckl, L., D.C. Lamb, and C. Bräuchle, *Super-resolved fluorescence microscopy: nobel prize in chemistry 2014 for eric betzig, stefan hell, and william e. moerner.* Angewandte Chemie International Edition, 2014. **53**(51): p. 13972-13977.

9. Prakash, K., et al., *Super-resolution microscopy: a brief history and new avenues.* Philosophical Transactions of the Royal Society A, 2022. **380**(2220): p. 20210110.

10. Lelek, M., et al., *Single-molecule localization microscopy.* Nature Reviews Methods Primers, 2021. **1**(1): p. 39.

11. Willig, K.I., et al., *STED microscopy reveals that synaptotagmin remains clustered after synaptic vesicle exocytosis.* Nature, 2006. **440**(7086): p. 935-939.

12. Heintzmann, R. and T. Huser, *Super-resolution structured illumination microscopy.* Chemical reviews, 2017. **117**(23): p. 13890-13908.

13. Pawlowska, M., et al., *Embracing the uncertainty: the evolution of SOFI into a diverse family of fluctuation-based super-resolution microscopy methods.* Journal of Physics: Photonics, 2021. **4**(1): p. 012002.

14. Wassie, A.T., Y. Zhao, and E.S. Boyden, *Expansion microscopy: principles and uses in biological research.* Nature methods, 2019. **16**(1): p. 33-41.

15. Ilgen, P., et al., *STED super-resolution microscopy of clinical paraffin-embedded human rectal cancer tissue.* PloS one, 2014. **9**(7): p. e101563.

16. Xu, J., et al., *Super-resolution imaging reveals the evolution of higher-order chromatin folding in early carcinogenesis.* Nature communications, 2020. **11**(1): p. 1899.

17. Creech, M.K., et al., *Superresolution imaging of clinical formalin fixed paraffin embedded breast cancer with single molecule localization microscopy.* Scientific reports, 2017. **7**(1): p. 1-10.

18. Artelt, N., et al., *Comparative analysis of podocyte foot process morphology in three species by 3D super-resolution microscopy.* Frontiers in Medicine, 2018. **5**: p. 292.

19. Siegerist, F., et al., *Structured illumination microscopy and automatized image processing as a rapid diagnostic tool for podocyte effacement.* Scientific reports, 2017. **7**(1): p. 11473.

20. Archetti, A., et al., *Waveguide-PAINT offers an open platform for large field-of-view super-resolution imaging.* Nature communications, 2019. **10**(1): p. 1267.

21. Helle, Ø.I., et al., *Nanoscopy on-a-chip: super-resolution imaging on the millimeter scale.* Optics express, 2019. **27**(5): p. 6700-6710.

22. Diekmann, R., et al., *Chip-based wide field-of-view nanoscopy.* Nature Photonics, 2017. **11**(5): p. 322-328.

23. Priyadarshi, A., et al., *A transparent waveguide chip for versatile total internal reflection fluorescence-based microscopy and nanoscopy.* Communications Materials, 2021. **2**(1): p. 85.

24. Jayakumar, N., et al., *On-chip TIRF nanoscopy by applying Haar wavelet kernel analysis on intensity fluctuations induced by chip illumination.* Optics Express, 2020. **28**(24): p. 35454-35468.

25. Opstad, I.S., et al., *Fluorescence fluctuation-based super-resolution microscopy using multimodal waveguided illumination.* Optics Express, 2021. **29**(15): p. 23368-23380.

26. Helle, Ø.I., et al., *Structured illumination microscopy using a photonic chip.* Nature photonics, 2020. **14**(7): p. 431-438.

27. Dubey, V., et al., *Multi-modal chip-based fluorescence and quantitative phase microscopy for studying inflammation in macrophages.* Optics express, 2018. **26**(16): p. 19864-19876.

28. Tinguely, J.-C., et al., *Photonic-chip assisted correlative light and electron microscopy.* Communications biology, 2020. **3**(1): p. 739.

29. Bonaque-González, S., et al., *The optics of the human eye at 8.6 μm resolution.* Scientific Reports, 2021. **11**(1): p. 23334.

30. Saleh, B.E.A. and M.C. Teich, *Fundamentals of Photonics, 2 Volume Set.* 2019: Wiley.

31. Villegas-Hernández, L.E., et al., *Visualizing ultrastructural details of placental tissue with super-resolution structured illumination microscopy.* Placenta, 2020. **97**: p. 42-45.

32. Douglass, K.M., et al., *Super-resolution imaging of multiple cells by optimized flat-field epi-illumination.* Nature photonics, 2016. **10**(11): p. 705-708.

33. Ghatak, A., *Optics.* 2010: McGraw Hill.

34. Kirshner, H., et al., *3-D PSF fitting for fluorescence microscopy: implementation and localization application.* Journal of microscopy, 2013. **249**(1): p. 13-25.

35. Kaderuppan, S.S., et al., *Smart nanoscopy: A review of computational approaches to achieve super-resolved optical microscopy.* IEEE Access, 2020. **8**: p. 214801-214831.

36. Lipson, A., S.G. Lipson, and H. Lipson, *Optical physics.* 2010: Cambridge University Press.

37. Ghosh, B. and K. Agarwal, *Viewing life without labels under optical microscopes.* Communications Biology, 2023. **6**(1): p. 559.

38. Pepperkok, R. and J. Ellenberg, *High-throughput fluorescence microscopy for systems biology.* Nature reviews Molecular cell biology, 2006. **7**(9): p. 690-696.

39. Beghin, A., et al., *Localization-based super-resolution imaging meets high-content screening.* Nature methods, 2017. **14**(12): p. 1184-1190.

40. Rowlands, C.J., et al., *Flat-field super-resolution localization microscopy with a low-cost refractive beam-shaping element.* Scientific Reports, 2018. **8**(1): p. 1-8.

41. Lleres, D., S. Swift , and A.I. Lamond, *Detecting Protein-Protein Interactions In Vivo with FRET using Multiphoton Fluorescence Lifetime Imaging Microscopy (FLIM).* Current Protocols in Cytometry, 2007.

42. Henriques, R., et al., *PALM and STORM: unlocking live-cell super-resolution.* Biopolymers, 2011. **95**(5): p. 322-331.

43. Oorschot, V., et al., *TEM, SEM, and STEM-based immuno-CLEM workflows offer complementary advantages.* Scientific Reports, 2021. **11**(1): p. 899.

44. Pawley, J., *Handbook of biological confocal microscopy.* Vol. 236. 2006: Springer Science & Business Media.

45. Olson, E., M.J. Levene, and R. Torres, *Multiphoton microscopy with clearing for three dimensional histology of kidney biopsies.* Biomedical optics express, 2016. **7**(8): p. 3089-3096.

46. Ströhl, F., et al., *Multifocus microscopy with optical sectioning and high axial resolution.* Optica, 2022. **9**(11): p. 1210-1218.

47. Fish, K.N., *Total internal reflection fluorescence (TIRF) microscopy.* Current protocols in cytometry, 2009. **50**(1): p. 12.18. 1-12.18. 13.

48. Sibarita, J.B., *Deconvolution microscopy.* Adv Biochem Eng Biotechnol, 2005. **95**: p. 201-43.

49. Zheng, C., et al., *De-scattering with excitation patterning enables rapid wide-field imaging through scattering media.* Science advances, 2021. **7**(28): p. eaay5496.

50. Komura, D. and S. Ishikawa, *Machine learning methods for histopathological image analysis.* Computational and structural biotechnology journal, 2018. **16**: p. 34-42.

51. Yanny, K., et al., *Deep learning for fast spatially varying deconvolution.* Optica, 2022. **9**(1): p. 96-99.

52. Martin-Fernandez, M., C. Tynan, and S. Webb, *A 'pocket guide'to total internal reflection fluorescence.* Journal of microscopy, 2013. **252**(1): p. 16-22.

53. Pang, C.-l., et al., *Chip-based waveguides for high-sensitivity biosensing and super-resolution imaging.* Frontiers of Information Technology & Electronic Engineering, 2020. **21**(8): p. 1134-1149.

54. Liu, P.Y., et al., *Cell refractive index for cell biology and disease diagnosis: past, present and future.* Lab on a Chip, 2016. **16**(4): p. 634-644.

55. Mattheyses, A.L., S.M. Simon, and J.Z. Rappoport, *Imaging with total internal reflection fluorescence microscopy for the cell biologist.* Journal of cell science, 2010. **123**(21): p. 3621-3628.

56.   Rames, M.J., et al., *Multiplexed and millimeter-scale superresolution imaging of cells and tissue sections via prism-illumination and microfluidics-enhanced DNA-PAINT.* bioRxiv, 2022: p. 2022.08. 07.503091.

57.   Renaud, L., A. Bodin, and J.P. Julien, *STochastic Optical Reconstruction Microscopy (STORM) reveals the nanoscale organization of pathological aggregates in human brain.* Neuropathology and Applied Neurobiology, 2021. **47**(1): p. 127-142.

58.   Gibbs, D.R., et al., *Build your own microscope: step-by-step guide for building a prism-based TIRF microscope.* Methods and Protocols, 2018. **1**(4): p. 40.

59.   Foylan, S., et al., *MesoTIRF: A prism-based Total Internal Reflection Fluorescence illuminator for high resolution, high contrast imaging of large cell populations.* Applied Physics Letters, 2023. **122**(11).

60.   Grandin, H., et al., *Waveguide excitation fluorescence microscopy: A new tool for sensing and imaging the biointerface.* Biosensors and Bioelectronics, 2006. **21**(8): p. 1476-1482.

61.   Hassanzadeh, A., et al., *Waveguide evanescent field fluorescence microscopy: Thin film fluorescence intensities and its application in cell biology.* Applied Physics Letters, 2008. **92**(23).

62.   Agnarsson, B., et al., *Evanescent-wave fluorescence microscopy using symmetric planar waveguides.* Optics express, 2009. **17**(7): p. 5075-5082.

63.   Agnarsson, B., et al., *On-chip modulation of evanescent illumination and live-cell imaging with polymer waveguides.* Optics express, 2011. **19**(23): p. 22929-22935.

64.   Ramachandran, S., et al., *High performance, LED powered, waveguide based total internal reflection microscopy.* Scientific reports, 2013. **3**(1): p. 2133.

65.   Ahluwalia, B.S., et al. *Integrated platform based on high refractive index contrast waveguide for optical guiding and sorting.* in *Complex Light and Optical Forces Iv.* 2010. SPIE.

66.   Ahluwalia, B.S., et al., *Fabrication of submicrometer high refractive index Tantalum Pentoxide waveguides for optical propulsion of microparticles.* IEEE Photonics Technology Letters, 2009. **21**(19): p. 1408-1410.

67.   Helle, Ø.I., et al. *Chip-based optical microscopy for imaging membrane sieve plates of liver scavenger cells.* in *Nanoimaging and Nanospectroscopy III.* 2015. SPIE.

68.   Tinguely, J.-C., Ø.I. Helle, and B.S. Ahluwalia, *Silicon nitride waveguide platform for fluorescence microscopy of living cells.* Optics express, 2017. **25**(22): p. 27678-27690.

69.   Opstad, I.S., et al., *A waveguide imaging platform for live-cell TIRF imaging of neurons over large fields of view.* Journal of Biophotonics, 2020. **13**(6): p. e201960222.

70.   Engdahl, A.K., et al., *Large field-of-view super-resolution optical microscopy based on planar polymer waveguides.* ACS Photonics, 2021. **8**(7): p. 1944-1950.

71.   Chen, F., et al., *Fundamentals of Ion Beam Technology, Waveguides, and Nanoparticle Systems.* Ion Irradiation of Dielectrics for Photonic Applications, 2020: p. 1-19.

72.   Fan, Z., et al., *Chip-based wide field-of-view total internal reflection fluorescence microscopy.* Optics Letters, 2022. **47**(17): p. 4303-4306.

73.   Engdahl, A.K., et al., *Dual-color single molecule localization microscopy on transparent polymer waveguide chips.* bioRxiv, 2022: p. 2022.11. 29.518375.

74. Shen, H., et al., *TIRF microscopy with ultra-short penetration depth.* Optics express, 2014. **22**(9): p. 10728-10734.

75. Agnarsson, B., et al., *Evanescent light-scattering microscopy for label-free interfacial imaging: from single sub-100 nm vesicles to live cells.* ACS nano, 2015. **9**(12): p. 11849-11862.

76. Lin, C., et al., *UV photonic integrated circuits for far-field structured illumination autofluorescence microscopy.* Nature communications, 2022. **13**(1): p. 4360.

77. Lahrberg, M., F.T. Dullo, and B.S. Ahluwalia, *Photonic-chip based free space beam shaping and steering for advanced optical microscopy application.* OSA Continuum, 2020. **3**(2): p. 359-378.

78. Coucheron, D.A., et al., *Study of waveguide background at visible wavelengths for on-chip nanoscopy.* Optics Express, 2021. **29**(13): p. 20735-20746.

79. Jayakumar, N., et al., *Label-free incoherent super-resolution optical microscopy.* arXiv preprint arXiv:2301.03451, 2023.

80. Liao, J., et al. *Comparison of two-and three-beam interference pattern generation in structured illumination microscopy.* in *Photonics.* 2021. MDPI.

81. Wei, F., et al., *Wide field super-resolution surface imaging through plasmonic structured illumination microscopy.* Nano letters, 2014. **14**(8): p. 4634-4639.

82. Stemmer, A., M. Beck, and R. Fiolka, *Widefield fluorescence microscopy with extended resolution.* Histochemistry and cell biology, 2008. **130**: p. 807-817.

83. Markwirth, A., et al., *Video-rate multi-color structured illumination microscopy with simultaneous real-time reconstruction.* Nature communications, 2019. **10**(1): p. 4315.

84. Wu, Y. and H. Shroff, *Faster, sharper, and deeper: structured illumination microscopy for biological imaging.* Nature methods, 2018. **15**(12): p. 1011-1019.

85. Schlichenmeyer, T.C., et al., *Video-rate structured illumination microscopy for high-throughput imaging of large tissue areas.* Biomedical Optics Express, 2014. **5**(2): p. 366-377.

86. Demmerle, J., et al., *Strategic and practical guidelines for successful structured illumination microscopy.* Nature protocols, 2017. **12**(5): p. 988-1010.

87. Ortkrass, H., et al., *High-speed TIRF and 2D super-resolution structured illumination microscopy with large field of view based on fiber optic components.* bioRxiv, 2023: p. 2023.05. 11.540319.

88. Samanta, K., et al., *Transmission structured illumination microscopy with tunable frequency illumination using tilt mirror assembly.* Scientific Reports, 2023. **13**(1): p. 1453.

89. Rust, M.J., M. Bates, and X. Zhuang, *Sub-diffraction-limit imaging by stochastic optical reconstruction microscopy (STORM).* Nature methods, 2006. **3**(10): p. 793-796.

90. Van de Linde, S., et al., *Direct stochastic optical reconstruction microscopy with standard fluorescent probes.* Nature protocols, 2011. **6**(7): p. 991-1009.

91. Fölling, J., et al., *Fluorescence nanoscopy by ground-state depletion and single-molecule return.* Nature methods, 2008. **5**(11): p. 943-945.

92.   Betzig, E., et al., *Imaging intracellular fluorescent proteins at nanometer resolution.* science, 2006. **313**(5793): p. 1642-1645.

93.   Jungmann, R., et al., *Single-molecule kinetics and super-resolution microscopy by fluorescence imaging of transient binding on DNA origami.* Nano letters, 2010. **10**(11): p. 4756-4761.

94.   Schnitzbauer, J., et al., *Super-resolution microscopy with DNA-PAINT.* Nature protocols, 2017. **12**(6): p. 1198-1228.

95.   Mortensen, K.I., et al., *Optimized localization analysis for single-molecule tracking and super-resolution microscopy.* Nature methods, 2010. **7**(5): p. 377-381.

96.   Sage, D., et al., *Quantitative evaluation of software packages for single-molecule localization microscopy.* Nature methods, 2015. **12**(8): p. 717-724.

97.   Coucheron, D.A., et al. *Chip-based nanoscopy: towards integration and high-throughput imaging.* in *SPIE Nanoscience + Engineering.* 2017. SPIE.

98.   Dertinger, T., et al., *Fast, background-free, 3D super-resolution optical fluctuation imaging (SOFI).* Proceedings of the National Academy of Sciences, 2009. **106**(52): p. 22287-22292.

99.   Alva, A., et al., *Fluorescence fluctuation-based super-resolution microscopy: Basic concepts for an easy start.* Journal of Microscopy, 2022. **288**(3): p. 218-241.

100.   Yahiatene, I., et al., *Entropy-based super-resolution imaging (ESI): From disorder to fine detail.* Acs Photonics, 2015. **2**(8): p. 1049-1056.

101.   Agarwal, K. and R. Macháň, *Multiple signal classification algorithm for super-resolution fluorescence microscopy.* Nature communications, 2016. **7**(1): p. 13752.

102.   Gustafsson, N., et al., *Fast live-cell conventional fluorophore nanoscopy with ImageJ through super-resolution radial fluctuations.* Nature communications, 2016. **7**(1): p. 12471.

103.   Zhao, W., et al., *Enhanced detection of fluorescence fluctuations for high-throughput super-resolution imaging.* Nature Photonics, 2023: p. 1-8.

104.   Marsh, R.J., et al., *Artifact-free high-density localization microscopy analysis.* Nature methods, 2018. **15**(9): p. 689-692.

105.   Kim, M., et al., *Superresolution imaging with optical fluctuation using speckle patterns illumination.* Scientific reports, 2015. **5**(1): p. 16525.

106.   Zhao, G., et al., *Resolution-enhanced SOFI via structured illumination.* Optics letters, 2017. **42**(19): p. 3956-3959.

107.   Descloux, A.C., et al., *Experimental combination of super-resolution optical fluctuation imaging with structured illumination microscopy for large fields-of-view.* Acs Photonics, 2021. **8**(8): p. 2440-2449.

108.   Acuña, S., et al., *Soft thresholding schemes for multiple signal classification algorithm.* Optics Express, 2020. **28**(23): p. 34434-34449.

109.   Laine, R.F., et al., *High-fidelity 3D live-cell nanoscopy through data-driven enhanced super-resolution radial fluctuation.* BioRxiv, 2022: p. 2022.04. 07.487490.

110. Opstad, I.S., et al., *Fluorescence fluctuations-based super-resolution microscopy techniques: an experimental comparative study.* arXiv preprint arXiv:2008.09195, 2020.

111. De Boer, P., J.P. Hoogenboom, and B.N. Giepmans, *Correlated light and electron microscopy: ultrastructure lights up!* Nature methods, 2015. **12**(6): p. 503-513.

112. Milo, R. and R. Phillips, *Cell Biology by the Numbers.* 2015: CRC Press.

113. Aeffner, F., et al., *Digital microscopy, image analysis, and virtual slide repository.* ILAR journal, 2018. **59**(1): p. 66-79.

114. Lu, J.-X., et al., *Molecular structure of β-amyloid fibrils in Alzheimer's disease brain tissue.* Cell, 2013. **154**(6): p. 1257-1268.

115. Damstra, H.G., et al., *Visualizing cellular and tissue ultrastructure using Ten-fold Robust Expansion Microscopy (TREx).* Elife, 2022. **11**: p. e73775.

116. Siegerist, F., et al., *Super-Resolution Microscopy: A Technique to Revolutionize Research and Diagnosis of Glomerulopathies.* Glomerular Diseases, 2023. **3**: p. 19-28.

117. Viegas, M., et al., *An improved and cost-effective methodology for the reduction of autofluorescence in direct immunofluorescence studies on formalin-fixed paraffin-embedded tissues.* European Journal of Histochemistry, 2007. **51**(1): p. 59-66.

118. Lee, K., et al., *Autofluorescence generation and elimination: a lesson from glutaraldehyde.* Chemical Communications, 2013. **49**(29): p. 3028-3030.

119. Costantini, I., et al., *In-vivo and ex-vivo optical clearing methods for biological tissues.* Biomedical optics express, 2019. **10**(10): p. 5251-5267.

120. Donczo, B. and A. Guttman, *Biomedical analysis of formalin-fixed, paraffin-embedded tissue samples: The Holy Grail for molecular diagnostics.* J Pharm Biomed Anal, 2018. **155**: p. 125-134.

121. Slaoui, M. and L. Fiette, *Histopathology procedures: from tissue sampling to histopathological evaluation.* Drug Safety Evaluation: Methods and Protocols, 2011: p. 69-82.

122. Tarling, T.E., J.A. Byrne, and P.H. Watson, *The Availability of Human Biospecimens to Support Biomarker Research.* Biomarker Insights, 2022. **17**: p. 11772719221091750.

123. Skrede, O.-J., et al., *Deep learning for prediction of colorectal cancer outcome: a discovery and validation study.* The Lancet, 2020. **395**(10221): p. 350-360.

124. Kennedy, R.D., et al., *Development and independent validation of a prognostic assay for stage II colon cancer using formalin-fixed paraffin-embedded tissue.* Journal of Clinical Oncology, 2011. **29**(35): p. 4620-4626.

125. Krenacs, L., et al., *Heat-induced antigen retrieval for immunohistochemical reactions in routinely processed paraffin sections.* Immunocytochemical Methods and Protocols, 2010: p. 103-119.

126. Silini, A.R., et al., *Perinatal derivatives: where do we stand? A roadmap of the human placenta and consensus for tissue and cell nomenclature.* Frontiers in bioengineering and biotechnology, 2020. **8**: p. 1438.

127. Zeldovich, V.B., et al., *Invasive extravillous trophoblasts restrict intracellular growth and spread of Listeria monocytogenes.* PLoS pathogens, 2011. **7**(3): p. e1002005.

128. Thornburg, K.L. and N. Marshall, *The placenta is the center of the chronic disease universe.* American Journal of Obstetrics & Gynecology, 2015. **213**(4): p. S14-S20.

129. Dimitriadis, E., et al., *Pre-eclampsia.* Nature Reviews Disease Primers, 2023. **9**(1): p. 8.

130. Redman, C., et al., *Does size matter? Placental debris and the pathophysiology of pre-eclampsia.* Placenta, 2012. **33**: p. S48-S54.

131. Thomson, E., et al., *Gigapixel imaging with a novel multi-camera array microscope.* Elife, 2022. **11**: p. e74988.

132. Im, K., et al., *An introduction to performing immunofluorescence staining.* Biobanking: methods and protocols, 2019: p. 299-311.

133. McDonald, K.L., *Rapid embedding methods into epoxy and LR White resins for morphological and immunological analysis of cryofixed biological specimens.* Microscopy and microanalysis, 2014. **20**(1): p. 152-163.

134. Smithson, K.G., B.A. MacVicar, and G.I. Hatton, *Polyethylene glycol embedding: a technique compatible with immunocytochemistry, enzyme histochemistry, histofluorescence and intracellular staining.* Journal of neuroscience methods, 1983. **7**(1): p. 27-41.

135. Koga, D., et al., *High-resolution imaging by scanning electron microscopy of semithin sections in correlation with light microscopy.* Journal of Electron Microscopy, 2015. **64**(6): p. 387-394.

136. Patrakka, J., et al., *The number of podocyte slit diaphragms is decreased in minimal change nephrotic syndrome.* Pediatric research, 2002. **52**(3): p. 349-355.

137. Rossberger, S., et al., *High-resolution imaging of autofluorescent particles within drusen using structured illumination microscopy.* British Journal of Ophthalmology, 2013. **97**(4): p. 518-523.

Appendix A. Paper I

Technical note

Visualizing ultrastructural details of placental tissue with super-resolution structured illumination microscopy

Luis E. Villegas-Hernández [a], Mona Nystad [b,c], Florian Ströhl [a], Purusotam Basnet [b,d], Ganesh Acharya [b,e,**], Balpreet S. Ahluwalia [a,e,*]

[a] *Department of Physics and Technology, UiT - The Arctic University of Norway, Tromsø, Norway*
[b] *Department of Clinical Medicine, Women's Health and Perinatology Research Group, Faculty of Health Sciences, UiT - The Arctic University of Norway, Tromsø, Norway*
[c] *Department of Medical Genetics, University Hospital of North Norway, Tromsø, Norway*
[d] *Department of Obstetrics and Gynecology, University Hospital of North Norway, Tromsø, Norway*
[e] *Division of Obstetrics and Gynecology, Department of Clinical Science, Intervention and Technology, Karolinska Institute, Stockholm, Sweden*

ARTICLE INFO

ABSTRACT

Super-resolution fluorescence microscopy is a widely employed technique in cell biology research, yet remains relatively unexplored in the field of histopathology. Here, we describe the sample preparation steps and acquisition parameters necessary to obtain fluorescent multicolor super-resolution structured illumination microscopy (SIM) images of both formalin-fixed paraffin-embedded and cryo-preserved placental tissue sections. We compare super-resolved images of chorionic villi against diffraction-limited deconvolution microscopy and show the significant contrast and resolution enhancement attainable with SIM, demonstrating the applicability of this imaging technique for both clinical diagnosis and biological research.

1. Introduction

Traditionally, fluorescent optical microscopy (OM) served as a tool to observe cellular dynamics with high specificity at low resolution, whereas electron microscopy (EM) helped to visualize ultrastructural details but at the cost of specificity. About two decades ago, the development of fluorescence-based super-resolution fluorescence microscopy (SRM), also known as optical nanoscopy, bridged the gap between OM and EM, enabling high specificity studies at the sub-cellular level [1]. Among the existing super-resolution methods, structured illumination microscopy (SIM) stands out as the fastest and most suitable technique for histological examination, enabling high-resolution and high-throughput imaging for decision support in clinical settings [2,3].

In placental biology, SRM studies have focused primarily on trophoblast cell cultures [4,5], leaving placental tissues comparatively unexplored. Here we describe the sample preparation steps and imaging parameters necessary to obtain super-resolved multicolor micrographs of both formalin-fixed paraffin-embedded (FFPE) and cryo-preserved placental sections with SIM. We report our observations of imaging

chorionic villi using optical nanoscopy and compare them with deconvolution microscopy (DV), a state-of-the-art diffraction-limited fluorescent microscopy technique [10] widely used in life sciences. To the best of our knowledge, this is the first report of SIM on placental tissue.

2. Materials and methods

Full-term placentae from 10 different Caucasian healthy patients were collected anonymously immediately after delivery at the University Hospital of North Norway. Written consent was obtained from the participants according to the protocol approved by the Regional Committee for Medical and Health Research Ethics of North Norway (REK Nord reference no. 2010/2058–4).

The samples were prepared in two ways according to the preservation technique, as outlined below and in Fig. 1 A,B.

2.1. Preparation of FFPE-sections

Placental tissue samples were fixed in formalin and embedded in

---

paraffin, according to standard histological procedures [6]. Sections of 4 μm thickness were cut from the paraffin blocks (HM 355S Automatic Microtome, Thermo Fisher Scientific, Waltham, Massachusetts, USA), placed on poly-L-lysine coated #1.5 coverslips, and deparaffinized in xylene (3 × 5 min), followed by rehydration in descendent series of ethanol: 100% (2 × 10 min), 96% (2 × 10 min) and 70% (10 min). To reduce the autofluorescence, the rehydrated samples were immersed in bleaching solution (30 min) and then washed with MilliQ water (5 min), before incubation with CellMask Orange (CMO) membrane staining (10 min). Thereafter, the samples were washed with PBS (2 × 5 min) and incubated with DAPI nuclear staining (5 min), followed by a wash with MilliQ water (2 × 5 min). The stained samples were mounted in the center of standard microscope glass slides with Prolong Gold and sealed with nail varnish after the mounting medium hardened. All incubations were performed at room temperature. For autofluorescence characterization, the samples were prepared according to the above-described steps, excluding fluorescent dyes. Supplementary information S1 provides a detailed list of the materials used in the study.

2.2. Preparation of cryosections

Chorionic tissue was collected, dissected and rinsed in 9 mg/mL sodium chloride as described elsewhere [7]. Collected tissue samples were transferred to 5 mL of 1 × PHEM-buffer. Placental samples of 1 mm³ were immersed in 5 mL 8% formaldehyde in PHEM buffer and incubated at 4 °C overnight. Tissue samples were immersed in 0.12% glycine at 37 °C (1 h), infiltrated with 2.3 M sucrose at 4 °C overnight and transferred to specimen pins before storage in liquid Nitrogen. The samples were cut into 1 μm thick cryosections (EMUC6 ultramicrotome, Leica Microsystems, Vienna, Austria), collected with a wire loop filled with a 1:1 mixture of 2% methylcellulose and 2.3 M sucrose per Tokuyasu method [8], and placed on poly-L-lysine coated #1.5 coverslips. The samples were washed with PBS (3 × 7 min) at 4 °C to dissolve the methylcellulose. Thereafter, the tissues were incubated in phalloidin-Atto 647 N for F-actin staining (15 min) and washed with PBS (2 × 5 min). The CMO membrane staining and successive steps were

performed identically as described for the FFPE sections, at room temperature.

After preparation, both FFPE and cryosections were protected from light and stored at 4 °C before imaging.

2.3. Optical nanoscopy

The samples were imaged in SIM mode using a commercial microscope DeltaVision OMX V4 Blaze imaging system (GE Healthcare, Chicago, USA) equipped with a 60X/NA1.42 oil-immersion objective lens (Olympus, Tokyo, Japan). The acquisition parameters were optimized following the steps depicted in Fig. 1 C. These include (1) refractive index matching of the immersion oil, (2) choice of appropriate excitation intensity and exposure time, (3) selection of sampling steps along the optical axis of the microscope, (4) sequential image acquisition from long to short wavelengths, and (5) overlap between adjacent fields of view to enable mosaic stitching of the data. After the acquisition, the super-resolved SIM images were reconstructed using the software package SoftWoRx provided by the microscope's manufacturer, and post-processed with the open-source software Fiji [9]. For comparative analysis, diffraction-limited deconvolution microscopy (DV) images were acquired with the same microscope. Supplementary information S2 provides a detailed description of the acquisition parameters used for both SIM and DV, as well as the working principle of these two microscopy techniques.

3. Results and discussion

The advantages of SIM include rejection of out-of-focus light and a two-fold resolution enhancement in all three axes (x, y, z) which gives an eight-fold contrast improvement as compared to diffraction-limited microscopy techniques such as DV. In the case of FFPE placental sections (Fig. 2 A,E,I), SIM provides a sharp visualization of biological structures such as the syncytiotrophoblast (SYN), individual cytotrophoblast (CT), fetal capillaries (FC), fetal red blood cells (fRBC) and maternal red blood cells (mRBC), as well as subcellular details such as
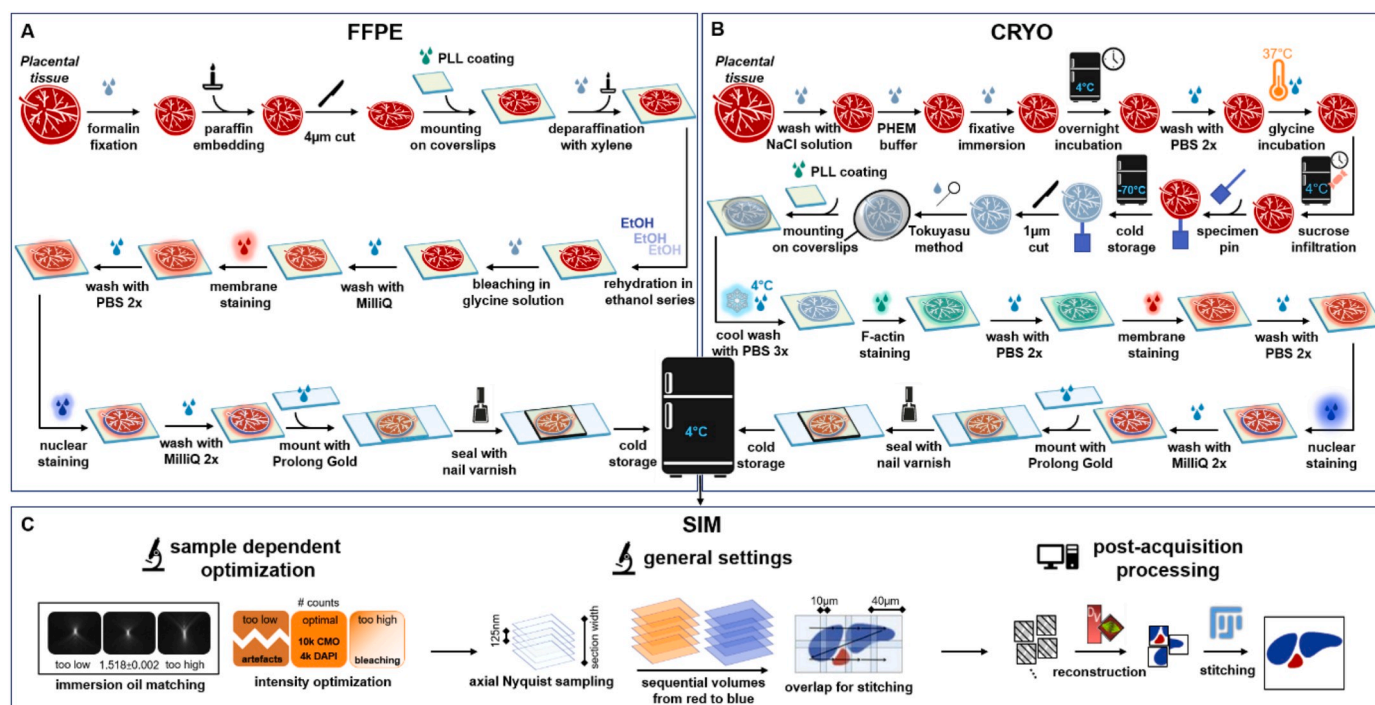

Fig. 1. Sample preparation protocols and imaging acquisition steps for successful super-resolution structured illumination microscopy (SIM) of placental tissue sections. (A) Sample preparation protocol for FFPE tissue sections. (B) Sample preparation protocol for cryopreserved tissue sections. (C) Imaging steps for SIM.
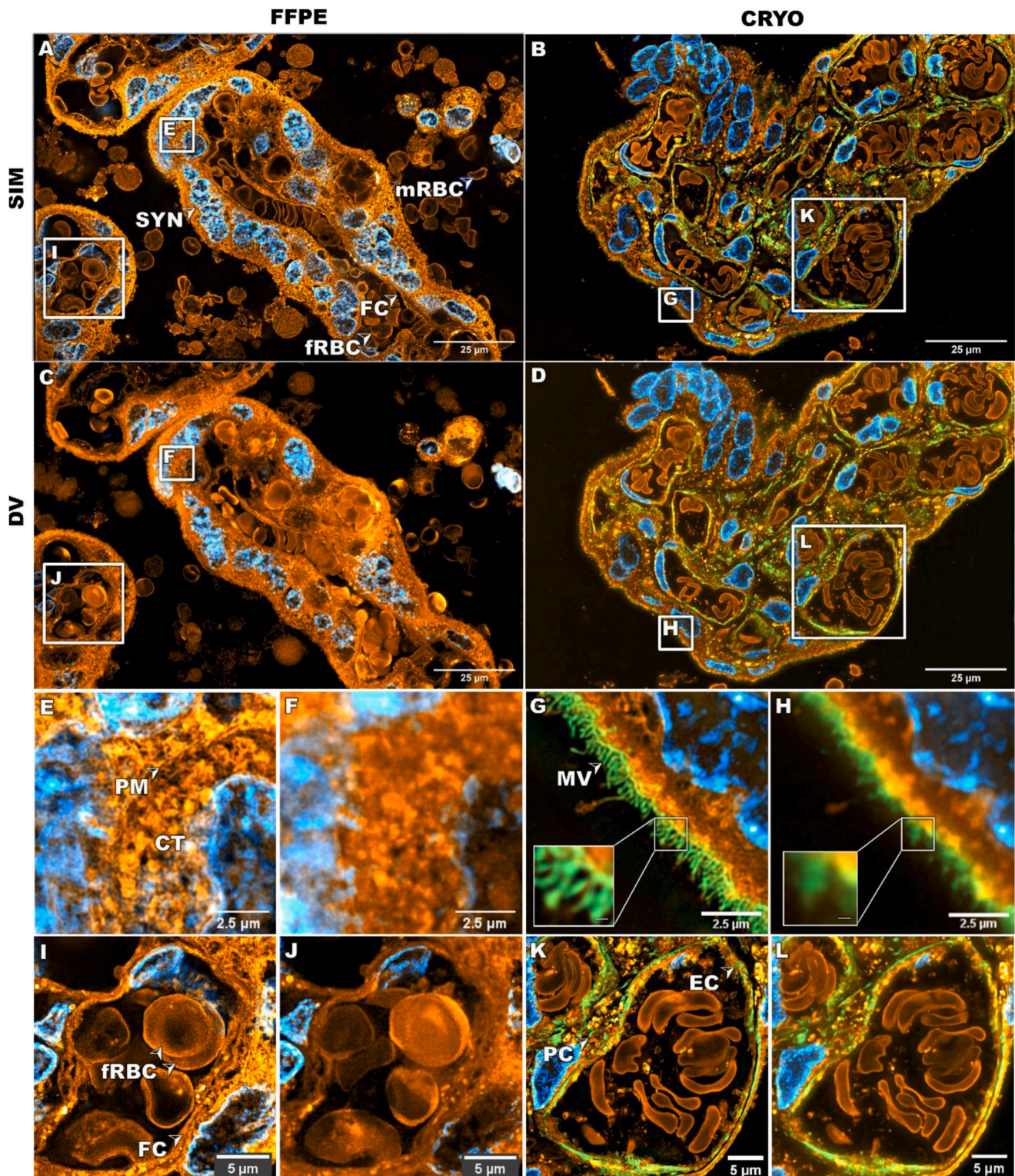
Fig. 2. Fluorescent micrographs of 4 μm thick FFPE and 1 μm thick cryo-preserved tissue sections of human chorionic villi imaged with both SIM and DV microscopy for comparison. F-actin stained with phalloidin-Atto 647 N (displayed in green), membranes stained with CMO (displayed in orange), and nuclei stained with DAPI (displayed in blue). (A,B,E,G,I,K) SIM images. (C,D,F,H,J,L) DV images. (A,C) The enhanced contrast of SIM compared to DV allows for a clearer visualization of relevant structures in the FFPE tissue section such as the syncytiotrophoblast «SYN», fetal capillaries «FC», fetal red blood cells «fRBC» and maternal red blood cells «mRBC». (E,F) Magnified views of the FFPE tissue section show the enhanced resolution of SIM over DV, revealing the plasma membrane «PM» of an individual cytotrophoblast «CT». (I,J) SIM enables the distinction of two adjacent «fRBCs» on a «FC» that are not discernible by DV. (B,D) The SIM image exhibits superior contrast as compared to the DV image of the cryo-preserved tissue section. (G,H) The enhanced resolution provided by SIM reveals the syncytiotrophoblast microvilli «MV» brush border, a morphological structure not resolvable by diffraction-limited OM techniques such as DV. Inlays have digitally enhanced contrast and scale bars of 200 nm. (K,L) SIM enables a clearer distinction of morphological features, such as a pericyte «PC» along with the underlying endothelial cell «EC» lining of a fetal capillary demostrated here, as compared to DV. (For interpretation of the references to color in this figure legend, the reader is referred to the Web version of this article.)

the plasma membrane border (PM) between adjacent cells. In comparison, results from diffraction-limited DV microscopy offer significantly fewer details and contrast (Fig. 2 C,F,J). Notably, the resolution attainable with SIM on FFPE sections was largely limited by the level of ultrastructural preservation of the sample during the preparation steps and not by the SIM method per se. The main challenges with FFPE sections were the autofluorescence signal and the refractive index mismatch between the specimen and the imaging medium, which often led to reconstruction artifacts on the SIM images. We successfully minimized the artifacts by introducing a bleaching step in the preparation protocol and a series of iterative oil changes to match the refractive index, as illustrated in supplementary information S2 and S3.

The SIM images obtained from placental cryosections were significantly sharper and richer in detail than their FFPE counterparts (Fig. 2 B, G,K). The ultrastructural preservation attainable with the Tokuyasu method allowed the visualization of ultrastructural details such as the syncytiotrophoblast's microvilli brush border (MV), a morphological feature not resolvable by diffraction-limited OM techniques. Moreover, the relatively low autofluorescent signal and the thin section thickness of these samples further aided the contrast enhancement of SIM by reducing the out-of-focus information, enabling the distinction of morphological features, such as a pericyte (PC) along with the underlying endothelial cell (EC) lining of a fetal capillary (Fig. 2 K, L).

A further advantage of imaging cryosections is the ease of tissue preparation, which allowed for sectioning, staining, and imaging within the same day. This positions SIM very favorably over traditional high-resolution techniques such as EM, where the sample preparation alone can take several days to weeks. The main drawback of imaging cryosections is the dependence of high precision cutting instruments together with highly skilled operators to obtain sections with minimal morphological damage.

Taken together, the availability of optical super-resolution SIM microscopes in conjunction with optimized tissue preparation and imaging parameters accelerate the imaging of placental tissue samples, aiding the identification of subcellular and ultrastructural features at high-throughput, hence improving the quality of histopathological diagnosis of placental disorders and image-based research in placental biology.

Declaration of competing interest

None.

Acknowledgments

Appendix A. Supplementary data

Supplementary data to this article can be found online at https://doi.org/10.1016/j.placenta.2020.06.007.

References

[1] S.W. Hell, S.J. Sahl, M. Bates, X. Zhuang, R. Heintzmann, M.J. Booth, J. Bewersdorf, G. Shtengel, H. Hess, P. Tinnefeld, A. Honigmann, S. Jakobs, I. Testa, L. Cognet, B. Lounis, H. Ewers, S.J. Davis, C. Eggeling, D. Klenerman, K. I. Willig, G. Vicidomini, M. Castello, A. Diaspro, T. Cordes, The 2015 super-resolution microscopy roadmap, J. Phys. Appl. Phys. 48 (44) (2015) 443001, https://doi.org/10.1088/0022-3727/48/44/443001.

[2] M. Wang, H.Z. Kimbrell, A.B. Sholl, D.B. Tulman, K.N. Elfer, T.C. Schlichenmeyer, B.R. Lee, M. Lacey, J.Q. Brown, High-resolution rapid diagnostic imaging of whole prostate biopsies using video-rate fluorescence structured illumination microscopy, Canc. Res. 75 (19) (2015) 4032–4041, https://doi.org/10.1158/0008-5472.Can-14-3806.

[3] F. Siegerist, S. Ribback, F. Dombrowski, K. Amann, U. Zimmermann, K. Endlich, N. Endlich, Structured illumination microscopy and automatized image processing as a rapid diagnostic tool for podocyte effacement, Sci. Rep. 7 (1) (2017) 11473, https://doi.org/10.1038/s41598-017-11553-x.

[4] R. Singh, D. Wolfson, V. Dubey, A. Ahmad, G. Acharya, D. Mehta, P. Basnet, B. Ahluwalia, Inflammatory response of macrophages and trophoblasts investigated using structured illumination microscopy and quantitative phase microscopy, Placenta 57 (2017), https://doi.org/10.1016/j.placenta.2017.07.339, 333-333.

[5] R. Wang, R. Yu, C. Zhu, H. Lin, X. Lu, H. Wang, Tubulin detyrosination promotes human trophoblast syncytium formation, J. Mol. Cell Biol. 11 (11) (2019) 967–978, https://doi.org/10.1093/jmcb/mjz084.

[6] M. Slaoui, L. Fiette, Histopathology procedures: from tissue sampling to histopathological evaluation, in: J.-C. Gautier (Ed.), Drug Safety Evaluation: Methods and Protocols, Humana Press, Totowa, NJ, 2011, pp. 69–82.

[7] V. Sitras, R. Paulssen, H. Grønaas, J. Leirvik, T. Hanssen, Å. Vårtun, G. Acharya, Differential placental gene expression in severe preeclampsia, Placenta 30 (5) (2009) 424–433, https://doi.org/10.1016/j.placenta.2009.01.012.

[8] P. Webster, A. Webster, Cryosectioning fixed and cryoprotected biological material for immunocytochemistry, in: J. Kuo (Ed.), Electron Microscopy: Methods and Protocols, Humana Press, Totowa, NJ, 2007, pp. 257–289.

[9] J. Schindelin, I. Arganda-Carreras, E. Frise, V. Kaynig, M. Longair, T. Pietzsch, S. Preibisch, C. Rueden, S. Saalfeld, B. Schmid, J.Y. Tinevez, D.J. White, V. Hartenstein, K. Eliceiri, P. Tomancak, A. Cardona, Fiji: an open-source platform for biological-image analysis, Nat. Methods 9 (7) (2012) 676–682, https://doi.org/10.1038/nmeth.2019.

[10] J.-B. Sibarita, Deconvolution microscopy, in: J. Rietdorf (Ed.), Microscopy Techniques. Advances in Biochemical Engineering, vol. 95, Springer Berlin Heidelberg, Berlin, Heidelberg, 2005, pp. 201–243.

Visualizing ultrastructural details of placental tissue with super-resolution structured illumination microscopy. Supplementary information

Luis E. VILLEGAS-HERNÁNDEZ[1], Mona NYSTAD[2,3], Florian STRÖHL[1], Purusotam BASNET[2,4], Ganesh ACHARYA[2,5], Balpreet S. AHLUWALIA[1,5]

1 Department of Physics and Technology, UiT - The Arctic University of Norway, Tromsø, Norway
2 Department of Clinical Medicine, Women's Health and Perinatology Research group, Faculty of Health Sciences, UiT - The Arctic University of Norway, Tromsø, Norway
3 Department of Medical Genetics, University Hospital of North Norway, Tromsø, Norway
4 Department of Obstetrics and Gynecology, University Hospital of North Norway, Tromsø, Norway
5 Division of Obstetrics and Gynecology, Department of Clinical Science, Intervention and Technology, Karolinska Institute, Stockholm, Sweden

Corresponding authors: ganesh.acharya@ki.se and balpreet.singh.ahluwalia@uit.no

S1.   Materials used in the study

Table S1 and Table S2 provide a detailed list of the materials, reagents, dyes and mounting medium used in the study.

Table S1. Materials, reagents, dyes and mounting medium used in the study

Material/ reagent	Manufacturer	Catalog number	Stock concentration	Working concentration	Purpose
#1.5 coverslip	VWR	48393-151	-	-	Coverslip, sample substrate
Poly-L-lysine	Sigma-Aldrich	P8920	0.1 % (w/v) in H_2O	1:1	Surface coating
Xylene	VWR	28975	≥98.5%	1:1	Deparaffinization steps
Ethanol (EtOH)	Sigma-Aldrich	32205-M	≥99.8%	100% 96% 70%	Rehydration of paraffin-embedded samples
Glycine	Sigma-Aldrich	G7126	≥99%	150 mM	Bleaching solution to reduce autofluorescence
Phalloidin-Atto 647N	Sigma-Aldrich	65906	10 μM	1:100	F-actin staining
CellMask Orange	ThermoFischer	C10045	5 mg/mL	1:2000	Membrane staining
DAPI	ThermoFischer	62247	1 mg/mL	1:1000	Nuclear staining
Prolong Gold	ThermoFischer	P36930	-	1:1	Mounting medium
Phosphate buffered saline (PBS)	Sigma-Aldrich	D8662	-	1:1	Washing steps
Sodium chloride	Fresenius Kabi	826968	9 mg/mL	1:1	Rinsing steps for cryosections
Methyl cellulose	Sigma-Aldrich	M6385	-	2%	Preservation steps of cryosections

Sucrose	Sigma-Aldrich	16104	-	2.3 M	Preservation steps of cryosections
Fixative	15 mL 0.2 M PBS 7.5 mL 8 % formaldehyde diluted in 4× PHEM 7.5 mL ddH2O				Fixation of cryosections

Table S2.Chemicals used to make the 4× PIPES-HEPES-EGTA-Magnesium sulfate (PHEM) buffer

Chemicals	Manufacturer	Reference	Purpose
EGTA[1]	Sigma-Aldrich	E4378-100G	Used in PHEM
HEPES[2]	VWR Chemicals	441476L	Used in PHEM
PIPES[3]	Sigma	P6757-500G	Used in PHEM
Magnesium sulfate	Sigma-Aldrich	M7506-500G	Used in PHEM
5 M sodium hydroxide	Sigma-Aldrich	30620-1KG-R	Used in PHEM

[1] Ethylene glucol tetraacetic acid (ethylene glycol-bis (β-aminoethyl ether)-N,N,N',N'-tetraacetic acid) (EGTA)
[2] 4-(2-hydroxyethyl)-1-piperazineethanesulfonic acid (HEPES)
[3] 1,4 piperazine bis (2-ethanosulfonic acid) (PIPES)

S2.   Imaging parameters

The OMX microscope

The samples were imaged in both structured illumination microscopy (SIM) mode and deconvolution microscopy (DV) mode using a commercial microscope DeltaVision OMX V4 Blaze imaging system (GE Healthcare, Chicago, USA). The system was equipped with a 60X/NA1.42 oil-immersion objective lens (Olympus, Tokyo, Japan), three sCMOS cameras, four excitation lasers (405 nm, 488 nm, 568 nm, 642 nm), four emission filters (419-450nm, 504-552 nm, 590-627 nm, 663-703 nm). In this study, only the 642 nm, 568 nm, and 488 nm channels were used for imaging of the phalloidin-Atto 647N, the CellMask Orange (CMO) and the DAPI, respectively.

Super-resolved SIM images were reconstructed using the software package SoftWoRx provided by the microscope's manufacturer, and post-processed with the open-source software Fiji to allow stitching of larger regions. Diffraction-limited deconvolution microscopy (DV) images were acquired for comparative analysis. The working principle of these microscopy techniques is hereby described.

Working principle of deconvolution microscopy (DV)

DV is a diffraction-limited technique used in fluorescence microscopy to enhance image contrast by removing out-of-focus information from adjacent planes above and below a given focal plane. The method involves the acquisition of multiple images along the optical axis of the microscope (e.g., z-stack), which are enhanced computationally in a post-processing step. During this step, following a mathematical model of diffraction and imaging noise, out-of-plane diffracted light is reassigned to its original location [11]. DV offers high-resolution fluorescent images near the optical resolution limit of the microscope, comparable to confocal microscopy.

Working principle of structured illumination microscopy (SIM)

SIM is a fluorescent-based optical super-resolution technique that employs multiple laser beams interference to create a striped illumination pattern with high spatial frequency for

the excitation of the fluorescent markers on the sample. Upon illumination, the very fine, conventionally unresolvable details of the sample become down-modulated, generating coarse-spaced Moiré fringes that are now resolvable by the microscope. To computationally extract the down-modulated details and obtain super-resolved information from the sample, a set of individual images are taken over the same field of view while varying the phase and the orientation of the illumination pattern. Typically, 15 images are used for 3D-SIM to gain an isotropic lateral resolution enhancement [12], corresponding to three orientations and five phases per orientation angle. Finally, a computational algorithm processes all the raw images and reconstructs a single super-resolved SIM image.

Mathematically, the resolution limit R of the microscope in the spatial domain is denoted as the cut-off frequency f_c in the frequency domain, and their relationship is given by equation (1). Hence, the objective lens can be described as a low-pass filter in the frequency domain with a characteristic cut-off frequency f_c.

$$R = \frac{1}{f_c} \tag{1}$$

For SIM, the resolution limit R_{SIM} is given by equation (2), where f_s is the spatial frequency of the illumination pattern projected onto the sample [13].

$$R_{SIM} = \frac{1}{f_c + f_s} \tag{2}$$

Theoretically, the resolution of SIM becomes unlimited by increasing f_c and f_s. In practice, when using the same objective lens to both generate the illumination pattern and to observe the sample, both f_c and f_s are limited by the diffraction of light. Thus, the practical resolution improvement of this technique is a factor of two-fold (2X) compared to diffraction-limited microscopy, in cases where the objective lens is used both for illumination and collection of light. In practical terms, it means a resolution limit is close to 100 nm.

Oil matching

Both DV and SIM require optimization of the point spread function (PSF) of the system by matching the refractive index of the immersion oil to that of the mounting medium. This is an iterative process done by observing the orthogonal view of single emitters along with fluorescent images arranged in a z-stack fashion, and changing the immersion oil to a different refractive index until a symmetric shape of the PSF is observed. The PSF optimization plays a key role in the quality of DV and SIM since the oil mismatch can introduce artifacts in the reconstructed images [11, 14].

In cryosections, we matched the oil using fluorescent z-stack raw images acquired in DV mode at 250 nm sampling steps along the optical axis, as a preliminary step for SIM imaging. In FFPE sections single emitters were scarce. Instead, we imaged areas of no clinical relevance in SIM mode with different oils until artifact-free SIM images were obtained. Once optimized, the microscope's stage was moved to the region of interest for the acquisition of SIM images. Typical refractive indices of the oils used range from 1.516 to 1.520.

Image acquisition

SIM images consist of a projection of multiple images (z-stack) acquired in controlled steps (z-sections, or optical sections) along the optical axis of the microscope. Following the

Nyquist sampling theorem, steps of 125 nm size are required to attain SIM images of maximum 250 nm axial resolution. Projected SIM images, commonly referred to as 3D-SIM images, require 15 two-dimensional raw frames per image plane of the z-stack, in correspondence to the three angles and five phase shifts of the illumination pattern used in this technique. The thickness of the z-stack is set according to the number of optical sections needed to cover the physical thickness of the tissue section. Analogously, in the case of deconvolution microscopy (DV), only one frame is required per optical section, with a coarser sampling step of 250 nm along the optical axis.

For multi-color imaging, we sequentially acquired z-stacks of individual channels, transitioning from longer to shorter excitation wavelengths. We used three excitation laser sources for SIM imaging, namely 642 nm for F-actin (phalloidin-Atto 647N), 568 nm for membranes (CMO) and 405 nm for nuclei (DAPI). Imaging parameters such as illumination intensity and exposure time were optimized during the imaging process to avoid photobleaching of the dyes. The maximum intensity count was approximately 10000 for both the phalloidin-Atto 647N and the CMO and approximately 4000 for DAPI. The field of view (FOV) of reconstructed 3D-SIM images was approximately 40 × 40 μm, corresponding to an image size of 1024 x 1024 pixels. For larger FOVs, the samples were scanned at lateral steps of 30 μm, i.e. with 10 μm overlap, and the collected images were computationally stitched as tile mosaic images using the grid/collection stitching plugin provided by the software package FIJI [15].

S3.   Autofluorescence quantification of placental FFPE sections

One of the main challenges faced during the study was the autofluorescent background. Autofluorescence is a phenomenon that refers to the ability of certain molecular structures to fluoresce naturally or due to chemical changes induced by fixation. Autofluorescence often exhibits a broad emission spectrum, making it difficult to separate its signal from that of fluorescent dyes linked to target structures in imaging experiments. Signal contribution from autofluorescence leads to reconstruction artifacts in SIM such as haloing and high-frequency noise, thus hampering the resolution capabilities of this technique. The effect is even more prominent in conventional fluorescence microscopy (e.g. DV), where autofluorescent signal increases the background noise, leading to image blurring.

We found autofluorescence mostly in FFPE prepared sections and thus limited its characterization to this preparation method. For characterization, FFPE sections were label-free prepared and imaged in DV mode on the OMX microscope. All channels were set to 50% excitation intensity and 50 ms acquisition time. The autofluorescence response of FFPE tissue sections is illustrated in Figure S1 with mean and maximum gray values listed in Table S3. The FFPE placental tissue sections show a broad autofluorescent response with a peak on channel 3, corresponding to an excitation wavelength of 488 nm. A significant part of the autofluorescent contribution in these samples came from the hemoglobin of red blood cells (RBCs), which is known to be autofluorescent at this wavelength range [16].

Diverse methods exist to reduce autofluorescence of histological samples, ranging from pre-bleaching via irradiation [17], to a series of chemical treatments [18-20]. The chosen method for autofluorescence reduction in this study consisted of a 30 min incubation step in 150 mM

glycine solution after rehydration of the tissue sections. Also, the extrinsic fluorescent dyes selected for structure labeling exhibited a signal strength at least two-fold higher than that of the autofluorescent signal in their given excitation channel.
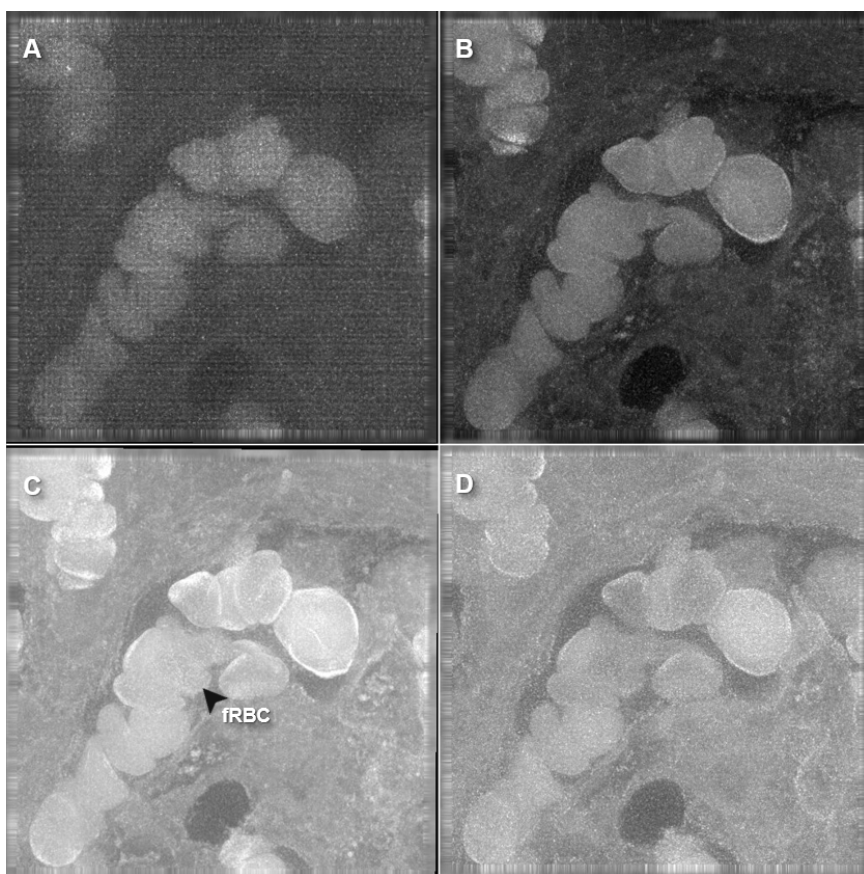

Figure S1. DV image of unlabeled FFPE human placental tissue section with fetal capillaries containing red blood cells. Grayscale images show autofluorescent signal upon illumination with (A) red light (λ = 642 nm), (B) green light (λ = 568 nm), (C) blue light (λ = 488 nm), and (D) violet light (λ = 405 nm). Bright areas indicate elevated autofluorescent signal, in this case corresponding to autofluorescence of fRBCs. Excitation intensity 50%, exposure time 50ms in all channels. FOV 80 × 80 μm.

Table S3. Imaging parameters and autofluorescence values of FFPE human placental tissue section.

Channel	Excitation wavelength (nm)	Intensity (%)	Exposure time (ms)	Gray value count			
				Min	Max	Mean	StdDev
CH1	642	50	50	0	647	209	58
CH2	568	50	50	437	2989	1151	299
CH3	488	50	50	0	8596	4875	901
CH4	405	50	50	0	2190	1294	165

References – Supplementary information

[11] J.-B. Sibarita, Deconvolution Microscopy, in: J. Rietdorf (Ed.), Microscopy Techniques. Advances in Biochemical Engineering. Springer Berlin Heidelberg, Berlin, Heidelberg, 95 (2005), pp. 201-243.

[12] B.J. Chang, L.J. Chou, Y.C. Chang, S.Y. Chiang, Isotropic image in structured illumination microscopy patterned with a spatial light modulator, Opt Express 17(17) (2009) 14710-21. https://doi.org/10.1364/oe.17.014710.

[13] A. Stemmer, M. Beck, R. Fiolka, Widefield fluorescence microscopy with extended resolution, Histochem Cell Biol 130(5) (2008) 807-17. https://doi.org/10.1007/s00418-008-0506-8.

[14] J. Demmerle, C. Innocent, A.J. North, G. Ball, M. Muller, E. Miron, A. Matsuda, I.M. Dobbie, Y. Markaki, L. Schermelleh, Strategic and practical guidelines for successful structured illumination microscopy, Nat Protoc 12(5) (2017) 988-1010. https://doi.org/10.1038/nprot.2017.019.

[15] S. Preibisch, S. Saalfeld, P. Tomancak, Globally optimal stitching of tiled 3D microscopic image acquisitions, Bioinformatics 25(11) (2009) 1463-5. https://doi.org/10.1093/bioinformatics/btp184.

[16] B. Gopalkrishnapillai, V. Nadanathangam, N. Karmakar, S. Anand, A. Misra, Evaluation of autofluorescent property of hemoglobin-advanced glycation end product as a long-term glycemic index of diabetes, Diabetes 52(4) (2003) 1041-1046. https://doi.org/10.2337/diabetes.52.4.1041.

[17] M. Neumann, D. Gabel, Simple method for reduction of autofluorescence in fluorescence microscopy, J Histochem Cytochem 50(3) (2002) 437-9. https://doi.org/10.1177/002215540205000315.

[18] N. Raghavachari, Y.P. Bao, G. Li, X. Xie, U.R. Muller, Reduction of autofluorescence on DNA microarrays and slide surfaces by treatment with sodium borohydride, Anal Biochem 312(2) (2003) 101-5. https://doi.org/10.1016/s0003-2697(02)00440-2.

[19] A.S. Davis, A. Richter, S. Becker, J.E. Moyer, A. Sandouk, J. Skinner, J.K. Taubenberger, Characterizing and Diminishing Autofluorescence in Formalin-fixed Paraffin-embedded Human Respiratory Tissue, J Histochem Cytochem 62(6) (2014) 405-423. https://doi.org/10.1369/0022155414531549.

[20] N.C. Whittington, S. Wray, Suppression of Red Blood Cell Autofluorescence for Immunocytochemistry on Fixed Embryonic Mouse Tissue, Curr Protoc Neurosci 81(1) (2017) 2 28 1-2 28 12. https://doi.org/10.1002/cpns.35.

Appendix B. Paper II

Chip-based multimodal super-resolution microscopy for histological investigations of cryopreserved tissue sections

Luis E. Villegas-Hernández[1], Vishesh Dubey[1], Mona Nystad[2,3], Jean-Claude Tinguely[1], David A. Coucheron[1], Firehun T. Dullo[1], Anish Priyadarshi[1], Sebastian Acuña[1], Azeem Ahmad[1], José M. Mateos[4], Gery Barmettler[4], Urs Ziegler[4], Åsa Birna Birgisdottir[5,6], Aud-Malin Karlsson Hovd[7], Kristin Andreassen Fenton[7], Ganesh Acharya[2,8], Krishna Agarwal[1] and Balpreet Singh Ahluwalia [iD][1,8✉]

Abstract

Histology involves the observation of structural features in tissues using a microscope. While diffraction-limited optical microscopes are commonly used in histological investigations, their resolving capabilities are insufficient to visualize details at subcellular level. Although a novel set of super-resolution optical microscopy techniques can fulfill the resolution demands in such cases, the system complexity, high operating cost, lack of multi-modality, and low-throughput imaging of these methods limit their wide adoption for histological analysis. In this study, we introduce the photonic chip as a feasible high-throughput microscopy platform for super-resolution imaging of histological samples. Using cryopreserved ultrathin tissue sections of human placenta, mouse kidney, pig heart, and zebrafish eye retina prepared by the Tokuyasu method, we demonstrate diverse imaging capabilities of the photonic chip including total internal reflection fluorescence microscopy, intensity fluctuation-based optical nanoscopy, single-molecule localization microscopy, and correlative light-electron microscopy. Our results validate the photonic chip as a feasible imaging platform for tissue sections and pave the way for the adoption of super-resolution high-throughput multimodal analysis of cryopreserved tissue samples both in research and clinical settings.

Introduction

Histology is the field of biology that studies the micro-anatomy and structure of tissues regarding their function in organisms. A typical histological analysis involves the extraction of a tissue sample from the body, fixation, and preservation followed by sectioning and labeling before observation through a microscope. In medical settings, histological investigations facilitate the identification and diagnosis of diseases, provide guidance for treatment, and assist in the prognosis of clinical outcomes.

Imaging throughput, contrast, and resolution are critical parameters for histological assessment. While whole slide imaging scanners provide fast imaging of several histological slides in a day, these automated optical microscopes are limited to a resolution power of ~250–500 nm (ref. [1]), which is insufficient for the observation of individual subcellular structures such as nanovesicles, filaments, tubules, brush border, gap junctions and several other intracellular features with an average size below ~250 nm. For decades, the visualization of such features was only possible through other imaging techniques such as electron microscopy[2–4], which supports a resolving power down to ~10 nm for fixed and embedded histological samples. While available published methods for fast[5] and automated correlation microscopy exist since years[6], the combination of traditionally lengthy sample preparation

Correspondence: Balpreet Singh Ahluwalia (balpreet.singh.ahluwalia@uit.no)
[1]Department of Physics and Technology, UiT The Arctic University of Norway, Klokkargårdsbakken N-9019, Tromsø, Norway
[2]Department of Clinical Medicine, Women's Health and Perinatology Research Group, UiT The Arctic University of Norway, Tromsø, Norway
Full list of author information is available at the end of the article
These authors contributed equally: Luis E. Villegas-Hernández, Vishesh Dubey

process, lack of specificity, low imaging throughput, system complexity, and high operational costs, has limited the adoption of electron microscopy in clinical settings, confining its implementation mostly to biology research.

Recently, the advent of super-resolution fluorescence optical microscopy techniques, also referred to as optical nanoscopy, bridged the resolution gap between the diffraction-limited optical microscopy and the electron microscopy methods, allowing for high-specificity imaging of biological specimens at high-resolution[7−9]. Present-day fluorescence-based super-resolution optical microscopy comprises a panel of methods that exploit engineered illumination and/or the photochemical and photokinetic properties of fluorescent markers to achieve high spatiotemporal resolution. These include structured illumination microscopy (SIM)[10], stimulated emission depletion microscopy (STED)[11], single-molecule localization microscopy (SMLM)[12,13], and intensity fluctuation-based optical nanoscopy techniques (IFON)[14].

While super-resolution fluorescence optical microscopy methods are commonly used in cell biology, their practical implementation in clinical settings for observations of tissue sections remains deferred due to multiple reasons: (a) the high labeling density of tissues poses challenges on super-resolution methods, especially for SMLM and IFON, where a high spatiotemporal sparsity is necessary for the reconstruction of structures beyond the diffraction limit of the microscope; (b) the susceptibility of the super-resolution methods to optical aberrations and light scattering introduced by refractive index variations across the samples[15]; (c) the imaging artifacts induced by autofluorescence signal of tissues[16]; and importantly, (d) the low-throughput, high-cost, lack of multi-modality, system complexity, and bulkiness of existing super-resolution optical microscopy setups.

Although limited work on using STED, SIM, and SMLM have been explored for super-resolution of histological samples[17−19], these methods fail to fulfill the throughput demands necessary for clinical assessment of tissue sections. For example, STED, albeit delivering a lateral resolution down to 20 nm (ref. [20]) and being a robust method to scattering challenges posed by tissues, is an inherently low-throughput point-scanning technique. Similarly, SMLM and SIM, despite being wide-field methods supporting sub-50 nm and ~110–130 nm lateral resolution respectively, are heavily dependent on the acquisition of multiple frames and subsequent reconstruction via post-processing algorithms. While SIM outperforms SMLM in terms of imaging speed, requiring only 9 or 15 images (2D/3D cases accordingly) as compared to the tens of thousands of images necessary for SMLM, the field of view obtained by commercial SIM systems is typically limited to about 40 μm × 40 μm. Importantly, among all the super-resolution methods,

SIM has been proposed for high-throughput imaging of tissue sections in clinical settings[18,21]. However, these approaches focused on the acquisition of large field of view images using low magnification and low numerical aperture objective lenses, compromising the lateral resolution to a maximum of 1.3 μm. In terms of system complexity, SMLM is simpler to implement as compared to SIM and STED, which require more sophisticated, bulkier, and costly setups. From an overall perspective, improvements in imaging throughput and reductions in system complexity, footprint, and cost are needed for the adoption of super-resolution fluorescence optical microscopy. Thus, to enable a widescale penetration in clinical settings, an imaging platform that can deliver different super-resolution capabilities using a standard optical microscopy setup is desirable.

Another important aspect necessary for the adoption of fluorescence-based super-resolution optical microscopy is the availability of a large selection of fluorophores. While SIM works with photo-stable and bright fluorophores, STED and SMLM are more restricted to a special type of fluorescent markers. Interestingly, some of the IFON techniques, such as the multiple signal classification algorithm (MUSICAL)[22], can exploit the pixel intensity variations arising not only from the intrinsic fluctuations of the fluorophores but also from the modulated emissions generated via engineered illumination, enabling a practical implementation with almost all kinds of fluorophores. Despite being an attractive route to follow for clinical applications, to the best of our knowledge the engineered illumination approach for IFON has not been explored in tissue imaging.

In recent years, photonic chip-based nanoscopy has emerged as a promising imaging platform for biological applications[23−26], supporting high-resolution, high-throughput, and multimodal capabilities. The technique consists of a photonic chip that is used both to hold the sample and to provide the excitation illumination necessary for fluorescent emission (Fig. 1a). The photonic chip is composed of two substrate layers of silicon (Si) and silicon dioxide (SiO$_2$), respectively, and a biocompatible waveguide core layer that transmits visible light, made of either silicon nitride (Si$_3$N$_4$)[24] or tantalum pentoxide (Ta$_2$O$_5$)[27]. Upon coupling, the excitation laser beam is tightly confined inside the optical waveguide layer and propagates through its geometry via total internal reflection (Fig. 1a, d). This generates an evanescent field on the top of the waveguide surface with an illumination reach of up to ~150–200 nm that is used to excite the fluorescent markers located in the vicinity of the waveguide surface (see Supplementary Information S1). The fluorescent emission is then collected by a standard upright microscope (Fig. 1c) equipped with conventional microscope objective lenses (Fig. 1d), enabling chip-based total
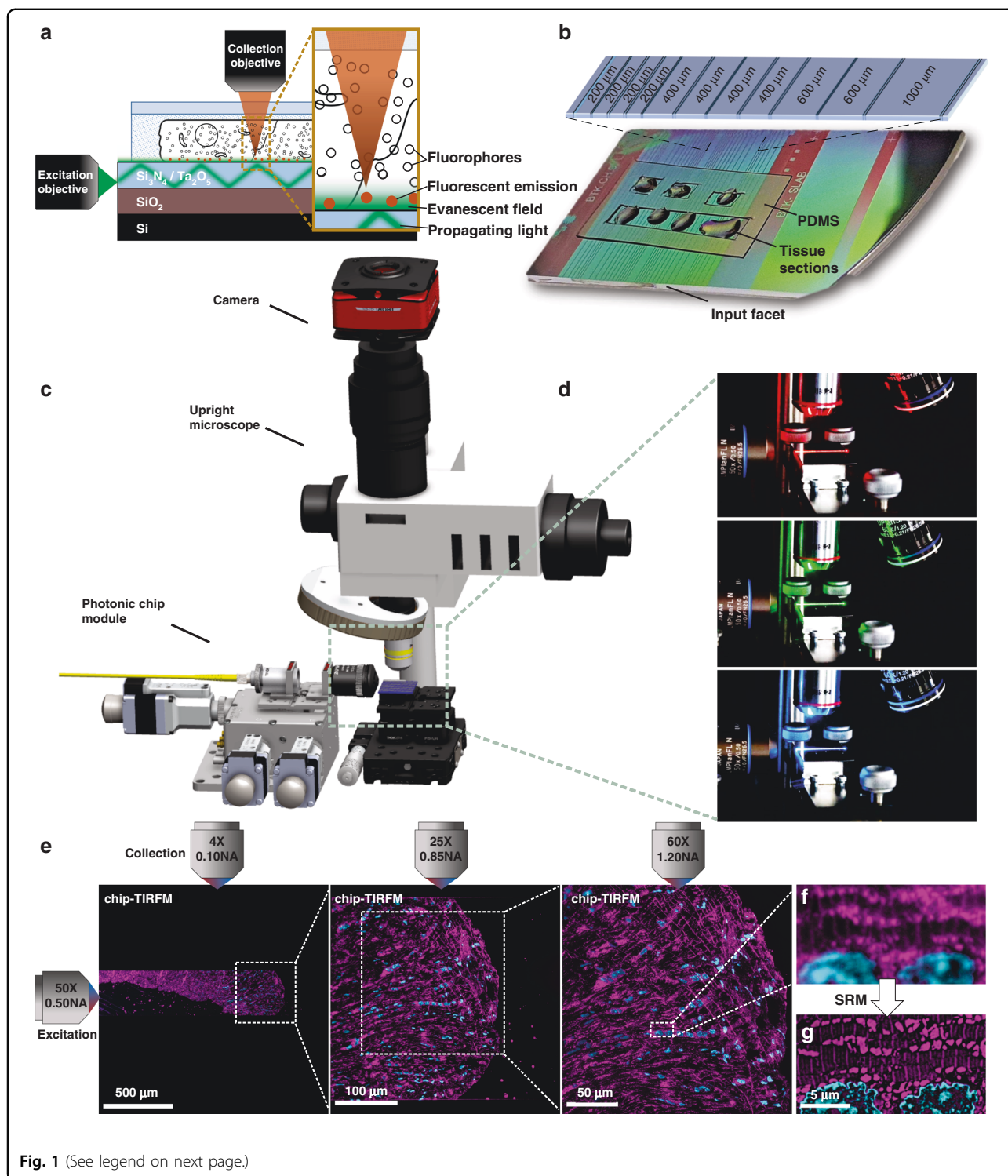
Fig. 1 (See legend on next page.)

internal reflection fluorescence microscopy over diverse fields of view (Fig. 1e).

To date, photonic chip-based microscopy studies have focused primarily on cellular biology[23–26,28,29], leaving on-chip histological imaging unexplored. In this work, we interrogate the photonic chip-based imaging platform to

address some of the challenges related to super-resolution imaging of tissue sections. We start by evaluating the viability of the photonic chip for diffraction-limited total internal reflection microscopy (chip-TIRFM). Then, we transition to more advanced chip-TIRFM based imaging methods such as SMLM, IFON, to conclude with a

(see figure on previous page)
Fig. 1 Schematic representation of the chip-based total internal reflection fluorescence microscopy (chip-TIRFM) setup. a Working principle of chip-TIRFM: upon coupling onto the input facet, the excitation light propagates through the waveguide core material due to total internal reflection. An evanescent field of ~150 nm height excites a thin layer of fluorescent dyes in the vicinity of the photonic chip surface, allowing for TIRFM imaging. **b** Top view of a photonic chip containing ultrathin Tokuyasu cryosections covered with a 1:1 cryoprotectant mixture of 2.3 M sucrose and 2% methylcellulose, and surrounded by a custom-made transparent polydimethylsiloxane (PDMS) frame. The inset illustrates the various strip waveguide widths available on the chip. **c** The chip-TIRFM setup is composed of a custom-made photonic chip module and a commercially available upright collection module. Upon coupling the excitation light on the photonic chip, the fluorescent signal is allowed through a filter set and captured with a scientific CMOS camera. **d** The photonic chip allows decoupling of the excitation and the collection light paths, enabling TIRFM imaging using conventional microscope objectives. Different wavelengths propagating on the waveguide core allow for multicolor TIRFM imaging. **e** TIRFM images of a 100 nm thick pig heart cryosection imaged on a photonic chip through different microscope objectives. Membranes in magenta and nuclei in cyan. Supplementary Information S9 provides a detailed view and an extended description of this tissue sample. **f** Magnified view of the diffraction-limited TIRFM image acquired with a 60X/1.20NA water immersion microscope objective. **g** Subsequent post-processing of the raw data enables super-resolution microscopy (SRM), allowing the visualization of structures beyond the diffraction limit of conventional optical microscopy. Image was taken by SIM

correlative light-electron microscopy (CLEM) analysis. Among the existing histological methods, we chose the Tokuyasu protocol[30] for the preparation of the tissue sections. This cryosectioning method provides excellent ultrastructural preservation, high molecular antigenicity, and a thin section thickness (70 nm to 1 μm) that assists both in reducing the light scattering artifacts associated with thicker samples[31] and in making optimal use of the illumination delivered by the photonic chip. We describe the staining protocols and the imaging parameters necessary for photonic chip-based microscopy of tissue samples and discuss the challenges and the advantages offered by this imaging platform for the investigation of tissue sections. By exploiting the engineered illumination delivered by the photonic chip-based microscopy, we validate this novel technique as a compact multimodal imaging platform suitable for the investigation of tissue sections, paving the way for future implementations of high-resolution, high-contrast, and high-throughput microscopy both in research and clinical settings. This is the first study of photonic chip-based super-resolution microscopy of tissue sections. Moreover, to the best of our knowledge, this is also the first super-resolution imaging study of human placenta and human kidney tissues using IFON methods.

Photonic chip-based microscopy for histology

Photonic chip-based illumination provides several advantages that can be exploited for super-resolution imaging of tissue sections, including:

a. The photonic chip allows decoupling of the excitation and the emission light paths, which translates into high-contrast images with improved imaging throughput. The propagating light enables a uniform illumination over the entire length of the waveguide while providing optical sectioning of the sample via evanescent field excitation[32]. As the illumination is provided by the photonic chip, the imaging objective lens can be freely changed (Fig. 1d), enabling the acquisition of images over large fields of view[26] (Fig. 1e), a feature not available in conventional TIRFM setups.

b. The multi-mode interference (MMI) illumination generated on the photonic chip assists in generating the necessary emission sparsity for diverse super-resolution fluorescent optical microscopy methods, as recently demonstrated via on-chip IFON[23,33], on-chip SMLM[23,26,34], and on-chip SIM[35]. Moreover, by using waveguide materials of high refractive index (for example, $n = 2$), it is possible both to tightly confine the light and to generate higher spatial frequencies as compared to free-space optical components[23,35], which can be exploited by IFON techniques such as MUSICAL. The MMI illumination further aids in providing spatiotemporal sparsity that is useful for highly dense and heterogeneous samples such as tissues.

c. Correlative imaging with other established methods including electron microscopy[36] and quantitative phase microscopy[27] can be seamlessly implemented on the photonic chip, expanding the opportunities both for routine analysis and for basic histology research.

d. The photonic chip-based microscopy can be implemented on standard optical microscopy platforms upon a few adaptations for the integration of a photonic chip module (Fig. 1c). The photonic chips can be manufactured in high-volumes following standard complementary metal-oxide-semiconductor (CMOS) photolithography processes, allowing for low operating costs in clinical settings.

Results
Chip-based multicolor TIRFM imaging

In this part of the study, we used chorionic villi tissue from the human placenta to assess the suitability of the photonic chip for histological observations. This tissue, present on the fetal side of the placenta, is responsible for

the air, nutrient, and waste exchange between the mother and the fetus during pregnancy[37], and is characterized by villous-like structures, namely villi, that sprout from the chorionic plate of the placenta to maximize the materno-fetal transfer processes and communication. When transversally sectioned, the chorionic villi appear in the form of rounded islands distributed across an open space surrounded by maternal blood, called the intervillous space.

Developed by Kiyoteru Tokuyasu in the '70s (refs. [38,39]), the so-called "Tokuyasu method" is still a gold standard protocol for ultrastructural analysis of cells and tissues[30]. Primarily established for EM techniques, recent studies have shown its versatility in fluorescence microscopy[40,41]. For chip-based multicolor TIRFM imaging, 400 nm thick chorionic villi cryosections were prepared following the Tokuyasu method (see detailed preparation protocol in Materials and Methods and Supplementary Information S2). After cutting the tissue blocks on a cryo-ultramicrotome, the sections were deposited onto a photonic chip previously coated with poly-L-lysine and equipped with a custom-made transparent polydimethylsiloxane (PDMS) frame (Fig. 1b). The membranes, F-actin, and nuclei were fluorescently stained following a direct-labeling approach using CellMask Deep Red, Phalloidin-Atto565, and Sytox Green, respectively (see Fig. 5 and Supplementary Information S7 and S8 for examples of indirect labeling, e.g., immunofluorescence, of diverse Tokuyasu cryosections).

For the excitation of the respective fluorescent dyes, three independent laser light wavelengths were used, namely 640, 561, and 488 nm (Fig. 1d). To obtain TIRF images (see detailed acquisition steps in Materials and Methods), the excitation light was coupled onto a single strip waveguide using a 50X/0.5NA microscope objective (Fig. 1c). Upon coupling, a multi-mode interference pattern was generated along the waveguide by the propagating light, which was then modulated by changing the position of the coupling objective relative to the chip (see Supplementary Information S3). To deliver a uniform illumination onto the sample, the coupling objective was laterally scanned along the input facet of the chip while individual frames were acquired. The fluorescent emission was collected by standard microscope objectives transitioning from lower to higher magnification to achieve different fields of view. Thereafter, the collected signal was averaged, pseudo-colored (membranes in red, F-actin in green, and nuclei in blue), and merged, allowing multicolor visualization of the different tissue components.

The large field of view provided by the 4X/0.1NA objective lens enabled us to locate the sample on the waveguide (Fig. 2a), while the 20X/0.45NA assisted for a contextual visualization of the tissue structure, supporting the identification of regions of interest for imaging with further magnification (white box in Fig. 2b). Finally, with the aid of a 60X/1.2NA water immersion objective lens (Fig. 2c), it was possible to visualize relevant structures of the chorionic villi, such as the apical layer of syncytio-trophoblastic cells, and the abundant fetal capillaries. Arguably, in this study, the absence of maternal red blood cells in the intervillous space can be attributed to the rinsing steps carried out along with the sample collection (see Materials and Methods). Figure 2c also allows the visualization of multinucleated cell aggregates that resemble the syncytial knots usually deported onto the maternal blood at different stages of the pregnancy[42]. Notably, the membrane marker not only allowed for an overall view of the tissue (Fig. 2b, c) but also enabled the distinction between adjacent cells such as a cytotrophoblast cell and a syncytiotrophoblast cell (white box in Fig. 2c and magnified view in Fig. 2d). Moreover, the observed F-actin signal (Fig. 2e) matched the locations reported in a previous study[43], allowing the identification of the microvilli brush border, the syncytiotrophoblastic's basal cell surface, and the capillary endothelial cells.

The cross-sectional dimensions of the Tokuyasu sections (typically ranging between 300 μm × 300 μm and 500 μm × 500 μm) perfectly suited the waveguide dimensions of the photonic chip used in this work. This configuration allows both complete imaging of the sample through a single optical waveguide and also supports independent illumination of adjacent waveguides on the chip with different tissue sections (Fig. 1b). This eliminates undesired excitation light of the samples outside the imaging region of interest, hence minimizing photo-bleaching. Moreover, the PDMS chambers (Fig. 1b) allowed multi-well experiments similarly to traditional microscope chamber slides, with the additional advantage of reducing the incubation volumes to ~10 to 20 μL per chamber, which translated into a cost-reduction of the fluorescence assays. After optimizing the sample preparation and imaging steps (see Optimization steps for successful on-chip tissue imaging), we were able to both fluorescently label and acquire chip-TIRFM images of placental tissue within a timeframe of three hours from cryosectioning to image post-processing. We also attempted chip-TIRFM imaging of formalin-fixed paraffin-embedded (FFPE) placental tissue sections (see Supplementary Information S10). While results were promising, we faced sample detachment issues that hampered the visualization of the overall FFPE slide. The optimization of these challenges will be carried out in a subsequent study.

For diffraction-limited imaging of tissue samples, such as shown in Fig. 2, the evanescent field illumination supported by TIRFM is not necessary. However, as it will be evident in further sections, for super-resolution methods such as SMLM and IFON the evanescent illumination generated by the photonic chip configuration
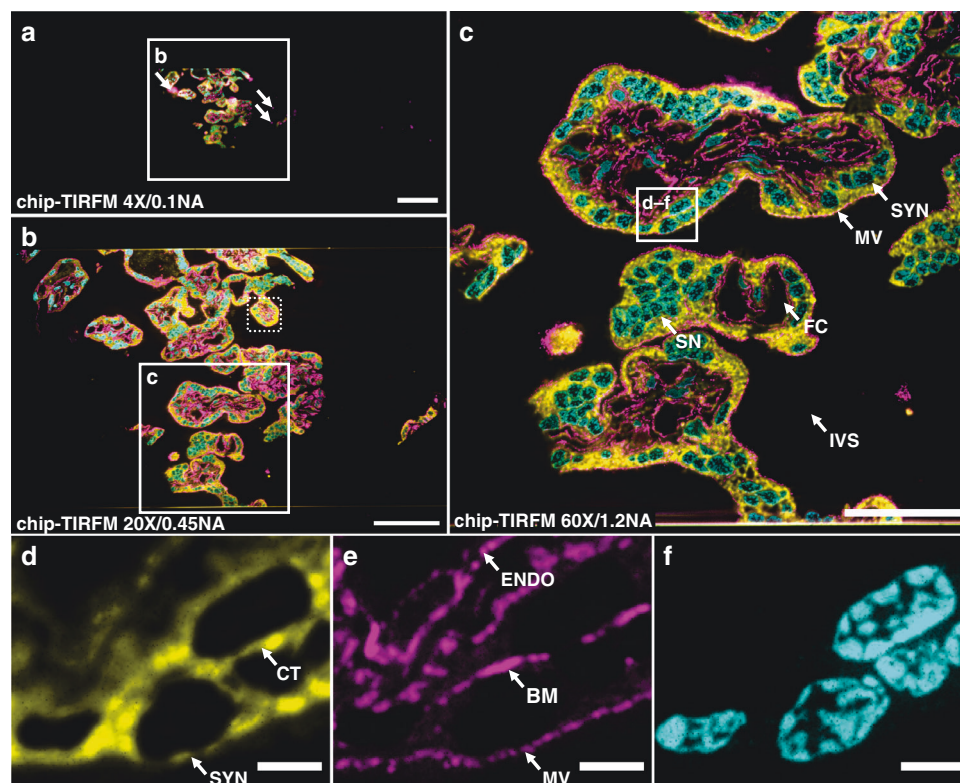
Fig. 2 Chip-based multicolor TIRFM imaging of a 400 nm placental tissue section prepared by Tokuyasu method. Membranes labeled with CellMask Deep Red (pseudo-colored in yellow), F-actin labeled with Phalloidin-Atto565 (pseudo-colored in magenta), and nuclei labeled with Sytox Green (pseudo-colored in cyan). **a** Large field of view chip-based multicolor TIRFM image acquired with a 4X/0.1NA microscope objective. The white arrows indicate the locations of unspecific binding of the F-actin marker to the waveguide. The white box represents the area imaged with a higher magnification objective lens in (**b**). **b** Chip-based multicolor TIRFM image acquired with a 20X/0.45NA microscope objective. The white box represents the area subsequently imaged with a higher magnification objective lens in (**c**). The white-dotted box illustrates the maximum field of view (50 μm × 50 μm) attainable in a conventional TIRFM setup. **c** Multicolor chip-TIRFM image acquired with a 60X/1.2NA microscope objective allows the identification of morphologically relevant structures of the chorionic villi such as the syncytiotrophoblastic cells (SYN), fetal capillaries (FC), syncytial knots (SN), and intervillous space (IVS) without maternal red blood cells due to thorough rinsing during sample preparation. The white box corresponds to the individual channels magnified in (**d**–**f**). **d** A magnified view of the membrane signal allows the distinction between a SYN and a cytotrophoblastic cell (CT). **e** A magnified view of the F-actin signal conforms to the expected location for this marker, in places such as the microvilli brush border (MV), the SYN's basal membrane (BM), and the capillary endothelial cell (ENDO). **f** Magnified view of syncytial and cytotrophoblast nuclei. Scale bars **a** 200 μm, **b** 100 μm, c 50 μm, **d**, **e** 5 μm

plays a key role in supporting optical sectioning of the specimen, reducing the out-of-focus light, increasing the signal-to-background ratio, and improving the axial resolution. Conventional TIRFM setups use oil-immersion high numerical aperture (N.A. 1.47–1.50) and high-magnification objective lenses (60X–100X) that limit their field of view to around 50 μm × 50 μm (ref. [26]) (dotted box in Fig. 2b). On contrary, the photonic chip-based TIRFM setup allows the use of essentially any imaging objective lens for the collection of the fluorescent signal, achieving scalable resolution and magnification on demand and opening possibilities for large TIRFM imaging areas up to the mm² scale (Fig. 2a, b). To this extent, the photonic chip-based TIRFM technique has the potential to outperform traditional ways of generating an evanescent field, which can be exploited for super-resolution imaging, as detailed in the next sections.

Chip-based SMLM imaging

In the previous section, we demonstrated the suitability of the photonic chip for diffraction-limited TIRFM imaging of tissues. Here, we explored on-chip super-resolution imaging of tissue samples using single-molecule localization microscopy (SMLM)[7]. SMLM comprises a set of methods that exploit the stochastic activation of individual fluorescent molecules to enable their precise localization within a sub-diffraction limited region. To achieve this, the fluorescent molecules are manipulated to obtain sparse blinking events over time. In practice, the majority of the fluorophores are switched off

(not emitting light), while only a small segment of them is switched on (emitting fluorescence). This implies the collection of several thousands of frames for the localization of the individual molecules in the sample.

There exist multiple variants of SMLM employing diverse switching mechanisms. Among them, the direct stochastic optical reconstruction microscopy (dSTORM) method supports conventional fluorophores, delivers a high photo-switching rate, and offers low photobleaching[44]. To explore the capabilities of the photonic chip for SMLM on histological samples, we used a 400 nm thick mouse kidney cryosection. We employed a dSTORM approach to visualize the nanostructural morphology of the filtration compartments present in the renal tissue, called glomeruli, whose physical dimensions are typically beyond the resolution limit of conventional optical microscopy and, therefore, often studied through electron microscopy.

The membranes and the nuclei were fluorescently stained with CellMask Deep Red and Sytox Green, respectively. All the preparation steps were performed identically to the chip-based multicolor TIRFM imaging experiments, except for the mounting medium that consisted of a water-based enzymatic oxygen scavenging system buffer[23,26] (see details in Supplementary Information S6). This oxygen scavenging buffer induces the blinking behavior by enhancing the probability of the fluorescent molecules to transition into the dark state, thereby contributing to the temporal sparsity of emission necessary for SMLM.

To find the features of interest, a TIRFM image of the sample was acquired (Fig. 3a) using low laser power to avoid photo-switching and reduce the chances of photobleaching. Next, the laser power was increased until sparse blinking was observed. The camera exposure time was set to around 30 ms to capture individual emission events of the membrane dye while the coupling objective was randomly scanned along the input facet of the chip. The collected image stack (>40,000 frames) was computationally processed to localize the spatial coordinates of the fluorophores, allowing for the reconstruction of a super-resolved image (Fig. 3b). A comparative view of both methods (Fig. 3c) reveals structural details in dSTORM that are not discernible in diffraction-limited TIRFM. In particular, dSTORM allows the visualization of a ~100 nm gap between the podocytes and the endothelial cells (see the empty gap between the white arrowheads in Fig. 3d, f), which is in agreement with the morphology of the glomerular basal membrane[45]. The identification of this feature, in particular, may be of critical value for a faster diagnosis of nephrotic diseases.

Chip-based SMLM/dSTORM supports three to fourfold resolution improvement over diffraction-limited imaging using a standard upright optical microscopy setup with a slight modification. Moreover, the chip-based SMLM/dSTORM approach benefits from the inherent advantage of decoupled illumination and collection light paths, which allows a user-defined choice of imaging objective lens without altering the TIRF excitation delivered by the chip. Recent advances in dye chemistry[46,47], in combination with further efforts in immunolabeling (see Supplementary Information S7 and S8) and system automation, could dramatically improve the imaging speed of chip-based SMLM, potentially assisting in the diagnostic of nephrotic diseases that, up to now, are identified via electron microscopy[48,49]. While chip-based illumination enables the imaging of large areas, the essential challenge of SMLM relies on the need for a large number of frames for the reconstruction of a super-resolved image. Therefore, for the practical implementation of chip-based microscopy in clinical settings, it is opportune to explore alternative imaging methods, e.g. IFON, with lower demands in the number of frames necessary for super-resolution.

Chip-based IFON imaging

To achieve a shorter acquisition time while maintaining imaging of large areas with improved contrast and resolution, we explored chip-based intensity fluctuation optical nanoscopy (IFON) of tissue samples. IFON comprises a set of techniques that exploit the photokinetic properties of fluorescent molecules to resolve structures beyond the diffraction limit of optical microscopes[14]. The techniques examine the stochastic emission of fluorophores through statistical analysis of the intensity levels of a given image stack, allowing the identification of fluorescent emitters with sub-pixel precision. Among the IFON techniques, the multiple signal classification algorithm (MUSICAL)[22] stands out as a promising tool for fast and reliable image reconstruction of biological data[14], achieving sub-diffraction resolution through low excitation intensities, fast acquisition, and relatively small datasets (100–1000 frames per image stack).

The main challenges to implementing IFON on histological samples are the high density and heterogeneity of the tissue samples. The spatiotemporal fluctuations are a decreasing function of the spatial density of the labels. In other words, a high density of labels results in a higher average signal at the cost of low variance in the fluorescence intensity over time. As a consequence, typically the IFON techniques are demonstrated on fine subcellular structures (e.g., actin filaments, microtubules, and mitochondria) fluorescently labeled on plated cells. Thus, densely labeled structures such as endoplasmic reticulum or lipid membranes are generally avoided. Tissue samples, with a higher density of labels, put even stronger demands on computational algorithms. Here, instead of relying only on the intrinsic fluctuations of the fluorophores, we
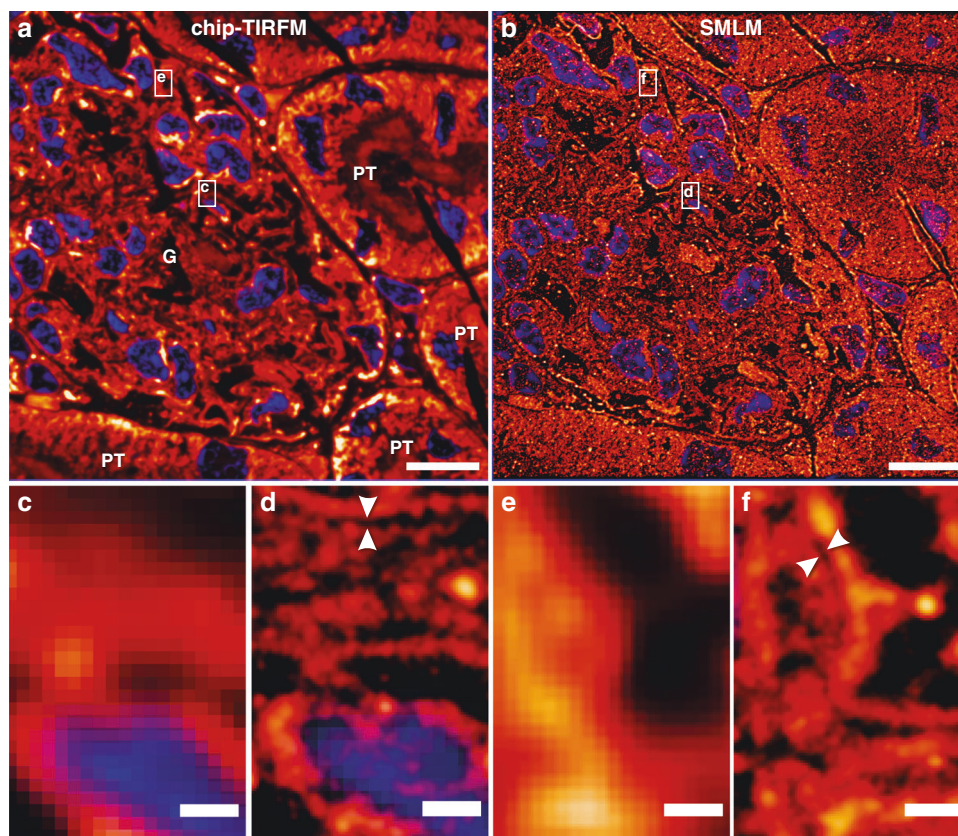
Fig. 3 Chip-based single-molecule localization microscopy of a 400 nm mouse kidney cryosection prepared by Tokuyasu method.
Membranes labeled with CellMask Deep Red (pseudo-colored in orange) and nuclei labeled with Sytox Green (pseudo-colored in blue). Images were collected using a 60X/1.2NA water immersion microscope objective. **a** Chip-TIRFM image of a glomerulus (G) surrounded by proximal tubuli (PT). **b** Chip-based SMLM image reconstructed with the dSTORM algorithm. **c–f** A magnified view of the white rectangles in (**a**, **b**) allows the comparison between the chip-TIRFM and dSTORM images. In particular, the white arrowheads in the SMLM segments show a separation of ~100 nm between cellular structures that are otherwise not observable in the TIRFM segments. Arguably, this nanostructural feature is in agreement with the dimensions of the glomerular basal membrane present in this filtration compartment of the kidney. Scale bars **a**, **b** 10 μm, **c** 500 nm

propose to exploit also the intensity variations induced by the multi-mode interference (MMI) pattern (speckle-like illumination) generated by the photonic chip (see Supplementary Information S3). In this approach, on-chip MMI illumination patterns are modulated over time by scanning the illumination spot over the waveguide input facet. This modulates the fluorescence emissions from the fluorophores with the spatial intensity distribution of the illumination pattern at any given time. Due to the constructive and destructive interferences, bright and dark regions are formed, artificially introducing sparsity in the spatiotemporal fluctuations. In addition, due to the high refractive index of the waveguide core ($n = 2.1$ for Ta_2O_5 and $n = 2$ for Si_3N_4), the MMI pattern obtained on top of the waveguide surface is sub-diffraction limit and thus carries higher spatial frequencies than what can be obtained using free-space optics[23]. Here, we used such on-chip engineered illumination for super-resolution imaging using the MUSICAL method.

To interrogate the capability of the photonic chip for IFON-based imaging of histological samples, we used chorionic villi tissue cryosections from the human placenta. For IFON studies, we focused on the visualization of nanostructural features in the microvilli. The microvilli are actin-based membrane protrusions that increase the contact area between the syncytiotrophoblastic cells and the maternal blood, facilitating the biochemical exchange between the maternal and the fetal side, and supporting mechano-sensorial functions of the placenta[50]. Due to the physical dimensions of these structures (on average, 100 nm in diameter and 500 nm in length[2,3]), and their tight confinement along the apical side of the syncytiotrophoblastic cells, the morphological features of the microvilli are not discernible through conventional optical microscopy and, therefore, represent an ideal element to benchmark the resolution possibilities offered by chip-based IFON.
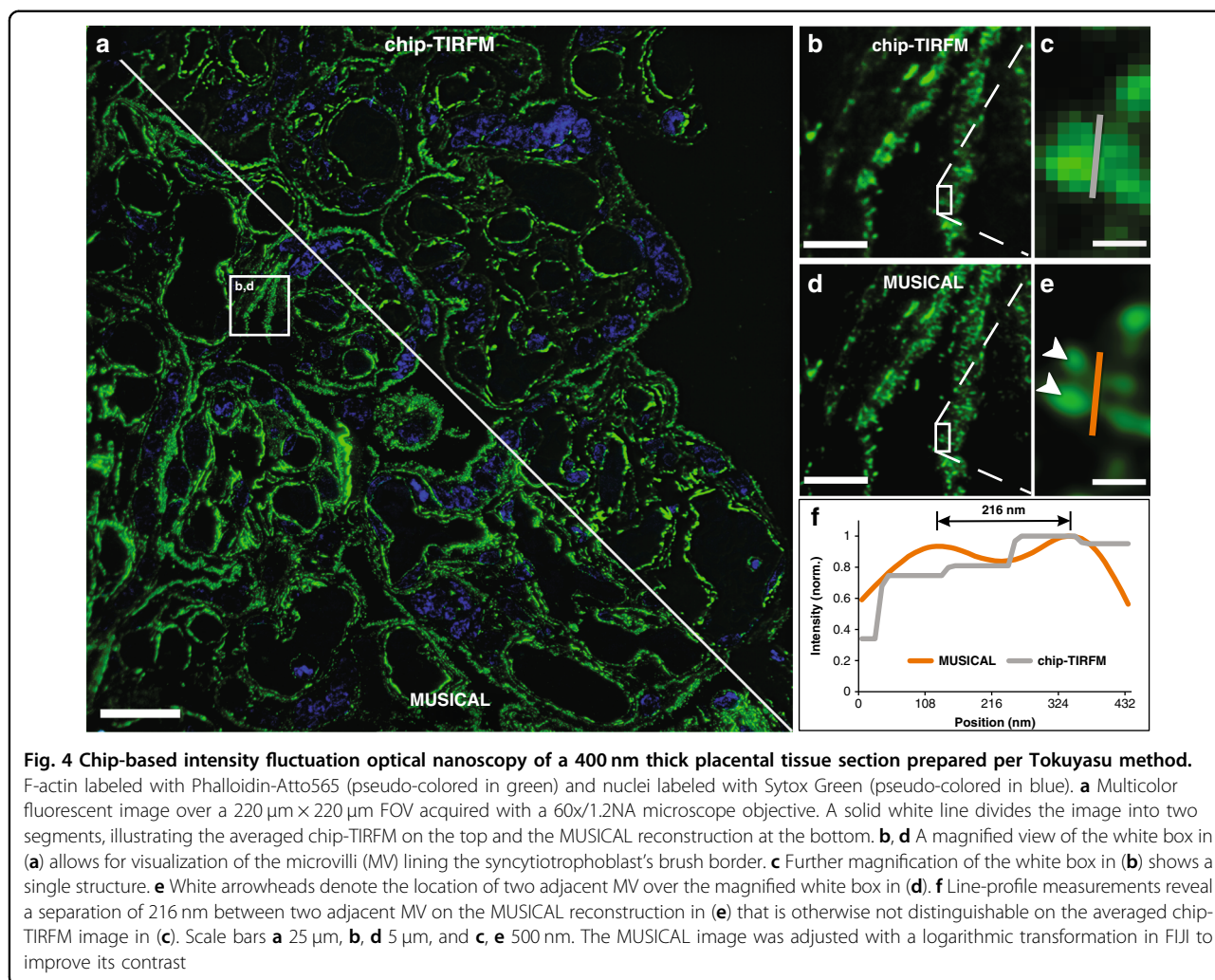
Fig. 4 Chip-based intensity fluctuation optical nanoscopy of a 400 nm thick placental tissue section prepared per Tokuyasu method. F-actin labeled with Phalloidin-Atto565 (pseudo-colored in green) and nuclei labeled with Sytox Green (pseudo-colored in blue). **a** Multicolor fluorescent image over a 220 μm × 220 μm FOV acquired with a 60x/1.2NA microscope objective. A solid white line divides the image into two segments, illustrating the averaged chip-TIRFM on the top and the MUSICAL reconstruction at the bottom. **b**, **d** A magnified view of the white box in (**a**) allows for visualization of the microvilli (MV) lining the syncytiotrophoblast's brush border. **c** Further magnification of the white box in (**b**) shows a single structure. **e** White arrowheads denote the location of two adjacent MV over the magnified white box in (**d**). **f** Line-profile measurements reveal a separation of 216 nm between two adjacent MV on the MUSICAL reconstruction in (**e**) that is otherwise not distinguishable on the averaged chip-TIRFM image in (**c**). Scale bars **a** 25 μm, **b**, **d** 5 μm, and **c**, **e** 500 nm. The MUSICAL image was adjusted with a logarithmic transformation in FIJI to improve its contrast

The samples were prepared and imaged with a 60X/1.2NA microscope objective following the steps described for Chip-based multicolor TIRFM imaging. To avoid unspecific background signal, only the F-actin and nuclei markers were used (Phalloidin-Atto565 and Sytox Green, respectively). Further, the 500-frames image stack corresponding to the F-actin was analyzed with MUSICAL, resulting in a super-resolved and improved contrast image over a field of view of 220 μm × 220 μm (Fig. 4a). The implementation of a soft thresholding scheme in MUSI-CAL[51] allowed the identification of individual microvilli along the syncytiotrophoblast's brush border (Fig. 4d), which were otherwise unclear in the averaged chip-TIRFM image (Fig. 4b). The resolution enhancement of MUSICAL was quantified in two different ways: (a) by performing line-profile measurements over two adjacent microvilli (Fig. 4c, e); and (b) by decorrelation analysis[52]. In the first case, the MUSICAL reconstruction (Fig. 4e) revealed a 216 nm separation between two microvilli, whereas the diffraction-limited chip-TIRFM image

(Fig. 4c) showed them as a single–merged–element. In the second case (see Supplementary Information S11), we were able to estimate a resolution of 195 nm on the MUSICAL reconstruction, compared to the 268 nm estimated for the chip-TIRFM counterpart. On-chip MUSI-CAL not only increases the resolution but improves the contrast of the image, which is a valuable parameter during visual investigations of tissue sections.

A recent study reported the visualization of individual microvilli with a twofold resolution improvement employing 3D-SIM[53]. Although several experts have proposed SIM as the fastest SRM technique for histological analysis[18,21,54,55], the typical FOV of this method with high-magnification microscope objectives (for example, 60X/1.42NA) is about 40 μm × 40 μm. Therefore, to match the same field of view achieved with the photonic chip, a tile mosaic of 7 × 7 SIM images would be required (see Supplementary Information S12). For conventional 3D-SIM, this not only implies a prolonged time for the data acquisition, but also a lengthy image

reconstruction that rounds up to 2.5 h. On contrary, the MUSICAL implementation we used here was able to obtain a high-resolution image over a large field of view within a combined collection and processing time of ~10 min for the 500-frames acquired on the photonic chip. While a 2D-SIM approach could potentially match, or even exceed, the acquisition and processing time of chip-based IFON, the photonic chip still outperforms 2D-SIM when it comes to the field of view size, system complexity, and cost.

From a practical perspective, the high-resolution visualization over large areas supported by chip-based IFON opens the door for improved assessment of placental microstructure both for basic research as well as for clinical assessment of placental dysfunctions associated with morphological changes in the microvilli, as documented in pre-eclampsia[2].

Chip-based CLEM imaging

Combining the specificity of fluorescence microscopy with the high resolution of electron microscopy allows the visualization of proteins of interest along with the ultrastructural context of the tissues. Although recent reports have proposed silicon wafers for correlative light and electron microscopy (CLEM)[56,57], they employed EPI-illumination through high-magnification microscope objectives, providing a limited field of view of the fluorescent signal. Here, we employed zebrafish eye retina cryosections of 110 nm thickness to demonstrate the compatibility of the chip platform with CLEM studies. Zebrafish is a well-established model for the study of retinal diseases[58]. The samples were prepared in the same manner as the placental and renal sections, except for the initial washing steps of the cryoprotectant. We found that the optimal washing temperature of the sucrose-methylcellulose solution for these samples was 0 °C, over an incubation time of 20 min (see detailed protocol in Materials and Methods). Three structures were labeled for the study: (a) the F-actin filaments, (b) the nuclei, and (c) the outer mitochondrial membrane. The first two structures were labeled through direct markers using Texas Red-X Phalloidin and Sytox Green, respectively, whereas the latter was labeled by immunofluorescence using rabbit anti-Tomm20 as a primary antibody, and Alexa Fluor 647-conjugated donkey anti-rabbit as a secondary antibody.

The samples were first imaged in chip-based TIRFM mode for each channel using a 60X/1.2NA to obtain a diffraction-limited multicolor image (Fig. 5a). Thereafter, the sections were platinum-coated and imaged on a scanning electron microscope over the same region of interest (Fig. 5b). A magnified view of the TIRFM image (Fig. 5c) allows for the observation of the F-actin filaments lining the outer segments of the photoreceptors

(in green), as well as the mitochondria clusters (in magenta), and the location of the nuclei (in cyan). The same TIRFM dataset is used for post-processing through MUSICAL, allowing for a precise correlation of both the F-actin and the mitochondrial signals with the corresponding SEM image (Fig. 5d–f).

Notably, the waveguide widths on the chip not only accommodated the whole zebrafish retina but also allowed the observation of several serial sections in a ribbon (see Supplementary information S14). Also, the combination of the thin section thickness of the Tokuyasu samples with the limited extent of the evanescent field dramatically improved the axial resolution of the fluorescent signal, enabling high-contrast images. Put together, these features are advantageous for confirming signal specificity throughout different subcellular compartments, opening up the possibility for 3D-stacking via serial section imaging[59,60]. Moreover, the flatness of the chip serves as an optimal platform for SEM, allowing autonomous imaging over large areas. A simple thin layer of platinum deposited on top of the chip minimizes the charging effects and enables a good correlation between the light and the electron microscopy images. Importantly, the photonic chip can incorporate coordinate landmarkings to facilitate the location and further correlation of the ROIs under study[36]. Lastly, the chip-based CLEM strategy presented here, in combination with the Tokuyasu method, can be executed within one working day from the sample sectioning steps to the SEM imaging, implying a significant time improvement as compared to the typical one-week imaging throughput associated with most CLEM approaches[41].

Optimization steps for successful on-chip tissue imaging

The experimental challenges of this study were mainly related to sample labeling and image acquisition. In the first place, the membrane tags investigated for labeling, namely CellMask Deep Red (CMDR), CellMask Orange (CMO), DiI, and DiO, showed high affinity to the photonic chip surface, inducing a high-background signal upon coupling of the excitation light onto the waveguides. Also, the combination of F-actin markers (Phalloidin-Atto647N, Phalloidin-Atto565) together with the CellMask family dyes (CMO and CMDR) led to the appearance of labeling artifacts in the form of dense spots (see white arrows in Fig. 2a), hampering the quality of the acquired images. We observed that after an initial bleaching step of the membrane dye (see Supplementary Information S4), the remaining fluorescent signal at the sample was generally stable through the image acquisition, allowing continuous imaging over prolonged time-scales (>5 min). We hypothesize that due to the exponential decay of the evanescent field (see Supplementary Information S1), the fluorophores in close
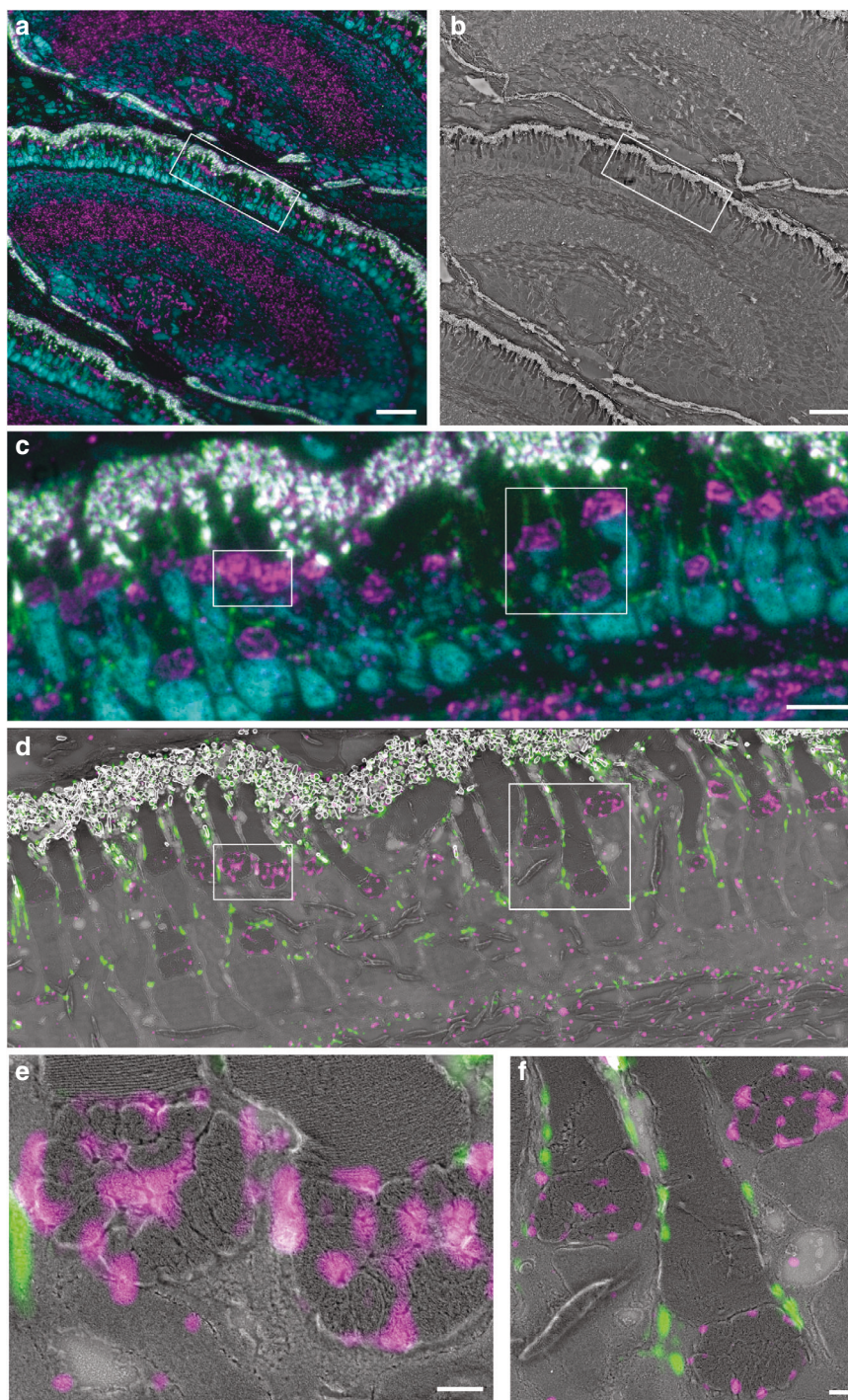
Fig. 5 Chip-based CLEM imaging of a 110 nm thick zebrafish retina cryosection prepared by Tokuyasu method on a 600 μm wide optical waveguide. a Diffraction-limited chip-TIRFM image. In magenta, mitochondrial clusters immunolabeled with rabbit anti-Tomm20 protein (primary antibody) and Alexa Fluor 647-conjugated donkey anti-rabbit (secondary antibody). In green, actin segments labeled with Texas Red-X Phalloidin. In cyan, nuclei labeled with Sytox Green. **b** Scanning electron microscope image of the same region shown in (**a**) scanned at 30 nm pixel size. **c** high-magnification image of the white frame in (**a**) showing the diffraction-limited chip-TIRFM signal of mitochondria, actin, and nuclei. **d** CLEM image of areas in frames (**a**) and (**b**). Scanning electron microscope image acquired at 4 nm pixel size correlates with the MUSICAL images of mitochondria (magenta) and actin (green). **e** CLEM image of the white region in (**d**). MUSICAL image of the Tomm20 signal (magenta) in the outer membrane of mitochondria correlating with the morphology of the complex clusters of mitochondria. The tightly packed membranes of the outer segment are clearly recognized.
f CLEM image of MUSICAL-processed actin signal along with the outer segments (green) and three mitochondria clusters. The MUSICAL signal in (**d**–**f**) were gamma-corrected to increase the contrast of the actin (γ = 1.2) and the Tomm20 signal (γ = 1.1). Scale bars **a**, **b** 20 μm, **c**, **d** 5 μm, **e**, **f** 500 nm

vicinity to the chip are more susceptible to irreversible photodamage than those located further away, hence allowing for localized bleaching at the waveguide-sample interface. Remarkably, no labeling artifacts were observed when F-actin markers were used separately from their membrane counterparts (see Figs. 4, 5).

Next, the decaying nature of the evanescent field showed troublesome for chip-based SMLM acquisition. We found that upon increasing the laser power necessary for SMLM, not only stochastic emission occurred (as desired), but also a spontaneous fluorescent emission remained present through the image acquisition, decreasing the signal-to-background and thus hindering the localization precision of the dSTORM algorithm. We argue that, while the laser intensity at the waveguide-sample interface was strong enough to induce the photo-switching of the selected marker (namely, the CMDR), the intensity at the tail of the evanescent field reaching deeper into the sample was too weak to enable photo-switching, yet sufficient enough to support spontaneous fluorescence emission. Also, due to the construct of our optical system, we observed a low photon count of the blinking molecules which further compromised the SMLM reconstruction. We foresee that further efforts could minimize the undesired background signal by (a) avoiding unspecific fluorophore binding via waveguide surface functionalization; (b) employing advanced labeling techniques such as on-chip point accumulation imaging in nanoscale topography (DNA-PAINT)[34] to ensure low background signal; (c) employing thinner tissue samples (~100 nm) to fully exploit the maximum intensities of the evanescent field; (d) modifying the optical setup to improve the photon collection at the camera sensor. When it comes to improving the optical setup, replacing the current beam splitters with dichroic mirrors would allow a higher transmission rate for the emission spectrum of the fluorescent markers (see Supplementary Information S13).

We also encountered initial challenges obtaining consistent labeling repeatability. In particular, we observed significant variability in the staining quality throughout this study, even after following identical labeling protocols across various experiments. We found that the sucrose-methylcellulose droplet (used for the collection of the slices after cryosectioning) was masking the binding sites on the samples, thus reducing the antigenicity of the targeted proteins. We solved this issue by adjusting the initial washing steps of the cryoprotectant until successful staining was obtained. To this, different temperatures and incubation times were explored, according to existing preparation guidelines for Tokuyasu cryosections[57,61–63]. Hence, the samples for chip-based TIRFM, IFON, and SMLM were optimally labeled following incubation in phosphate-buffered saline (PBS) at 37 °C for 30 min, while the samples for chip-based CLEM were successfully stained after incubation in PBS at 0 °C for 20 min (see Supplementary Information S2).

Lastly, sectioning artifacts in the form of knife marks, tissue folds, and tissue rupture were also observed along with this study (see Supplementary Information S5). These problems were resolved by ensuring optimum blade sharpness on the cryo-ultramicrotome and by adjusting both the sectioning temperature and the slice thickness for each tissue type.

Discussion

In this study, we demonstrated the capabilities of the photonic chip as a feasible imaging platform for the morphological assessment of thin Tokuyasu sections of a variety of tissues. The photonic chip-based microscopy technique offers several advantages for histology: (a) it allows a broad range of imaging modalities over large fields of view including TIRFM, SMLM, IFON, and CLEM using a single standard optical microscope setup; (b) the imaging process can be seamlessly performed on conventional optical microscopes upon some modifications; (c) the photonic chip withstands all the chemical incubations and thermal conditions associated with the sample preparation. These features make the photonic chip an attractive platform for fluorescence-based histological investigations where high-throughput, high-contrast, and high-resolution are essential for the study of diseases[21]. In particular, we anticipate that upon specific labeling and image processing efforts, the photonic chip could assist both in reducing the processing time and in improving the assessment quality of histopathological analyses requiring sub-diffraction resolution. Despite optical nanoscopy probably not replacing the EM in these cases, we foresee that, by enabling more affordable and flexible imaging capabilities in terms of multi-modality and high-throughout, chip-based microscopy could potentially widen the adoption of optical nanoscopy for the diagnosis of diseases. Additionally, in CLEM experiments, the photonic chip could be used for fast assessment of ultrastructural preservation in tissues.

The photonic chip approach also reduces the complexity of the optical nanoscopy setups by miniaturization of the excitation light path, simplifying the implementation of multimodal imaging and facilitating a larger adoption of super-resolution microscopy in clinics and hospitals. In addition, the photonic chip can be mass-produced through standard semiconductor lithography processes, benefitting from low-cost manufacturing scalability. We foresee that further developments in coupling automation and the integration of microfluidics systems could dramatically improve the performance of the photonic chip platform, enabling more efficient and repeatable labeling, as well as fast multiplexed imaging.

Moreover, the implementation of advanced labeling strategies such as DNA-PAINT[34] and Exchange-PAINT[64] can effectively reduce the background signal, improve resolution, and support multiplexed acquisition. Also, on-chip technology facilitates the integration of other on-chip optical functions such as Raman spectroscopy[65], waveguide trapping[66], microfluidics[67], phase microscopy[27], among others.

While the photonic chip illumination strategy allows excitation over large areas, e.g., several centimeters in the present case, the light collection area is presently limited by the collection objective lens. Thus, it can be envisioned that the integration of microlens arrays[68] for light collection will open avenues that would make on-chip technology capable of handling the high-throughput imaging needed for routine histopathology. Moreover, the photonic chip can be designed and manufactured into standard microscope glass slide dimensions, allowing for a fully automated sample preparation through commercially available immunoassay analyzers, or via novel microfluidic techniques for multiplex immunofluorescence staining of clinically-relevant biomarkers[69].

Despite the encouraging imaging results obtained in this study, we acknowledge that the Tokuyasu samples represent a minority among the available histological methods. Also, we are aware that the maximum section area possible with the Tokuyasu cryosections (500 μm × 500 μm) may be insufficient for large-scale histopathological evaluation. However, this is an inherent limitation imposed by the sample preparation technique rather than the photonic chip imaging surface. Future chip-based histology studies should address the compatibility of this microscopy platform with widely accessible samples including FFPE and cryostat-sliced sections. Further, as stated in the CLEM section, chip-based microscopy can be exploited for volumetric observations of tissue sections via 3D-stacking of serial section imaging[59,60].

Materials and methods
Photonic chip description and fabrication

The photonic chip is composed of three layers: (i) a bottom silicon (Si) substrate, (ii) an intermediate cladding of silicon dioxide (SiO_2), and (iii) a top waveguide layer of a high refractive index material made of either silicon nitride (Si_3N_4, $n = 2.0$) or tantalum pentoxide (Ta_2O_5, $n = 2.1$) (see Fig. 1a). The high refractive index contrast (HIC) between the waveguide materials and the adjacent imaging medium and sample ($n \approx 1.4$), allows the confinement and propagation of the excitation light via total internal reflection (TIR), enabling chip-based total internal reflection fluorescence microscopy (chip-TIRFM) (Fig. 1c). Diverse geometries have been previously studied for chip-TIRFM, including slab, rib, and strip waveguides[23].

Here, we chose uncladded strip waveguides with heights ranging from 150 to 250 nm and widths varying from 200 to 1000 μm (see Fig. 1b).

In this study, we used both Si_3N_4 and Ta_2O_5 chips for chip-TIRFM imaging of tissue sections. While both materials exhibit similar optical and biocompatibility properties, the selection between Si_3N_4 and Ta_2O_5 was made purely on the availability of either type of chips. These were fabricated in distinct places: (i) the Si_3N_4 waveguide chips were manufactured according to CMOS fabrication process at the Institute of Microelectronics Barcelona (IMB-CNM, Barcelona, Spain) as detailed elsewhere[23,24]; (ii) the Ta_2O_5 chips were manufactured at the Optoelectronics Research Center (ORC, University of Southampton, UK), following the process herewith detailed[70]. Waveguides of 250 nm thickness were fabricated by deposition of Ta_2O_5 film on a commercially available 4" Si substrate having a 2.5 μm thick SiO_2 lower cladding layer (Si-Mat Silicon Materials, Germany) using a magnetron sputtering system (Plasmalab System 400, Oxford Instruments). The base pressure of the Ta_2O_5 deposition chamber was kept below 1×10^{-6} Torr with $Ar:O_2$ flow rates of 20 sccm: 5 sccm and the substrate temperature was maintained at 200 °C throughout the deposition process. Photolithography was used to create a photoresist mask for further dry etching to fabricate strip waveguides. First, 1 μm thick positive resist (Shipley, S1813) was coated on top of a 250 nm Ta_2O_5 film and then prebaked (1×30 min) at 90 °C. Then, the wafer was placed into a mask aligner (MA6, Süss MicroTec), and illuminated with the waveguide pattern. The Ta_2O_5 layer, which was not covered with photoresist, was fully etched to obtain strip waveguides of 250 nm height using an ion beam system (Ionfab 300+, Oxford Instruments) fed with argon at a flow rate of 6 sccm. The process pressure (2.3×10^{-4} Torr), beam voltage (500 V), beam current (100 mA), radiofrequency power (500 W), and substrate temperature (15 °C) were kept constant. Finally, the wafers were placed in a three-zone semiconductor furnace at 600 °C in an oxygen environment for 3 h (in batch) to reduce the stress and supplement the oxygen deficiency created in Ta_2O_5 during the sputtering and the etching process[31].

Upon reception, the wafers were split into individual chips using a cleaving system (Latticegear, LatticeAx 225). The remaining photoresist layer from the manufacturing process was removed by immersion in acetone (1×1 min). The chips were then cleaned in 1% Hellmanex in deionized water on a 70 °C hotplate (1×10 min), followed by rinsing steps with isopropanol and deionized water. The chips were finally dried with nitrogen using an air blowgun. To improve the adhesion of the tissue sections, the chips were rinsed with 0.1% w v^{-1} poly-L-lysine solution in H_2O and let dry in a vertical position (1×30 min).

Sample collection and preparation
Ethical statement

Both animal and human samples were handled according to relevant ethical guidelines. Healthy placental tissues were collected after delivery at the University Hospital of North Norway. Written consent was obtained from the participants following the protocol approved by the Regional Committee for Medical and Health Research Ethics of North Norway (REK Nord reference no. 2010/2058-4). Human kidney samples were anonymously obtained with written consent from the patients according to the protocol approved by the Regional Committee for Medical and Health Research Ethics of North Norway (REK Nord reference no. 2014/1693-1). Treatment and care of mice and pigs were conducted following the guidelines of the Norwegian Ethical and Welfare Board for Animal Research. Zebrafish experiments were conducted according to Swiss Laws and approved by the veterinary administration of the Canton of Zurich, Switzerland.

Preparation of Tokuyasu sections for chip-based TIRFM, IFON, and SMLM

Human placental and murine (NZBxNZW)F1 kidney tissue samples were cryopreserved following the Tokuyasu method for ultracryotomy described elsewhere[53,71]. In short, biopsies blocks of ~1 mm³ were collected, rinsed in 9 mg mL⁻¹ sodium chloride, fixed in 8% formaldehyde at 4 °C overnight, infiltrated with 2.3 M sucrose at 4 °C overnight, mounted onto specimen pins, and frozen in liquid nitrogen. Thereafter, the samples were transferred to a cryo-ultramicrotome (EMUC6, Leica Microsystems) and sectioned with a diamond knife into thin slices ranging from 100 nm to 1 μm thickness. The sections were collected with a wire loop containing a 1:1 cryoprotectant mixture of 2% methylcellulose and 2.3 M sucrose and transferred to photonic chips coated with poly-L-lysine and equipped with custom-made polydimethylsiloxane (PDMS) chambers of approximately 130 μm-height[24] (Fig. 1b). The samples were stored on Petri dishes at 4 °C before subsequent steps.

Diverse staining strategies were employed according to each imaging modality:

i. For Chip-based multicolor TIRFM imaging, human placental sections of 400 nm were direct-labeled for membranes, F-actin, and nuclei as described herewith. First, the cryoprotectant mixture was dissolved by incubating the samples in phosphate-buffered saline (PBS) (3 × 10 min) at 37 °C. Thereafter, the samples were incubated in a 1:2000 solution of CellMask Deep Red in PBS (1 × 15 min) at room temperature (RT) and subsequently washed with PBS (2 × 5 min). Next, the sections were incubated in 1:100 Phalloidin-Atto565 in PBS (1 × 15 min) and washed with PBS (2 × 5 min). Further, the samples were incubated in 1:500 Sytox Green in PBS (1 × 10 min) and washed with PBS (2 × 5 min). Finally, the sections were mounted with #1.5 coverslips using Prolong Diamond and sealed with Picodent Twinsil.

ii. For Chip-based SMLM imaging, mouse kidney cryosections of 400 nm were labeled for membranes and nuclei using CellMask Deep Red and Sytox Green, respectively, following identical concentrations and incubation steps as for the Chip-based multicolor TIRFM imaging experiments. To enable photo-switching of the fluorescent molecules, the samples were mounted with a water-based enzymatic oxygen scavenging system buffer as described in previous works[23,26]. Thereafter, the sections were covered with #1.5 coverslips and sealed with Picodent Twinsil.

iii. For Chip-based IFON imaging, human placental sections of 400 nm were prepared identically to the Chip-based multicolor TIRFM imaging experiment, except for the membrane labeling and subsequent washing steps that were omitted. In all cases, the labeled cryosections were stored at 4 °C and protected from light before imaging. Supplementary Information S6 provides a detailed description of the materials and reagents used in this protocol.

Preparation of Tokuyasu sections for chip-based CLEM

For Chip-based CLEM imaging, zebrafish eyes were prepared as described elsewhere[56]. Briefly, 5 days post-fertilization larvae were euthanized in tricaine and fixed with 4% formaldehyde and 0.025% glutaraldehyde in 0.1 M sodium cacodylate buffer (1 × 16 h) at 4 °C. Subsequently, eyes were dissected and washed in PBS, placed in 12% gelatin (1 × 10 min) at 40 °C, and finally left to harden at 4 °C. Embedded eyes were immersed in 2.3 M sucrose and stored at 4 °C before further storage in liquid nitrogen. Ultrathin sections of 110 nm thickness were obtained with a cryo-ultramicrotome (Ultracut EM FC6, Leica Microsystems) using a cryo-immuno diamond knife (35° - size 2 mm, Diatome). The cryosections were transferred to photonic chips fitted with a PDMS frame and stored at 4 °C before staining. The samples were incubated in PBS (1 × 20 min) at 0 °C, followed by two washing steps in PBS (2 × 2 min) at RT to dissolve the cryoprotectant. Then, the samples were preincubated with a blocking solution (PBG) for 5 min, followed by incubation (1 × 45 min) in a 1:50 solution of rabbit anti-Tomm20 in PBG blocking buffer at RT. After several rinsing (6 × 2 sec) and washing (1 × 5 min) in PBG, the specimens were incubated (1 × 45 min) with an Alexa Fluor 647-conjugated secondary donkey anti-rabbit antibody at 1:200 concentration in PBG at RT. For the acting staining, the samples were

washed in PBS (6 × 1 min), followed by incubation with Texas Red-X Phalloidin (1 × 10 min) at 1:50 concentration in PBS. After washes in PBS (2 × 5 min), the samples were incubated in a 1:500 solution of Sytox Green nuclear staining in PBS (1 × 10 min), followed by washes in PBS (2 × 5 min), and mounting with a 1:1 mixture of PBS and glycerol (49782, Sigma-Aldrich) and covered with a #1.5 glass coverslip before chip-TIRFM imaging. Supplementary Information S6 provides a detailed description of the materials and reagents used in this protocol.

Chip imaging and processing
Chip-based imaging
The chip-TIRFM setup was assembled using a modular upright microscope (BXFM, Olympus), together with a custom-built photonic chip module as shown in Fig. 1c and Supplementary Information S13. A fiber-coupled multi-wavelength laser light source (iChrome CLE, Toptica) was expanded and collimated through an optical fiber collimator (F280APC-A, Thorlabs) to fill the back aperture of the coupling MO (NPlan 50X/NA0.5, Olympus). Typical illumination wavelengths used were $\lambda_1 = 640$ nm, $\lambda_2 = 561$ nm, and $\lambda_3 = 488$ nm. Both the optical fiber collimator and the coupling objective were mounted on an XYZ translation stage (Nanomax300, Thorlabs) fitted with an XY piezo-controllable platform (Q-522 Q-motion, PI) for fine adjustments of the coupling light into the waveguides. The photonic chips were placed on a custom-made vacuum chuck fitted on an X-axis translation stage (XRN25P, Thorlabs) for large-range scanning of parallel waveguides. Fluorescent emission of the samples was achieved via evanescent field excitation upon coupling of the laser onto a chosen waveguide, as detailed elsewhere[23] (Fig. 1a, c). Various MO lenses were used to collect the fluorescent signal, depending on the desired FOV, magnification, and resolution (4X/0.1NA, 20X/0.45NA, and 60X/1.2NA water immersion). An emission filter set composed of a long-pass filter and a band-pass filter was used to block out the excitation signal at each wavelength channel (see Supplementary Information S13 for details). The emission signal passed through the microscope's 1X tube lens (U-TV1X-2, Olympus) before reaching the sCMOS camera image plane (Orca-flash4.0, Hamamatsu). Both the camera exposure time and the laser intensity were adjusted according to the experimental goal. For TIRFM imaging, the camera exposure time was set between 50 and 100 ms, and the input power was incrementally adjusted until the mean histogram values surpassed 500 counts. For SMLM, the acquisition time was set to 30 ms while the input power was set to its maximum level to enable photo-switching. Depending on the coupling efficiency, typical input powers were between 10 and 60% for TIRFM imaging, and between 90 to 100% for SMLM

imaging. To reduce photobleaching of the fluorescent markers, the image acquisition was sequentially performed from less energetic to more energetic excitation wavelengths. To deal with the anisotropic mode distribution of the multi-mode interference pattern at the waveguide, the coupling objective was laterally scanned at <1 μm steps over a 50–200 μm travel span along the input facet of the chip while individual images were taken. Image stacks of various sizes were acquired according to the imaging technique. Typically, 100–1000 frames for TIRFM and 30,000–50,000 frames for SMLM. White light from a halogen lamp (KL1600 LED, Olympus) was used for bright-field illumination to identify the regions of interest (ROI) through the collection objective. To reduce mechanical instability, the collection path of the system was fixed to the optical table, while the photonic chip module was placed onto a motorized stage (8MTF, Standa) for scanning across the XY directions. An optical table (CleanTop, TMC) was used as the main platform for the chip-TIRFM setup. Supplementary Information S13 offers a detailed description of the chip-TIRFM setup.

CLEM imaging
After chip-TIRFM imaging, both the coverslip and the PDMS frame were removed and the samples were fixed with 0.1% glutaraldehyde. Thereafter, the samples were incubated with methylcellulose followed by centrifugation at 4700 rpm (Heraeus Megafuge 40 R, Thermo Scientific) in a falcon tube. After drying (2 × 10 min) at 40 °C on a heating plate, the photonic chips were transferred to an electron beam evaporator (MED 020, Leica Microsystems). The specimen was then coated with platinum/carbon (Pt/C, 10 nm) by rotary shadowing at an angle of 8°[57]. Thereafter, the photonic chips were mounted on a 25 mm Pin Mount SEMclip (#16144-9-30, Ted Pella) and imaged at 4 nm pixel size with a scanning electron microscope (Auriga 40 CrossBeam, Carl Zeiss Microscopy) at a low-accelerating voltage (1.5 keV). Supplementary Information S14 illustrates various steps of SEM imaging on a photonic chip.

Image processing
The acquired frames were computationally processed on the open-source software Fiji[72] according to the desired imaging technique. To obtain diffraction-limited TIRFM images, the image stacks were computationally averaged using the Z Project tool. Thereafter, the averaged images were deconvolved with the DeconvolutionLab2 plugin[73], using a synthetic 2D point spread function (PSF) matching the effective pixel size of the optical system. Lastly, the Merge Channels tool was used to merge and pseudocolor independent averaged channels into a multicolor composite TIRFM image.

SMLM images were reconstructed using the thunder-STORM plugin[74]. For CLEM, the acquired TIRFM stacks were first processed with the NanoJ SRRF plugin[75] and then correlated with the EM images using the TrakEM2 plugin[76].

Author details
[1]Department of Physics and Technology, UiT The Arctic University of Norway, Klokkargårdsbakken N-9019, Tromsø, Norway. [2]Department of Clinical Medicine, Women's Health and Perinatology Research Group, UiT The Arctic University of Norway, Tromsø, Norway. [3]Department of Obstetrics and Gynecology, University Hospital of North Norway, Tromsø, Norway. [4]Center for Microscopy and Image Analysis, University of Zurich, Zürich, Switzerland. [5]Division of Cardiothoracic and Respiratory Medicine, University Hospital of North Norway, Tromsø, Norway. [6]Department of Clinical Medicine, Clinical Cardiovascular Research Group, UiT The Arctic University of Norway, Tromsø, Norway. [7]Department of Medical Biology, RNA and Molecular Pathology Research Group, UiT The Arctic University of Norway, Tromsø, Norway. [8]Division of Obstetrics and Gynecology, Department of Clinical Science, Intervention and Technology, Karolinska Institute, Stockholm, Sweden

Author contributions
BSA conceived the idea and supervised the project. LEVH. and VD planned and coordinated the experiments, performed sample labeling, chip-TIRFM imaging, and post-processing of the data. JCT, AA, and VD built the chip-based microscope setup. SA and KA performed MUSICAL reconstruction. DAC, VD, and LEVH. performed SMLM acquisition. DAC performed the dSTORM reconstruction. LEVH, JCT, and JMM performed chip-TIRFM imaging of the zebrafish eye. GB provided the zebrafish cryosections. GB, JMM, and UZ designed the experimental conditions for SEM imaging. JMM performed the SEM imaging for CLEM. FTD and AP respectively designed and fabricated the Ta_2O_5 photonic chips. GA provided the human placental sample. MN collected and preserved the human placental samples. GA and MN helped with the placental image interpretations. AMKH and KAF collected and preserved the mouse kidney tissue and assisted with the renal image interpretations. ÅBB collected and preserved the pig heart tissue and assisted with the cardiac image interpretation. LEVH. and VD analyzed the data, prepared the figures. LEVH, VD, and BSA wrote the manuscript. All authors contributed to writing and revising selected sections of the manuscript.

Conflict of interest
BSA has applied for a patent for chip-based optical nanoscopy and he is co-founder of the company Chip NanoImaging AS, which commercializes on-chip super-resolution microscopy systems.

References
1. Aeffner, F. et al. Digital microscopy, image analysis, and virtual slide repository. *ILAR J.* **59**, 66–79 (2018).
2. Redman, C. W. G. et al. Does size matter? Placental debris and the pathophysiology of pre-eclampsia. *Placenta* **33**, S48–S54 (2012).
3. Lange, K. Fundamental role of microvilli in the main functions of differentiated cells: outline of an universal regulating and signaling system at the cell periphery. *J. Cell. Physiol.* **226**, 896–927 (2011).
4. Unwin, P. N. T. & Zampighi, G. Structure of the junction between communicating cells. *Nature* **283**, 545–549 (1980).
5. Inaga, S. et al. Rapid three-dimensional analysis of renal biopsy sections by low vacuum scanning electron microscopy. *Arch. Histol. Cytol.* **73**, 113–125 (2011).
6. Micheva, K. D. & Smith, S. J. Array tomography: a new tool for imaging the molecular architecture and ultrastructure of neural circuits. *Neuron* **55**, 25–36 (2007).
7. Hell, S. W. et al. The 2015 super-resolution microscopy roadmap. *J. Phys. D Appl. Phys.* **48**, 443001 (2015).
8. Schermelleh, L., Heintzmann, R. & Leonhardt, H. A guide to super-resolution fluorescence microscopy. *J. Cell Biol.* **190**, 165–175 (2010).
9. Sahl, S. J., Hell, S. W. & Jakobs, S. Fluorescence nanoscopy in cell biology. *Nat. Rev. Mol. Cell Biol.* **18**, 685–701 (2017).
10. Heintzmann, R. & Huser, T. Super-resolution structured illumination microscopy. *Chem. Rev.* **117**, 13890–13908 (2017).
11. Willig, K. I. et al. STED microscopy reveals that synaptotagmin remains clustered after synaptic vesicle exocytosis. *Nature* **440**, 935–939 (2006).
12. Betzig, E. et al. Imaging intracellular fluorescent proteins at nanometer resolution. *Science* **313**, 1642–1645 (2006).
13. Rust, M. J., Bates, M. & Zhuang, X. W. Sub-diffraction-limit imaging by stochastic optical reconstruction microscopy (STORM). *Nat. Methods* **3**, 793–796 (2006).
14. Opstad, I. S. et al. Fluorescence fluctuations-based super-resolution microscopy techniques: an experimental comparative study. Preprint at *arXiv:2008.09195v1* (2020).
15. Booth, M. et al. Aberrations and adaptive optics in super-resolution microscopy. *Microscopy* **64**, 251–261 (2015).
16. Baschong, W., Suetterlin, R. & Laeng, R. H. Control of autofluorescence of archival formaldehyde-fixed, paraffin-embedded tissue in confocal laser scanning microscopy (CLSM). *J. Histochem. Cytochem.* **49**, 1565–1571 (2001).
17. Creech, M. K., Wang, J., Nan, X. & Gibbs, S. L. Superresolution imaging of clinical formalin fixed paraffin embedded breast cancer with single molecule localization microscopy. *Sci. Rep.* **7**, 40766 (2017).
18. Wang, M. et al. High-resolution rapid diagnostic imaging of whole prostate biopsies using video-rate fluorescence structured illumination microscopy. *Cancer Res.* **75**, 4032–4041 (2015).
19. Ilgen, P. et al. STED super-resolution microscopy of clinical paraffin-embedded human rectal cancer tissue. *PLoS ONE* **9**, e101563 (2014).
20. Göttfert, F. et al. Coaligned dual-channel STED nanoscopy and molecular diffusion analysis at 20 nm resolution. *Biophys. J.* **105**, L01–L03 (2013).
21. Schlichenmeyer, T. C., Wang, M., Elfer, K. N. & Brown, J. Q. Video-rate structured illumination microscopy for high-throughput imaging of large tissue areas. *Biomed. Opt. Express* **5**, 366–377 (2014).
22. Agarwal, K. & Macháň, R. Multiple signal classification algorithm for super-resolution fluorescence microscopy. *Nat. Commun.* **7**, 13752 (2016).
23. Diekmann, R. et al. Chip-based wide field-of-view nanoscopy. *Nat. Photonics* **11**, 322–328 (2017).
24. Tinguely, J. C., Helle, Ø. I. & Ahluwalia, B. S. Silicon nitride waveguide platform for fluorescence microscopy of living cells. *Opt. Express* **25**, 27678–27690 (2017).
25. Opstad, I. S. et al. A waveguide imaging platform for live-cell TIRF imaging of neurons over large fields of view. *J. Biophotonics* **13**, e201960222 (2020).
26. Helle, Ø. I. et al. Nanoscopy on-a-chip: super-resolution imaging on the millimeter scale. *Opt. Express* **27**, 6700–6710 (2019).
27. Dubey, V. et al. Multi-modal chip-based fluorescence and quantitative phase microscopy for studying inflammation in macrophages. *Opt. Express* **26**, 19864–19876 (2018).
28. Coucheron, D. A. et al. High-throughput total internal reflection fluorescence and direct stochastic optical reconstruction microscopy using a photonic chip. *J. Vis. Exp.* https://doi.org/10.3791/60378-v (2019).

29. Agnarsson, B., Jonsdottir, A. B., Arnfinnsdottir, N. B. & Leosson, K. On-chip modulation of evanescent illumination and live-cell imaging with polymer waveguides. *Opt. Express* **19**, 22929–22935 (2011).

30. Griffiths, G., Slot, J. W. & Webster, P. Kiyoteru Tokuyasu: a pioneer of cryo-ultramicrotomy. *J. Microsc.* **260**, 235–237 (2015).

31. Priyadarshi, A. et al. A transparent waveguide chip for versatile total internal reflection fluorescence-based microscopy and nanoscopy. *Commun. Mater.* **2**, 85 (2021).

32. Mittler, S. In *Optics, Photonics and Laser Technology* (eds Ribeiro, P. A. & Raposo, M.) Ch. 1 (Springer, 2018).

33. Jayakumar, N., Helle, Ø. I., Agarwal, K. & Ahluwalia, B. S. On-chip TIRF nanoscopy by applying Haar wavelet kernel analysis on intensity fluctuations induced by chip illumination. *Opt. Express* **28**, 35454–35468 (2020).

34. Archetti, A. et al. Waveguide-PAINT offers an open platform for large field-of-view super-resolution imaging. *Nat. Commun.* **10**, 1267 (2019).

35. Helle, Ø. I. et al. Structured illumination microscopy using a photonic chip. *Nat. Photonics* **14**, 431–438 (2020).

36. Tinguely, J. C. et al. Photonic-chip assisted correlative light and electron microscopy. *Commun. Biol.* **3**, 739 (2020).

37. Silini, A. R. et al. Perinatal derivatives: where do we stand? A roadmap of the human placenta and consensus for tissue and cell nomenclature. *Front. Bioeng. Biotechnol.* **8**, 610544 (2020).

38. Tokuyasu, K. T. A technique for ultracryotomy of cell suspensions and tissues. *J. Cell Biol.* **57**, 551–565 (1973).

39. Tokuyasu, K. T. A study of positive staining of ultrathin frozen sections. *J. Ultrastruct. Res.* **63**, 287–307 (1978).

40. Loussert-Fonta, C. et al. Correlation of fluorescence microscopy, electron microscopy, and NanoSIMS stable isotope imaging on a single tissue section. *Commun. Biol.* **3**, 362 (2020).

41. Kopek, B. G. et al. Diverse protocols for correlative super-resolution fluorescence imaging and electron microscopy of chemically fixed samples. *Nat. Protoc.* **12**, 916–946 (2017).

42. Askelund, K. J. & Chamley, L. W. Trophoblast deportation part I: review of the evidence demonstrating trophoblast shedding and deportation during human pregnancy. *Placenta* **32**, 716–723 (2011).

43. King, B. F. The organization of actin filaments in human placental villi. *J. Ultrastruct. Res.* **85**, 320–328 (1983).

44. van de Linde, S. et al. Direct stochastic optical reconstruction microscopy with standard fluorescent probes. *Nat. Protoc.* **6**, 991–1009 (2011).

45. Carlson, E. C. et al. Significant glomerular basement membrane thickening in hyperglycemic and normoglycemic diabetic-prone BB Wistar rats. *Anat. Rec. A Discov. Mol. Cell. Evol. Biol.* **281**, 1308–1318 (2004).

46. Chi, W. et al. Descriptor ΔGC-O enables the quantitative design of spontaneously blinking rhodamines for live-cell super-resolution imaging. *Angew. Chem.* **132**, 20390–20398 (2020).

47. Uno, S. N. et al. A spontaneously blinking fluorophore based on intramolecular spirocyclization for live-cell super-resolution imaging. *Nat. Chem.* **6**, 681–689 (2014).

48. Darouich, S. et al. Value of electron microscopy in the diagnosis of glomerular diseases. *Ultrastruct. Pathol.* **34**, 49–61 (2010).

49. Shore, I. & Moss, J. Electron microscopy in diagnostic renal pathology. *Curr. Diagnostic Pathol.* **8**, 207–215 (2002).

50. Miura, S. et al. Fluid shear triggers microvilli formation via mechanosensitive activation of TRPV6. *Nat. Commun.* **6**, 8871 (2015).

51. Acuña, S. et al. Soft thresholding schemes for multiple signal classification algorithm. *Opt. Express* **28**, 34434–34449 (2020).

52. Descloux, A., Grußmayer, K. S. & Radenovic, A. Parameter-free image resolution estimation based on decorrelation analysis. *Nat. Methods* **16**, 918–924 (2019).

53. Villegas-Hernández, L. E. et al. Visualizing ultrastructural details of placental tissue with super-resolution structured illumination microscopy. *Placenta* **97**, 42–45 (2020).

54. Wang, M. et al. Gigapixel surface imaging of radical prostatectomy specimens for comprehensive detection of cancer-positive surgical margins using structured illumination microscopy. *Sci. Rep.* **6**, 27419 (2016).

55. Johnson, K. A. & Hagen, G. M. Artifact-free whole-slide imaging with structured illumination microscopy and Bayesian image reconstruction. *GigaScience* **9**, giaa035 (2020).

56. Mateos, J. M. et al. Correlative super-resolution and electron microscopy to resolve protein localization in zebrafish retina. *J. Vis. Exp.* https://doi.org/10.3791/56113 (2017).

57. Mateos, J. M. et al. Topographic contrast of ultrathin cryo-sections for correlative super-resolution light and electron microscopy. *Sci. Rep.* **6**, 34062 (2016).

58. Link, B. A. & Collery, R. F. Zebrafish models of retinal disease. *Annu. Rev. Vis. Sci.* **1**, 125–153 (2015).

59. Reichelt, M. et al. 3D reconstruction of VZV infected cell nuclei and PML nuclear cages by serial section array scanning electron microscopy and electron tomography. *PLoS Pathog.* **8**, e1002740 (2012).

60. Arganda-Carreras, I., Fernández-González, R., Muñoz-Barrutia, A. & Ortiz-De-Solorzano, C. 3D reconstruction of histological sections: application to mammary gland tissue. *Microsc. Res. Tech.* **73**, 1019–1029 (2010).

61. Slot, J. W. & Geuze, H. J. Cryosectioning and immunolabeling. *Nat. Protoc.* **2**, 2480–2491 (2007).

62. van Rijnsoever, C., Oorschot, V. & Klumperman, J. Correlative light-electron microscopy (CLEM) combining live-cell imaging and immunolabeling of ultrathin cryosections. *Nat. Methods* **5**, 973–980 (2008).

63. Griffith, J. M. & Posthuma, G. A reliable and convenient method to store ultrathin thawed cryosections prior to immunolabeling. *J. Histochem. Cytochem.* **50**, 57–62 (2002).

64. Werbin, J. L. et al. Multiplexed exchange-PAINT imaging reveals ligand-dependent EGFR and Met interactions in the plasma membrane. *Sci. Rep.* **7**, 12150 (2017).

65. Løvhaugen, P., Ahluwalia, B. S., Huser, T. R. & Hellesø, O. G. Serial Raman spectroscopy of particles trapped on a waveguide. *Opt. Express* **21**, 2964–2970 (2013).

66. Helle, Ø. I., Ahluwalia, B. S. & Hellesø, O. G. Optical transport, lifting and trapping of micro-particles by planar waveguides. *Opt. Express* **23**, 6601–6612 (2015).

67. Wang, X. et al. Enhanced cell sorting and manipulation with combined optical tweezer and microfluidic chip technologies. *Lab Chip* **11**, 3656–3662 (2011).

68. Orth, A. & Crozier, K. Gigapixel fluorescence microscopy with a water immersion microlens array. *Opt. Express* **21**, 2361–2368 (2013).

69. Cappi, G., Dupouy, D. G., Comino, M. A. & Ciftlik, A. T. Ultra-fast and automated immunohistofluorescent multistaining using a microfluidic tissue processor. *Sci. Rep.* **9**, 4489 (2019).

70. Ahluwalia, B. S. et al. Fabrication of submicrometer high refractive index tantalum pentoxide waveguides for optical propulsion of microparticles. *IEEE Photonics Technol. Lett.* **21**, 1408–1410 (2009).

71. Fenton, K. et al. Anti-dsDNA antibodies promote initiation, and acquired loss of renal Dnase1 promotes progression of lupus nephritis in autoimmune (NZBxNZW)F1 mice. *PLoS ONE* **4**, e8474 (2009).

72. Schindelin, J. et al. Fiji: an open-source platform for biological-image analysis. *Nat. Methods* **9**, 676–682 (2012).

73. Sage, D. et al. DeconvolutionLab2: an open-source software for deconvolution microscopy. *Methods* **115**, 28–41 (2017).

74. Ovesný, M. et al. ThunderSTORM: a comprehensive ImageJ plug-in for PALM and STORM data analysis and super-resolution imaging. *Bioinformatics* **30**, 2389–2390 (2014).

75. Gustafsson, N. et al. Fast live-cell conventional fluorophore nanoscopy with ImageJ through super-resolution radial fluctuations. *Nat. Commun.* **7**, 12471 (2016).

76. Cardona, A. et al. TrakEM2 software for neural circuit reconstruction. *PLoS ONE* **7**, e38011 (2012).

Supplementary information

Chip-based multimodal super-resolution microscopy for histological investigations of cryopreserved tissue sections

Luis E. Villegas-Hernández[1,#], Vishesh Dubey[1,#], Mona Nystad[2,3], Jean-Claude Tinguely[1], David A. Coucheron[1], Firehun T. Dullo[1], Anish Priyadarshi[1], Sebastian Acuña[1], Azeem Ahmad[1], José M. Mateos[4], Gery Barmettler[4], Urs Ziegler[4], Åsa Birna Birgisdottir[5,6], Aud-Malin Karlsson Hovd[7], Kristin Andreassen Fenton[7], Ganesh Acharya[2,8], Krishna Agarwal[1], Balpreet Singh Ahluwalia[1,8,*]

[1] Department of Physics and Technology, UiT The Arctic University of Norway, Klokkargårdsbakken N-9019, Tromsø, Norway

[2] Department of Clinical Medicine, Women's Health and Perinatology Research Group, UiT The Arctic University of Norway, Tromsø, Norway

[3] Department of Obstetrics and Gynecology, University Hospital of North Norway, Tromsø, Norway

[4] Center for Microscopy and Image Analysis, University of Zurich, Zürich, Switzerland

[5] Division of Cardiothoracic and Respiratory Medicine, University Hospital of North Norway, Tromsø, Norway

[6] Department of Clinical Medicine, Clinical Cardiovascular Research Group, UiT The Arctic University of Norway, Tromsø, Norway

[7] Department of Medical Biology, RNA and Molecular Pathology Research Group, UiT The Arctic University of Norway, Tromsø, Norway

[8] Division of Obstetrics and Gynecology, Department of Clinical Science, Intervention and Technology, Karolinska Institute, Stockholm, Sweden

[#] These authors contributed equally to this work

[*] Corresponding author: balpreet.singh.ahluwalia@uit.no

S1. Evanescent field simulations

For the estimation of the waveguide parameters such as surface intensity and extent of evanescent field, simulations with Fimmwave (Photon Design) were performed for a strip waveguide having a width of 200 µm. Figure S1a shows the schematic diagram of a strip waveguide. The waveguides are fabricated on the SiO_2 coated Si substrate. Figure S1b shows the distribution of the fundamental TE mode along the width and core thickness of the waveguide structure. The coupled light propagates through the length of the waveguide generating an evanescent field on its top. The surface intensity of the evanescent field depends highly on the geometry of the waveguide, refractive index differences of the core and surrounding material, and the wavelength of the coupled light. Figure S1c shows the variation in surface intensity and relative depth of the evanescent field (penetration depth) as a function of core thickness. As the core thickness increases, the surface intensity decreases dramatically. The amplitude of the penetration depth also decreases with increasing core thickness and becomes almost stable after 150 nm. The simulation results allow choosing a core thickness between 150 nm and 250 nm for chip-TIRFM applications.
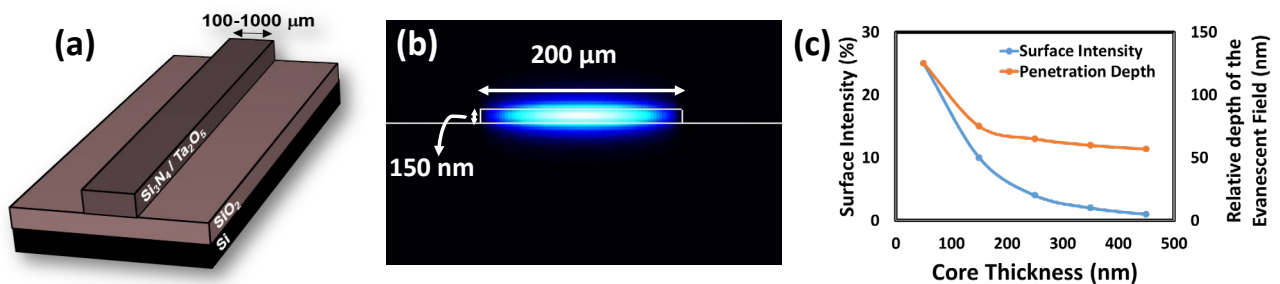

Figure S1. Evanescent field simulations on a Ta_2O_5 strip waveguide. (a) *Schematic diagram of a photonic chip with a strip waveguide core width varying from 100 µm to 1000 µm.* **(b)** *Simulated field distribution of a fundamental transverse electrical (TE) mode on a Ta_2O_5 waveguide of 200 µm wide and 150 nm thickness.* **(c)** *The strength (surface intensity) and the penetration depth of the evanescent field vary as a function of the waveguide thickness. The wavelength considered in the simulation corresponds to 561 nm and the waveguide core material Ta_2O_5.*

S2. Sample preparation work-flow for chip-TIRFM of Tokuyasu sections

Sample preparation plays a key role in the imaging outcome of chip-based microscopy. Figure S2 provides a schematic workflow of the preparation steps for chip-TIRFM imaging of placental cryosections per the Tokuyasu method. The protocol is based on an existing procedure for fluorescent labeling of Tokuyasu sections on glass coverslip[53]. From the orange-dotted line in Figure S2a, all the steps are optimized according to the specific needs of each sample. In particular, the washing steps of the cryoprotectant (step after orange box in Figure S2a) can be carried out at temperatures ranging from 0 °C to 37 °C.
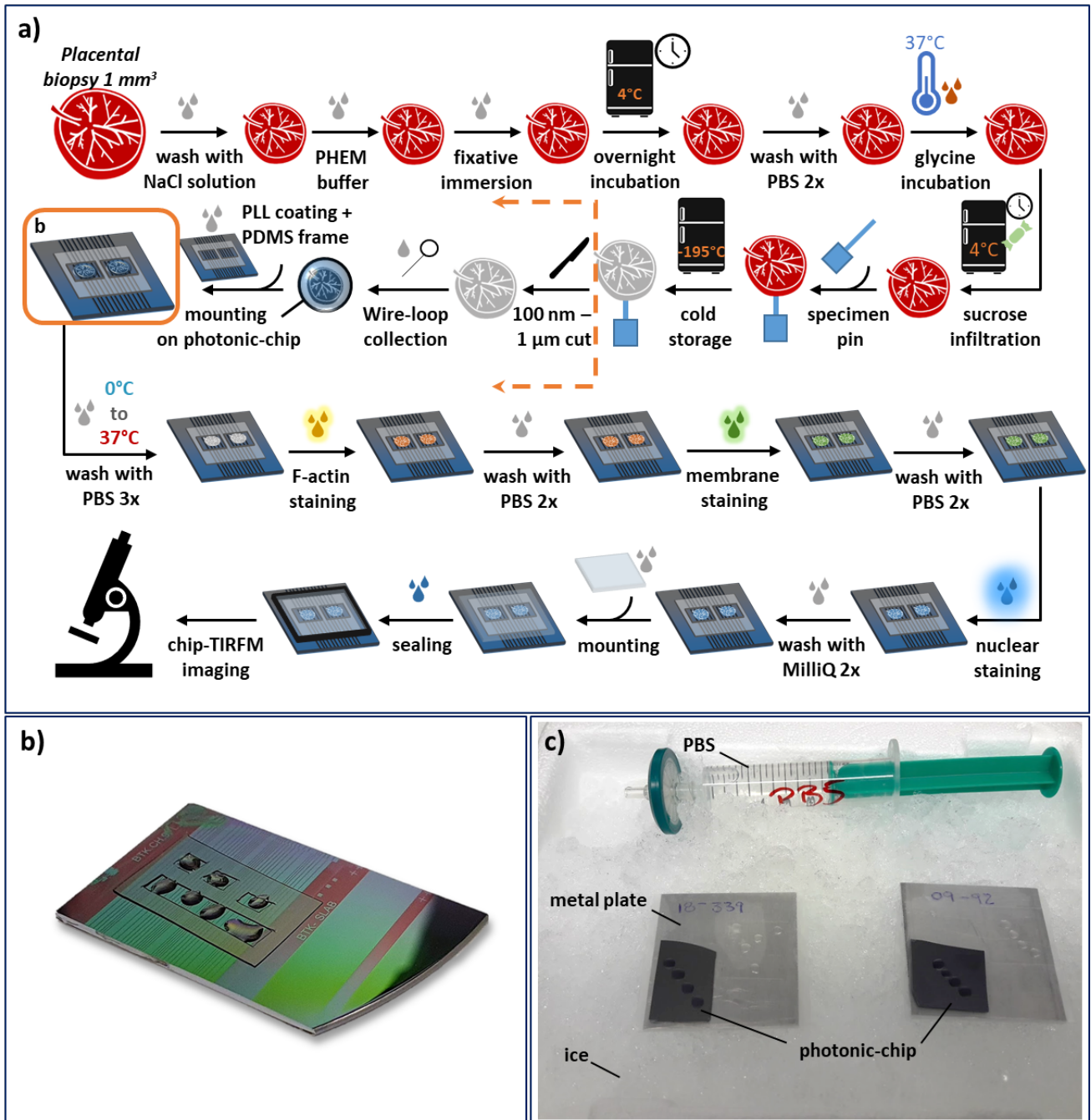

Figure S2. Sample preparation protocol for fluorescence staining of Tokuyasu cryosections on a photonic chip. (a) Schematic workflow of the sample preparation steps per the Tokuyasu method of a placental section. (b) Depiction of the orange box in (a) illustrating a photonic chip with Tokuyasu cryosections on top and surrounded by a custom-made PDMS frame. (c) The photonic chips are placed on top of metal plates on ice for the washing step in cold PBS following the orange box in (a).

S3. Mode-averaging for homogeneous illumination in chip-TIRFM imaging

The waveguides used for tissue imaging are wide, supporting the propagation of several light modes (Figure S3a). Upon coupling of the excitation beam onto the waveguide, a non-uniform intensity distribution is observed due to multiple mode interference (MMI) patterns (Figure S3b). These patterns change depending on the position of the coupling objective. To achieve isotropic illumination of the specimen, the coupling objective is scanned along the input facet of the chip while individual frames are acquired (Figure S3c). The collected image stack is averaged (Figure S3d) and then deconvolved (Figure S3e) to obtain a diffraction-limited chip-TIRFM image.

Interestingly, on-chip MMI patterns assist the IFON methods, especially for dense samples such as tissues. The spatio-temporal fluctuations from the sample are a decreasing function of the spatial density of the labels. For a dense tissue sample, this results in a higher average signal at the cost of low variance in the fluorescence intensity over time. This makes super-resolution imaging of tissue samples using IFON methods difficult. By using non-uniform MMI patterns not all regions (fluorophores) are excited at the same time, which helps to alleviate the issues with dense labeling. Furthermore, as these MMI patterns are generated inside the photonic chip, they carry high spatial frequencies due to the high refractive index of the waveguide material.
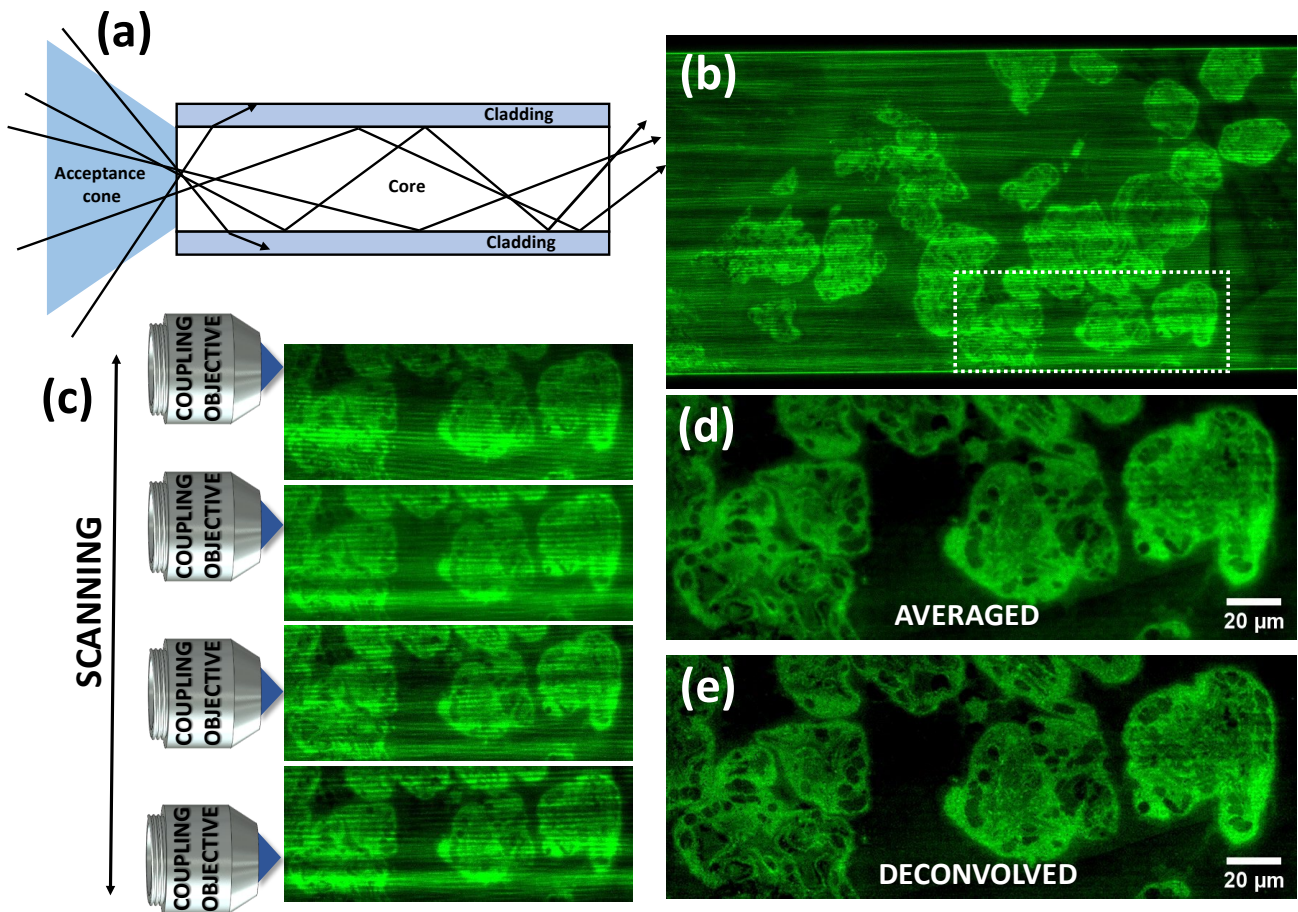

Figure S3. Mode-averaging for chip-TIRFM imaging of a 400 nm thick human chorionic villi cryosection. Membranes with CellMask Orange (pseudocolored in green). (a) Schematic diagram of a multi-mode waveguide supporting the propagation of multiple light modes. (b) Top view of a multi-mode pattern generated by the interference of multiple propagating light modes. (c) The excitation beam is scanned across the input facet of the waveguide while individual frames are collected (in this example four frames are illustrated). (d) The acquired stack is post-processed to obtain an averaged image with uniform intensity distribution. (e) The averaged image is deconvolved to obtain a high-contrast diffraction-limit chip-TIRFM image of the tissue section.

S4. Photobleaching of membrane markers

To obtain an overall view of tissue sections, a membrane marker is desired. However, membrane probes exhibit a high affinity to the photonic chip surface, resulting in strong absorption of the propagating light along the waveguide. This phenomenon not only limits the excitation intensity reaching the sample but also introduces an undesired background signal that hampers the quality of the chip-TIRFM imaging. To overcome this problem, the power of the excitation beam is temporarily increased to photobleach the fluorescent molecules in the vicinity of the imaging waveguide. Although the emission intensity at the sample location is also reduced, the fluorescent signal of the non-bleached molecules deeper in the sample remains stable through the image acquisition, allowing continuous illumination over prolonged timescales (> 5 min). Arguably, this phenomenon is due to the decaying nature of the evanescent field (see Supplementary Information S1). We hypothesize that, since the illumination intensity of the evanescent field is significantly higher at the interface between the coupled waveguide and the sample, the fluorophores in its close vicinity are more susceptible to irreversible photodamage. Further away from the waveguide, the fluorescent markers are exposed to lower excitation intensities and, consequently, less prone to photobleaching. Depending on the coupling efficiency and the geometry of the waveguide, the bleaching process can take a few seconds (2 – 10 sec), to around 1 min. Figure S4 shows a 400 µm wide waveguide containing a placental tissue cryosection labeled with CellMask Deep Red. Consecutive frames (1-5) illustrate diverse time points of the bleaching process over a fixed field of view.
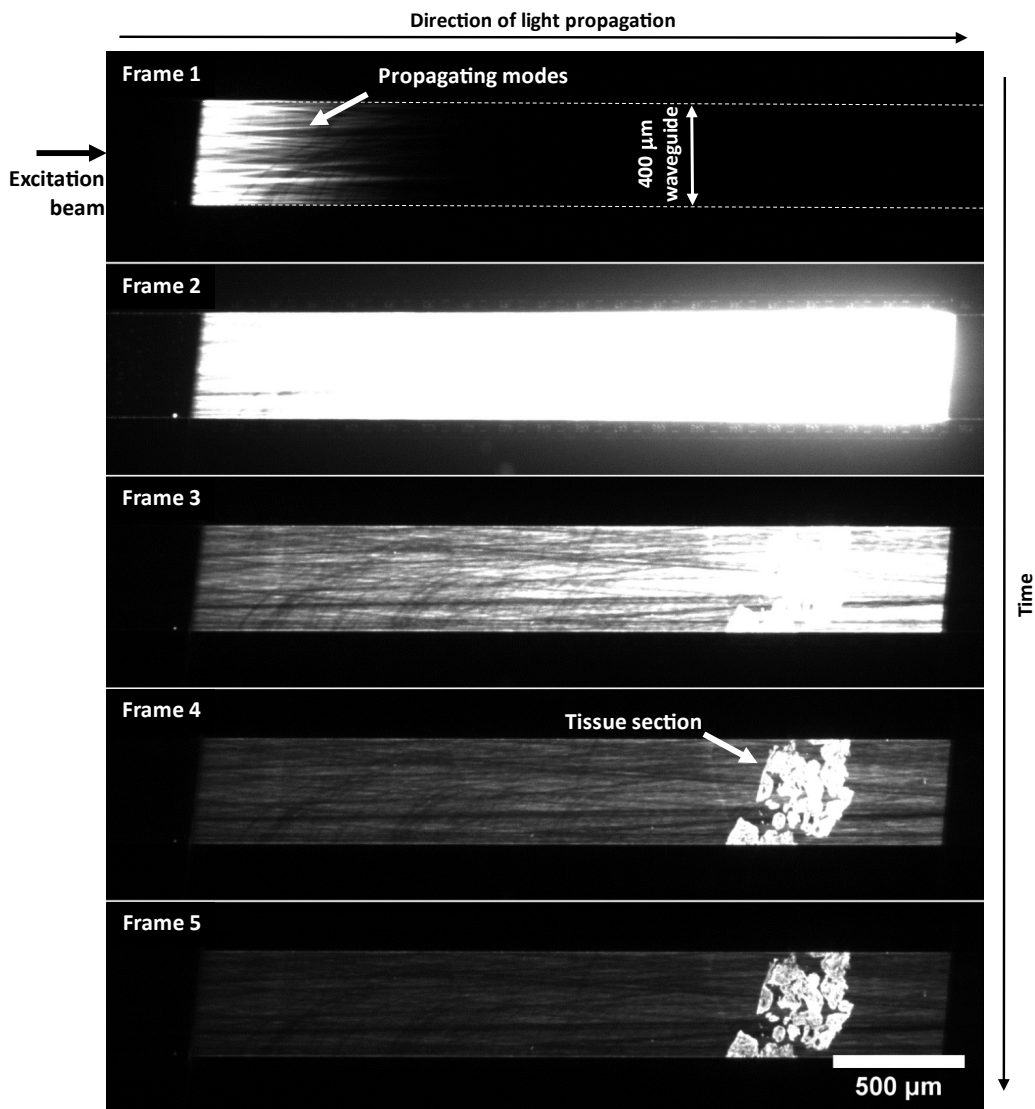

Figure S4. Photobleaching process of a membrane marker bind to a 400 µm waveguide. *The power of the excitation beam is temporarily increased to induce photobleaching of the fluorescent molecules in the vicinity of the waveguide (frame 1 to frame 3). After a few seconds, the tissue section is revealed (frame 3 to frame 4). Further bleaching dramatically reduces the background signal of the membrane marker, allowing for high-contrast chip-TIRFM imaging (frame 5).*

S5. Sectioning artifacts

To conduct histological analysis, adequate morphological preservation is required. Sectioning artifacts in the form of knife marks (Figure S5a), tissue folds (Figure S5b), and tissue rupture (Figure S5c) are commonly present on the Tokuyasu cryosections. Sectioning parameters such as chamber temperature, slide thickness, and blade sharpness must be carefully adjusted to preserve the structure of the cryosections.
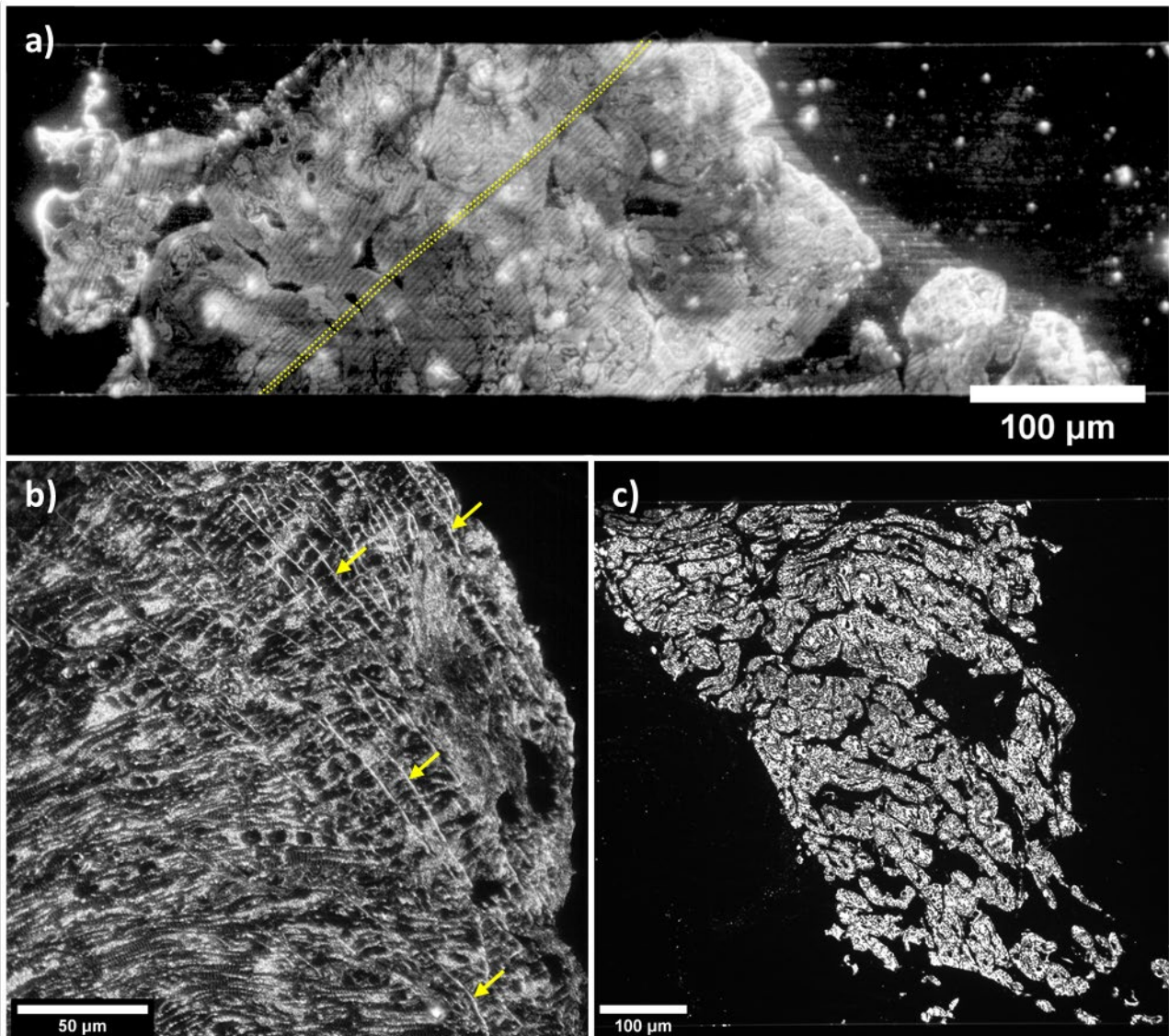

Figure S5. Sectioning artifacts of Tokuyasu cryosections. (a) The yellow-dotted lines illustrate the knife marks along a human placental cryosection. (b) The yellow arrows denote the location of folds on a pig heart cryosection. (c) Illustration of a pig heart tissue sample ruptured during cryosectioning.

S6. Materials and reagents used for the preparation of Tokuyasu sections

Table S6a. Materials and reagents used for the preparation of Tokuyasu sections.

Material/ reagent	Manufacturer	Catalog number	Stock concentration	Working concentration	Purpose
#1.5 coverslip	VWR	48393-151	-	-	Coverslip
Picodent twinsil	Picodent	1300 1000	-	1:1 mixture of solution A and B	Dental cement. Gluing and sealing.
Poly-L-lysine	Sigma-Aldrich	P8920	0.1 % (w v^{-1}) in H$_2$O	1:1	Chip-surface coating for improved adhesion of biological samples
CellMask Deep Red (CMDR)	Invitrogen	C10046	5 mg mL^{-1}	1:2000	Membrane staining
Phalloidin-Atto565	Sigma-Aldrich	94072	27.88 mg mL^{-1}	1:100	F-actin staining
Sytox Green	Invitrogen	S7020	5 mM	1:500	Nuclear staining
Ethyl 3-aminobenzoate methanesulfonate (Tricaine)	Sigma-Aldrich	E10521	98%	1:1	Euthanasia of zebrafish
rabbit anti-Tomm20	Santa Cruz Biotechnology	FL-145		1:50	Primary antibody for TOMM20 mitochondrial staining of the zebrafish eye retina
AlexaFluor 647 AffiniPure F(ab')2 fragment donkey anti rabbit IgG	Jackson Immuno-Research	711-606-152		1:200	Secondary antibody for TOMM20 mitochondrial staining in zebrafish eye retina
Texas Red-X Phalloidin	Invitrogen	T7471		1:50	F-actin staining of zebrafish eye
Podoplanin (hamster anti-mouse) Monoclonal Antibody	ThermoFisher	14-5381-85	0.5 mg mL^{-1}	1:100	Primary antibody for Podoplanin staining in mouse kidney
Goat anti-Hamster IgG (H+L) Alexa Fluor 568	ThermoFisher	A-21112	2 mg mL^{-1}	1:250	Secondary antibody for Podoplanin staining in mouse kidney
Phosphate buffered saline (PBS)	Sigma-Aldrich	D8662	-	1:1	Washing steps
Prolong Diamond	ThermoFisher	P36961	-	1:1	Antifade mountant

Table S6b. Buffers for sample preparation and imaging of Tokuyasu sections.

Buffer name	Working concentration	Purpose
PBG blocking buffer	0.5% bovine serum albumin PBS (A6588.0050, Applichem) and 0.2 % gelatin type B (G-6650, Sigma) in PBS	Blocking buffer for immunolabeling of zebrafish eye for CLEM
Goat blocking buffer	10% goat serum into 1% BSA in PBS	Blocking buffer for immunolabeling of mouse kidney for chip-TIRFM
SMLM imaging buffer	Oxygen scavenger system (0.5 mg mL^{-1} glucose oxidase (Sigma), 40 µg mL^{-1} catalase (Roche Applied Science), 10% (w v^{-1}) glucose in phosphate buffer (pH 7.4), and 100 mM Mercaptoethylamine (MEA, Sigma) in PBS	Imaging buffer for SMLM experiments on mouse kidney tissue

S7. Chip-TIRFM imaging of immunolabeled mouse kidney samples

Fluorescent immunolabeling allows the identification of proteins of interest on the biological samples. The photonic chip not only withstands the chemical and thermal conditions of the sample preparation steps for Tokuyasu cryosections but also allows fluorescent immunolabeling of these samples. Figure S7 shows a 60X magnification image of a 400 nm thick Tokuyasu cryosection of a mouse kidney fluorescently labeled using CellMask Deep Red for membranes (shown in red) and Sytox Green for nuclei (shown in blue). The podoplanin protein was immunolabeled using hamster anti-mouse podoplanin as a primary antibody, and goat anti-hamster conjugated to Alexa Fluor 568 as a secondary antibody (shown in green). Supplementary Information S6 provides a detailed description of the dyes used for immunolabeling of the mouse kidney cryosection.
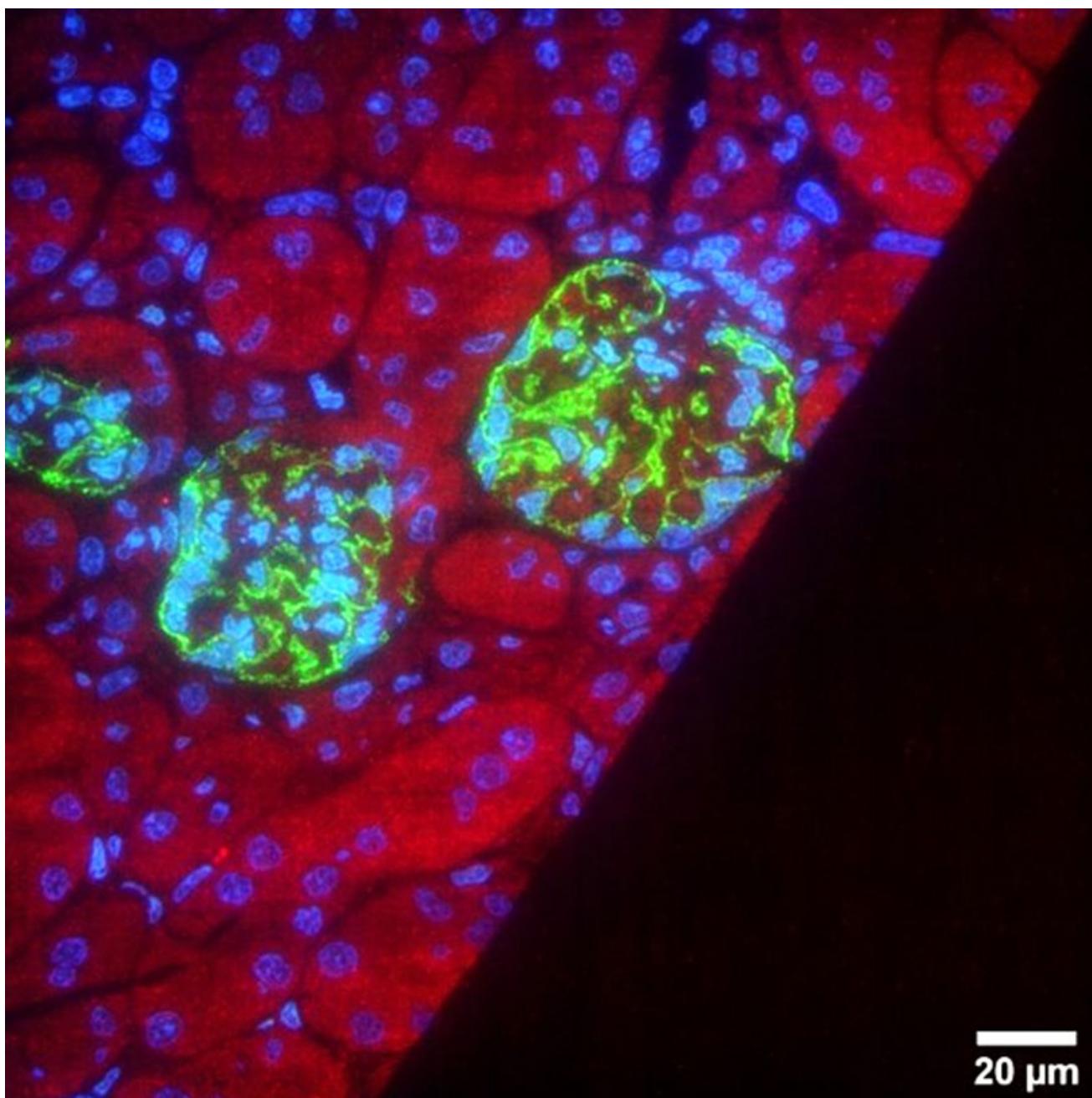

Figure S7. Chip-TIRFM image of a 400 nm thick mouse kidney cryosection fluorescently immunolabeled by Tokuyasu method. Membranes labeled with CellMask Deep Red (pseudo-colored in red) and nuclei labeled with Sytox Green (pseudo-colored in blue). The glomeruli were labeled with hamster anti-mouse podoplanin as a primary antibody, and goat anti-hamster conjugated to Alexa Fluor 568 as a secondary antibody (pseudo-colored in green). The image was collected with a 60X/1.2NA water immersion objective lens.

S8. Chip-TIRFM imaging of immunolabeled human kidney samples

Figure S8 shows a chip-based multicolor TIRFM image of a 200 nm thick human kidney section prepared by Tokuyasu method. The sample was fluorescently labeled with Phalloidin ATTO565 for F-actin (displayed in magenta), and Sytox Green for nuclei (displayed in cyan). The mitochondria were immunolabeled using rabbit anti-TOMM20 mitochondrial marker as a primary antibody (Abcam, #AB186734), followed by donkey anti-rabbit AF647 as a secondary antibody (Invitrogen, #A31573). Figure S8c shows relevant kidney structures including proximal tubuli (PT), distal tubuli (DT), collecting duct (CD), microcapillary (white arrow), as well as the thin and the thick loops of Henle (white and yellow arrowheads, respectively). A magnified view of the white-dotted box in Figure S8c illustrates the improved contrast provided by MUSICAL (Figure S8e), as compared to the TIRF image (Figure S8d).
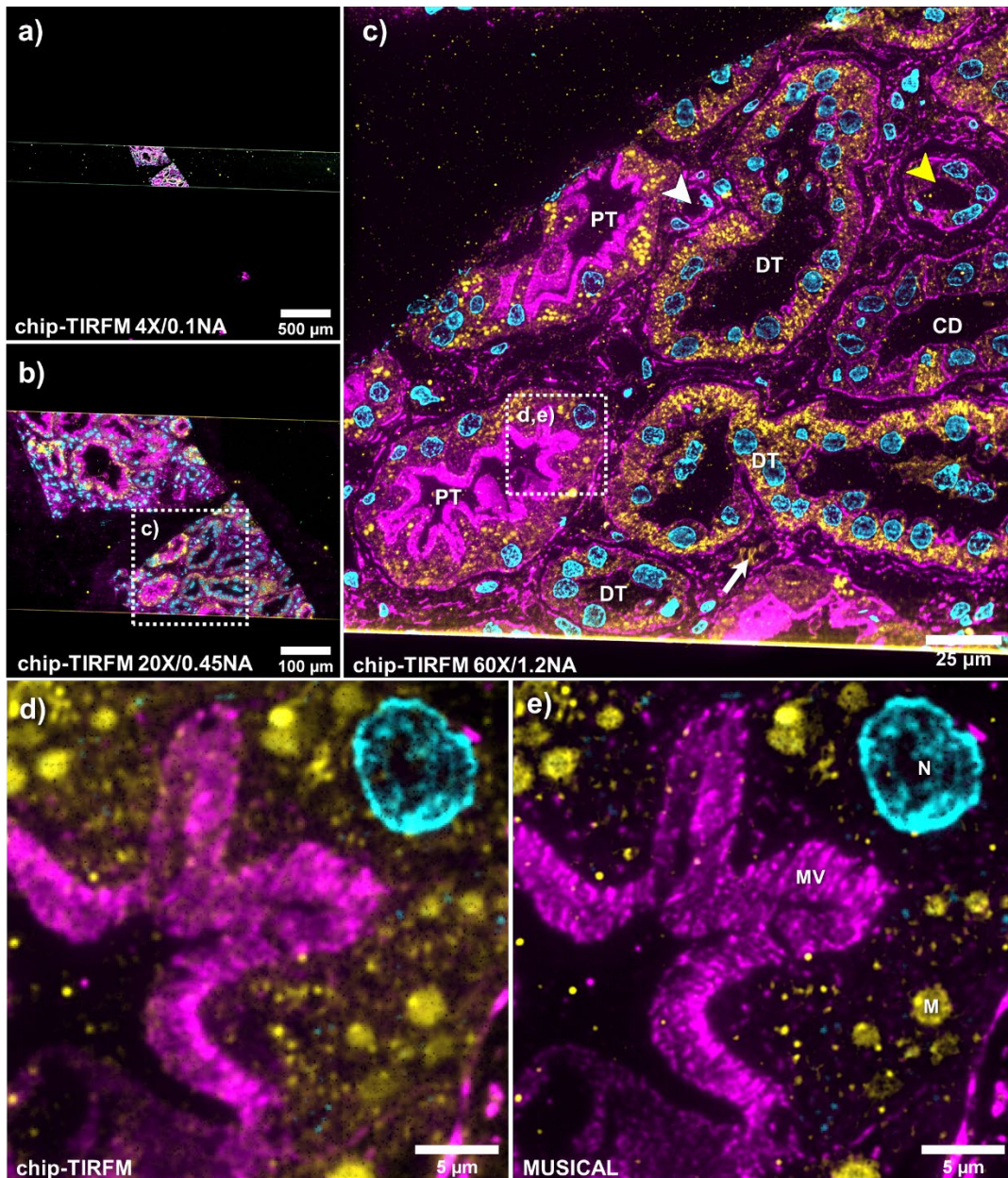

Figure S8. Chip-TIRFM image of a 200 nm thick human kidney cryosection fluorescently immunolabeled by Tokuyasu method. F-actin labeled with Phalloidin ATTO565 (pseudo-colored in magenta) and nuclei labeled with Sytox Green (pseudo-colored in cyan). The mitochondria were immunolabeled using rabbit anti-TOMM20 mitochondrial marker as a primary antibody, and donkey anti-rabbit conjugated to AF647 as a secondary antibody (pseudo-colored in yellow). *(a)* Large FOV chip-TIRFM image using a 4X/0.1NA microscope objective lens. *(b)* chip-TIRFM image using a 20X/0.45NA microscope objective lens. The white-dotted box illustrates the region of interest imaged in (c). *(c)* chip-TIRFM image using a 60X/1.2NA microscope objective lens showing proximal tubuli (PT), distal tubuli (DT), collecting duct (CD), microcapillary (white arrow), the thin loop of Henle (white arrowhead), and the thick loop of Henle (yellow arrowhead). The white-dotted box illustrates the region of interest magnified in (d,e). *(d)* Magnified view of the chip-TIRFM image in (c). *(e)* MUSICAL provides enhanced contrast over the chip-TIRFM image, allowing for clear visualization of the microvilli (MV), nucleus (N), and individual mitochondria (M).

S9. Chip-TIRFM imaging of Pig heart tissue

The photonic chip allows for TIRF microscopy imaging of diverse cryo-preserved tissues from human and not human origin. Figure S9 shows a chip-based multicolor TIRFM of a longitudinal ultrathin (100 nm) tissue cryosection from a pig heart prepared by Tokuyasu method and fluorescently labeled with CellMask Orange for membranes (shown in magenta), and Sytox Green for nuclei (shown in cyan). The photonic chip allows high-contrast TIRF imaging with microscope objective lenses of low magnification and low numerical apertures (Figure S9a,b), a feature not available in conventional TIRF microscope objectives. A magnified view of the 60X/1.2NA objective (Figure S9d) reveals perinuclear mitochondrial clusters (white arrowhead), as well as mitochondrial rows (yellow arrowhead) aligned in parallel with the contractile units (the sarcomeres) of the tissue. Furthermore, since the CellMask Orange is a membrane stain, the transverse-tubules (t-tubules) also become visible in a characteristic periodic pattern, appearing as striations denoting the sarcomere length/spacing (white arrow in Figure S9d).
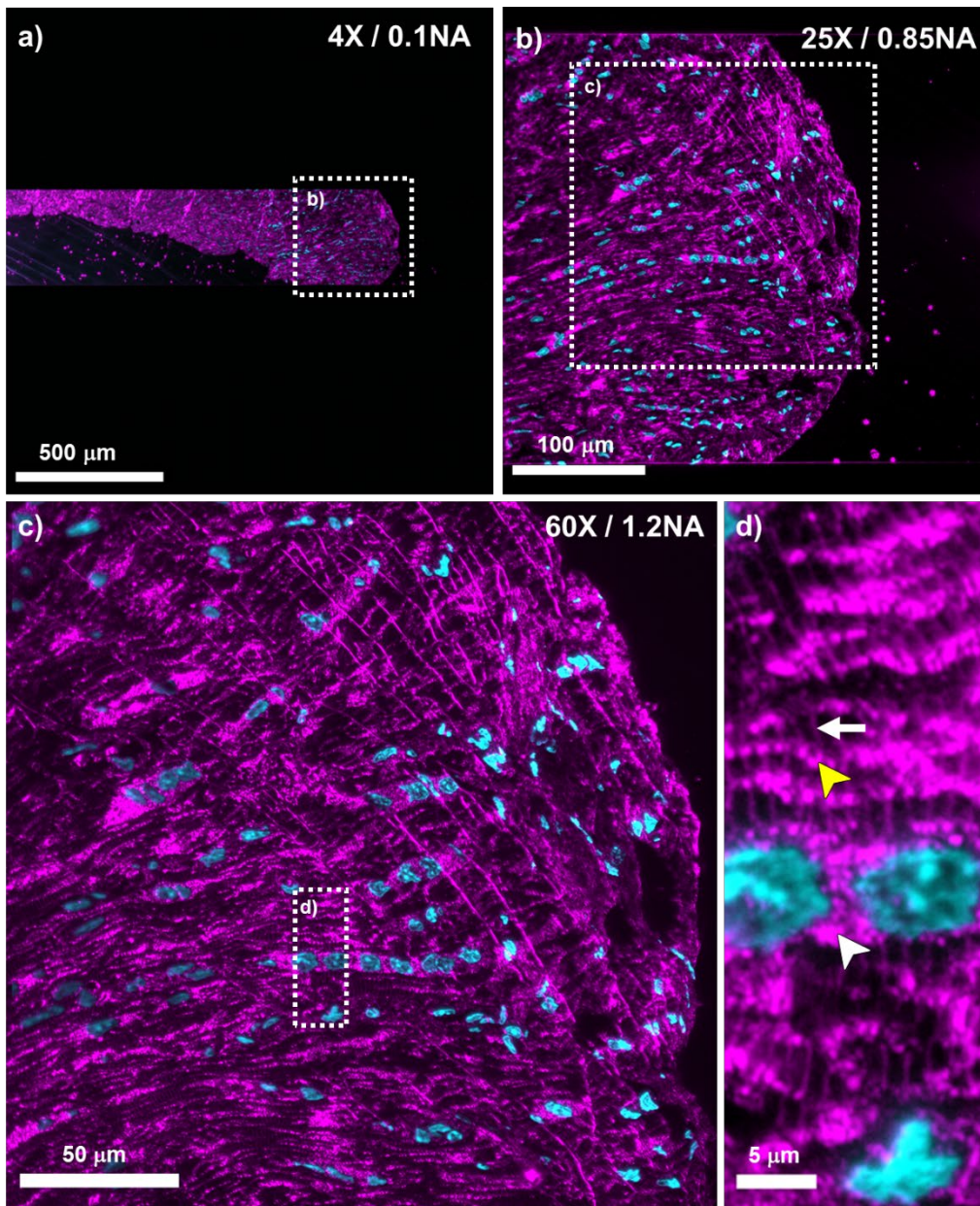

Figure S9. Chip-TIRFM image of a 100 nm thick pig heart cryosection harvested from the left ventricle and prepared by Tokuyasu method. Membranes labeled with CellMask Orange (pseudo-colored in magenta) and nuclei labeled with Sytox Green (pseudo-colored in cyan). (a) Large FOV chip-TIRFM image using a 4X/0.1NA microscope objective lens. The white-dotted box illustrates the region of interest imaged in (b). (b) chip-TIRFM image using a 25X/0.85NA microscope objective lens. The white-dotted box illustrates the region of interest imaged in (c). (c) chip-TIRFM image using a 60X/1.2NA microscope objective lens. The white-dotted box illustrates the region of interest magnified in (d). (d) A magnified view of the white-dotted box in (c) reveals prominent features of the cardiac tissue such as perinuclear mitochondrial clusters (white arrowhead), mitochondrial rows (yellow arrowhead) aligned in parallel with the sarcomeres, and the transverse-tubules (t-tubules) appearing as striations denoting the sarcomere length/spacing (white arrow).

S10. Large FOV imaging of paraffin-embedded samples using chip-TIRFM

Formalin-fixed paraffin-embedding (FFPE) accounts for the most common preservation method employed for histological examinations worldwide. It entails chemical fixation of samples in formalin (e.g. an aqueous solution of formaldehyde) and subsequent embedding in paraffin to allow for long-time storage at room temperature. Preparation of FFPE samples for fluorescence microscopy imaging starts with sectioning the paraffin block into thin slices of approximately 4 µm in thickness. Thereafter, the sections are placed onto microscope glass slides for incubation in successive baths of xylene and rehydration in descent grades of ethanol. After staining with fluorescent probes, the sample is mounted with imaging media and covered with a glass coverslip before imaging under the microscope[53]. In chip-based microscopy, instead of a microscope glass slide, a photonic chip is used throughout the whole sample preparation and imaging process. Figure S10a shows a human placental FFPE sample sequentially imaged in TIRF mode over adjacent waveguides (denoted as "WG#") using a 4X/0.1NA microscope objective. The individual images are merged into a large FOV TIRF image, as illustrated in Figure S10b. The dark horizontal stripes in Figure S10b correspond to the spacing between adjacent waveguides in the chip. The number of stripes can be minimized by: a) by reducing the spacing between waveguides to approx. 1 µm, and b) by increasing the waveguide width to approx. 3.5 mm (as a reference, the widest waveguide shown in Figure S10b corresponds to WG5, with a width of 1 mm). The acquisition process can be repeated over specific regions of interest with higher magnification/numerical aperture microscope objectives, to obtain sharper visualization of the tissue structure (Figure S10c,d). The dark patches observed in Figure S10c (shown with arrowheads) suggest sample detachment of the tissue section from the waveguide surface in these areas, impeding the evanescent field to reach and uniformly excite all the fluorescent molecules in the sample. Our future work will focus on optimizing the sample adhesion to improve chip-TIRFM imaging of FFPE sections.
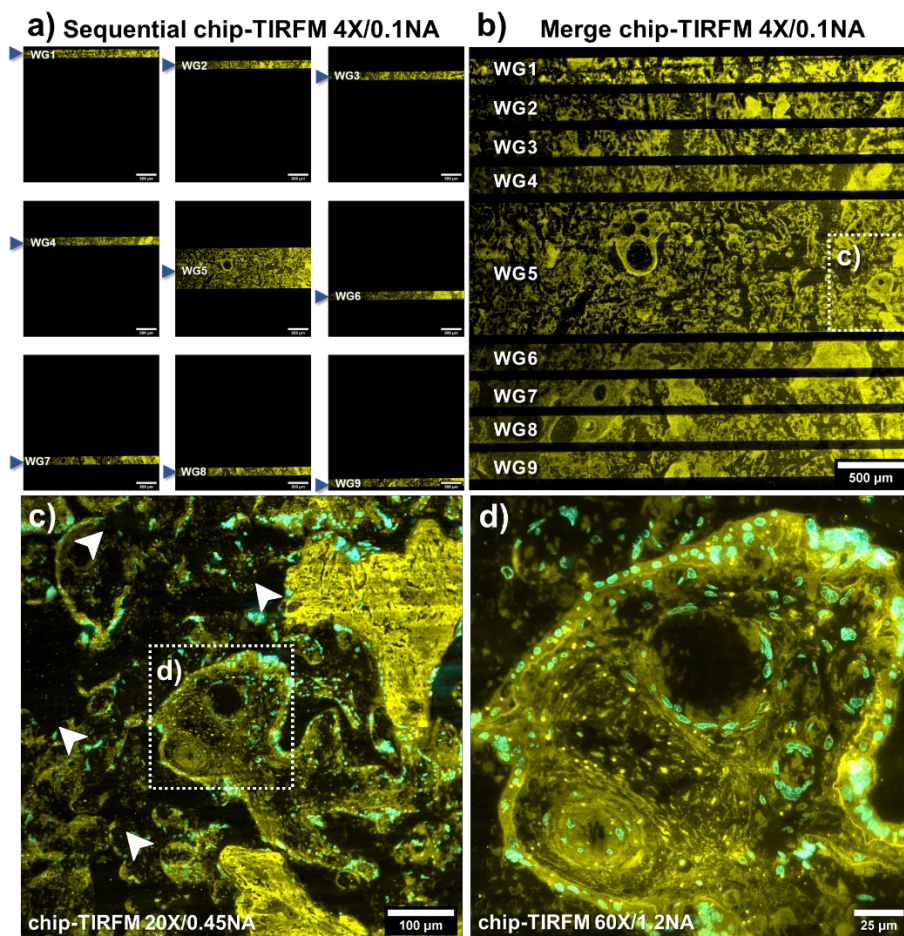

***Figure S10. Chip-TIRFM image of a 4µm thick FFPE human placenta**. Membranes labeled with MitoTracker Deep Red (pseudo-colored in yellow) and nuclei labeled with Sytox Green (pseudo-colored in cyan). **(a)** Sequential imaging in TIRF mode over adjacent waveguides (WG) using a 4X/0.1NA microscope objective. The blue arrowheads indicate the position of the coupling objective. **(b)** Large FOV merge of the TIRF images acquired in (a). The white-dotted box corresponds to the area imaged in (c). **(c-d)** TIRF images of the FFPE placental section using a 20X/0.45NA and a 60X/1.2NA microscope objective, respectively. The arrowheads in (c) indicate dark areas in the image as a consequence of sample detachment from the waveguide surface. Scalebar (a) 500 µm.*

S11.   Quantification of resolution improvement based on decorrelation analysis

To quantify the resolution enhancement obtained with MUSICAL, we used decorrelation analysis[52]. This algorithm allows to estimate the resolution of single images based on the spatial frequency content and it is suitable for bandwidth-limited signals, as is the case of microscopy images. The decorrelation algorithm analyses the images under a series of high-pass filters that reduce the signal of interest to, eventually, leave it alone with the noise. As the noise is assumed to be in the entire spectrum, with this approach it is possible to estimate the point at which the signal is completely lost and, therefore, estimate the maximum spatial frequency at which it is still possible to obtain information from the sample. We used the MATLAB version of the algorithm to analyze both the average chip-TIRFM and the MUSICAL images, setting the number of sample points to 100 and the number of filters to 50. For the average chip-TIRF image, the estimated resolution was 268 nm, whereas for the MUSICAL image the resolution was estimated to be 195 nm. Importantly, the MUSICAL images were not post-processed to attenuate possible artifacts located in the high-end of the spatial frequency spectrum. Therefore, we expect the result to be an optimistic approximation of the resolution. Figure S11 shows the corresponding plots for resolution estimation per decorrelation analysis. The resolution is calculated with the formula $resolution = 2 \times pixel\ size/k_c$, where k_c corresponds to the maximum normalized spatial frequency shown in the plot (e.g. k_c = 0.8053 for chip-TIRFM, and k_c = 0.1111 for MUSICAL).
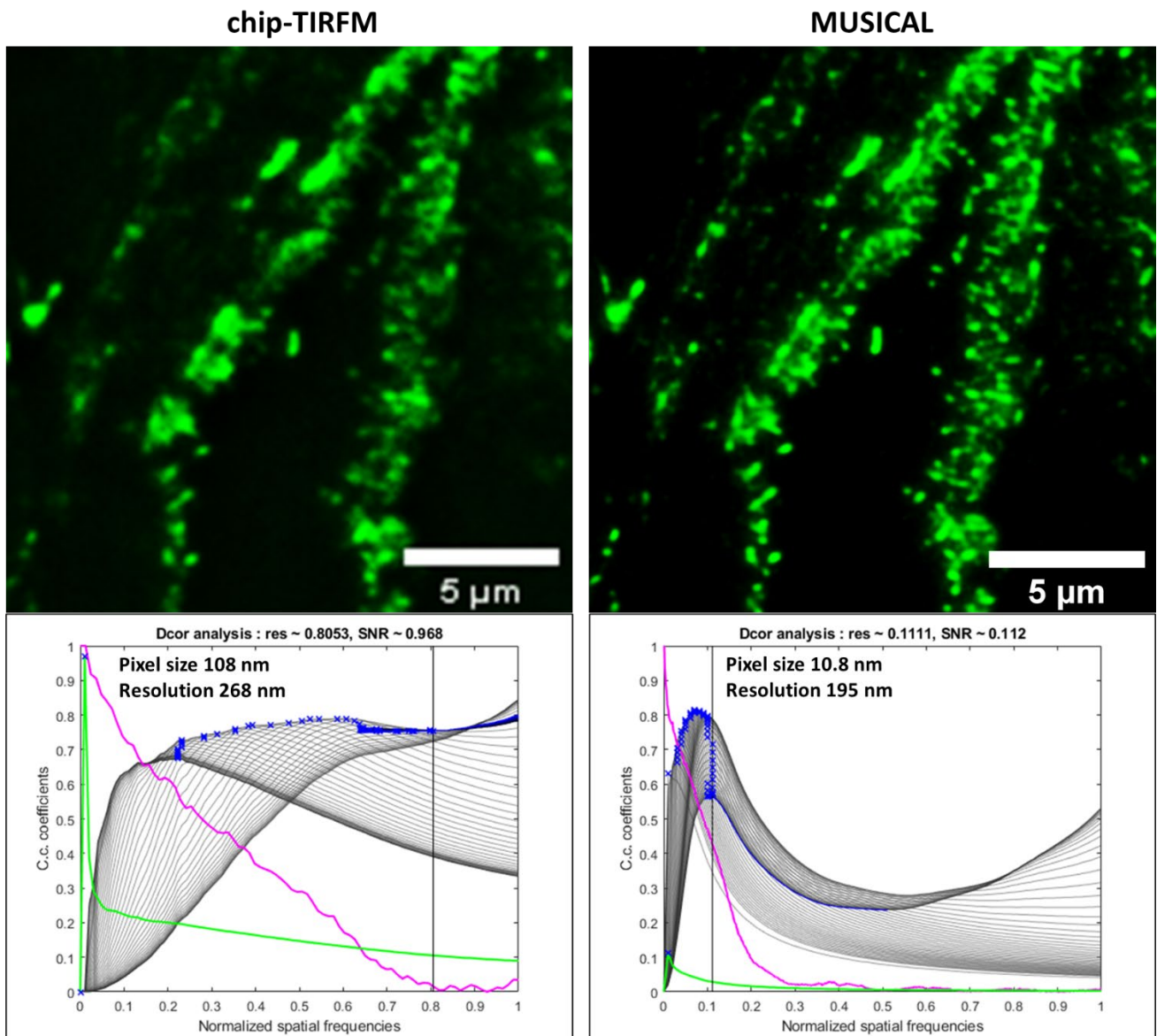

Figure S11. Decorrelation analysis for resolution estimation of chip-TIRFM and MUSICAL images. *Placental chorionic villi tissue cryosection labeled with Phalloidin ATTO565 for F-actin (pseudocolored in green). The estimated resolution for chip-TIRFM is 268 nm, and 195 nm for MUSICAL. The MUSICAL image was adjusted with a logarithmic transformation in FIJI to improve its contrast.*

S12. Comparative FOV between chip-based IFON and SIM

The photonic chip allows the implementation of advanced microscopy techniques including intensity fluctuation-based optical nanoscopy (IFON) over large FOV (Figure S12a). Although structured illumination microscopy (SIM) has been proposed as the fastest super-resolution method for histopathological analyses[18,21,54], the FOV achieved by this technique is limited to a much smaller area than chip-based IFON when a high magnification objective lens is used. A typical commercial SIM system, e.g., OMX V4 Blaze, GE Healthcare, allows for reconstructed 3D-SIM images of approximately 40 x 40 μm^2 using a 60X/1.42NA oil immersion objective. Hence, to achieve a similar FOV to that of chip-based IFON, a tile mosaic composed of 7 x 7 reconstructed 3D-SIM images is needed (Figure S12b). Considering that a set of 15 raw images are required for each of the 8 z-planes necessaries to reconstruct a single SIM image, and accounting for the 10 μm overlap between adjacent images (Figure S12b), a total of 5880 SIM raw images are needed for an equivalent FOV as the one obtained with the photonic chip (15 raw images/z-plane x 8 z-planes/3D-SIM x 49 3D-SIM = 5880 raw images). Also, considering a typical image acquisition of 30 msec per raw image and a reconstruction time of 3 min per 3D-SIM image rounds up to a total imaging time of 2.5h from acquisition (30 msec/raw image x 5880 raw images = 176.4 sec $\approx$ 3 min) to 3D-SIM reconstruction (3 min/3D-SIM image x 49 3D-SIM images = 147 min). Importantly, we achieved a high-resolution chip-based IFON image over a fixed FOV of 220 x 220 μm^2 after collecting a relatively small image stack of 500-frames using a 60X/1.2 water immersion objective, requiring approximately 10 min from acquisition to image reconstruction. We acknowledge that the implementation of a 2D-SIM scheme reduces the amount of acquired data (e.g., 9 raw images/2D-SIM x 49 2D-SIM = 441 raw images) and, consequently improves the processing time for a single-plane 2D-SIM, potentially becoming faster than chip-based IFON. We could not benchmark the exact numbers for this premise, since the SIM microscope available at our facilities only allows for 3D-SIM, and requires a z-stack of at least 7 to 8 planes to properly reconstruct an imaging area of 40 x 40 μm^2. Nevertheless, the chip-based method offers a much less complex and highly cost-effective alternative to a commercial SIM instrument.
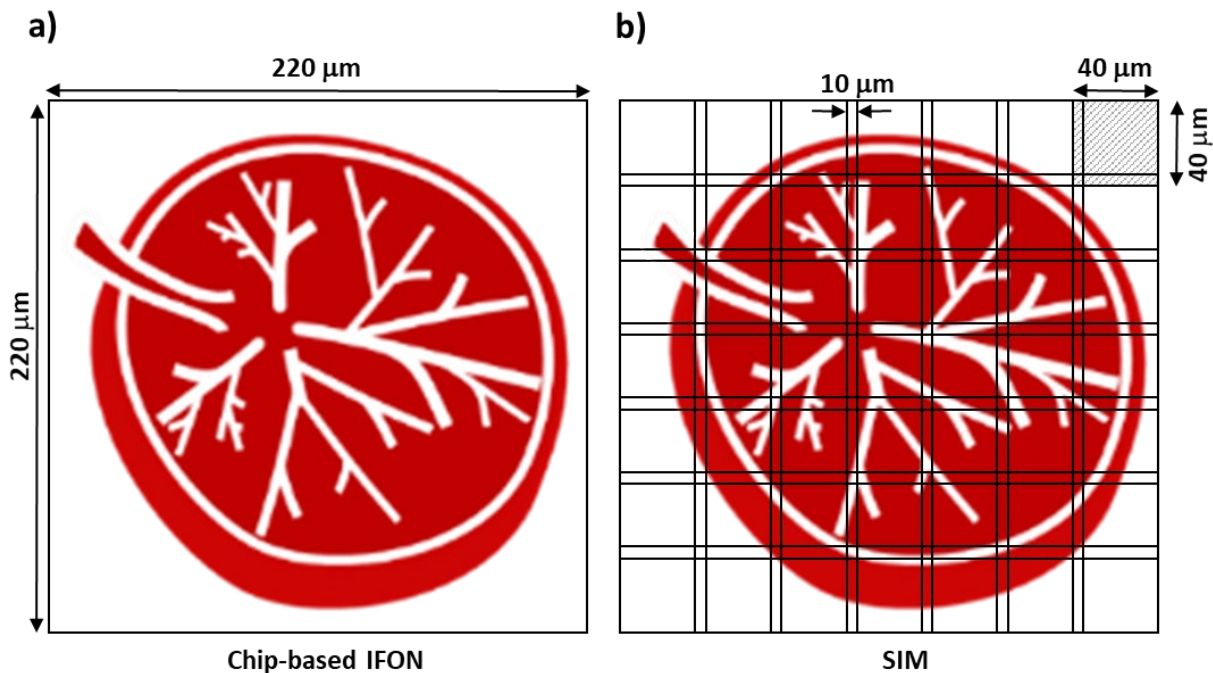
Figure S12. Comparative FOV between chip-based IFON and 3D-SIM. (a) *Chip-based IFON allows a FOV of 220 x 220 μm^2 after collection of an image stack of 500-frames and reconstruction time of approx. 10 min.* *(b)* *To achieve a similar FOV with 3D-SIM, a tile mosaic image is constructed. It requires the acquisition of 5880 raw images and a reconstruction time of 2.5h. The upper-right square denotes the typical FOV attainable with 3D-SIM (40 x 40 μm^2).*

S13. Detailed description of the chip-TIRFM setup

The chip-TIRFM setup is composed of two main parts, namely the collection path and a photonic chip module, as illustrated in Figure S13a. The collection path consists of a commercial upright microscope equipped with an emission filter set (see Table S13), a sCMOS camera, and conventional microscope objective lenses of diverse magnifications, which can be interchanged depending on the imaging needs. Figures S13b and S13c provide a detailed view of the chip-TIRFM setup.

Table S13. Longpass and bandpass filters used in the setup for image acquisition

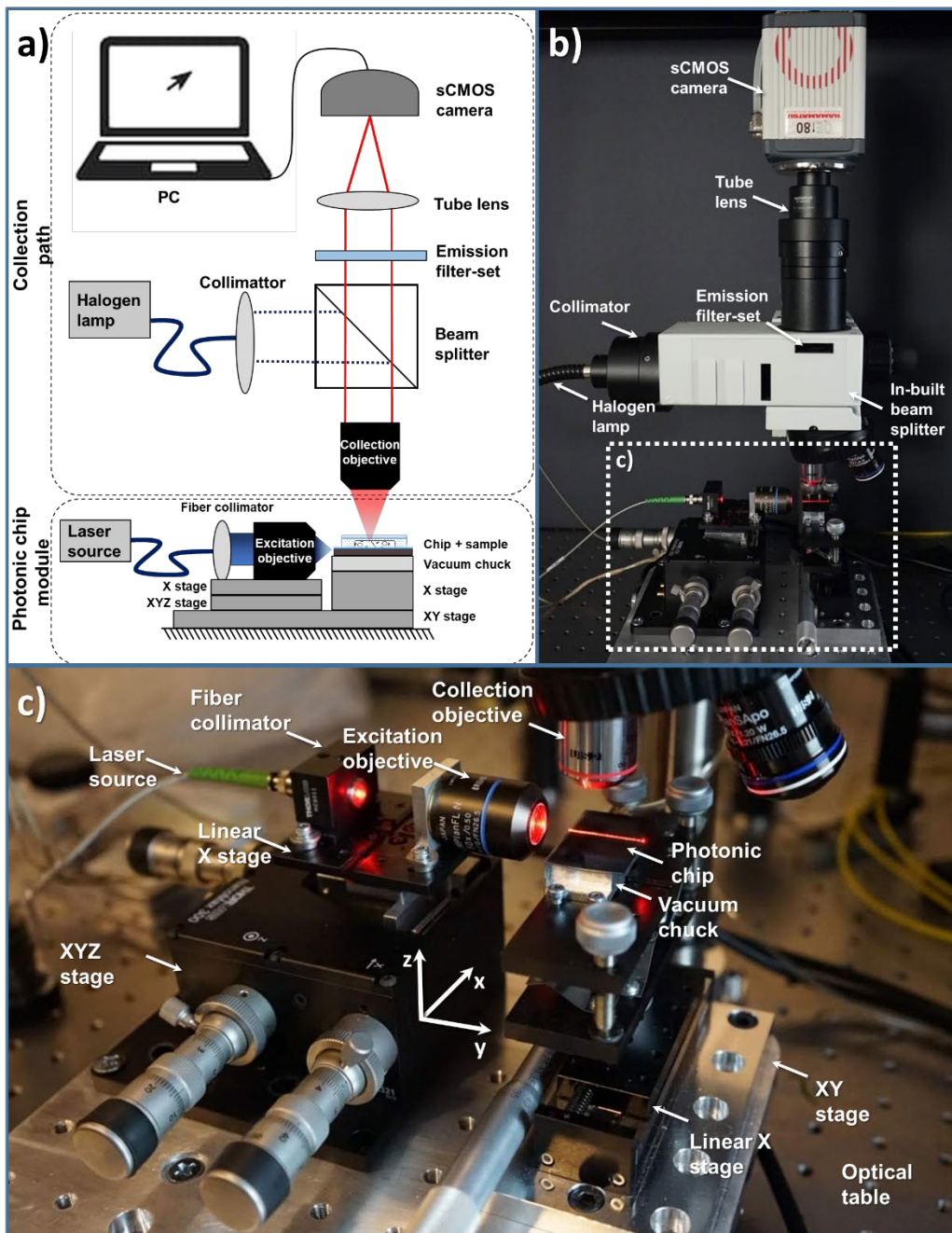| Excitation wavelength (nm)	Emission filter set	
	Long-pass filter (nm)	Band-pass filter (nm)
488	488	520/36
561	561	591/43
640	664	690/40

Figure S13. Chip-TIRFM setup. (a) *Schematic representation of the chip-TIRFM setup illustrating the collection path and the photonic chip module.* ***(b)*** *Side view of a chip-TIRFM setup denoting the collection path components. The dotted-white box represents the photonic chip module shown in (c).* ***(c)*** *Close view of the photonic chip module components.*

S14. SEM imaging on a photonic chip

For correlative light-electron microscopy (CLEM), the Tokuyasu cryosections are imaged on a scanning electron microscope (SEM) after completion of chip-TIRFM imaging. To this, the coverslip and the PDMS frame are removed. Then, the sample is post-fixed with 0.1% glutaraldehyde, masked with methylcellulose, and further coated with a 10 nm layer of platinum/carbon. The photonic chip is placed on a 25 mm Pin Mount (Figure S14A) and transferred to a SEM. A bright-field image assists in finding the sample (Figure S14B). A low accelerating voltage allows high-resolution SEM imaging of the sample (Figure S14C).
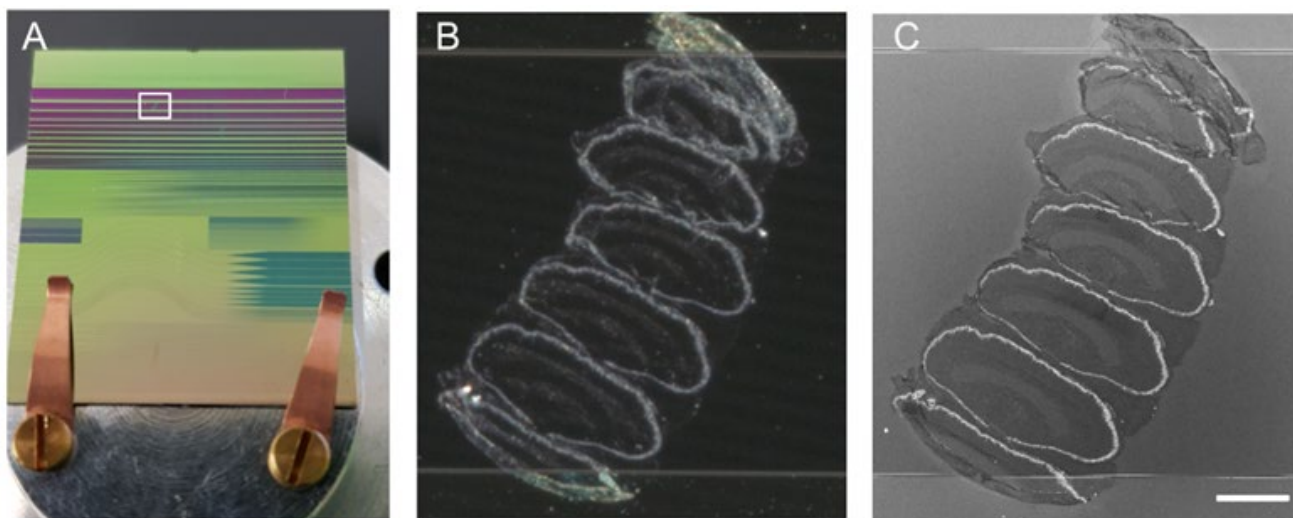

Figure S14. Chip-based CLEM imaging. (A) Photonic chip mounted on a 25 mm pin stub for imaging in the SEM. The white frame corresponds to the zoomed area in (B) and (C). *(B)* Bright-field image of zebrafish retina serial sections on a 600 µm strip waveguide. *(C)* The same area acquired with SEM. Scale bar 100 µm.

S15. References – Supplementary Information

18. Wang, M. *et al.* High-resolution rapid diagnostic imaging of whole prostate biopsies using video-rate fluorescence structured illumination microscopy. *Cancer Research* **75**, 4032-4041 (2015).

21. Schlichenmeyer, T. C., Wang, M., Elfer, K. N. & Brown, J. Q. Video-rate structured illumination microscopy for high-throughput imaging of large tissue areas. *Biomedical Optics Express* **5**, 366-377 (2014).

52. Descloux, A., Grußmayer, K. S. & Radenovic, A. Parameter-free image resolution estimation based on decorrelation analysis. *Nature Methods* **16**, 918-924 (2019).

53. Villegas-Hernández, L. E. *et al.* Visualizing ultrastructural details of placental tissue with super-resolution structured illumination microscopy. *Placenta* **97**, 42-45 (2020).

54. Wang, M. *et al.* Gigapixel surface imaging of radical prostatectomy specimens for comprehensive detection of cancer-positive surgical margins using structured illumination microscopy. *Scientific Reports* **6**, 27419 (2016).

Appendix C. Paper III

Super-resolution histology of paraffin-embedded samples via photonic chip-based microscopy

Luis E. Villegas-Hernández[1], Vishesh K. Dubey[1], Hong Mao[1], Manohar Pradhan[2], Jean-Claude Tinguely[1], Daniel H. Hansen[1], Sebastián Acuña[1], Bartłomiej Zapotoczny[3], Krishna Agarwal[1], Mona Nystad[4,5,6], Ganesh Acharya[4,10], Kristin A. Fenton[7], Håvard E. Danielsen[2,8,9], Balpreet Singh Ahluwalia[1,10,*]

[1] Department of Physics and Technology, UiT The Arctic University of Norway, Klokkargårdsbakken NO-9019 Tromsø, Norway

[2] Institute for Cancer Genetics and Informatics, Oslo University Hospital, NO-0424 Oslo, Norway

[3] Department of Biophysical Microstructures, Institute of Nuclear Physics, Polish Academy of Sciences, Kraków, Poland

[4] Department of Clinical Medicine, Women's Health and Perinatology Research group, UiT The Arctic University of Norway, Tromsø, Norway

[5] Department of Obstetrics and Gynecology, University Hospital of North Norway, Tromsø, Norway

[6] Department of Medical Biology, Vascular Biology Research Group (VBRG), UiT The Arctic University of Norway, Tromsø, Norway

[7] Department of Medical Biology, RNA and Molecular Pathology Research Group, UiT The Arctic University of Norway, Tromsø, Norway

[8] Department of Informatics, University of Oslo, NO-0316 Oslo, Norway

[9] Nuffield Division of Clinical Laboratory Sciences, University of Oxford, Oxford OX3 9DU, United Kingdom

[10] Division of Obstetrics and Gynecology, Department of Clinical Science, Intervention and Technology, Karolinska Institute, Stockholm, Sweden

[*] corresponding author: balpreet.singh.ahluwalia@uit.no

Abstract

Fluorescence-based super-resolution optical microscopy (SRM) techniques allow the visualization of biological structures beyond the diffraction limit of conventional microscopes. Despite its successful adoption in cell biology, the integration of SRM into the field of histology has been deferred due to several obstacles. These include limited imaging throughput, high cost, and the need for complex sample preparation. Additionally, the refractive index heterogeneity and high labeling density of commonly available formalin-fixed paraffin-embedded (FFPE) tissue samples pose major challenges to applying existing super-resolution microscopy methods. Here, we demonstrate that photonic chip-based microscopy alleviates several of these challenges and opens avenues for super-resolution imaging of FFPE tissue sections. By illuminating samples through a high refractive-index waveguide material, the photonic chip-based platform enables ultra-thin optical sectioning via evanescent field excitation, which reduces signal scattering and enhances both the signal-to-noise ratio and the contrast. Furthermore, the photonic chip provides decoupled illumination and collection light paths, allowing for total internal reflection fluorescence (TIRF) imaging over large and scalable fields of view. By exploiting the spatiotemporal signal emission via MUSICAL, a fluorescence fluctuation-based super-resolution microscopy (FF-SRM) algorithm, we demonstrate the versatility of this novel microscopy method in achieving superior contrast super-resolution images of diverse FFPE tissue sections derived from human colon, prostate, and placenta. The photonic chip is compatible with routine histological workflows and allows multimodal analysis such as correlative light-electron microscopy (CLEM), offering a promising tool for the adoption of super-resolution imaging of FFPE sections in both research and clinical settings.

Introduction

Histology refers to the study of the structure and organization of the different cell groups within biological organisms by analyzing the microanatomy of tissues. It involves the use of specialized laboratory techniques and instruments to prepare and examine tissue samples in a microscope. In life sciences, histology is of particular importance for several reasons. Firstly, it enables the identification of structural and functional changes during various physiological and pathological processes, including the development of diseases. This information is essential for accurate diagnosis, treatment planning, and monitoring of disease progression. Secondly, histological analyzes permit a better understanding of the mechanisms of disease development and progression, which can lead to the advancement of new and improved treatments. Finally, histology plays a crucial role in many other fields of research, including developmental biology, genetics, and neuroscience, by providing insights into the fundamental structure and organization of the different cells and tissues in plants, animals, and humans.

A standard histological analysis involves several steps including tissue sampling, fixation, sectioning, and labeling, before observation under a microscope. Out of several methods, formalin-fixation paraffin-embedding (FFPE) has become the standard histological processing technique in light microscopy, since it allows an easy, repetitive, reliable, and cost-effective way for preserving, slicing, and archiving tissue samples for decades[1]. Moreover, the FFPE processing method supports several labeling procedures, including light-absorbing dyes such as hematoxylin and eosin

(H&E), immunohistochemical markers, and fluorophores. Nowadays, FFPE is estimated to be the most common histological preservation method, with hundreds of millions of samples stored in biobanks around the world[2,3]. All these features make FFPE a valuable source of biological material for a wide variety of studies ranging from genomics[4,5] and proteomics[6] to aid in diagnosis[1] and prognosis[7,8] of diseases.

High resolution is a desirable feature in histology, as it enables the identification of morphological features relevant both for basic research and clinical purposes. Conventional optical microscopes and slide scanners offer a fast and relatively inexpensive way to observe biological samples, at the cost of limited resolution (~250 nm), whereas electron microscopes allow for nanoscale resolution at the expense of high operating costs and low throughput. In histopathology, the selection between light and electron microscopy is highly dependent on the level of detail necessary to visualize the structures of interest that are essential to render a clinical diagnosis. While a vast majority of pathologies can be analyzed with conventional diffraction-limited optical microscopy, some other disorders such as minimal change disease[9], primary ciliary dyskinesia[10], and amyloidosis[11], require the high-resolution power of electron microscopy for diagnosis.

Recently, a new set of optical microscopy methods have emerged, allowing sub-diffraction resolution via manipulation of the illumination patterns and/or of the photochemical and photokinetic properties of fluorescently-labeled samples[12]. This new set of techniques referred to as fluorescence-based super-resolution optical microscopy (SRM), or optical nanoscopy, breached the resolution gap between light and electron microscopy, some of them reaching down to sub-20 nm resolution, opening new avenues for the investigation of biological mechanisms under optical instruments. To date, several techniques have emerged under the umbrella of SRM, categorized into four main sub-types, namely, single-molecule localization microscopy (SMLM)[13], stimulated emission depletion microscopy (STED)[14], structured illumination microscopy (SIM)[15], and fluorescence fluctuation-based super-resolution microscopy (FF-SRM)[16].

The development of optical super-resolution methods has given us a glimpse of its potential impact on histopathological applications, allowing for detailed observations of ultrastructural features on standard FFPE sections[3,17-20]. However, multiple barriers defer the adoption of super-resolution methods in clinical settings. These include: 1) the limited throughput, in terms of field of view; 2) the susceptibility of the super-resolution methods to refractive index heterogeneity and high labeling density inherently present on FFPE tissues; 3) high operational costs of the existing super-resolution techniques; and 4) the system complexity. For example, SMLM methods support sub-50 nm lateral resolution over relatively large fields of view but typically require thousands of frames for successful image reconstruction[21]. Although SIM approaches require significantly fewer images than SMLM (9 or 15 images for 2D-SIM or 3D-SIM, respectively), commercially available SIM systems are commonly limited to fields of view of approximately 50 μm × 50 μm. Recent approaches such as transmission-SIM[22] have demonstrated an extended field of view, however, at the cost of a compromised resolution. Moreover, SIM methods are prone to reconstruction artifacts, particularly in the presence of refractive index mismatch[23], which is a potential issue for heterogeneous samples such as FFPE tissue sections. STED, despite being a reconstruction-free method, is a point-scanning technique with low throughput for scanning the centimeter-scale tissue areas commonly used in histology. Furthermore, the light scattering aberrations experienced by the depletion laser ultimately compromises the lateral resolution achievable with STED in FFPE samples[24]. The FF-SRM comprises a set of statistical methods capable of resolving fine structures out of conventional wide-field image stacks, without the need for special equipment or complex sample preparation. However, FF-SRM methods also face reconstruction challenges due to the high density of fluorescent labels present in tissue samples. Hence, an SRM method capable of addressing these challenges while being compatible with the routinary histological workflow of FFPE samples will prove advantageous for embracing super-resolution histology both in research and clinical settings.

Recently, photonic chip-based optical microscopy has been proposed as a versatile tool for the observation of biological samples, allowing for multimodal high-resolution imaging over large fields of view[21,25-27]. The method consists of a photonic integrated circuit (in short, a photonic chip), that holds the sample while providing it with the necessary illumination for fluorescence microscopy. The photonic chip employed in this work is composed of a silicon substrate layer of silicon (Si), an intermediate layer of silicon dioxide (SiO_2), and a top optical waveguide core layer of silicon nitride (Si_3N_4) that transmits light in its visible spectrum[26] (Figure 1a). For microscopy analysis, the biological sample is placed in the imaging area (Figure 1b) and further prepared for fluorescence labeling. Thereafter, an

excitation beam source is coupled to a chosen waveguide facet, allowing for confined light propagation along the core material via total internal reflection. Upon coupling, an evanescent field with a penetration depth of <50 nm for the chosen photonic-chip forms at the waveguide-sample interface, exciting the fluorescent molecules in its reach. The waveguide geometries support multi-mode interference (MMI) patterns that provide a semi-stochastic, non-uniform illumination to the sample[25,28,29]. To achieve isotropic illumination, the MMI patterns are modulated by translating the coupling objective along the input facet of the chip, while individual frames are collected (see Supplementary Video V1 and Supplementary Information S1). For multicolor imaging, the process is repeated using the specific excitation wavelength for each fluorescent marker. Finally, the acquired image stacks are computationally averaged, pseudo-colored, and merged to obtain a chip-based total internal reflection fluorescence (chip-TIRF) image. Contrary to the conventional TIRF that uses a high numerical aperture (NA) and high magnification lenses (usually 60X to 100X, and 1.49 NA) to generate the evanescent fields, the evanescent field here is generated by a photonic chip. Thus, by using conventional microscope objectives of diverse magnifications (see Supplementary Information S2), the photonic chip enables high-contrast TIRF images over diverse fields of view (Figure 1c).
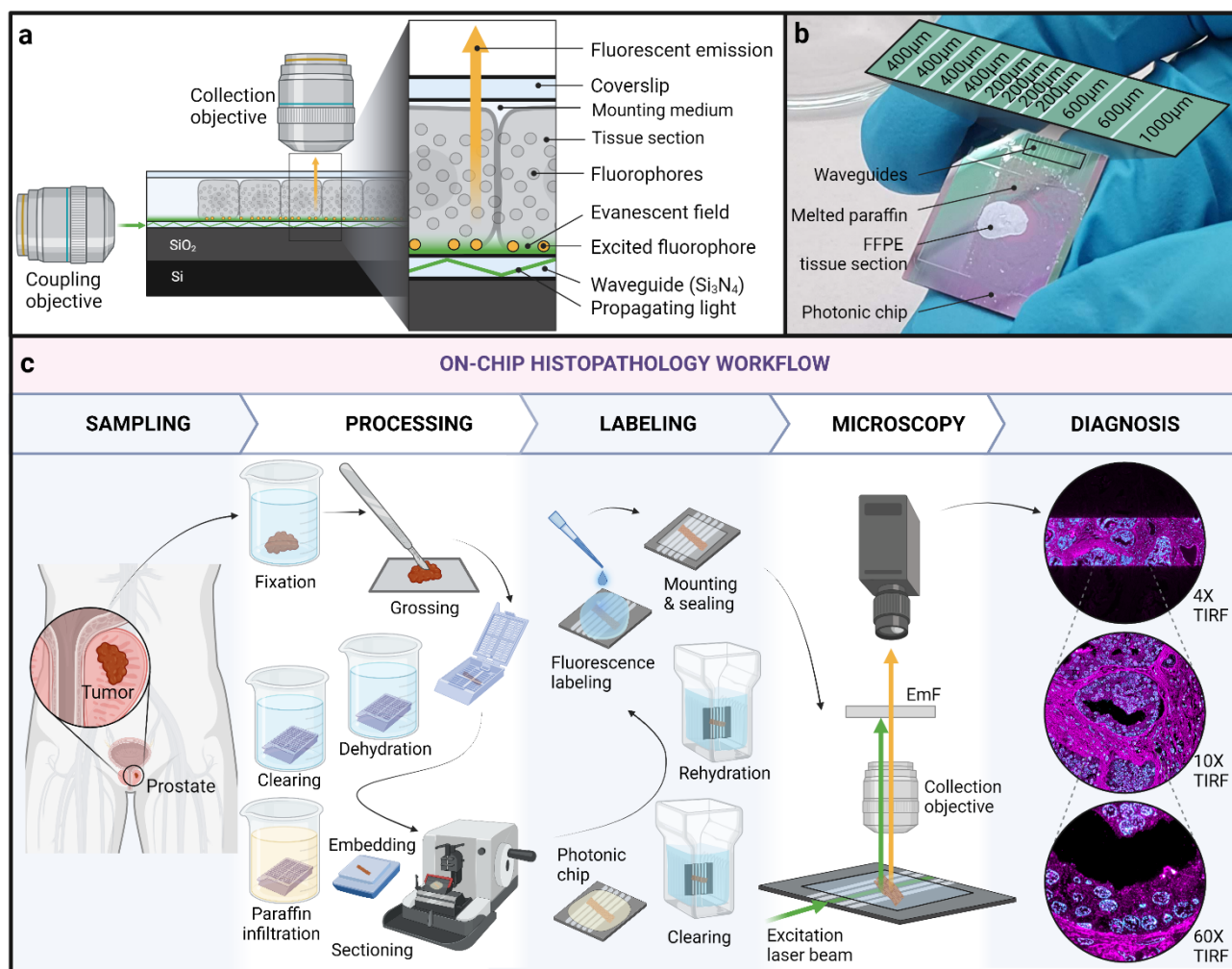

*Figure 1. **Photonic chip-based microscopy for FFPE samples. a)** Working principle: upon coupling, the excitation laser beam propagates along the optical waveguide due to the phenomenon of total internal reflection. An evanescent field of <50 nm forms at the waveguide surface, exciting the fluorophores on its reach. The fluorescent emission is collected by a conventional microscope objective lens. **b)** View of a photonic chip containing an FFPE tissue sample after oven incubation at 60 °C for paraffin melting. The zoomed-in area illustrates diverse waveguide widths available on the photonic chip (200 μm, 400 μm, 600 μm, and 1000 μm). **c)** Photonic chip-based microscopy is compatible with standard histological workflows: following extraction from the diseased organ, the tissue sample is further processed via FFPE steps including fixation in formalin, grossing, dehydration, clearing, paraffin infiltration, and embedding. Thereafter, the tissue block is sliced on a microtome into a thin section (2 μm - 4 μm). Subsequently, the tissue section is floated in a water bath and then scooped onto a photonic chip for further paraffin melting, clearing, rehydration, and fluorescence labeling. After mounting and sealing, the chip is placed on a standard upright microscope equipped with a side excitation laser beam. Upon coupling onto a chosen waveguide, the fluorescent signal is collected by a conventional microscope objective while the excitation light is further blocked using an emission filter (EmF). By transitioning from low to high magnification collection objectives, photonic chip-based microscopy offers high-contrast and super-resolution visualizations of FFPE tissue samples over scalable fields of view, facilitating the histological interpretation and subsequent diagnosis of diseases.*

In a previous study[30], photonic chip-based microscopy was shown as a multimodal platform for super-resolution imaging of tissue sections prepared using Tokuyasu cryopreservation method[31]. Particularly, the implementation of

photonic chip-based FF-SRM via multiple signal classification algorithm[32] (MUSICAL) revealed promising potential as a fast super-resolution imaging method for tissue sections. However, previous efforts were somehow limited in throughput and did not cover standard FFPE tissue sections.

In this study, we propose photonic chip-based optical microscopy as a high-contrast super-resolution tool for the observation of FFPE samples over large fields of view. By using FFPE-processed samples of human organs with diverse clinical conditions, namely, colorectal cancer, prostate cancer, and healthy placenta, we demonstrate full compatibility of the photonic chip with conventional histological workflows, including the incubation steps for deparaffinization, re-hydration, and labeling necessaries for fluorescence imaging (Figure 1c). Furthermore, by exploiting the evanescent field excitation offered by the chip, we show the superior contrast and super-resolution capabilities of the chip-based FF-SRM and highlight the interplay between the contrast and the resolution offered by the photonic chip across scalable magnifications. We further demonstrate the multimodality supported by the photonic chip for high-resolution correlative light and electron microscopy. To the best of our knowledge, this is the first study of FFPE sections on a photonic chip-based microscope and the first report of FF-SRM on FFPE sections. Photonic chip-based optical microscopy has the potential to assist in high-contrast and high-throughput super-resolution fluorescence imaging of paraffin-embedded samples, paving the road for super-resolution histology both in research and clinical settings.

Contrast enhancement approaches for histology

Contrast is an essential parameter for the visual interpretation of microscopy images. Broadly speaking, contrast is the difference between the sample signal and its surroundings, either in terms of intensity or color. In histology, a high contrast allows for clear visualization of features of interest located at the microscope objective's focal plane. However, most tissue samples are translucent, which makes it difficult to observe them under a light microscope. There are diverse mechanisms to add contrast to histological samples. These are divided into two categories, namely, label-free and histochemical methods. The first group exploits physical phenomena such as light interference in phase-contrast computed tomography[33] and differential interference contrast[34]; or light scattering in Raman spectroscopy[35], darkfield and optical coherence tomography[36]; or nonlinear optics in second harmonic generation[37] to retrieve high contrast information from the unlabeled samples. The latter group employs either light-absorbing or light-emitting compounds to chemically stain specific areas of the tissues to improve their visualization under the microscope.

Traditionally, the histology field has relied on light-absorbing dyes for the pigmentation of tissue samples. The most popular staining, hematoxylin and eosin (H&E), enables the distinction between cell nuclei, extracellular matrix, and cytoplasmic content within the tissues[38]. In addition, the immunohistochemical techniques improve the labeling specificity as compared to H&E, supporting low contrast identification of protein expression within the tissues. In combination with immunogenic approaches, the fluorescent markers also enable high labeling specificity, which makes them suitable for diverse analyses such as multiplexing[39], quantitative tissue cytometry[40], and image segmentation[41], among others. Nonetheless, the contrast ratio of fluorescent signals is greatly affected by the out-of-focus blur arising from emitting fluorophores located in the foreground and/or the background of the focal plane. Therefore, removing the off-focus information is essential for an accurate interpretation of the fluorescent data. This can be achieved in three ways:

a) **By mechanically slicing the samples into thin sections.** Typically, the thinnest section thickness for FFPE samples is approximately 2 μm – 4 μm, which is insufficient for reducing the out-of-focus signal of fluorescently-labeled tissue samples. To obtain even thinner tissue sections (down to 70 nm thickness), alternative histological approaches, such as ultrathin sectioning of resin-embedded or cryopreserved samples, have been proposed.

b) **By optical sectioning.** By manipulating the excitation and/or emission light paths to selectively illuminate and collect information from specific planes of the sample, a method called optical sectioning, it is possible to minimize the out-of-focus information. Examples of these are confocal microscopy[42], multi-photon excitation microscopy[43], total internal reflection fluorescence (TIRF) microscopy[44], and light-sheet microscopy[45].

c) **By image post-processing.** A new set of computational methods have emerged as an appealing alternative to enhance contrast by artificially removing the blurring effects caused by the out-of-focus light and the optical aberrations of the microscope system. These methods, based on mathematical algorithms such as deconvolution[46,47], structured illumination[15], computational clearing[48], and machine learning[49], greatly improve the contrast and assist in restoring the latent high-resolution signal out of the observed low-resolution fluorescence data.

Proposing TIRF for high-throughput FF-SRM histology

Contrast plays a key role in fluorescence super-resolution optical microscopy, as it defines the extent to which fine details can be observed. From a physics perspective, the optical transfer function of the imaging system acts as a low-pass filter that favors the visualization of coarse features, at the expense of a low-contrast view of the finer structures in the sample. The characteristic triangular shape of the optical transfer function dictates the contrast achievable at diverse spatial frequencies present in the sample[50]. Thus, low spatial frequencies (larger sample features) benefit from high contrast, while high spatial frequencies (smaller sample features) experience low contrast. Moreover, the recorded grayscale intensity of high spatial frequencies often matches the base level of diverse high-frequency system disturbances such as Poisson noise, electronic noise, and dark noise, which makes it even more difficult to differentiate small sample features from noise[51].

Consequently, contrast enhancement strategies are frequently implemented to improve the performance of the super-resolution methods. Among these, TIRF is an attractive route for achieving high contrast fluorescence on biological specimens, as it limits the axial illumination to a thin layer that provides optical sectioning at the interface between substrate and sample[52]. In recent studies, TIRF illumination was used in combination with single-molecule localization to achieve sub-diffraction views of FFPE samples[3,20]. However, the fields of view obtained in these studies (roughly, 50 μm × 50 μm) are too small for routine histological analysis. Although a novel prism-based SMLM approach recently showed 40 nm resolution over a half-millimeter field of view[53], like conventional SMLM approaches, the method required a large number of frames (30,000) to reconstruct a single super-resolved image. These two limitations make SMLM unattractive for high-throughput imaging of FFPE samples. Albeit not achieving as good resolution as SMLM, FF-SRM requires significantly less number of frames (usually hundreds but as low as 30 frames have been demonstrated[54]). Thus, the combination of FF-SRM with the excellent optical sectioning provided by TIRF illumination is an attractive route for high-speed imaging of FFPE tissue sections.

Results

Enabling FF-SRM histology via chip-TIRF modulation

In this part of the study, we used a human placental tissue section to demonstrate the superior performance of the photonic chip-based TIRF (chip-TIRF) over epifluorescence (in short, EPI) illumination for achieving FF-SRM on FFPE samples. Here, a chorionic villi sample was taken from the fetal side of a human placenta, dissected, and further embedded in paraffin following a standard FFPE method. Thereafter, the tissue block was sectioned into a 3 μm slice and placed on a photonic chip for further histological processing (see detailed preparation protocols in the Materials and Methods section). After fluorescence labeling, two image stacks (500 frames each) were collected over the same field of view using a 60X/1.2NA water immersion objective under EPI and chip-TIRF, respectively.

The upper segment in Figure 2a illustrates a single EPI image of an FFPE human placental tissue section. Using EPI modality, the microscope objective is utilized both for the excitation and the collection of the fluorescent signal. In the acquisition process, the excitation light beam interacts with the whole sample volume, illuminating all the fluorophores along its path, as shown in Figure 2c. Consequently, the microscope objective captures the fluorescent emission from the illuminated volume, causing out-of-focus blur. In photonic chip-based microscopy (Figure 2d), on the contrary, only the bottom part of the sample is illuminated, enabling ultrathin optical sectioning <50 nm that improves the contrast of the fluorescence microscopy image (upper segment in Figure 2b) as compared to EPI.

To further compare the performance of EPI and chip-TIRF under FF-SRM, we chose the multiple signal classification algorithm[32] (MUSICAL). Through singular value decomposition, this method achieves super-resolution by discriminating between signal and noise spaces across a given diffraction-limited fluorescence image stack. In addition, MUSICAL enables super-resolution imaging even in situations of low excitation intensities, fast acquisition, and relatively small datasets. Here, we post-processed the previously collected EPI and chip-TIRF stacks with MUSICAL. The results are illustrated in the lower segments of Figure 2a and Figure 2b, respectively. Although the EPI-MUSICAL reconstruction resulted in neither noticeable resolution nor contrast enhancement compared to the diffraction-limited EPI fluorescence image, chip-MUSICAL improved both the resolution and contrast when compared to the diffraction-limited chip-TIRF image. This improvement enabled a clearer visualization of the placental tissue structure.

The discrepancy in MUSICAL performance observed here can be attributed to the difference in fluorescence intensity fluctuations, both spatially and temporally, between the EPI and chip-TIRF imaging modalities. Specifically, the FF-SRM algorithms require high signal variance among adjacent fluorophores to successfully perform statistical analysis of the fluorescent data within an image stack. Typically, the temporal variance is derived from the gray value fluctuations occurring within consecutive frames, while the spatial variance is achieved through sparse labeling and/or illumination of the sample. As further elaborated herein, unlike EPI, the combination of MMI pattern modulation and ultrathin optical sectioning supported by the photonic chip enables the necessary fluorescence intensity fluctuations for optimal FF-SRM reconstruction of FFPE tissue sections.

In EPI, the temporal fluctuations are determined by the stochastic emission of the fluorophores. Therefore, short acquisition rates are required to minimize the averaging effects of the camera exposure time. In photonic chip-based microscopy, on the contrary, the temporal fluctuations are achieved by modulating the MMI illumination patterns on a frame-to-frame basis, which allows for longer camera exposure times. Here, this aspect is illustrated by plotting the gray values of an arbitrary pixel over the collected image stacks (blue and orange asterisks in Figure 2a and Figure 2b, respectively). Despite the longer acquisition time of the chip-TIRF modality (50 ms per frame) as compared to the short camera exposure time of the EPI modality (10 ms per frame), the photonic chip-based method enabled over 30 % frame-to-frame variability (orange line in Figure 2e), whereas EPI supported, at most, 7 % variability at the same sample location (blue line in Figure 2e). Arguably, the low variance of EPI compromised the statistical analysis of the chosen FF-SRM algorithm. The chip-TIRF stack, in turn, resulted in optimal data for FF-SRM reconstruction, as reported in previous observations[25,28-30]. Supplementary Video V2 provides a detailed view of the fluorescence fluctuations obtained in EPI and chip-TIRF modalities.

Another important parameter for successful FF-SRM reconstruction is spatial sparsity. Although FF-SRM algorithms are designed for multi-emitter datasets, these methods perform best for signals where the information is sparsely distributed in the spatial domain. The signal sparsity can be achieved by means of sparse sample labeling and/or by modulation of the illumination source. In the case of the relatively thick and densely labeled FFPE sections, spatial sparsity can be achieved by combining random illumination and thin optical sectioning. While the first can be implemented in EPI via speckle illumination[55], the optical sectioning capabilities of this imaging modality are limited by the depth of field (DOF) of the microscope objective (Figure 2c and Figure 2f), resulting in an averaged signal with low spatial sparsity. In chip-TIRF modality, on the contrary, the sample is illuminated by an evanescent field that restricts the fluorescence emission to a thin sample layer (Figure 2d and Figure 2g) and semi-stochastic MMI patters that allow both for ultrathin optical sectioning and for random illumination. In the placental section, for example, despite the relatively short DOF (approx. 520 nm) used for EPI, the abundance of fluorophores within the excited sample volume resulted in a dense signal with low spatial sparsity that complicated the EPI-MUSICAL reconstruction. In chip-based microscopy, however, the combined optical sectioning and random illumination supported by this technique successfully enabled chip-MUSICAL reconstruction. Supplementary Information S3 provides detailed information about the DOF of the diverse microscope objectives used in this study.

The high refractive index of the waveguide core material ($n \approx 2$, for Si_3N_4) provides additional advantages for histology. Firstly, it allows for high spatial frequencies in the illumination that prove advantageous for improved lateral resolution of other SRM methods such as SMLM[25] and SIM[56]. Secondly, it limits the penetration depth of the evanescent field below 50 nm for our chosen photonic chip design (Figure 2g), allowing superior optical sectioning compared to glass-based TIRF approaches employing lower refractive index materials such as borosilicate glass ($n \approx 1.52$). Furthermore, alternative waveguide materials with even higher refractive index such as titanium dioxide (TiO2, n ≈ 2.6) could potentially improve the optical sectioning to around 20 nm (see Supplementary Information S4 for details). In the next section, we further investigate how chip-TIRF assists in the histological assessment of FFPE tissue sections.
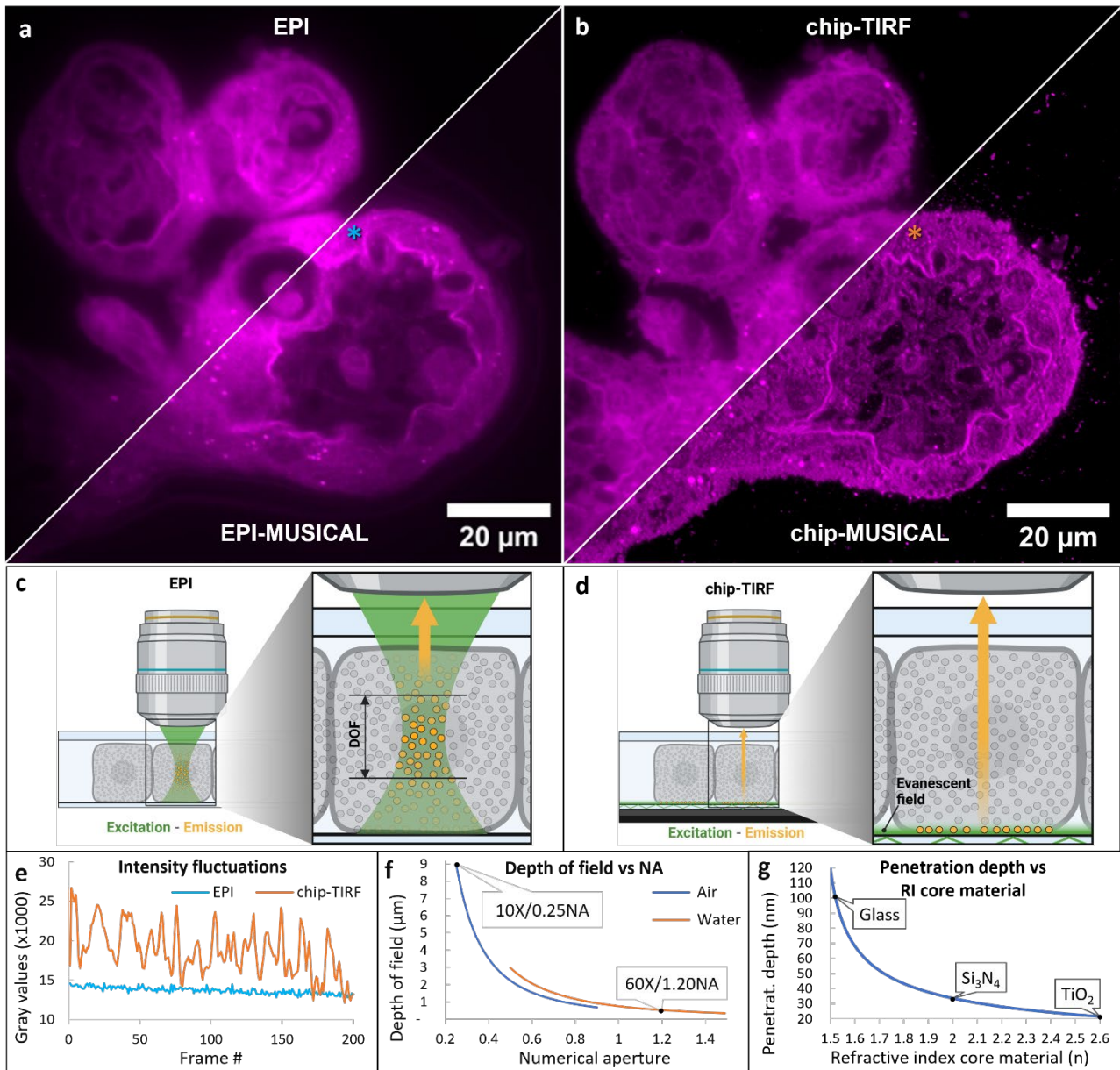
*Figure 2. **FF-SRM comparison on a human placental FFPE tissue section via EPI and chip-TIRF illumination. a)** The upper segment illustrates an EPI fluorescence image of the tissue sample. The lower segment shows the EPI-based MUSICAL reconstruction. The blue asterisk illustrates a single pixel chosen for plotting the intensity fluctuations in e). **b)** The upper segment illustrates a diffraction-limited chip-TIRF image. The lower segment shows the chip-based super-resolved image via MUSICAL. The orange asterisk illustrates a single pixel chosen for plotting the intensity fluctuations in e). **c)** Schematic representation of an EPI fluorescence image acquisition. In EPI modality, the microscope objective lens is used both for the illumination and collection of the fluorescent signal. The fluorescent signal is collected from a sample volume corresponding to the depth of field (DOF) of the objective that, for densely-labeled samples such as FFPE sections, results in a highly-averaged signal with low frame-to-frame variance. **d)** In chip-TIRF, the sample is illuminated via evanescent field excitation, allowing for ultrathin optical sectioning that minimizes the signal averaging issues while providing superior spatial and temporal variance that contribute to optimal FF-SRM reconstructions via MUSICAL. **e)** Intensity fluctuations of a single pixel over 200 frames of EPI and chip-TIRF image stacks. Chip-TIRF provides higher temporal variance compared to EPI. See Supplementary Video V2 for details. **f)** Theoretical simulation of DOF vs numerical aperture of air and water-immersion objective lenses. While in EPI the DOF leads to signal averaging, in photonic chip-based microscopy the illumination and the collection light paths are decoupled, which allows for FF-SRM irrespective of the DOF of the collection objective. See Supplementary Information S3 for details. **g)** Theoretical simulation of penetration depth vs refractive index. The penetration depth of TIRF systems is highly dependent on the refractive index contrast between the sample media (n ≈ 1.4) and the core material used for TIRF. The waveguide material (Si$_3$N$_4$, n ≈ 2) used in this work enables superior optical sectioning capabilities (<50 nm), compared to existing glass-based TIRF approaches employing materials with lower refractive index (borosilicate, n ≈ 1.52). Alternative waveguide materials such as titanium dioxide (TiO$_2$, n ≈ 2.6) can potentially improve the optical sectioning to around 20 nm. See Supplementary Information S4 for details.*

Evanescent field excitation for high-contrast histology

In this part of the study, we used an FFPE-preserved colorectal cancer sample to demonstrate two features of the photonic chip-based microscopy: a) its compatibility with standard histochemical processing techniques, and b) the superior contrast capabilities offered by this novel technique as compared to other fluorescence-based microscopy methods. To achieve this, we first explored the transition from conventional hematoxylin and eosin (H&E) staining to

fluorescent labeling and, subsequently, we focused on the contrast performance of the photonic chip-based microscopy.

Here, an FFPE colorectal sample was sectioned into two consecutive slices of approx. 1 cm × 1 cm × 3 µm (width, height, thickness) and subsequently floated in a water bath (see detailed preparation protocols in the Materials and Methods section). For conventional histology, one slice was mounted on a glass slide and histochemically prepared following H&E staining procedures. For fluorescence imaging, the remaining slice was mounted on a photonic chip and further stained with fluorescent markers against membranes and nuclei. The photonic chip withstood all the harsh steps of the histochemical processing (see Supplementary Information S5), including water immersion for sample scooping (see Supplementary Video V3), 60 °C oven incubation for paraffin melting, xylene baths for paraffin clearing, sample rehydration through descendent ethanol series, and fluorescent labeling. In addition, we successfully tested antigen retrieval steps on a different paraffin-embedded sample (see Supplementary Information S6) by microwave boiling the tissue section on the chip before immunolabeling.

The H&E-stained sample was imaged on a whole slide scanner device (Virtual Slide System V120, Olympus) using a 20X/0.85NA objective lens. The images were automatically stitched to obtain a complete view of the sample, as shown in Figure 3a. The hematoxylin, shown in purplish hues/colors, allowed the identification of nuclei whereas the eosin, in shades of pink, facilitated the observation of the cytoplasmic content and extracellular matrix. Here, the H&E staining enabled the identification of four major microanatomical areas in the colorectal sample (black-dotted lines in Figure 3a), namely, smooth muscle (Sm), necrotic tissue (Ne), benign colonic epithelium (Be), and adenocarcinoma (Ad). The identification of the diseased sections was carried out by the pathologist. While a zoom-in view of the adenocarcinoma region is sufficient to reveal the cancer cells forming glands (inset in Figure 3a), a higher resolution and contrast could further aid the visualization of the diagnostic features (see Supplementary Information S7).

Similarly, the on-chip colorectal sample was imaged on a commercial EPI fluorescence microscope (DeltaVision Elite Deconvolution Microscope, GE Healthcare) using a 10X/0.4NA objective lens. For each field of view, two consecutive images were taken using different fluorescent channels, namely, far-red channel for membranes, and green channel for nuclei (see details in the Materials and Methods section). Upon pseudocoloring and merging, the 10X EPI fluorescence images were stitched in an 8 × 8 tile mosaic to enable full visualization of the sample. The resulting image (Figure 3b) offers a full visualization of the fluorescently-labeled colorectal sample, with membranes shown in magenta and nuclei shown in cyan. Here, the grid-like artifact on the mosaic image is largely due to the non-uniform Gaussian profile characteristic of EPI illumination, which is further illustrated in Figure 4. Notably, the fluorescent labeling improves the contrast between the labeled structures, allowing for a much clearer distinction between the diverse regions of interest in the sample (white-dotted lines in Figure 3b), as compared to the H&E slide (Figure 3a). For example, in Figure 3b, the smooth muscle (Sm) region shows a dominant magenta color as compared to the neighboring adenocarcinoma (Ad) part, indicating a different distribution of nuclear content between these two regions. Similarly, it is possible to observe a higher density of nuclei (in cyan color) on the necrotic region (Ne) as compared to the other regions in the sample. Arguably, these differences are much more difficult to spot on the low-contrast view of the H&E sample, as illustrated in Figure 3a.

Further on, to prove the contrast capabilities of the photonic chip-based, we focused our attention on a region of interest within the adenocarcinoma area (yellow box in Figure 3b) and proceeded with fluorescence imaging at higher magnification using four different approaches, namely, epifluorescence microscopy (EPI, Figure 3c), deconvolution microscopy (DV, Figure 3d), photonic chip-based TIRF microscopy (chip-TIRF, Figure 3e), and chip-based FF-SRM (chip-MUSICAL, Figure 3f). Both EPI and deconvolution images were acquired on a commercial DeltaVision Elite High-resolution microscope using a 60X/1.42 oil immersion objective, while the chip-based images were taken with a 60X/1.2 water immersion objective on a custom-made upright microscopy setup (see Supplementary Information S2).

In EPI fluorescence, the off-focus light increases both the foreground and the background signal levels, introducing blur and reducing the contrast ratio between the in-focus signal and its surroundings. This blurring effect can be observed in the magnified views of nuclei and membranes (Figure 3c1 and Figure 3c2, respectively), where the background signal exhibits a characteristic fuzzy appearance inherently present in EPI fluorescence images (Figure 3c3). Hence, to improve the contrast of EPI fluorescence images, a method for out-of-focus signal removal is required.

Deconvolution microscopy (DV) is a well-established diffraction-limited method for contrast enhancement of fluorescent-based images via out-of-focus signal removal[47]. In the context of the colorectal sample used in this study, DV offers a sharper visualization of both the nuclei (Figure 3d1) and the membranes (Figure 3d2), as compared to their corresponding EPI fluorescence images (Figure 3c1 and Figure 3c2, respectively). DV offers high-contrast images near the resolution limit of the microscope (Figure 3d3). However, a close look at Figure 3d1 reveals the overlay of nuclear structures (denoted by a white-dotted box in Figure 3d1), which hampers the interpretation of the data in, for example, nuclei quantification. Arguably, the reason for the nuclear overlay seen in Figure 3d1 is the poor axial resolution. DV microscopy, like any other diffraction-limited technique, has a poorer axial resolution ($d_{axial} = 2\lambda/NA^2$) compared to its lateral resolution ($d_{lateral} = \lambda/2NA$). In practical terms, for a nuclear marker with emission wavelength $\lambda_{emission} = 523$ nm and an objective lens with numerical aperture $NA = 1.42$, this implies a theoretical axial resolution of ~520 nm versus a theoretical lateral resolution of ~184 nm. Hence, the DV method does a good job resolving side-to-side structures, but it struggles to differentiate them when they are too close in the axial direction, as is usually the case with tissue samples.

Photonic chip-based microscopy circumvents this challenge. Besides improving the contrast and the lateral resolution of the fluorescence image[57], the ultrathin optical sectioning supported by this method enables a clear identification of the nuclei shape (denoted by a white-dotted box in Figure 3e1), which further facilitates the quantification of these structures during histological analysis. In addition, chip-TIRF allows for a sharp visualization of the membrane structures in contact with the propagating waveguide (Figure 3e2). Despite the FFPE colorectal sample being relatively thick (3 µm), the photonic chip-based microscopy offered optical sectioning that resulted in a histological visualization comparable to that obtained through more advanced, complex, and expensive semithin (0.5 µm - 1 µm) and ultrathin (<100 nm) mechanical sectioning of resin-embedded samples used for light and electron microscopy, respectively[58,59].

The chip-TIRF image (Figure 3e3) can be further improved by FF-SRM algorithms to achieve an even better visualization of the colorectal sample. Here, by implementing MUSICAL on the chip-TIRF raw data, we substantially improved the contrast over the chip-TIRF images of both nuclei (Figure 3f1) and membranes (Figure 3f2), allowing for a sharp merged image (Figure 3f3) with superior contrast and resolution as compared to all fluorescence-based imaging methods illustrated in Figure 3. Importantly, the chip-based images (TIRF and MUSICAL), were acquired with a lower numerical aperture objective ($NA = 1.2$) compared to the lens ($NA = 1.42$) used for the EPI-based imaging (EPI and DV). This explains, for example, the superior boundary sharpness obtained in the DV image of nuclei (Figure 3d1) as compared to the corresponding chip-MUSICAL image (Figure 3f1). Nevertheless, photonic chip-based microscopy outperforms EPI-based methods offering superior contrast visualization of FFPE samples over large fields of view. In the next section, we explore the lateral resolution scalability offered by photonic chip-based microscopy for the study of paraffin-embedded sections.
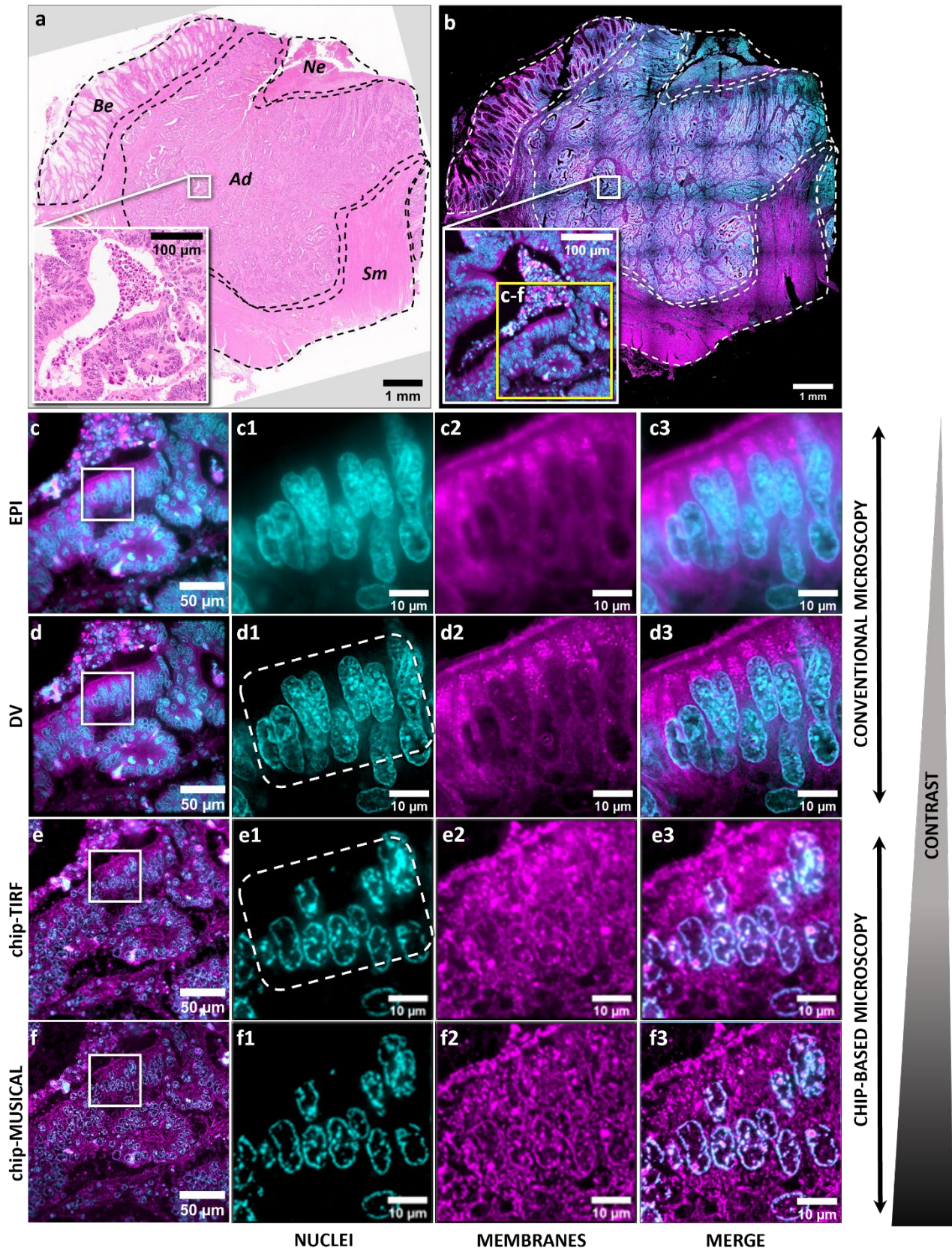
*Figure 3. **High-contrast histology via photonic chip-based total internal reflection fluorescence microscopy**. a) Bright-field image of a human FFPE colorectal cancer tissue section stained with hematoxylin and eosin. Back-dotted lines denote four major regions within the sample, namely, smooth muscle (Sm), necrotic tissue (Ne), benign colonic epithelium (Be), and adenocarcinoma (Ad). A close-up view of the Ad area allows for the identification of gland-forming tumor cells, with nuclei in purple and cytoplasm content in pink. **b)** Multicolor EPI fluorescence image of a consecutive slice, labeled with fluorescent markers against nuclei, and membranes, and pseudo-colored in cyan and magenta, respectively. The grid-like artifact is a consequence of the non-uniform Gaussian profile characteristic of EPI illumination. The fluorescent labeling not only improves the contrast between nuclei and membranes, as shown in the close-up box, but also enables a clearer distinction among the four regions of the sample compared to H&E. For example, between the Ad, the Ne, and the Sm areas. **c-f)** 60X view of the yellow box in b) under various fluorescence-based microscopy methods. **c)** EPI fluorescence microscopy image of a region of interest within the Ad. Close-up views **c1** and **c2** illustrate the nuclei and membrane channels, respectively. The merged view in **c3** exhibits a characteristic blur inherent to EPI illumination. **d)** Deconvolution microscopy image of the same region of interest in Ad. Close-up views **d1, d2,** and **d3** show a significant contrast improvement compared to their*

*corresponding EPI images. However, a detailed view inside the white-dotted line in d1 reveals the superposition of the nuclear signal that hampers the quantification of these structures. **e)** Photonic chip-based microscopy (chip-TIRF) offers ultrathin optical sectioning of the colorectal sample, enabling contrast improvement both in the lateral and axial domains. Particularly, individual nuclei can be easily identified inside the white-dotted line in e1, enabling the quantification of such structures. **f)** Statistical post-processing of the photonic chip-based microscopy raw data via fluorescence fluctuation-based SRM algorithms such as MUSICAL (chip-MUSICAL) further improves the contrast and resolution of the chip-TIRF images, enabling a detailed view of the sample. Chip-based microscopy acquired with a 60X/1.2NA provides superior contrast as compared to conventional EPI fluorescence-based methods such as EPI and DV acquired with a 60X/1.42NA.*

Super-resolution chip-based histology over scalable fields of view

Histological examination, regardless of the labeling method, often requires visualization of the tissue sample with diverse levels of magnification. Typically, low-magnification objectives are used for contextual interpretation of the sample, while higher magnification lenses are employed for the study of finer details and subcellular structures within a region of interest for the observer. Low magnification, for example, assists in the identification of large morphological features in the tissue such as cellular epithelium, glands, vessels, inflammation processes, and cancer proliferation, whereas higher magnification enables detailed views of cellular features such as organelle dynamics, nuclei shape, extracellular matrix, and protein localization. In this part of the study, we used an FFPE prostate cancer sample to illustrate the enhanced resolution offered by photonic chip-based microscopy over scalable fields of view.

Here, a prostate specimen was taken from a patient, fixed, grossed, processed, and further embedded in paraffin following standard FFPE method. Thereafter, the tissue block was sectioned to a 3 μm thin slice using a microtome and floated on a water bath. Then, the sample was scooped onto a photonic chip and further stained for nuclei and membranes (see detailed preparation protocols in the Materials and Methods section).

The fluorescence imaging was performed on a custom-made microscopy setup equipped with a photonic chip module and epifluorescence (see Supplementary Information S2). Along with the chip-based images, EPI images were also collected for the sake of direct comparison. First, the tumor area was located using a 10X/0.25NA objective lens. Thereafter, a region of interest was further examined using a 60X/1.2NA water immersion objective lens. Upon collecting individual channels, the images were pseudo-colored (nuclei in cyan, and membranes in magenta), and further merged. Figure 4a illustrates a 10X EPI fluorescent multicolor image of the prostate cancer sample with the presence of multiple glands forming cancer cells. Notably, the vignetting observed in the image, namely, the darker areas toward the borders of Figure 4a, originates from the gaussian distribution of the EPI illumination. This non-uniformity not only introduces grid-like stitching artifacts as shown in Figure 3b, but also constrains the exploitable field of view to the center of the EPI image, thereby decreasing the imaging throughput and quantitative capabilities of the microscopy system. This is similar to other approaches that have been proposed to achieve a flat field EPI illumination[60-63], which require additional optical components and calibration.

Photonic chip-based microscopy circumvents this issue providing the sample with a uniform illumination via waveguide light propagation. Figure 4b shows a 10X chip-TIRF multicolor image of the same sample region as in Figure 4a. Contrary to EPI, chip-TIRF enables a high-contrast observation of the prostate tissue sample across the whole field of view (see Supplementary Video V4). To acquire the chip-based image in Figure 4b, the excitation laser was sequentially coupled to each one of the waveguides in the field of view while TIRF images were collected with a low-magnification and low numerical aperture (10X/0.25NA) objective lens. Upon FF-SRM post-processing via MUSICAL, the individual images were finally merged to obtain a multicolor high-contrast image across a field of view spanning 1.3 mm × 1.3 mm (see Supplementary Information S8). This, in our opinion, is an important advantage offered by photonic chip-based microscopy for histology. By decoupling the excitation and the collection light paths, it is possible to uniformly excite large sample areas through evanescent field illumination, and capture the fluorescent emission essentially with any microscope objective, regardless of its numerical aperture and magnification. Conventional TIRF microscopy techniques, on the contrary, require dedicated EPI objective lenses with high numerical aperture and high magnification (for example, 60X/1.49NA) that, due to the non-uniform Gaussian illumination distribution, support an exploitable field of view of approximately 50 μm × 50 μm (ref. 21). Certainly, the waveguide spacing gaps of 25 μm (dark horizontal lines in Figure 4b) hinder the full visualization of the sample features inside the image field of view. However, this is not a scientific limitation. Future chip designs can address this issue by, for example, widening the waveguides, reducing the spacing gap down to 1 μm, or simply using chips with slab geometries with no gaps.
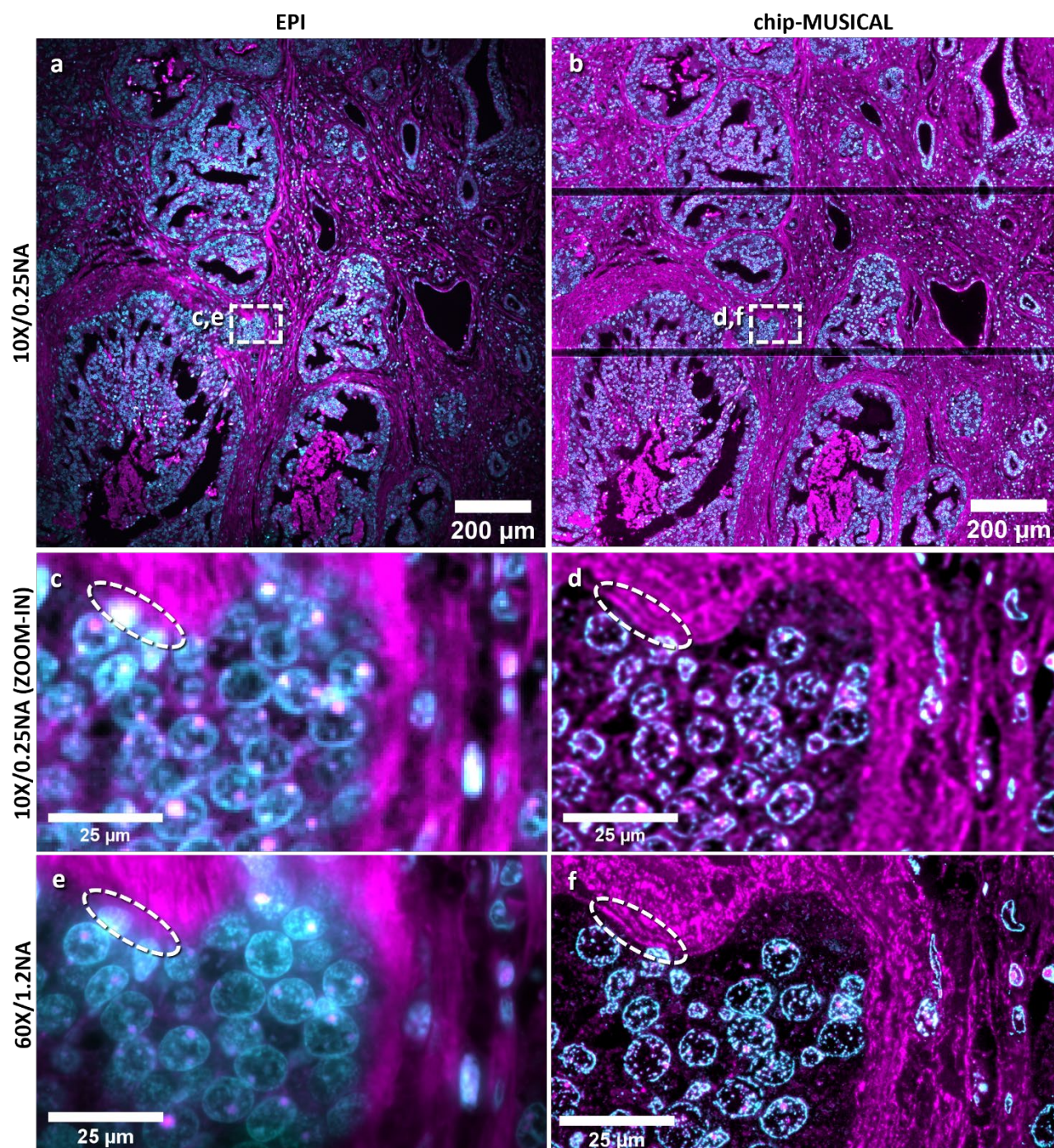
*Figure 4. **Super-resolution chip-based histology over scalable fields of view. a)** EPI fluorescence image of an FFPE prostate cancer sample acquired in low magnification with a 10X/0.25 objective lens. Nuclei are shown in cyan and membranes in magenta. The vignetting pattern around the borders of the image is due to the non-uniform Gaussian profile characteristic of EPI illumination. The white-dotted box represents the region of interest further discussed in c) and e). **b)** Same sample area as in a) imaged with chip-based TIRF illumination using a 10X/0.25 objective lens and further analyzed with MUSICAL. The dark horizontal lines denote the location of 25 µm-wide spacing gaps between adjacent waveguides. The white-dotted box represents the region of interest further discussed in d) and f). **c)** Zoom-in view of the white-dotted box segment in a). **d)** Zoom-in view of the white-dotted box segment in b). The white-dotted oval in the 10X chip-MUSICAL image denotes the location of membrane structures that are otherwise not distinguishable in the same region of the 10X EPI fluorescence image. **e)** EPI fluorescence image of the white-dotted box segment in a) acquired in higher magnification using a 60X/1.2NA objective lens. Despite the highly detailed visualization achieved here, 10X/0.25NA chip-MUSICAL outperforms 60X/1.2NA EPI fluorescence in visualizing the membrane structures denoted by the white-dotted oval. **f)** Chip-MUSICAL image acquired with a 60X/1.2NA surpasses the lateral resolution of 60X/1.2NA EPI, reaching down to 194 nm, thus allowing for a sharper visualization of the cellular features previously seen in d).*

Further on, a zoom-in view of the white-dotted box areas in Figure 4a and Figure 4b, respectively, revealed the advantages of photonic chip-based microscopy (Figure 4d) over conventional EPI fluorescence microscopy (Figure 4c). In particular, chip-MUSICAL not only improved the sample contrast but also allowed the visualization of membrane structures (denoted by the white-dotted oval inside Figure 4d) that otherwise were not visible in EPI (denoted by the white-dotted oval inside Figure 4c). To estimate the resolution of these two microscopy methods, we performed a decorrelation analysis[64] over the 10X images of membranes (see Supplementary Information S9). While the EPI

fluorescence image rendered a lateral resolution of 1.56 µm, chip-MUSICAL delivered nearly a 1.2-fold improvement compared to EPI, achieving a lateral resolution of 1.31 µm.

To achieve an even higher resolution over the same region as in Figure 4c and Figure 4d, we swapped the collection objective lens to a higher magnification and higher numerical aperture (60X/1.2NA) and repeated the image acquisition steps both for EPI fluorescence and chip-MUSICAL. While the 60X images provided a clearer definition of the cellular elements as compared to its corresponding 10X images, a decorrelation analysis (see Supplementary Information S10) revealed a ~2.4-fold lateral resolution gap between the high-magnification EPI fluorescence (Figure 4e) and the high-magnification chip-MUSICAL (Figure 4f). More specifically, 461 nm in EPI versus 194 nm in chip-MUSICAL using a 60X/1.2NA objective lens. Notably, the 10X/0.25NA chip-MUSICAL (Figure 4d) outperformed the 60X/1.2NA EPI fluorescence (Figure 4e) in, for example, visualizing the membrane features located inside the white-dotted oval. This result suggests that chip-based histology could potentially enable high-resolution and high-throughput imaging of tissues over large fields of view, employing low magnification objectives, which could further facilitate the screening of FFPE samples in clinical settings.

Chip-based CLEM histology

Both fluorescence and electron microscopy provide unique information about the samples under observation. While fluorescence microscopy offers high specificity and high-contrast details, electron microscopy enables the visualization of features down to the ultrastructural level. Hence, combining these two microscopy modalities is advantageous for histological analysis. While several correlative light and electron microscopy (CLEM) studies exist in the histological field [65-67], the tissue preservation method employed in conventional approaches consisted mainly of cryo-preservation or resin embedding. Over the last decade, however, innovative research has shown the potential of incorporating FFPE samples into the CLEM analysis to, for example, study inflammatory processes[68], identify virus particles in diseased organs[69], and render a high-definition topographic visualization of thick tissue sections[70]. Here, we propose photonic chip-based microscopy as a feasible platform for combining high-contrast fluorescence-based imaging with high-resolution scanning electron microscopy (SEM) of paraffin-embedded sections.

In this part of the study, we used a human placental tissue section to demonstrate the compatibility of the photonic chip for correlative light and electron microscopy of FFPE samples. Here, a chorionic villi sample was taken from the fetal side of a human placenta, dissected, and further embedded in paraffin following standard FFPE method. Thereafter, the tissue block was sectioned into a 3 µm slice and fluorescently labeled for nuclei and membranes (see detailed preparation protocols in the Materials and Methods section).

A common challenge for correlative imaging is finding the same region of interest across different microscopy systems. The photonic chip can be fabricated with a landmark coordinate system along the spacing gaps between the waveguides that facilitates the navigation through the sample[71]. To perform CLEM imaging on the FFPE placental sample, we first used a low-magnification objective (10X/0.25NA) in EPI fluorescence mode to find a region of interest (ROI). Thereafter, we switched to bright field imaging mode to visualize the landmarks around the ROI and, further on, we combined the bright field and the EPI images (Figure 5a) to obtain a combined view of both the landmarks (Figure 5c) and the fluorescent signal (membranes in magenta and nuclei in cyan) within the same field of view. Then, to achieve a detailed visualization of the ROI, we transitioned to a higher magnification collection objective (60x/1.2NA) and performed chip-based FF-SRM via MUSICAL (Figure 5e). Upon completion of fluorescence imaging, the coverslip was carefully removed and the sample was subsequently dehydrated and coated with a gold/palladium alloy following the preparation steps for SEM (see Materials and Methods section). Thereafter, the chip was placed on an SEM device (GeminiSEM 300, Zeiss) and imaged at low magnification to navigate through the chip landmark coordinates (Figure 5d) and quickly find the region of interest (Figure 5b). Further SEM magnification allowed for a topographic visualization (Figure 5f) of the same ROI obtained via waveguide illumination (Figure 5e). This feature enabled a high-detail identification of structures observed both in fluorescence and in electron microscopy. For example, a zoomed-in view of the placental tissue in Figure 5g revealed the microvilli (MV) brush border outlining the apical side of the syncytiotrophoblasts (SYN). Similarly, a zoomed-in view of the same region in SEM (Figure 5h) validated the previous observation indicating that, in fact, the microvilli imaged through chip-based illumination matched the structures at the bottom of the tissue sample in direct contact with the waveguide surface. This demonstrated the ground truth for on-chip MUSICAL with SEM images. Moreover, the overlay between the chip-based and the SEM images (Figure 5i)

showed a perfect correlation between the two imaging methods, which was further scalable to the complete field of view (see Supplementary Video V5).

The CLEM study also allowed us to further evaluate our hypothesis of FFPE sample detachment. In the case of the placental section (see details in Supplementary Information S12), for example, the fluorescence signal discontinuity observed in the chip-TIRF image around the apical side of the upper villus (yellow asterisk in Figure 5e), matched the location of a micro-detachment gap visualized in the subsequent SEM image (yellow asterisk in Figure 5f). Supplementary Information S13 summarizes the optimization steps carried out to enable optimal sample adhesion.
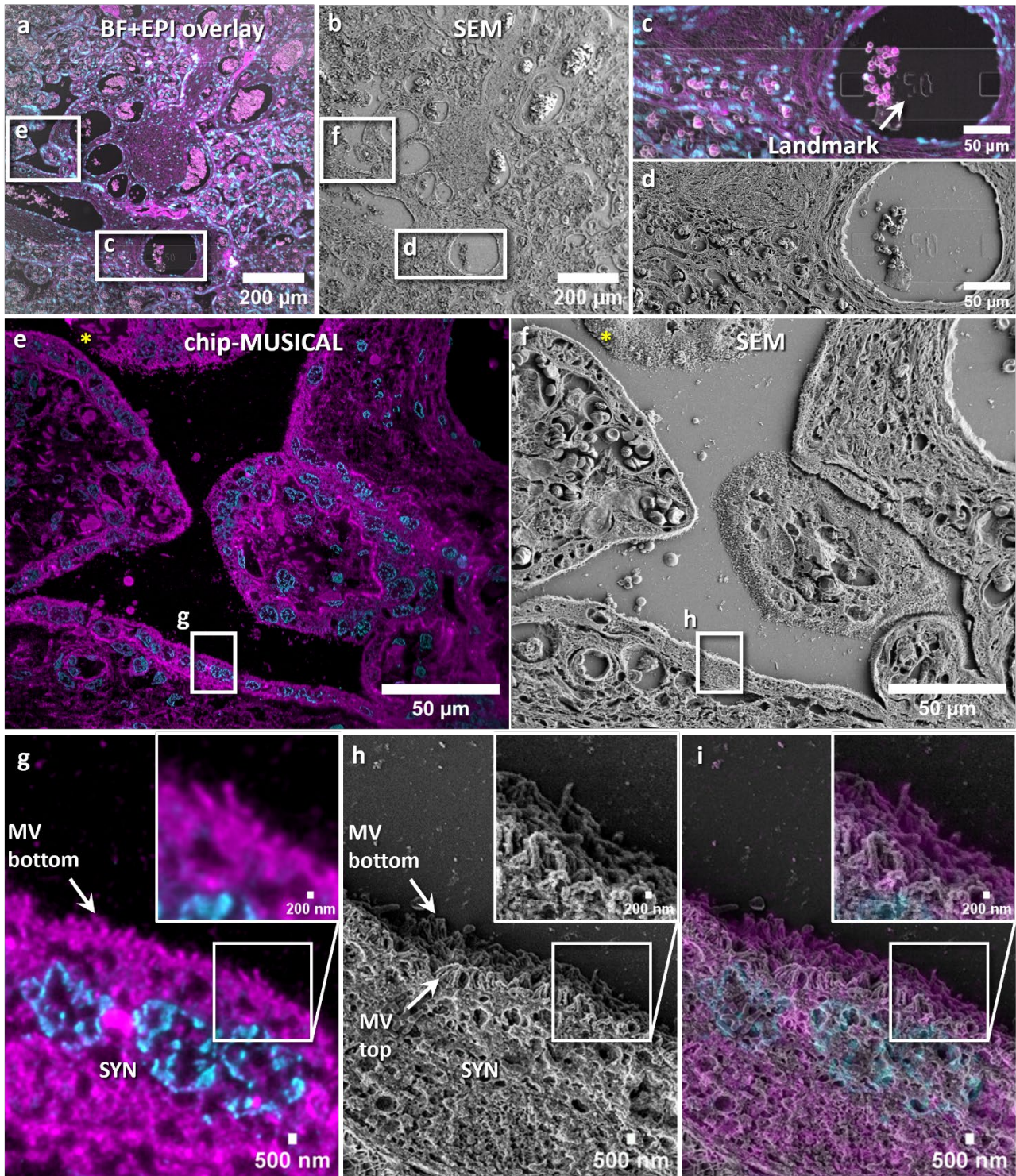
Figure 5. **Chip-based CLEM histology of an FFPE placental tissue section. a)** *10X magnification bright field and EPI fluorescence overlay image of a region of interest within the placental sample. Membranes are shown in magenta and nuclei in cyan. The white box at the bottom denotes the location of a landmark that is used to find the sample in the scanning electron microscope (SEM). The white box to the left side of the image denotes the region of interest imaged at higher magnification in e).* **b)** *Low-magnification SEM image of the same region imaged in a). The white box at the bottom denotes the location of the landmark coordinate described in a). The white box to the left side of the image denotes the region of interest imaged at higher magnification in f).* **c-d)** *Zoom-in view of the landmark coordinate (Y50) used for the localization of the same region of interest among different microscope systems.* **e)** *Chip-based super-resolution image of chorionic villi reconstructed via MUSICAL. The white box at the bottom of the image denotes the*

location of a region of interest further described in g). The yellow asterisk denotes a detached sample region (see details in Supplementary Information S12). ***f)*** *SEM image of the same sample region imaged in e). The white box at the bottom of the image denotes the location of a region of interest further described in h). The yellow asterisk denotes a detached sample region (see details in Supplementary Information S12).* ***g)*** *Zoom-in view of the chip-based image reveals the microvilli brush border outlining the syncytiotrophoblast (SYN).* ***h)*** *Zoom-in view of the same sample region as g) confirms the presence of microvilli along the volume of the sample.* ***i)*** *The image overlay shows an excellent correlation between the chip-based and the SEM images. Importantly, the microvilli outline in g) matches the location of the structures in direct contact with the waveguide surface at the bottom of h).*

Conclusion and Discussion

The FFPE on-chip method proposed here offers advantages for the practical adoption of fluorescence-based super-resolution histology (see details in Supplementary Information S11). In particular, the ultrathin optical sectioning combined with the MMI illumination pattern modulation supported by the photonic chip allows for a seamless implementation of FF-SRM methods such as MUSICAL, which otherwise fail for densely labeled samples such as FFPE tissue sections, as shown in Figure 2. Moreover, the TIRF illumination offered by the photonic chip enables high-contrast images, allowing for accurate identification of morphological features irrespective of the objective lens magnification used, as highlighted in Figure 4. The photonic-chip illuminates the sample along the entire length of the waveguide and, with future integration of microlens arrays[72] in the collection light path, it could be envisioned a dramatic speed enhancement of the photonic chip-based system, supporting image acquisition along the entire length of guiding waveguides. Similarly, the incorporation of multiplex coupling automation could also boost the imaging throughput of photonic chip-based microscopy by, for example, allowing for simultaneous image acquisition of several waveguides in a similar fashion to existing whole slide scanners used in routine histopathology laboratories. Another key advantage of photonic chip-based microscopy is the uniform sample visualization delivered by waveguide illumination (Figure 4). Chip-TIRF enables the exploration of the whole image field of view, therefore increasing the imaging throughput as compared to conventional EPI-based microscopy methods that suffer from reduced field flatness. We envision that, upon further assistance of machine-learning approaches[49,73], the big data of high-resolution images over large fields of view supported by photonic chip-based microscopy could also facilitate histological interpretability and diagnosis.

Another benefit of the photonic chip for histology is its compatibility with the conventional FFPE sample preparation protocols. Notably, the chips used in this study resisted all the harsh processing steps associated with deparaffinization, rehydration, and antigen retrieval for fluorescence (immuno)labeling. Admittedly, the relatively small size of the photonic chips utilized here (roughly, 2.5 cm × 2.5 cm), resulted in manual processing of the samples (see Supplementary Information S5). However, the chips could be manufactured with the same dimensions as traditional glass slides, enabling compatibility with commercial histochemical processing devices and fluorescence immunostaining machines. Similarly, the current imaging limitation imposed by the spacing gaps (Figure 4b) could easily be addressed by redesigning the photonic chip top layer geometry to accommodate wider optical waveguides, for example, ~5 mm wide, which can fill the entire field of view of low magnification objectives, or by narrowing the spacing gap width down to ~1 μm or using a slab waveguide with no gap.

In this study, we focused our florescence labeling efforts on two direct markers, for nuclei and membranes, respectively, to enable a one-to-one comparison with standard H&E staining (see details in the Materials and Methods section). However, photonic chip-based microscopy is also compatible with fluorescence immunolabeling approaches (Supplementary Information S6), enabling a highly specific visualization of histological features that are relevant both for research and clinical diagnosis. We envision that, upon integration of microfluidic systems, the photonic chip could also be used in combination with advanced fluorescent labeling techniques such as DNA-PAINT[74] and exchange-PAINT[75] for high-content multi-omic screening[76], as well as for multiplex super-resolution imaging of FFPE samples via SMLM[3].

We did encounter sample detachment challenges that deserve further attention, as they compromise the imaging capabilities of the photonic chip (see Supplementary Information S12). Future studies should address the adhesion of the paraffin-embedded slices to the chip surface, to successfully achieve whole-sample TIRF imaging. Alternative histochemical processing methods such as resin embedding could also be explored to enable optimal sample attachment and subsequent chip-based imaging.

Importantly, chip-TIRF is limited to a 2D visualization of the part of the sample in contact with the waveguide surface. However, as demonstrated here, the photonic chip is compatible with alternative fluorescence-based imaging

modalities, such as EPI and DV, which provide a complementary volumetric view of the tissue section that further assists in the histological interpretation. In addition, the embedded landmark coordinate system allows for effortless navigation over large tissue samples to localize the same regions of interest among different imaging systems. This proved useful, for example, in the correlative light and electron microscopy study of the placental section. Lastly, the combination of section thickness (2 – 4 μm) and refractive index heterogeneity imposed by the FFPE samples, can introduce optical aberrations in the form of light scattering[77] that could potentially hinder the contrast and resolution of the chip-based microscopy. To mitigate this, two approaches can be explored: a) homogenizing the refractive index of the tissue via optical clearing[78], or b) using transparent chips in combination with an inverted microscope setup to avoid light scattering of the fluorescent signal[57].

Acknowledgments

Author contribution

BSA conceived the idea, secured the project, and supervised the project. LEVH and BSA planned and coordinated the experiments. LEVH, VD, and HM performed sample labeling, chip-TIRF imaging, and post-processing of the data. VD built the chip-based microscope setup. SA and KA assisted with MUSICAL reconstructions. HED coordinated and provided the colorectal and prostatic FFPE sections. MP assisted in the interpretation of the colorectal and prostatic samples. HM and LEVH performed the SEM imaging of the placental section. JCT assisted in the photonic chip design and fabrication logistics and the design and assembly of the chip-based microscope setup. DHH assisted with the software integration and mechanical engineering for chip-TIRF imaging. GA provided the placental sample. MN helped with the collection, preservation, and image interpretation of the placental sample. KAF collected and preserved the mouse kidney tissue (supplementary) and assisted with the renal image interpretations. BZ assisted with the measurements and interpretation of the AFM data of the colorectal sample (supplementary). LEVH analyzed the data, prepared the figures and the supplementary videos of the manuscript, and wrote the manuscript. LEVH and BSA wrote the first draft of the manuscript and all authors contributed to writing and revising selected sections of the manuscript.

Ethics declarations

Conflict of interest

BSA has applied for a patent for chip-based optical nanoscopy and he is co-founder of the company Chip NanoImaging AS, which commercializes on-chip super-resolution microscopy systems. Other authors declare no conflicts of interest.

Materials and Methods

Photonic chip description and fabrication

The photonic chip is made of three layers (see Figure 1a), namely, a substrate of silicon (Si), an intermediate layer of silicon dioxide (SiO_2), and a top optical waveguide layer of silicon nitride (Si_3N_4). The high refractive index contrast between the waveguide material ($n \approx 2.0$) and the sample medium ($n \approx 1.4$), allows a confined propagation of the

excitation light along the waveguide via total internal reflection (TIR), which in turn provides evanescent field excitation to the fluorescent molecules in the vicinity of the waveguide (see Supplementary Information S4), hence enabling chip-based total internal reflection fluorescence (chip-TIRF) microscopy. Previous studies have explored diverse waveguide geometries for chip-TIRF microscopy. These include slab, rib, and strip waveguides[25]. In this work, we chose 140 nm height uncladded strip waveguides with widths varying from 200 µm to 1000 µm (see Figure 1b).

The photonic chips used here were manufactured at SINTEF MiNaLab (Oslo, Norway), following a standard photolithography CMOS fabrication process as described elsewhere[25,26]. Briefly, a silicon dioxide layer of 2 µm thickness was thermally grown on a silicon chip. Thereafter, a layer of silicon nitride was deposited using low-pressure chemical vapor deposition at 800°C. To delineate the diverse strip waveguide geometries, reactive ion etching (RIE) over a photoresist mask was employed. Next, the remaining photoresist was removed before depositing a top cladding layer of 2 µm via plasma-enhanced chemical vapor deposition at 300°C. To allow for TIRF imaging, the top cladding was removed from the central portion of the chip using RIE and wet etching. All waveguides were fabricated with a thickness of 140 nm.

Sample origin and ethical approvals

Human prostate samples were obtained from male patients following radical prostatectomy at the Norwegian Radium Hospital (Oslo, Norway). Colorectal samples were obtained after resection from human patients at Aker University Hospital (Oslo, Norway). Full-term placentas from healthy patients were collected immediately after delivery at the University Hospital of North Norway (Tromsø, Norway). All samples were fixed in formalin and embedded in paraffin following standard histological methods. All samples were anonymized following the guidelines of the Regional Committees for Medical and Health Research Ethics of Norway (REK). No personal data was attached to the biological samples used in this study.

FFPE tissue sectioning

The paraffin blocks were cooled down at 4 °C before sectioning into 3 µm to 4 µm slices. The FFPE samples were sectioned using two automatic microtomes (HM 355S, Thermo Fisher Scientific) equipped with a water bath. The FFPE prostate and colorectal samples were sectioned at the Institute for Cancer Genetics and Informatics (Oslo, Norway). The placental samples were sectioned at the Department of Clinical Medicine at UiT – The Arctic University of Norway (Tromsø, Norway).

H&E staining and widefield imaging of the colorectal sample

Upon sectioning, the paraffin-embedded colorectal slice was placed on a superfrost plus glass slide (J1800AMNZ, Epredia) and histochemically stained with H&E. Thereafter, the colorectal sample was imaged on a whole slide scanner device (Virtual Slide System V120, Olympus) using a 20X/0.85NA objective lens in widefield illumination. The individual images were automatically stitched in a tile-mosaic array by the proprietary software available on the scanning device. An experienced pathologist identified and annotated the four regions of the sample (adenocarcinoma, benign epithelium, necrosis, and smooth muscle).

On-chip FFPE fluorescence labeling

The on-chip FFPE samples were manually processed as follows (see Supplementary Information S5): the photonic chips were first coated with 0.1 % poly-L-lysine (P8920, Sigma-Aldrich) and then glued to conventional glass slides for easier handling using picodent twinsil dental glue (1300-1000, Picodent). Upon sectioning, the paraffin-embedded slices were scooped from the water bath and deposited on the central portion of the photonic chips (see Supplementary Video V3). The sections were dried on a flat surface at room temperature (1 × 1 h) and then transferred to a 60 °C incubation oven (TS4057, Termaks) for overnight melting (approx. 16h) of the paraffin. Thereafter, the samples were transferred to a wash-N-dry coverslip rack (Z688568, Sigma-Aldrich) for further processing steps in glass beakers of 100 mL capacity. The samples were deparaffinized in xylene (3 × 5 min), and rehydrated in descendent series of ethanol starting from 100 % (2 × 10 min), to 96 % (2 × 10 min), and finally 70 % (1 × 10 min). Subsequently, the samples were washed with MilliQ water (5 min) before placing them on a flat surface for fluorescence labeling. For membrane staining, the samples were incubated (1 × 15 min) in a 1:2000 solution of MitoTracker Deep Red FM (M22426, Invitrogen) in phosphate-buffered saline (PBS), (D8662, Sigma-Aldrich). Except for the FFPE placental section in Figure 2, all the other FFPE sections in this study were subsequently labeled for nuclei. For this, the samples were rinsed (1 ×

10 sec) and washed with PBS (2 × 5 min), and further incubated in a 5 µM solution of Sytox Green (S7020, Invitrogen) in PBS for nuclei staining. Next, the samples were rinsed (1 × 10 sec) and washed with PBS (2 × 5 min) before mounting with glycerol (G5516, Sigma Life Science) and covering with #1.5 coverslips of 22 mm × 22 mm (631-0125, VWR). The staining and washing steps were performed with single-channel micropipettes (Finnpipette F2, Thermo Scientific) and an aspirator pump (FTA-1, BioSan). The incubation volumes were between 300 µL and 500 µL depending on the sample area dimensions. The samples were sealed with picodent twinsil dental glue and stored at 4 °C protected from the light until imaging. The microscopy observations were performed within 1 to 3 days after labeling. Supplementary Information S16 provides a detailed description of the materials and reagents used for on-chip FFPE fluorescence labeling.

EPI fluorescence and DV imaging of the FFPE colorectal sample

Upon on-chip deposition and fluorescence labeling, the photonic chip containing the colorectal cancer was glued to a standard glass slide employing adhesive tape and turned upside down for observation on an inverted fluorescence microscope (DeltaVision Elite Deconvolution Microscope, GE Healthcare). To visualize the totality of the colorectal sample (Figure 3b), a 10X/0.4NA air objective lens in EPI fluorescence mode was used. To achieve multicolor images, two consecutive images were taken for each field of view. The far-red channel ($\lambda_{\mathrm{excitation}}$ = 632 ± 11 nm, $\lambda_{\mathrm{emission}}$ = 679 ± 17 nm) for membranes, and green channel ($\lambda_{\mathrm{excitation}}$ = 475 ± 14 nm, $\lambda_{\mathrm{emission}}$ = 525 ± 24 nm) for nuclei. The exposure time and the illumination power were adjusted to obtain a maximum of 10000 grayscale counts on the camera chip. The frames were automatically stitched into an 8 × 8 tile mosaic image by the built-in software package SoftWoRx available on the instrument and further pseudo-colored in the open-source software Fiji[79]. The regions of interest were mapped to the annotations made by the expert pathologist on the H&E colorectal slide.

For a higher magnification view of the colorectal sample, a 60X/1.42NA oil immersion objective was used. To obtain optimal results, we used an immersion oil with a refractive index n = 1.516. For EPI fluorescence observation (Figure 3c), two consecutive single-plane images were taken over the same field of view, following the imaging strategy of 10X EPI fluorescence. For DV imaging (Figure 3d), a total of 48 z-plane frames with z-steps of 250 nm were collected on each imaging channel along the optical axis of the objective. Thereafter, individual z-planes were deconvolved with the built-in SoftWoRx package. Finally, a deconvolved frame at the center of the stack (z = 29) was chosen for the analysis.

Chip-based imaging of FFPE samples

To build up the photonic chip-based microscope setup, a modular upright microscope (BXFM, Olympus) and a custom-built photonic chip module were used (Supplementary Information S2). The excitation light was provided by a multi-wavelength fiber-coupled laser (iChrome CLE, Toptica), which was expanded and collimated through an optical fiber collimator (F280APC-A, Thorlabs) to fill the back aperture of the coupling objective (NPlan 50X/0.5NA, Olympus). The excitation wavelengths used in this study were mainly λ_1 = 640 nm, and λ_2 = 488 nm. To optimize the light coupling and subsequent scanning along the waveguide input facet, both the optical fiber collimator and the coupling objective were mounted onto an ensembled translation system consisting of a miniature piezo-controllable X-axis stage (Q-522 Q-motion, PI) fitted onto an XYZ translation stage (Nanomax300, Thorlabs). The photonic chips were placed on a custom-made vacuum chuck fitted on an X-axis translation stage (XRN25P, Thorlabs) for large-range scanning of parallel waveguides. Upon coupling the excitation light onto a selected waveguide, the fluorescent emission of the samples was accomplished via evanescent field excitation (Figure 1a). The fluorescent signal was collected using a variety of MO lenses depending on the desired FOV, magnification, and resolution. These include 4X/0.1NA air, 10X/0.25NA air, 20X/0.75NA air, and 60X/1.2NA water immersion. To block out the excitation signal at each wavelength channel, an emission filter set comprising a long-pass filter and a band-pass filter was employed (details in Supplementary Information S2). After passing the 1X tube lens (U-TV1X-2, Olympus), the fluorescence signal was captured by an sCMOS camera (Orca-flash4.0, Hamamatsu). Both the camera exposure time and the laser intensity were adjusted according to the experimental requirements. In the case of chip-TIRF imaging, the camera exposure time was set between 50 ms and 100 ms, and the input power was gradually increased until the mean histogram values exceeded 500 counts. Typical input powers were between 10 % and 60 % depending on the coupling efficiency and the waveguide width. To minimize photobleaching of the fluorescent tags, the chip-TIRF acquisition was sequentially performed from less energetic (λ_1 = 640 nm) to more energetic (λ_2 = 488 nm) excitation wavelengths. To achieve uniform illumination of the sample, the coupling objective was scanned along the waveguide's input facet

width in lateral steps of < 1 μm while individual images were acquired. Usually, image stacks between 200 and 1000 frames were collected. To obtain multicolor images, the process was repeated at different excitation wavelengths according to the fluorescent markers available on the sample. To ensure mechanical stability, the microscope body was fixed to the optical table, while the photonic chip module was placed onto a motorized stage (8MTF, Standa) for scanning across the XY directions. An optical table (CleanTop, TMC) was used as the main platform for the chip-TIRFM setup.

EPI fluorescence imaging of FFPE samples on a chip-based setup

To enable a volumetric view of the FFPE samples in bright field (BF) and EPI fluorescence modes, respectively, the chip-based microscope setup was equipped with a halogen lamp (KL1600 LED, Olympus) and a secondary multi-wavelength fiber-coupled laser (iChrome CLE, Toptica) with the same laser spectrum as for the waveguide illumination. Both the BF and the EPI signals were acquired using a beam splitter and a series of dichroic mirrors (details in Supplementary Information S2).

For the FF-SRM comparison shown in Figure 2, the placental section was imaged in EPI fluorescence mode, using a 640 nm laser wavelength at 3 % transmission power. To collect the intrinsic fluorescence fluctuations of the fluorophores, the camera was set to a short acquisition time of 10 ms. The collected EPI image stack consisted of 500 frames. For illustration purposes, the image stack shown in Supplementary Video V2 was shortened to only the first 200 frames.

Correlative light-electron microscopy of placenta

After chip-TIRF imaging, the placental sample was brought to the Advanced Microscopy Core Facility at UiT – The Arctic University of Norway (Tromsø, Norway) for further preparation and SEM imaging. First, the picodent twinsil glue was removed from the edges of the coverslip. Thereafter, the photonic chip was immersed and washed with PHEM buffer[46] to dilute the glycerol and facilitate the coverslip detachment. Then, the sample was treated in freshly made 1 % tannic acid in 0.15 M cacodylic buffer for 1 hour, followed by 1 % osmium tetroxide (OsO_4) in 0.1 M cacodylic buffer for 1 hour, and dehydrated in incremental ethanol series (30 %, 60 %, 90 % for 5 minutes each, and 5 times 100 % ethanol for 4 minutes). Next, the sample was incubated twice in hexamethyldisilazane for 2 minutes each and carbon-taped to a 25 mm diameter SEM stub followed by silver glue for electrical conduction. Then, the chip with the sample was stored in a desiccator overnight to allow dehydration. Subsequently, the chip was coated with a 10 nm layer of gold/palladium alloy and brought to a scanning electron microscope (GeminiSEM 300, Zeiss) for SEM imaging at low accelerating voltage using an in-lens detector. Also, to enable a topographic view of the placenta, the sample was tilted 25 degrees and imaged with a secondary electron detector using low accelerating voltage.

Image processing and analysis

The acquired chip-TIRF stacks were computationally averaged using the *Z Project* tool in Fiji[79]. Thereafter, the averaged channels were merged and pseudo-colored with the *Merge Channels* tool (FIJI) to obtain multicolor chip-TIRF images.

For chip-MUSICAL reconstructions, a Python implementation of soft-MUSICAL[80] was used. The size of the sliding window was set to 7 x 7 pixels, and the sub-pixelation to 5. Pixel sizes of 650 nm and 108 nm were used for the 10X/0.25NA and the 60X/1.2NA image stacks, respectively. The signal wavelength was set according to the emission wavelength of the given marker, namely 670 nm for the MTDR, and 520 nm for the Sytox Green. The MUSICAL reconstructions were further adjusted using the *Log* transform and pseudo-colored in FIJI.

For CLEM, the acquired chip-TIRF stacks were first processed with soft-MUSICAL and then correlated with the SEM image using the TrakEM2 plugin[81].

Figure and video rendering

The schematic representations shown in this manuscript were created with BioRender.com. The supplementary videos were assembled with Microsoft´s Clipchamp app.

References

1. Donczo, B. & Guttman, A. Biomedical analysis of formalin-fixed, paraffin-embedded tissue samples: The Holy Grail for molecular diagnostics. *J Pharm Biomed Anal* **155**, 125-134 (2018).

2. Tarling, T. E., Byrne, J. A. & Watson, P. H. The Availability of Human Biospecimens to Support Biomarker Research. *Biomarker Insights* **17**, 11772719221091750 (2022).

3. Creech, M. K., Wang, J., Nan, X. & Gibbs, S. L. Superresolution imaging of clinical formalin fixed paraffin embedded breast cancer with single molecule localization microscopy. *Scientific reports* **7**, 1-10 (2017).

4. Schobesberger, M. *et al.* Gene expression variation between distinct areas of breast cancer measured from paraffin-embedded tissue cores. *BMC cancer* **8**, 1-7 (2008).

5. Kalmar, A. *et al.* Gene expression analysis of normal and colorectal cancer tissue samples from fresh frozen and matched formalin-fixed, paraffin-embedded (FFPE) specimens after manual and automated RNA isolation. *Methods* **59**, S16-S19 (2013).

6. Piehowski, P. D. *et al.* Residual tissue repositories as a resource for population-based cancer proteomic studies. *Clinical Proteomics* **15**, 1-12 (2018).

7. Skrede, O.-J. *et al.* Deep learning for prediction of colorectal cancer outcome: a discovery and validation study. *The Lancet* **395**, 350-360 (2020).

8. Kennedy, R. D. *et al.* Development and independent validation of a prognostic assay for stage II colon cancer using formalin-fixed paraffin-embedded tissue. *Journal of Clinical Oncology* **29**, 4620-4626 (2011).

9. Kopp, J. B. *et al.* Podocytopathies. *Nature Reviews Disease Primers* **6**, 68 (2020).

10. Werner, C., Onnebrink, J. G. & Omran, H. Diagnosis and management of primary ciliary dyskinesia. *Cilia* **4**, 1-9 (2015).

11. Lu, J.-X. *et al.* Molecular structure of β-amyloid fibrils in Alzheimer's disease brain tissue. *Cell* **154**, 1257-1268 (2013).

12. Prakash, K., Diederich, B., Heintzmann, R. & Schermelleh, L. Super-resolution microscopy: a brief history and new avenues. *Philosophical Transactions of the Royal Society A* **380**, 20210110 (2022).

13. Lelek, M. *et al.* Single-molecule localization microscopy. *Nature Reviews Methods Primers* **1**, 39 (2021).

14. Willig, K. I. *et al.* STED microscopy reveals that synaptotagmin remains clustered after synaptic vesicle exocytosis. *Nature* **440**, 935-939 (2006).

15. Heintzmann, R. & Huser, T. Super-resolution structured illumination microscopy. *Chemical reviews* **117**, 13890-13908 (2017).

16. Pawlowska, M. *et al.* Embracing the uncertainty: the evolution of SOFI into a diverse family of fluctuation-based super-resolution microscopy methods. *Journal of Physics: Photonics* **4**, 012002 (2021).

17. Artelt, N. *et al.* Comparative analysis of podocyte foot process morphology in three species by 3D super-resolution microscopy. *Frontiers in Medicine* **5**, 292 (2018).

18. Siegerist, F. *et al.* Structured illumination microscopy and automatized image processing as a rapid diagnostic tool for podocyte effacement. *Scientific reports* **7**, 11473 (2017).

19. Xu, J. *et al.* Super-resolution imaging reveals the evolution of higher-order chromatin folding in early carcinogenesis. *Nature communications* **11**, 1899 (2020).

20. Wunderlich, L. C. *et al.* Superresolving the kidney—a practical comparison of fluorescence nanoscopy of the glomerular filtration barrier. *Analytical and Bioanalytical Chemistry* **413**, 1203-1214 (2021).

21. Helle, Ø. I. *et al.* Nanoscopy on-a-chip: super-resolution imaging on the millimeter scale. *Optics express* **27**, 6700-6710 (2019).

22. Samanta, K. *et al.* Transmission structured illumination microscopy with tunable frequency illumination using tilt mirror assembly. *Scientific Reports* **13**, 1453 (2023).

23. Demmerle, J. *et al.* Strategic and practical guidelines for successful structured illumination microscopy. *Nature protocols* **12**, 988-1010 (2017).

24. Siegerist, F. *et al.* Super-Resolution Microscopy: A Technique to Revolutionize Research and Diagnosis of Glomerulopathies. *Glomerular Diseases* **3**, 19-28 (2023).

25. Diekmann, R. *et al.* Chip-based wide field-of-view nanoscopy. *Nature Photonics* **11**, 322-328 (2017).

26. Tinguely, J.-C., Helle, Ø. I. & Ahluwalia, B. S. Silicon nitride waveguide platform for fluorescence microscopy of living cells. *Optics express* **25**, 27678-27690 (2017).

27. Opstad, I. S. *et al.* A waveguide imaging platform for live‐cell TIRF imaging of neurons over large fields of view. *Journal of Biophotonics* **13**, e201960222 (2020).

28. Jayakumar, N., Helle, Ø. I., Agarwal, K. & Ahluwalia, B. S. On-chip TIRF nanoscopy by applying Haar wavelet kernel analysis on intensity fluctuations induced by chip illumination. *Optics Express* **28**, 35454-35468 (2020).

29. Opstad, I. S. *et al.* Fluorescence fluctuation-based super-resolution microscopy using multimodal waveguided illumination. *Optics Express* **29**, 23368-23380 (2021).

30. Villegas-Hernández, L. E. *et al.* Chip-based multimodal super-resolution microscopy for histological investigations of cryopreserved tissue sections. *Light: Science & Applications* **11**, 1-17 (2022).

31. Tokuyasu, K. A technique for ultracryotomy of cell suspensions and tissues. *The Journal of cell biology* **57**, 551-565 (1973).

32. Agarwal, K. & Macháň, R. Multiple signal classification algorithm for super-resolution fluorescence microscopy. *Nature communications* **7**, 13752 (2016).

33. Eckermann, M. *et al.* Three-dimensional virtual histology of the human hippocampus based on phase-contrast computed tomography. *Proceedings of the National Academy of Sciences* **118**, e2113835118 (2021).

34. Wang, X. *et al.* Single-shot isotropic differential interference contrast microscopy. *Nature Communications* **14**, 2063 (2023).

35. Kast, R. E. *et al.* Emerging technology: applications of Raman spectroscopy for prostate cancer. *Cancer and Metastasis Reviews* **33**, 673-693 (2014).

36. Huang, D. *et al.* Optical coherence tomography. *science* **254**, 1178-1181 (1991).

37. Haluszka, D. *et al.* In vivo second‐harmonic generation and ex vivo coherent anti‐stokes raman scattering microscopy to study the effect of obesity to fibroblast cell function using an Yb‐fiber laser‐based CARS extension unit. *Microscopy Research and Technique* **78**, 823-830 (2015).

38. Wittekind, D. Traditional staining for routine diagnostic pathology including the role of tannic acid. 1. Value and limitations of the hematoxylin-eosin stain. *Biotechnic & histochemistry* **78**, 261-270 (2003).

39. Tan, W. C. C. *et al.* Overview of multiplex immunohistochemistry/immunofluorescence techniques in the era of cancer immunotherapy. *Cancer Communications* **40**, 135-153 (2020).

40. Winfree, S. *et al.* Quantitative three-dimensional tissue cytometry to study kidney tissue and resident immune cells. *Journal of the American Society of Nephrology* **28**, 2108-2118 (2017).

41. Raza, S. E. A. *et al.* Micro-Net: A unified model for segmentation of various objects in microscopy images. *Medical image analysis* **52**, 160-173 (2019).

42. Pawley, J. *Handbook of biological confocal microscopy*. Vol. 236 (Springer Science & Business Media, 2006).

43. Olson, E., Levene, M. J. & Torres, R. Multiphoton microscopy with clearing for three dimensional histology of kidney biopsies. *Biomedical optics express* **7**, 3089-3096 (2016).

44. Martin‐Fernandez, M., Tynan, C. & Webb, S. A 'pocket guide' to total internal reflection fluorescence. *Journal of microscopy* **252**, 16-22 (2013).

45. Poola, P. K. *et al.* Light sheet microscopy for histopathology applications. *Biomedical engineering letters* **9**, 279-291 (2019).

46. Villegas-Hernández, L. E. *et al.* Visualizing ultrastructural details of placental tissue with super-resolution structured illumination microscopy. *Placenta* **97**, 42-45 (2020).

47. Sibarita, J.-B. Deconvolution microscopy. *Microscopy Techniques: -/-*, 201-243 (2005).

48. Schumacher, J. & Bertrand, L. THUNDER imagers: how do they really work. *THUNDER Imager Technical Note* (2019).

49. Zheng, C. *et al.* De-scattering with excitation patterning enables rapid wide-field imaging through scattering media. *Science advances* **7**, eaay5496 (2021).

50. Wen, G. *et al.* High-fidelity structured illumination microscopy by point-spread-function engineering. *Light: Science & Applications* **10**, 70 (2021).

51. Acuña, S. *et al.* Deriving high contrast fluorescence microscopy images through low contrast noisy image stacks. *Biomedical Optics Express* **12**, 5529-5543 (2021).

52. Mattheyses, A. L., Simon, S. M. & Rappoport, J. Z. Imaging with total internal reflection fluorescence microscopy for the cell biologist. *Journal of cell science* **123**, 3621-3628 (2010).

53. Rames, M. J. *et al.* Multiplexed and millimeter-scale superresolution imaging of cells and tissue sections via prism-illumination and microfluidics-enhanced DNA-PAINT. *bioRxiv*, 2022.2008. 2007.503091 (2022).

54. Alva, A. *et al.* Fluorescence fluctuation‐based super‐resolution microscopy: Basic concepts for an easy start. *Journal of Microscopy* **288**, 218-241 (2022).

55. Kim, M. *et al.* Superresolution imaging with optical fluctuation using speckle patterns illumination. *Scientific reports* **5**, 16525 (2015).

56. Helle, Ø. I. *et al.* Structured illumination microscopy using a photonic chip. *Nature photonics* **14**, 431-438 (2020).

57. Priyadarshi, A. *et al.* A transparent waveguide chip for versatile total internal reflection fluorescence-based microscopy and nanoscopy. *Communications Materials* **2**, 85 (2021).

58. Relucenti, M. *et al.* The Ultrastructural Analysis of Human Colorectal Cancer Stem Cell-Derived Spheroids and Their Mouse Xenograft Shows That the Same Cells Types Have Different Ratios. *Biology* **10**, 929 (2021).

59. Winterford, C. M., Walsh, M. D., Leggett, B. A. & Jass, J. R. Ultrastructural localization of epithelial mucin core proteins in colorectal tissues. *Journal of Histochemistry & Cytochemistry* **47**, 1063-1074 (1999).

60. Mau, A. *et al.* Fast widefield scan provides tunable and uniform illumination optimizing super-resolution microscopy on large fields. *Nature communications* **12**, 3077 (2021).

61. Douglass, K. M. *et al.* Super-resolution imaging of multiple cells by optimized flat-field epi-illumination. *Nature photonics* **10**, 705-708 (2016).

62. Khaw, I. *et al.* Flat-field illumination for quantitative fluorescence imaging. *Optics express* **26**, 15276-15288 (2018).

63. Rowlands, C. J. *et al.* Flat-field super-resolution localization microscopy with a low-cost refractive beam-shaping element. *Scientific Reports* **8**, 1-8 (2018).

64. Descloux, A., Grußmayer, K. S. & Radenovic, A. Parameter-free image resolution estimation based on decorrelation analysis. *Nature methods* **16**, 918-924 (2019).

65. De Boer, P., Hoogenboom, J. P. & Giepmans, B. N. Correlated light and electron microscopy: ultrastructure lights up! *Nature methods* **12**, 503-513 (2015).

66. Mironov, A. & Beznoussenko, G. Correlative microscopy: a potent tool for the study of rare or unique cellular and tissue events. *Journal of microscopy* **235**, 308-321 (2009).

67. McDonald, K. A review of high‐pressure freezing preparation techniques for correlative light and electron microscopy of the same cells and tissues. *Journal of microscopy* **235**, 273-281 (2009).

68. Onouchi, T. *et al.* Visualization of neutrophil extracellular traps and fibrin meshwork in human fibrinopurulent inflammatory lesions: III. Correlative light and electron microscopic study. *Acta histochemica et cytochemica* **49**, 141-147 (2016).

69. Itoh, T. *et al.* Identifying Active Progeny Virus Particles in Formalin-Fixed, Paraffin-Embedded Sections Using Correlative Light and Scanning Electron Microscopy. *Laboratory Investigation* **103**, 100020 (2023).

70. Sawaguchi, A. *et al.* Informative three-dimensional survey of cell/tissue architectures in thick paraffin sections by simple low-vacuum scanning electron microscopy. *Scientific reports* **8**, 1-11 (2018).

71. Tinguely, J.-C. *et al.* Photonic-chip assisted correlative light and electron microscopy. *Communications biology* **3**, 739 (2020).

72. Thomson, E. *et al.* Gigapixel imaging with a novel multi-camera array microscope. *Elife* **11**, e74988 (2022).

73. Komura, D. & Ishikawa, S. Machine learning methods for histopathological image analysis. *Computational and structural biotechnology journal* **16**, 34-42 (2018).

74. Archetti, A. *et al.* Waveguide-PAINT offers an open platform for large field-of-view super-resolution imaging. *Nature communications* **10**, 1267 (2019).

75. Werbin, J. L. *et al.* Multiplexed Exchange-PAINT imaging reveals ligand-dependent EGFR and Met interactions in the plasma membrane. *Scientific reports* **7**, 12150 (2017).

76. He, S. *et al.* High-plex multiomic analysis in FFPE tissue at single-cellular and subcellular resolution by spatial molecular imaging. *bioRxiv*, 2021.2011. 2003.467020 (2021).

77. Moretti, C. & Gigan, S. Readout of fluorescence functional signals through highly scattering tissue. *Nature Photonics* **14**, 361-364 (2020).

78. Costantini, I. *et al.* In-vivo and ex-vivo optical clearing methods for biological tissues. *Biomedical optics express* **10**, 5251-5267 (2019).

79. Schindelin, J. *et al.* Fiji: an open-source platform for biological-image analysis. *Nature methods* **9**, 676-682 (2012).

80. Acuña, S. *et al.* Soft thresholding schemes for multiple signal classification algorithm. *Optics Express* **28**, 34434-34449 (2020).

81. Cardona, A. *et al.* TrakEM2 software for neural circuit reconstruction. *PloS one* **7**, e38011 (2012).

Supplementary Information

Super-resolution histology of paraffin-embedded samples via photonic chip-based microscopy

Luis E. Villegas-Hernández[1], Vishesh K. Dubey[1], Hong Mao[1], Manohar Pradhan[2], Jean-Claude Tinguely[1], Daniel H. Hansen[1], Sebastián Acuña[1], Bartłomiej Zapotoczny[3], Krishna Agarwal[1], Mona Nystad[4,5,6], Ganesh Acharya[4,10], Kristin A. Fenton[7], Håvard E. Danielsen[2,8,9], Balpreet Singh Ahluwalia[1,10,*]

[1] Department of Physics and Technology, UiT The Arctic University of Norway, Klokkargårdsbakken NO-9019 Tromsø, Norway

[2] Institute for Cancer Genetics and Informatics, Oslo University Hospital, NO-0424 Oslo, Norway

[3] Department of Biophysical Microstructures, Institute of Nuclear Physics, Polish Academy of Sciences, Kraków, Poland

[4] Department of Clinical Medicine, Women's Health and Perinatology Research group, UiT The Arctic University of Norway, Tromsø, Norway

[5] Department of Obstetrics and Gynecology, University Hospital of North Norway, Tromsø, Norway

[6] Department of Medical Biology, Vascular Biology Research Group (VBRG), UiT The Arctic University of Norway, Tromsø, Norway

[7] Department of Medical Biology, RNA and Molecular Pathology Research Group, UiT The Arctic University of Norway, Tromsø, Norway

[8] Department of Informatics, University of Oslo, NO-0316 Oslo, Norway

[9] Nuffield Division of Clinical Laboratory Sciences, University of Oxford, Oxford OX3 9DU, United Kingdom

[10] Division of Obstetrics and Gynecology, Department of Clinical Science, Intervention and Technology, Karolinska Institute, Stockholm, Sweden

[*] corresponding author: balpreet.singh.ahluwalia@uit.no

S1. Mode-averaging for chip-TIRF

In this study, we used photonic chips with strip waveguides of various widths (200 µm, 400 µm, 600 µm, and 1000 µm) to evaluate the performance of chip-TIRF under different geometrical configurations. For chip-TIRF imaging, a side illumination laser is coupled onto a selected waveguide using a microscope objective. Upon coupling, the excitation light propagates through the waveguide in the form of an anisotropic intensity distribution called multi-mode interference (MMI) pattern, which can be further modulated by changing the position of the coupling objective (Supplementary Figure S1a). To attain uniform illumination of the specimen, the coupling objective is scanned along the input facet of the chip while individual frames are acquired (Supplementary Figure S1b). To achieve a uniform chip-TIRF image, the collected image stack is then averaged (Supplementary Figure S1c). Supplementary Video V1 provides a visual animation of the on-chip mode averaging process.
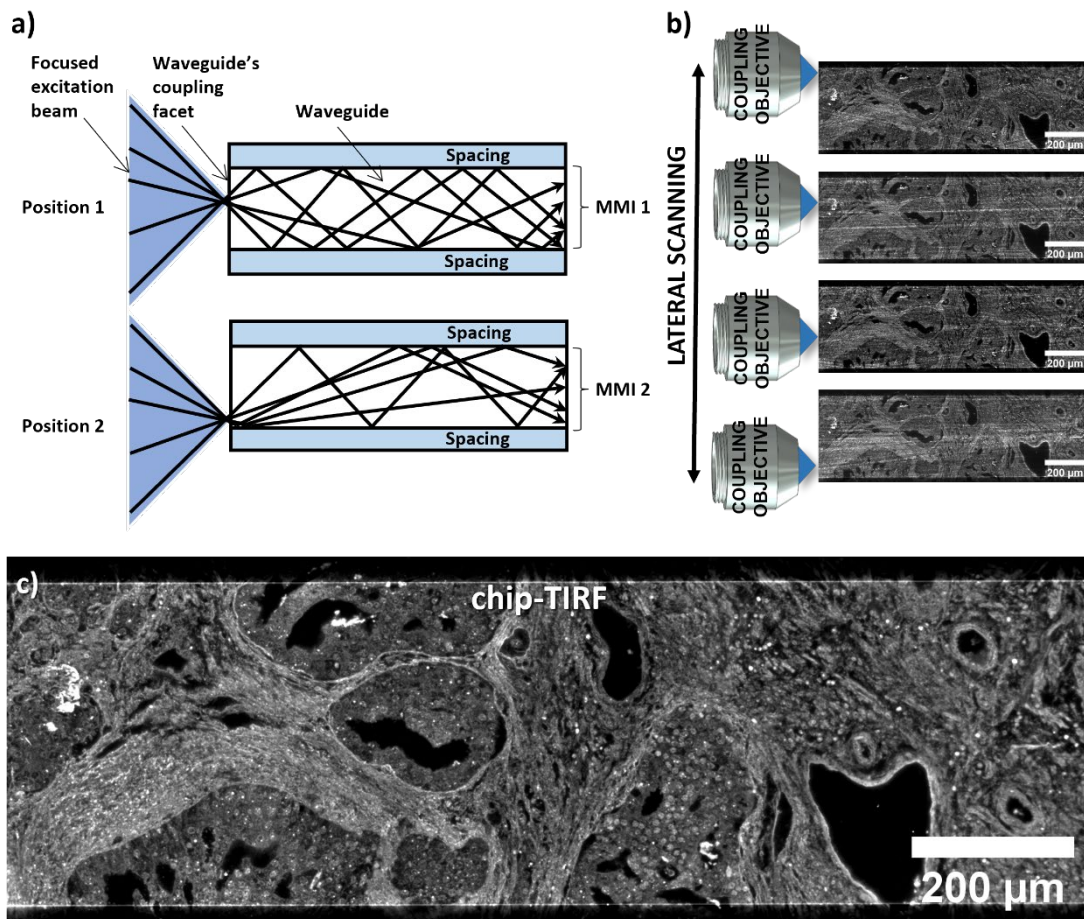

Supplementary Figure S1. **Mode-averaging for chip-TIRF images.** **a)** Upon coupling the excitation laser, the excitation light propagates along the selected waveguide via total internal reflection. The geometry of the waveguide supports multi-mode interference (MMI) patterns that can be modulated by scanning the coupling objective relative to the input facet of the chip. **b)** An image stack is collected by acquiring one frame for each position of the coupling objective. **c)** The image stack is then averaged in FIJI to obtain a diffraction-limited high-contrast chip-TIRF image.

S2. Chip-based microscopy setup

The chip-based microscope is composed of two main sections, namely the collection module and a photonic chip module, as illustrated in Supplementary Figure S2a. The collection module consists of a commercial upright microscope equipped with an emission filter set (see Supplementary Table S2), an sCMOS camera, and conventional microscope objective lenses of diverse magnifications, which can be interchanged depending on the imaging needs. The photonic chip module consists of a set of translation stages to enable precise control of the excitation laser source for chip-based TIRF imaging. By using a beam splitter and dichroic mirrors, it is also possible to image the sample via widefield and EPI fluorescence illumination. Supplementary Figure S2b and Supplementary Figure S2c provide a detailed view of the chip-based microscope setup.

Supplementary Table S2. Dichroic mirrors and bandpass filters used for EPI and chip-TIRF image acquisition.

Excitation wavelength (nm)	Emission filter set	
	Dichroic mirror/Long-pass filter (nm)	Band-pass filter (nm)
488	515 (CHR-T515LP, Chroma)	535/30 (CHR-ET535/30M, Chroma)
561	585 (CHR-T585LPXR, Chroma)	630/75 (CHR-ET630/75M, Chroma)
640	655 (CHR-AT655DC, Chroma)	690/50 (CHR-AT690/50M, Chroma)
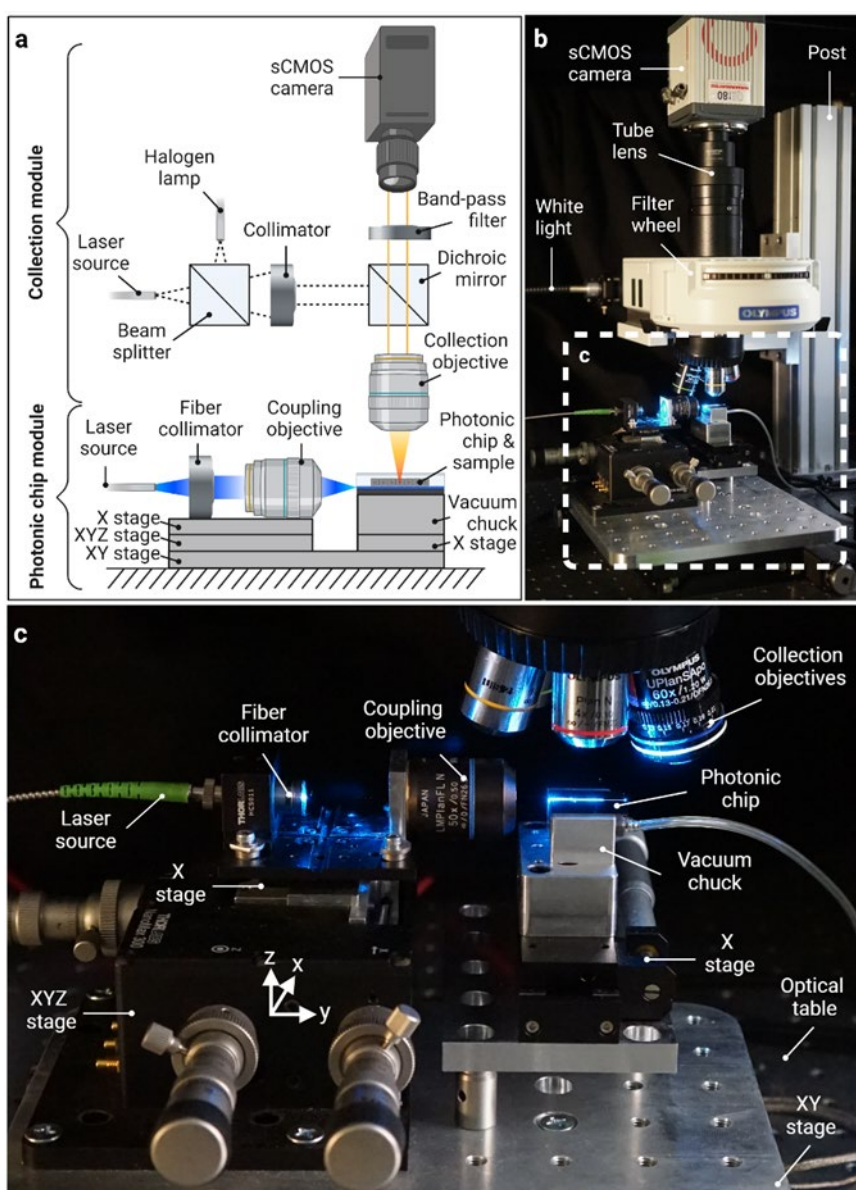
*Supplementary Figure S2. **Chip-based microscopy setup. a)** Schematic representation of the chip-based microscopy setup illustrating the collection and the photonic chip modules, respectively. **b)** Side view of a chip-based microscope setup. The white-dotted box denotes the photonic chip module shown in c). **c)** Magnified view of the photonic chip module including part of the collection module (collection objectives).*

S3. Depth of field of microscope objectives

The depth of field (DOF) refers to the distance between the closest and the further objects that can be sharply imaged along the focal plane of a lens. In microscopy, the DOF is dictated by the formula $\text{DOF} = \lambda n / NA^2$, where λ is the wavelength of the excitation light, n is the refractive index of the medium between the coverslip and the microscope objective, and NA is the numerical aperture of the microscope objective. The DOF plays a crucial role both in the lateral resolution and contrast of fluorescence microscopy. Supplementary Figure S3 illustrates a theoretical simulation of DOF vs the NA of commonly available air ($n = 1$), water immersion ($n = 1.33$) and oil immersion microscope objectives using the aforementioned formula. As shown in the graph, low NA objectives exhibit larger DOF while higher NA objectives allow for shorter DOF. In EPI fluorescence, low NA objectives are usually employed for a contextual view of the sample (for example, in Figure 4a) whereas, for detailed views, higher NA objectives are needed. However, the DOF of high NA lenses still limits the axial resolution of advanced microscopy techniques such as DV (Figure 3d) and FF-SRM methods such as MUSICAL (Figure 2a). Photonic chip-based microscopy, on the contrary, supports <50 nm optical sectioning via evanescent field waveguide-based excitation (see Supplementary Information S4), allowing for high-contrast fluorescent imaging through virtually any microscope objective, irrespective of its DOF.
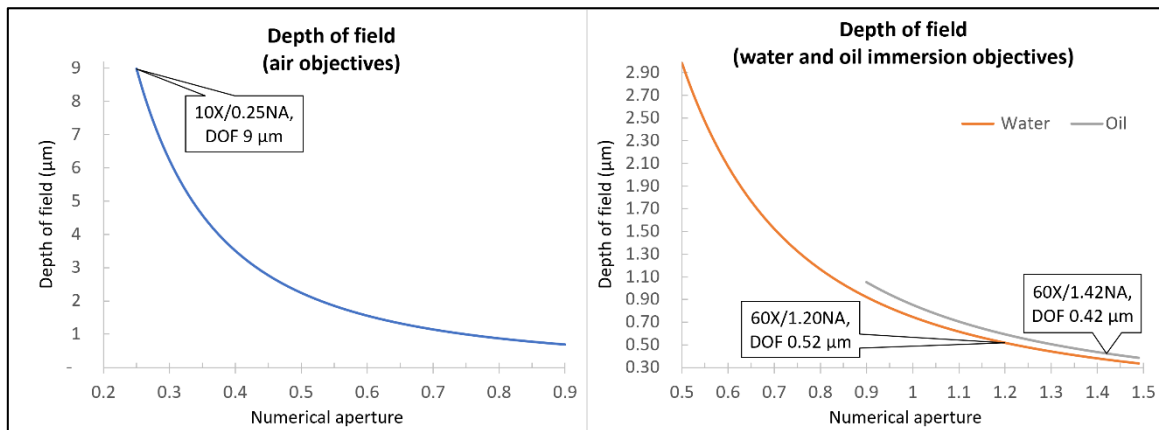

*Supplementary Figure S3. **Depth of field vs numerical aperture**. a) DOF vs NA of air objectives. The call-out sign illustrates the DOF of the 10X/0.25NA objective used in this study, which extends up to 9 µm. b) DOF vs NA of oil and water immersion objectives used in this study. The call-out texts show a DOF of 0.52 µm for the 60X/1.2NA water immersion objective and a DOF of 0.42 µm for the 60X/1.42NA oil immersion objective.*

S4. Penetration depth vs refractive index

In total internal reflection fluorescence (TIRF) microscopy, the sample is illuminated by a thin evanescent field originating at the interface between the sample media and the core material used as a sample substrate (Supplementary Figure S4a). The illumination intensity decays exponentially according to the formula $I(z) = I_0 e^{-z/d}$, where I_0 is the intensity at the sample-substrate interface, z is the distance in the z-direction perpendicular to the core material surface (sample substrate), and d is the depth of penetration of the evanescent field[44]. As a convention, the penetration depth of the evanescent field is defined as the distance at which the intensity equals 1/e (roughly, 37%) of the surface intensity (I_0). The penetration depth (d) is given by the formula $d = \lambda/4\pi(N_{eff}^2 - n_1^2)^{1/2}$, where λ is the excitation wavelength, n_1 is the refractive index of the sample media, and N_{eff} is the effective refractive index of the core material (sample substrate). For glass-based TIRF, this last term is given by $N_{glass} = n_2 sin\theta$, where θ is the illumination angle, and n_2 is the refractive index of the glass substrate. Thus, the penetration depth of the evanescent intensity for glass-based TIRF is given by the formula $d_{glass} = \lambda/4\pi(n_2^2 sin^2\theta - n_1^2)^{1/2}$. Similarly, for multimode waveguide-based TIRF, the penetration depth $d_{wg} = \lambda/4\pi(N_{wg}^2 - n_1^2)^{1/2}$ is dependent on the effective refractive index of the core material N_{wg}, which varies for each guiding mode[82]. Typically, the N_{wg} values are solved by numerical simulations.

Supplementary Figure S4b provides a theoretical simulation of the penetration depth as a function of the effective refractive index used for TIRF microscopy. In this example, we considered a refractive index $n_1 \approx 1.4$ for the sample media, an excitation wavelength $\lambda = 561$ nm and, for glass-TIRF, a fixed illumination angle $\theta = 75$ degrees. Therefore, for borosilicate glass ($n_{glass} \approx 1.52$), an effective refractive index $N_{glass} \approx 1.47$ was considered. Similarly, based on numerical simulations, for chip-TIRF, we assumed an effective refractive index $N_{Si3N4} \approx 1.75$. In this configuration, glass-TIRF provides a theoretical penetration depth of ~101 nm, while the high refractive index of the waveguide core material used in this study (Si$_3$N$_4$) allows for a theoretical penetration depth of ~43 nm. By employing higher refractive index materials on the waveguide core, such as titanium dioxide (TiO$_2$, $N_{TiO2} \approx 2.5$), the penetration depth can be further narrowed down to ~20 nm (ref. 83).

Although sub-100 nm penetration depth can be achieved on glass-based TIRF approaches via high illumination angles, these methods pose other limitations for clinical applications. In objective-based TIRF, for example, high-numerical aperture objectives (NA $\geqslant$ 1.4) are required for achieving the high illumination angles necessary for evanescent field excitation. As a consequence, high magnifications ($\geqslant$ 60X) are also necessary, therefore restricting the exploitable TIRF field of view to around 50 μm x 50 μm. While prism-based TIRF allows fluorescence imaging with conventional objectives by decoupling the illumination and the collection paths, these approaches require precise optical alignment to control the penetration depth extent, contrary to the photonic chip, where ultrathin optical sectioning is achieved irrespective of the coupling precision.
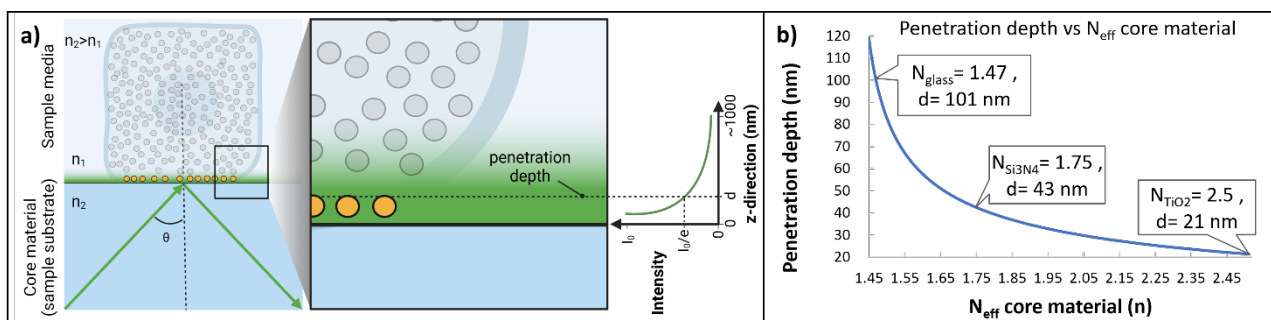
*Supplementary Figure S4. **Penetration depth in TIRF microscopy**. a) Schematic representation of total internal reflection fluorescence (TIRF). A light beam (green arrow) travels in a core material (sample substrate) with a refractive index n$_2$ toward a sample media with a lower refractive index n$_1$. Due to Snell's law, upon hitting the substrate-sample interface on an angle θ greater than the critical angle $\theta_c = sin^{-1}(n_1/n_2)$, the light beam is reflected into the core material medium. At the core material surface, however, a decaying field known as evanescent field appears, enabling the excitation of fluorescent molecules in its reach. The penetration depth of the evanescent field is defined as the distance in the z-direction perpendicular to the core material surface at which the illumination intensity equals 1/e of the illumination intensity (I$_0$) at the sample-core interface. b) Theoretical simulation of the penetration depth as a function of the effective refractive indices of the core material. Here, the high index of refraction of the chip provides ultrathin optical sectioning as compared to glass-based TIRF systems.*

S5. Sample preparation workflow

Photonic chip-based microscopy is compatible with the conventional histology workflow of FFPE sections. Supplementary Figure S5 illustrates the sample preparation steps for chip-based microscopy of FFPE sections. The lateral dimensions (roughly, 2.5 cm × 2.5 cm) of the photonic chips used in this study made it necessary for manual handling of the sample throughout the complete preparation process. However, the photonic chip can be manufactured in identical sizes as conventional glass slides, making it possible for automated sample preparation via commercially-available tissue processing and immunostaining devices.
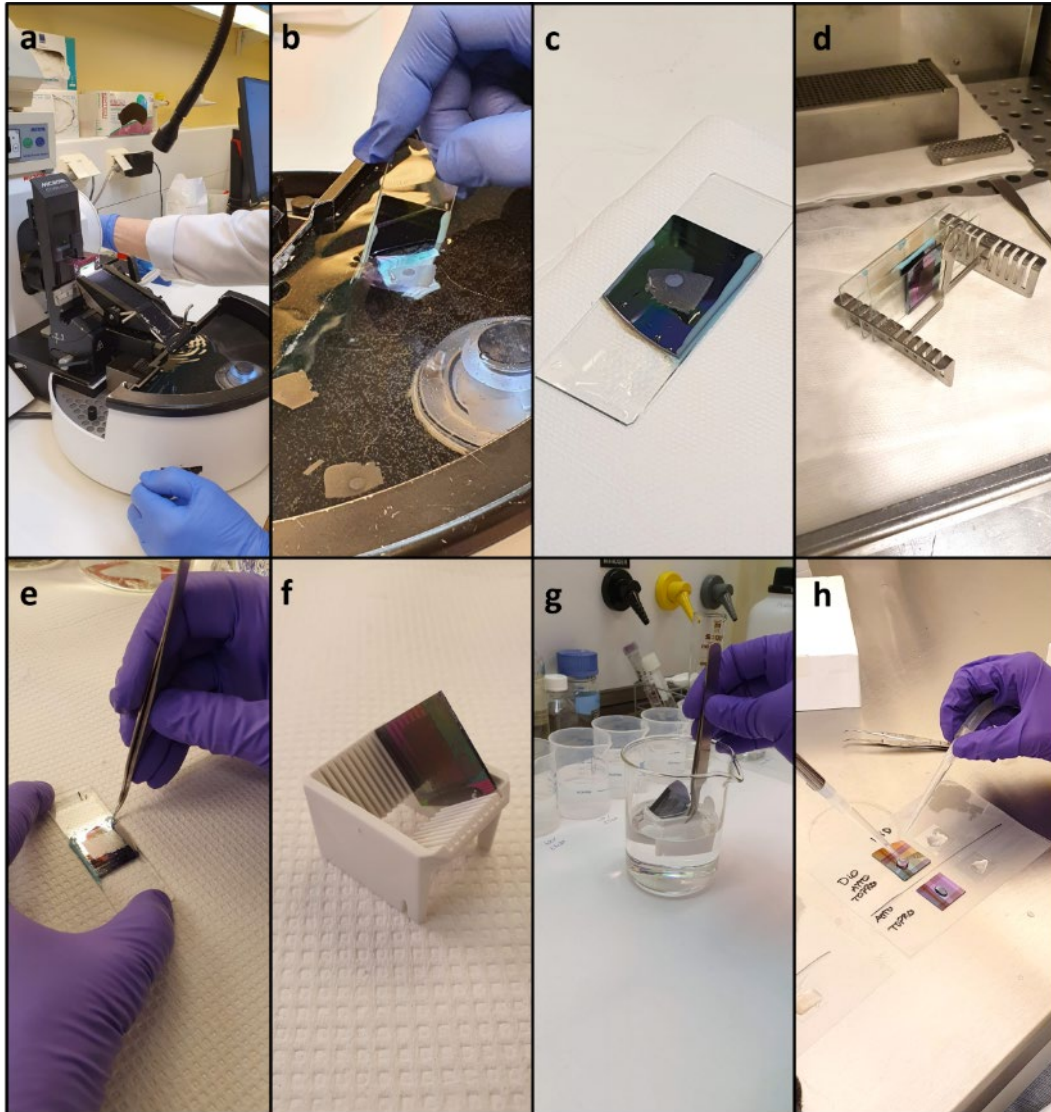
*Supplementary Figure S5. **Sample preparation workflow for on-chip FFPE histology. a)** The paraffin block is sectioned on a microtome equipped with a water bath. **b)** Upon sectioning, the sample is floated on the water bath and further scooped with a photonic chip previously glued to a conventional glass slide. See details in Supplementary Video V3. **c)** The photonic chip is placed on a flat surface at room temperature for an hour, for drying. **d)** The photonic chip is placed inside a 60 °C oven for overnight melting of the paraffin. **e)** The photonic chip is carefully detached from the glass slide by peeling off the picodent twinsil glue. **f)** The photonic chip is placed on a coverslip rack. **g)** The photonic chip is immersed in several reagents for deparaffinization and rehydration of the sample. **h)** The sample is fluorescently labeled using a single-channel micropipette and an aspirator pump.*

S6. Mouse kidney immunolabeling

The photonic chip is compatible with immunolabeling approaches. In this example, a zinc-fixed paraffin-embedded (ZnFPE) mouse kidney section was fluorescently immunolabeled using recombinant anti-alpha smooth muscle actin (α-SMA) antibody (ab124964, Abcam). To enable optimal immunolabeling, after deparaffinization and rehydration (see Supplementary Information S5), the photonic chip was immersed in citrate buffer and microwave-heated for ten minutes at maximum power. For a contextual visualization, the sample was also labeled against membranes. Supplementary Figure S6 shows the ZnFPE mouse kidney sample in different levels of magnification (10X and 20X). The α-SMA is displayed in cyan and the membranes are shown in magenta.
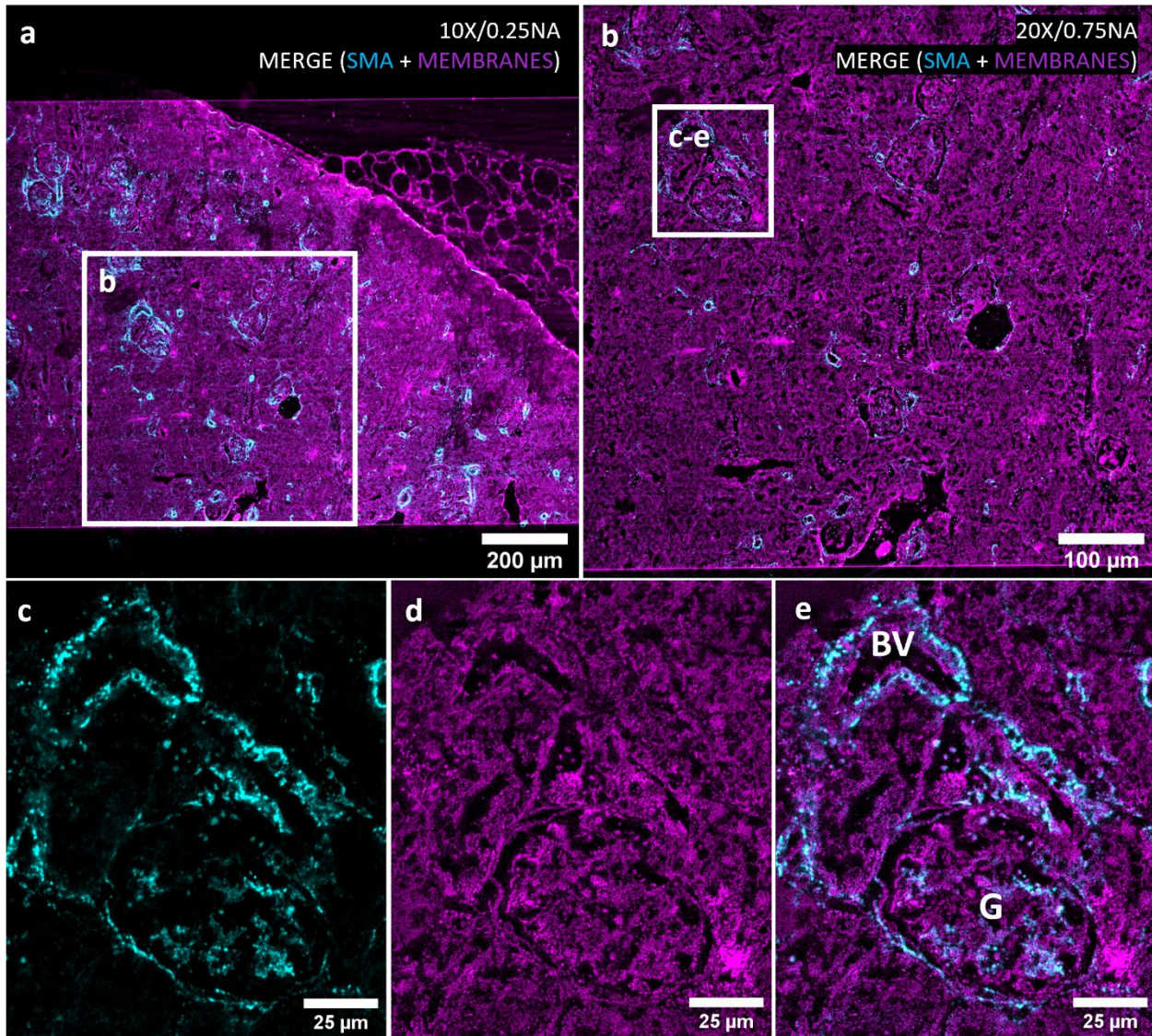
*Supplementary Figure S6. **Photonic chip-based immunolabeling of paraffin sections. a)** 10X/0.25NA chip-TIRF image of a ZnFPE mouse kidney showing α-SMA in cyan and membranes in magenta. The white box denotes the region further described in b). **b)** 20x/0.75NA chip-TIRF image of the mouse kidney section. The white box denotes a sample region containing a glomerulus and an artery. **c-e)** A zoom-in view of the selected region allows for detailed visualization of the sample structure. BV: blood vessel; G: glomerulus.*

## S7. Magnified view of the H&E colorectal sample

Magnified view of the adenocarcinoma region (Ad) in the colorectal sample.
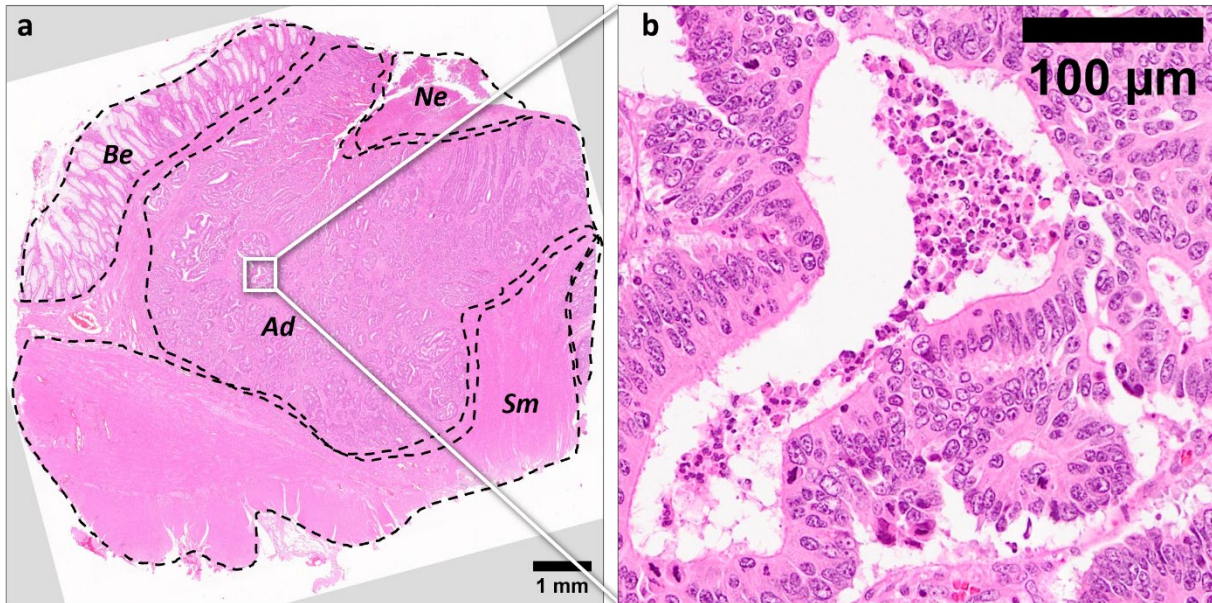
*Supplementary Figure S7. **Zoom-in view of the adenocarcinoma region (Ad).** The high magnification allows the distinction of structural features (glands lined with pseudostratified cancer cells showing varying degrees of pleomorphism and a lumen with necrotic debris) in the colorectal sample that are not distinguishable in low magnification (Figure 3a).*
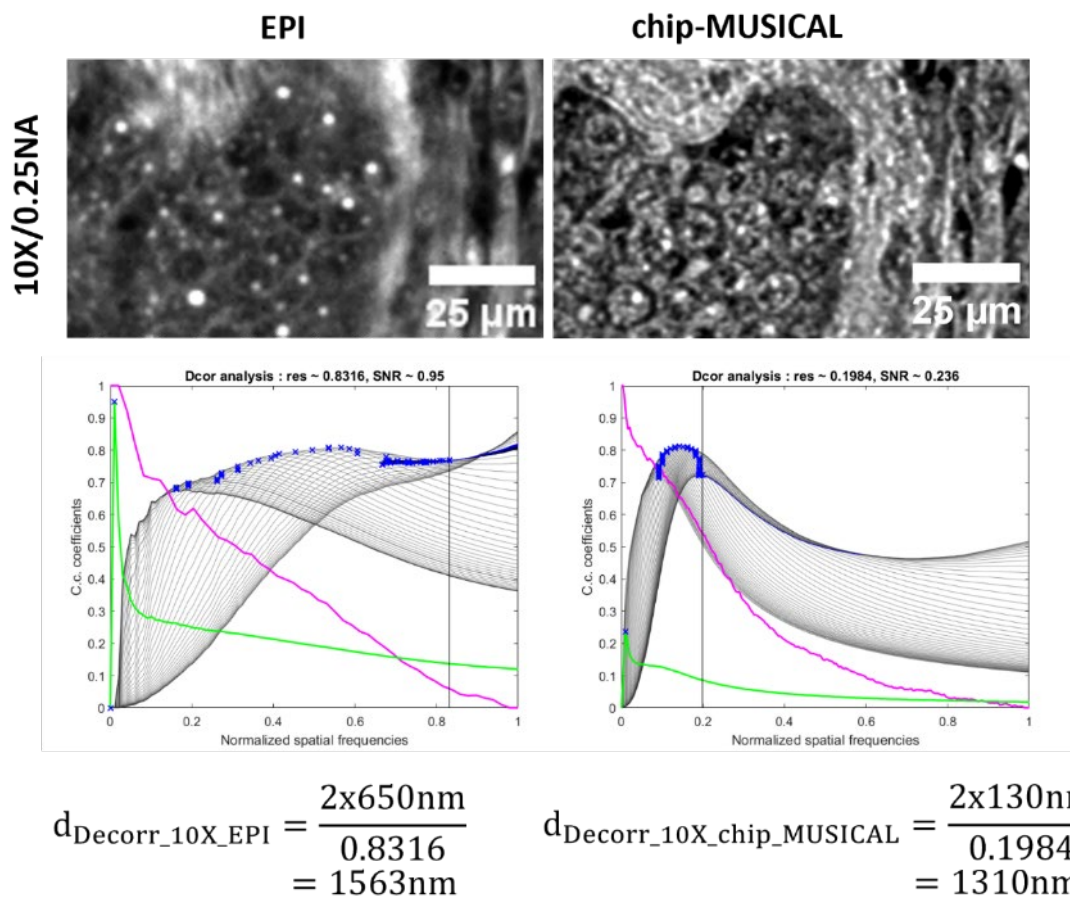
S8. Multicolor chip-TIRF image acquisition

Supplementary Figure S8 illustrates the acquisition steps for a multicolor chip-TIRF image of an FFPE prostate tissue section using a 10X/0.25NA collection objective. After selecting the region of interest, consecutive waveguides are imaged in chip-TIRF modality (Supplementary Figure S8a). Thereafter, the membrane images are stacked and projected using the maximum projection option in FIJI. The process is repeated for a different labeled channel, in this case, nuclei (Supplementary Figure S8b), using a specific excitation laser wavelength and corresponding emission filter. Finally, the membrane and nuclei images are merged in FIJI to obtain a multicolor chip-TIRF image.
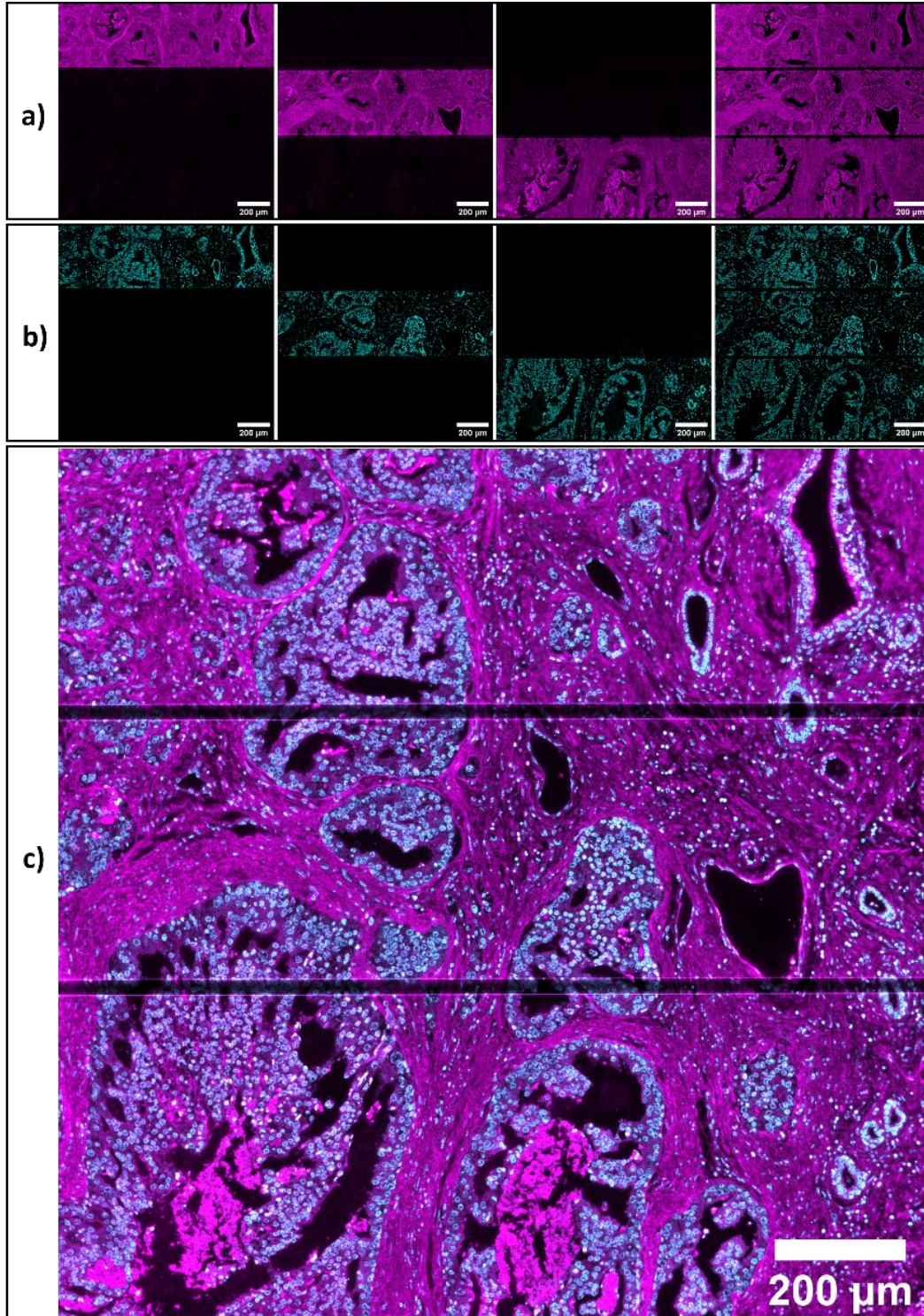
*Supplementary Figure S8. **Multicolor chip-TIRF acquisition**. a) Three individual images of membranes are collected in chip-TIRF modality and further projected into a single image in FIJI. b) The process is repeated for the nuclei signal. c) Finally, the projected images are merged in FIJI to obtain a multicolor chip-TIRF image.*
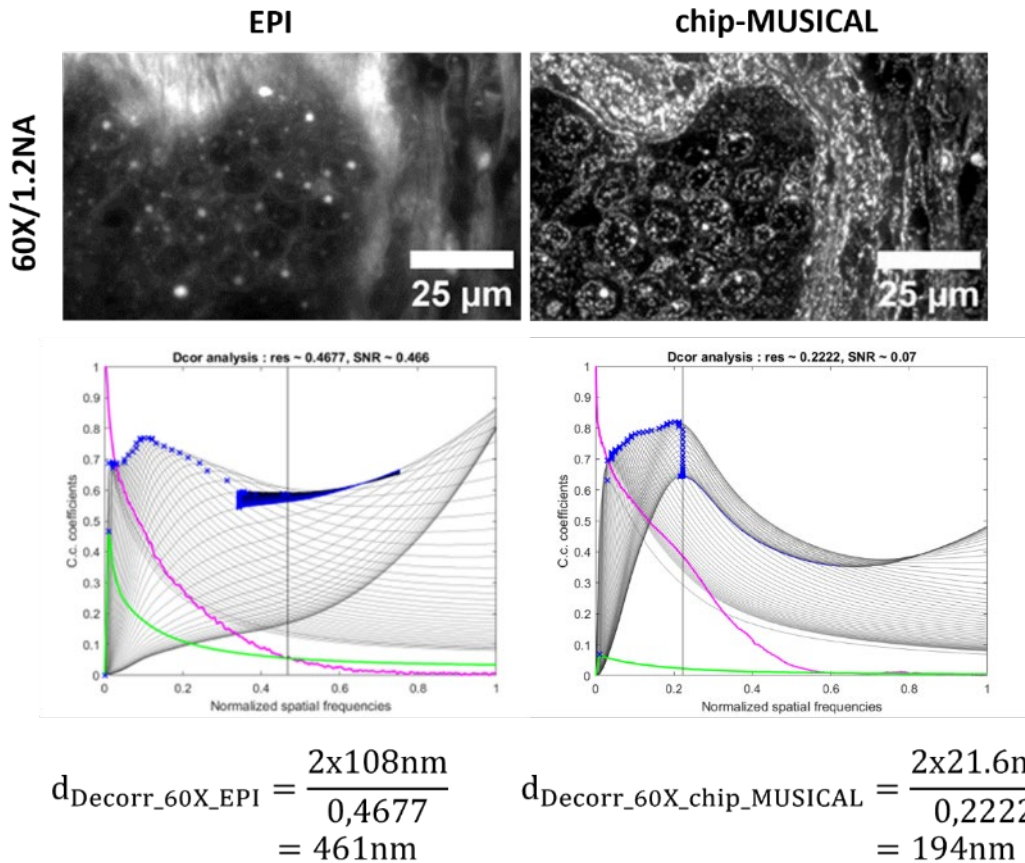
S9. Decorrelation analysis 10X/0.25 images

A decorrelation analysis[64] was used to quantify the resolution enhancement of chip-MUSICAL over conventional EPI fluorescence images (Supplementary Figure S9). Both chip-MUSICAL and EPI images were acquired with a 10X/0.25NA objective over the same field of view. By analyzing the images under a series of high-pass filters, the decorrelation algorithm computes the maximum spatial frequency at which it is still possible to distinguish between signal and noise, enabling resolution estimation of microscopy images. For this analysis, the MATLAB version of the algorithm was used. In both cases (i.e. EPI and chip-TIRF), the number of sample points (Nr) was set to 100 and the number of filters (Ng) to 50. The results revealed an estimated resolution of 1563 nm and 1310 nm for the EPI and chip-MUSICAL images, respectively, suggesting nearly a 1.2-fold resolution improvement of chip-MUSICAL over EPI. We acknowledge that the chip-based microscopy setup used in this study does not perform at the theoretical limit of diffraction due to minor imperfections along the optical path length of the system. Supplementary Figure S9 shows the corresponding plots for resolution estimation on each decorrelation analysis. The resolution is calculated with the formula $d_{Decorr} = \frac{2xPixel\ size}{k_c}$, where k_c corresponds to the maximum normalized spatial frequency shown in the plot (e.g. $k_c = 0.8316$ for EPI, and $k_c = 0.1984$ for chip-MUSICAL).

$$d_{Decorr\_10X\_EPI} = \frac{2x650nm}{0.8316} = 1563nm$$

$$d_{Decorr\_10X\_chip\_MUSICAL} = \frac{2x130nm}{0.1984} = 1310nm$$

Supplementary Figure S9. **Decorrelation analysis of 10X/0.25NA EPI and chip-MUSICAL images**. Photonic chip-based microscopy enables resolution improvement over conventional EPI fluorescence methods. In this example, the membrane channels of the FFPE prostate sample shown in Figure 4c and Figure 4d were used for resolution estimation via decorrelation method. The results obtained here revealed a resolution of 1563 nm and 1310 nm in EPI and chip-MUSICAL, respectively, which suggest a nearly 1.2-fold resolution improvement via chip-MUSICAL over EPI.

S10. Decorrelation analysis 60X/1.2 images

Following the steps described in Supplementary Information S9, a decorrelation analysis was performed on the 60X/1.2NA EPI and chip-MUSICAL images corresponding to the membrane channels of Figure 4e and Figure 4f, respectively. Here, the decorrelation algorithm estimated a resolution of 461 nm and 194 nm for the EPI and chip-MUSICAL images, respectively, which suggests nearly a 2.4-fold resolution improvement of chip-MUSICAL over EPI. Supplementary Figure S10 shows the corresponding plots for resolution estimation on each decorrelation analysis. The resolution is calculated with the formula $d_{Decorr} = \frac{2 x Pixel\ size}{k_c}$, where k_c corresponds to the maximum normalized spatial frequency shown in the plot (e.g. $k_c = 0.4677$ for EPI, and $k_c = 0.2222$ for chip-MUSICAL).

$$d_{Decorr\_60X\_EPI} = \frac{2 x 108nm}{0,4677} = 461nm$$

$$d_{Decorr\_60X\_chip\_MUSICAL} = \frac{2 x 21.6nm}{0,2222} = 194nm$$

*Supplementary Figure S10. **Decorrelation analysis of 10X/0.25NA EPI and chip-MUSICAL images**. Photonic chip-based microscopy enables resolution improvement over conventional EPI fluorescence methods. In this example, the membrane channels of the FFPE prostate sample shown in Figure 4e and Figure 4f were used for resolution estimation via decorrelation method. The results obtained here revealed a resolution of 461 nm and 194 nm in EPI and chip-MUSICAL, respectively, which suggest a nearly 2.4-fold resolution improvement via chip-MUSICAL over EPI.*

S11. Advantages of photonic chip-based microscopy for FFPE histology

Photonic chip-based microscopy offers several advantages for histological analysis of FFPE sections. These include:

a. **Compatibility with standard histological workflows**. The photonic chip withstands all the steps necessary for sample preparation of FFPE sections, including water immersion for sample scooping, oven incubation at 60 °C for paraffin melting, xylene immersion for deparaffinization, descendent alcohol incubations for sample rehydration, and heat-induced antigen retrieval for immunolabeling. In addition, the photonic chip can be fabricated to match the dimensions of standard microscopy glass slides, facilitating seamless integration with automated processing equipment used in clinical settings.

b. **High contrast over large fields of view**. The evanescent field provided by the photonic chip enables ultra-thin optical sectioning (<50 nm) of the FFPE samples along the entire length of the waveguide, supporting illumination on the centimeter scale. In addition, the decoupled excitation and collection light paths enable the acquisition of TIRF images using any arbitrary magnification objective lens, thus opening avenues for high-contrast images over large areas[21], thus overcoming the field of view limitations of conventional TIRF systems, typically restricted to approx. 50 μm × 50 μm.

c. **Multimodal imaging**. The photonic chip enables diverse imaging modalities such as TIRF, FF-SRM, SMLM, SIM, and CLEM[25,27,29,56,71]. Also, the chip fabrication supports the inclusion of landmarks that can further aid in the identification of specific regions of interest across different microscopy methods including atomic force microscopes (AFM) and scanning electron microscopes (SEM), as illustrated in Figure 5. In addition, the photonic chip is compatible with complementary imaging tools such as microfluidics[74], which are often used in multi-omic research.

d. **Support of high-spatial frequency illumination**. The high refractive index of the waveguide core material ($n \approx 2$ for Si_3N_4) supports much higher spatial frequencies than supported by conventional free-space illumination, which further assists in an improved lateral resolution of FF-SRM methods[25]. While in EPI illumination approaches the highest spatial frequency illuminating the sample is limited by diffraction according to the excitation wavelength and the numerical aperture of the objective lens, the spatial frequencies supported by the waveguide material on the photonic chip platform are determined by the effective refractive index of the waveguide material, allowing for high-spatial frequency illumination beneficial for SRM[25].

e. **Compact footprint and retrofittable**. Photonic chip-based microscopy can be integrated into standard upright microscopes upon a few adaptations, making it an attractive solution for super-resolution multimodal imaging of tissue sections. In addition, the system operability allows for a quick and simple adoption for non-expert users of super-resolution fluorescence-based microscopy methods. Also, the photonic chips can be mass fabricated following standard semiconductor techniques and re-utilized in multiple assays, which makes them a suitable option for routine laboratories.

S12.   FFPE placental sample detachment

An indispensable requisite for successful TIRF imaging is sample adhesion. Throughout this study, we faced sample micro-detachment issues that hampered the imaging capabilities of the chip-TIRF technique. When these micro-detachments occurred, discontinuities in the chip-TIRF signal were observed. Supplementary Figure S12 illustrates a sample micro-detachment of an FFPE placental section. The white-dotted oval in Supplementary Figure S12a denotes a region of a chip-TIRF image with signal discontinuity. Further observation on a scanning electron microscope (Supplementary Figure S12b) reveals a sample micro-detachment at the same location.
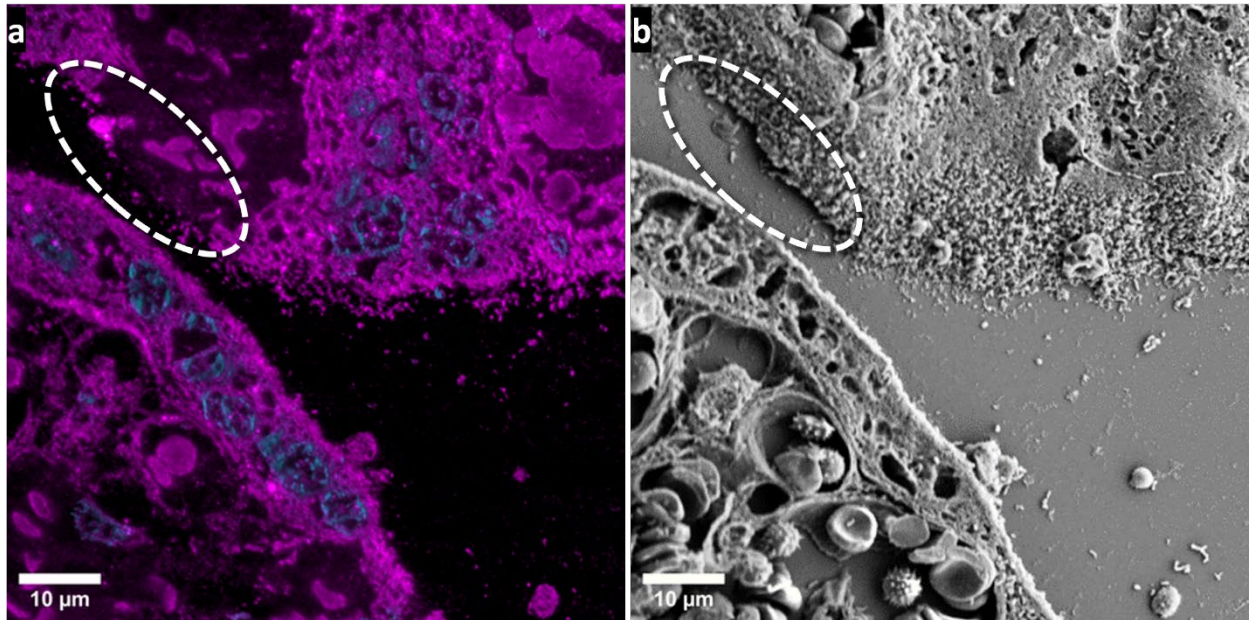
*Supplementary Figure S12**. Detachment example of a placental FFPE sample on a photonic chip**. a)* *The white-dotted oval denotes a region of a chip-TIRF image with signal discontinuity.* *b)* *Further observation under a scanning electron microscope (SEM) revealed a sample micro-detachment at the same region.*

## S13. Optimization steps for on-chip FFPE tissue imaging

The main experimental challenge of this study was sample detachment. While photonic chip-based microscopy enables superior optical sectioning, it requires the tissue section to lay perfectly flat on the waveguide surface to enable fluorescent emission via evanescent field excitation. As a consequence, micro-detachment gaps greater than the evanescent field depth render dark patches along the chip-TIRF image that hamper the visualization of the samples (see Supplementary Information S12). We tried to address this issue in different ways including a) mechanical pressure, b) limited sample hydration, and c) chip coating. In the first attempt, mechanical pressure, we aimed at pushing down the detached FFPE sample to establish contact with the waveguide surface. To achieve this, we followed the chip-based fluorescence labeling process as outlined in the Materials and Methods section, and then placed the chip in between a ferromagnetic plate at the bottom and four cylindrical magnets of 1 mm in diameter on the corners of the coverslip to exert uniform pressure over the tissue section. This method, however, did not improve the detachment issues of the FFPE samples. To further understand the detachment issue, we performed a topographical assessment of deparaffinized tissue samples using atomic force microscopy (AFM). In this process, we found out that FFPE tissues exhibited swelling along with the rehydration process (see Supplementary Information S14). This brought us to our second attempt, limiting the sample hydration to a maximum ratio of 5:95 H_2O to ethanol, to minimize the chances of swelling and, therefore, reduce the sample detachment. Despite the effort, we observed no significant differences in sample detachment compared to further hydrated samples in 30:70 H_2O to ethanol. A plausible explanation for this is that, despite the limited H_2O content in the rehydration steps, the samples inevitably underwent further incubation steps in aqueous media for the fluorescence labeling and washing, thus absorbing more H_2O and, subsequently, swelling. Finally, we explored functionalizing the chip surface to ensure sample adhesion through the preparation process. Here, we tested various coating alternatives including poly-L-lysine, histogrip, and protected isocyanate[84] (see Supplementary Information S15). While we observed a better sample adhesion compared to uncoated chips, we could not appreciate significant differences between the coating strategies. Instead, we noticed that the detachment issues were more dependent on the sample type than on the coating method. For example, in the colorectal sample, the adenocarcinoma area (Figure 3) showed optimal adhesion while the benign epithelium region showed significant detachment (see Supplementary Information S14). Similarly, the placental section exhibited more detachment issues along the apical side of the chorionic villi, in comparison with the stromal region (see Supplementary Information S11 and S15). Hence, we opted for the easiest and most affordable coating option, poly-L-lysine, to carry out this study.

The second challenge we encountered was labeling. In the attempt to find a membrane marker that could give us a contextual visualization of the sample, we tried the different variations of the CellMask dye family (CellMask Green, CellMask Orange, and CellMask Deep Red), as well as the Vybrant DiI and DiO fluorophores, but all these showed high affinity to the waveguide surface, which led to a high background signal during imaging acquisition[30]. We tried to address this issue by using blocking reagents such as bovine serum albumin and increasing the number of washing steps after fluorescence labeling, but we observed no reduction in the background signal. Interestingly, we found out that the MitoTracker Deep Red FM (MTDR) rendered unspecific labeling of paraffin-embedded samples while producing negligible background on the waveguide surface. We acknowledge that the MTDR is intended for live cell analysis of mitochondria. However, the results obtained in this study suggest that this marker serves the purpose of contextual visualization as eosin does in the H&E staining. For example, the comparative view of the colorectal sample showed a clear correspondence between the pink areas in Figure 3a, and the magenta structures in Figure 3b. In addition, the CLEM imaging of the placenta (Figure 5) confirmed that the labeled structures in magenta color matched the features observed in the SEM image.

Lastly, we faced issues with unguided light. In the initial imaging attempts, we experienced unwanted side illumination along the sample volume stemming from uncoupled light traveling in free space and reaching the sample region. This issue severely affected the contrast of the chip-TIRF images, hindering the imaging capabilities of the system. We successfully blocked the unguided light by incorporating a small piece (~1 × 1 × 10 mm) of custom-made black polydimethylsiloxane (PDMS) near the coupling facet of the photonic chip, which served as shielding against the unguided light.

## S14. Atomic force microscopy (AFM) analysis of FFPE sections

In this study, we observed a heterogeneous behavior of the micro-detachment phenomena (see Supplementary Information S12). For example, in the FFPE colorectal sample (Supplementary Figure S14a), the benign colonic epithelium region became commonly micro-detached after sample preparation. While the sample was still optimal for EPI fluorescence microscopy (Supplementary Figure S14b), the signal discontinuities on the chip-TIRF image (white arrows in Supplementary Figure S14c) suggested signal micro-detachments of the cell walls of the enterocytes in this region. To further understand the root cause of such micro-detachments, we performed a height characterization over a colonic crypt section of an FFPE colorectal tissue using an atomic force microscope (AFM) (Supplementary Figure S14d). For this, we set the AFM to quantitative imaging mode and measured the height of the sample under 95 % ethanol incubation to enable a topographical visualization of the sample in a dehydrated state (Supplementary Figure S14e). Thereafter, we repeated the measurement over the same region, this time under 50 % ethanol incubation, to visualize the morphological changes of the sample induced by hydration (Supplementary Figure S14f). A line profile measurement over the same region revealed significant morphological changes on the sample, particularly over the lumen of the enterocytes, suggesting that this vacuolated region undergoes swelling upon hydration (Supplementary Figure S14g). We also performed force measurements on the colorectal sample (not shown) and found that the cell wall of the enterocytes was significantly stiffer than the vacuolated regions exhibiting swell. Although the root source of the sample micro-detachment phenomena remains unclear, we hypothesize that, upon hydration, the vacuolated structures undergo swelling, expanding in all directions and therefore pulling out the enterocytes' cell wall from the chip surface.
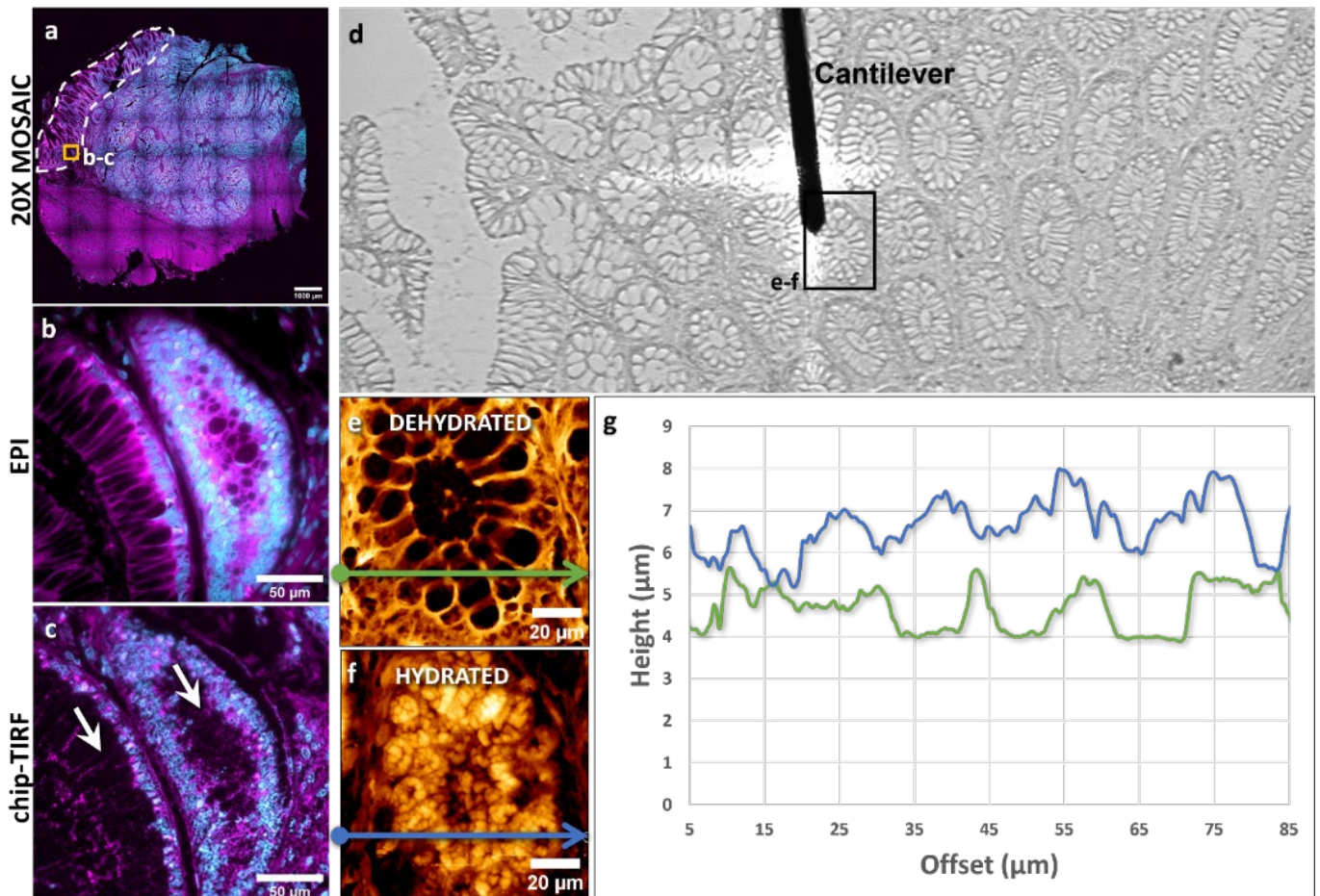
*Supplementary Figure S14. **AFM measurements on an FFPE colorectal tissue section over different hydration stages. a)** EPI fluorescent mosaic image of a colorectal sample. The white-dotted line denotes the benign colonic epithelium region. The yellow box denotes the regions imaged in b) and c), respectively. **b)** EPI fluorescent image of a colonic epithelium. Membranes are displayed in magenta and nuclei in cyan. **c)** chip-TIRF image of the same region. The white arrows illustrate the regions with signal discontinuity due to sample micro-detachment. **d)** Wide-field image of a colorectal sample on an AFM system. The black box denotes the region of the sample measured in e) and f) under different hydration conditions. **e)** Height measurement of a colonic crypt under 95 % ethanol incubation. The green line denotes the direction of the line profile measurement performed over the dehydrated sample. **f)** Height measurement of a colonic crypt under 50 % ethanol incubation. The blue line denotes the direction of the line profile measurement performed over the hydrated sample. **g)** The line profile measurements show significant swelling of the FFPE sample in a hydrated state as compared to the dehydrated state.*

S15.   Coating strategies for on-chip FFPE sample adhesion

To improve the FFPE sample adhesion to the photonic chip, diverse coating methods were tested, including histogrip (cat. # 8050, ThermoFisher Scientific), protected isocyanate[84] and poly-L-lysine coating (cat. # P8920, Sigma-Aldrich). In this case, three chips were used for the comparison, each one with a different coating. An individual FFPE placental section from the same block was placed on top of each coated chip and further labeled as described in the Materials and Methods section. To enable a comparative view, the samples were imaged both in EPI (top view) and chip-TIRF (bottom view). Supplementary Figure S15 illustrates the adhesion effect of different coatings on photonic chips. While all coating agents successfully retained the samples on the chip, we observed sample micro detachments that hampered the imaging capabilities of the photonic chip (yellow arrows on the bottom panels). Having found no significant differences among the three coating methods, in this work, we opted for the most user-friendly and economical method of all three, namely, the poly-L-lysine coating.
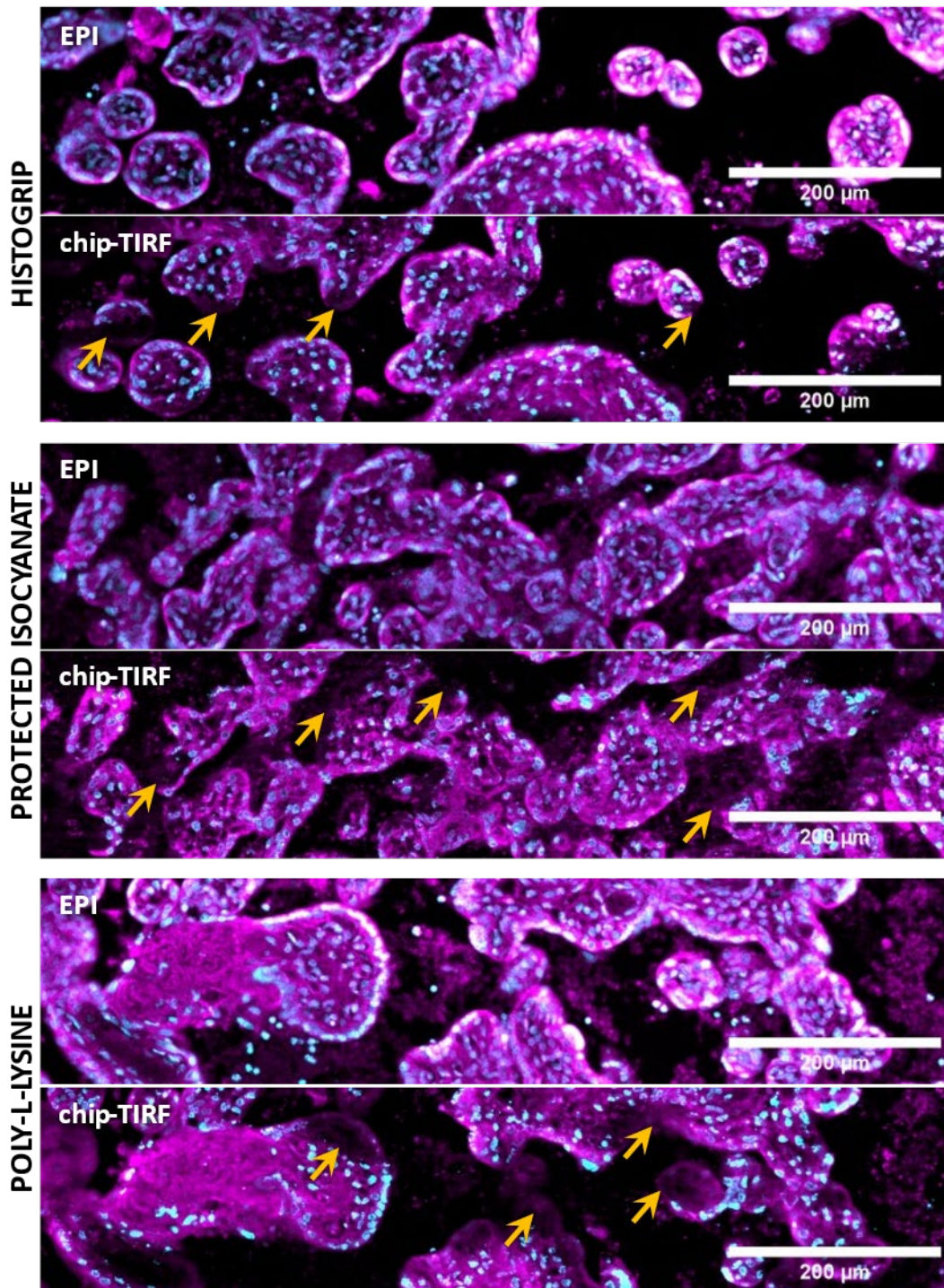
*Supplementary Figure S15. **Coating strategies for on-chip FFPE sample adhesion**. Despite retaining the FFPE samples on the chip, none of the coating methods tested, namely, histogrip, protected isocyanate (PI), and poly-L-lysine (PLL) provided full sample adhesion. Instead, sample micro-detachments were observed in all of them.*

## S16. Materials and reagents used for on-chip FFPE fluorescence labeling

Supplementary Table S16 provides a detailed description of the materials and reagents used for on-chip FFPE sample preparation.

Supplementary Table S16. Materials and reagents used for on-chip FFPE sample preparation.

Material/ reagent	Manufacturer	Catalog number	Stock concentration	Working concentration	Purpose
#1.5 coverslip	VWR	631-0125	-	-	22 mm x 22 mm #1.5 coverslip
Picodent twinsil	Picodent	1300 1000	-	1:1 mixture of solution A and B	Dental cement. Gluing and sealing.
Poly-L-lysine	Sigma-Aldrich	P8920	0.1 % (w v^{-1}) in H$_2$O	1:1	Chip-surface coating for improved adhesion of biological samples
MitoTracker™ Deep Red FM	Invitrogen	M22426	1 mM	1:2000	Unspecific staining for contextual information (similar to membrane dyes)
Sytox Green	Invitrogen	S7020	5 mM	1:1000	Nuclear staining
Phosphate-buffered saline (PBS)	Sigma-Aldrich	D8662	-	1:1	Washing steps
Glycerol	Sigma-Aldrich	G5516	-	1:1	Mountant medium
Xylenes	Sigma-Aldrich	214736	-	1:1	Sample deparaffinization
Ethanol absolute	VWR Chemicals	20821.296	>99.8 %	1:1	Sample rehydration
Ethanol 96 %	VWR Chemicals	20823.362	96 %	1:1	Sample rehydration

V1. chip-TIRF mode-averaging

Link: https://uitno.box.com/s/ycaj9q50q6526bls4ah7f4ab91ovy30o
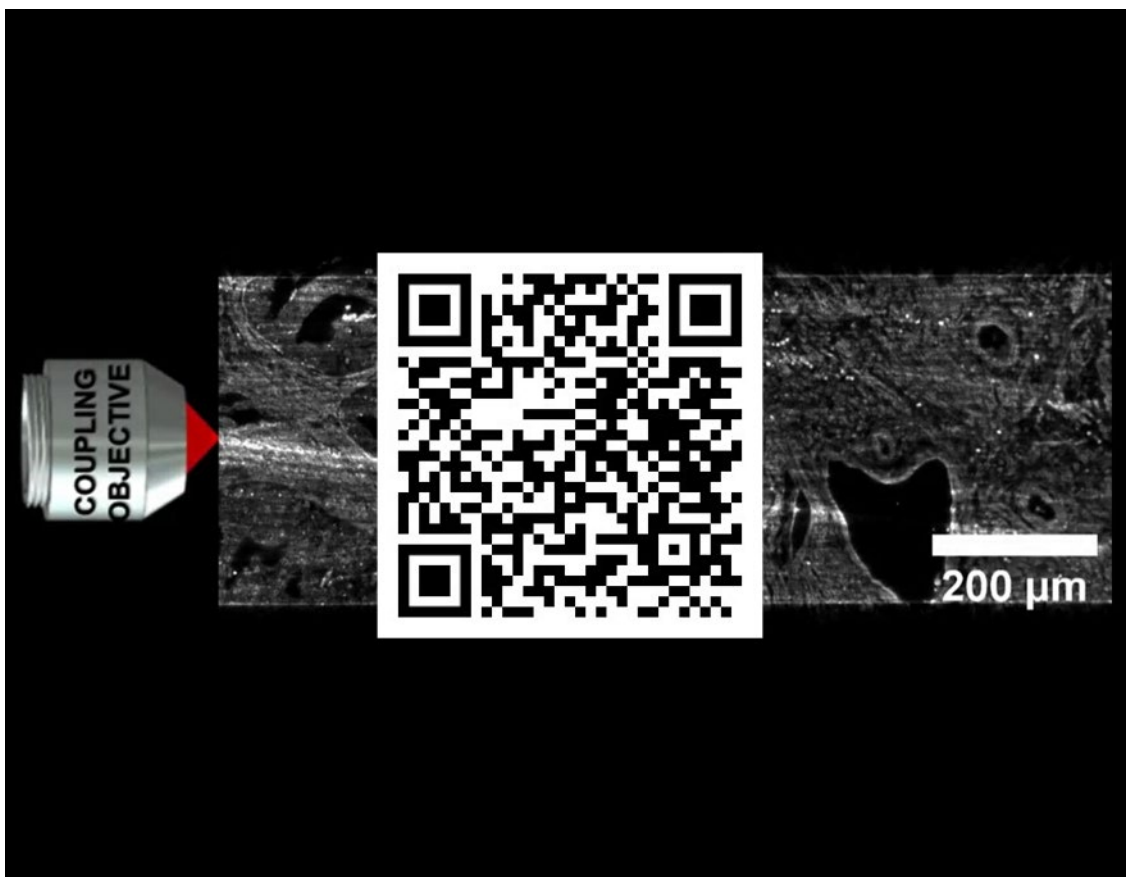
Supplementary Video V1. **Chip-TIRF mode-averaging.**

V2. Comparison between EPI-MUSICAL and chip-MUSICAL

Link: https://uitno.box.com/s/rxsne0m3pdtgl3n3caj0rc6bvw4rqa0e
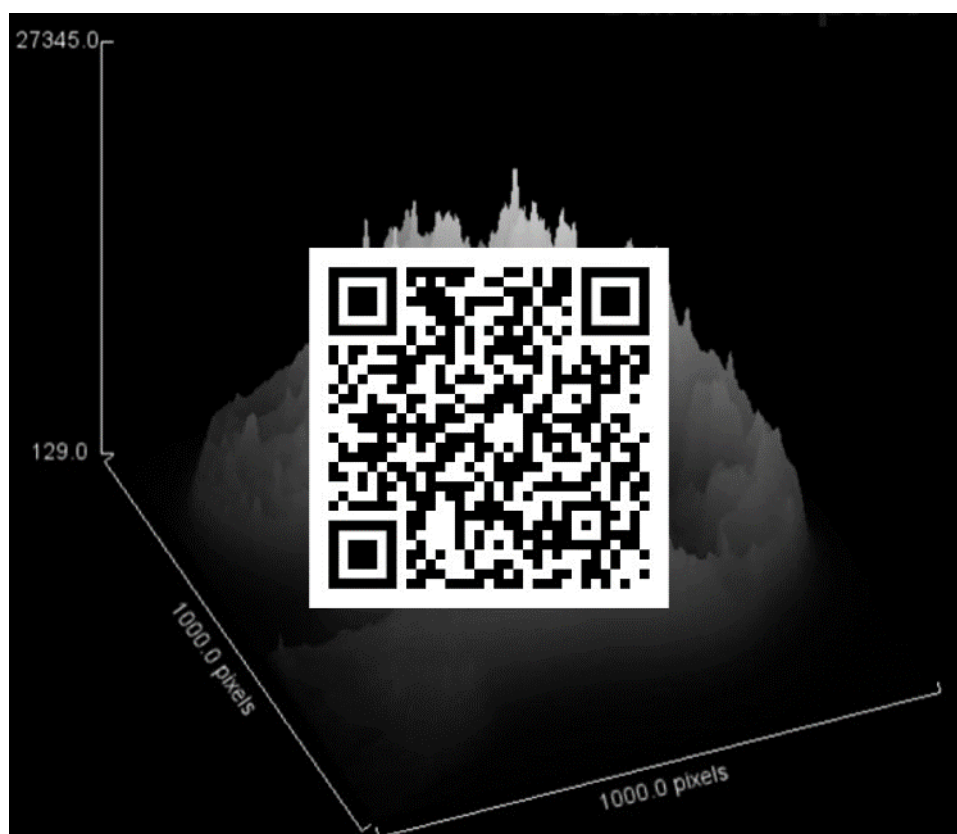
*Supplementary Video V2. **EPI-MUSICAL vs chip-MUSICAL comparison.***

V3. On-chip tissue scooping

Link: https://uitno.box.com/s/5cbrbpd1vyus4i3dmojgw89afdnvxafd

Supplementary Video V3. **On-chip FFPE tissue scooping.**

V4. EPI vs chip-TIRF over large FOV

Link: https://uitno.box.com/s/vr3d0h4ku5y5q2irn4at5vgrlxgq4c2u
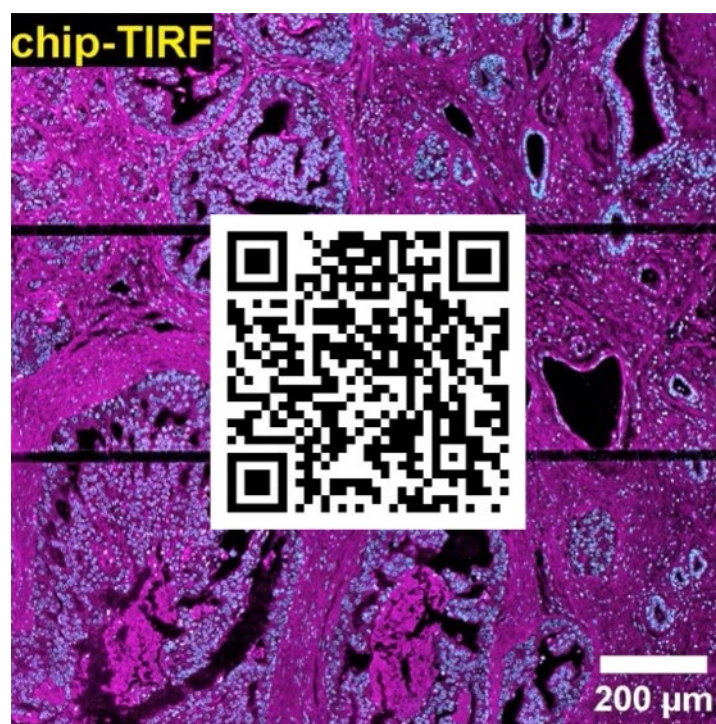
Supplementary Video V4. **EPI vs chip-TIRF over large FOV.**

V5. FFPE CLEM imaging over large fields of view

Link: https://uitno.box.com/s/9kl4x0lq7gqst6d1vnr5nrqvyebfofef
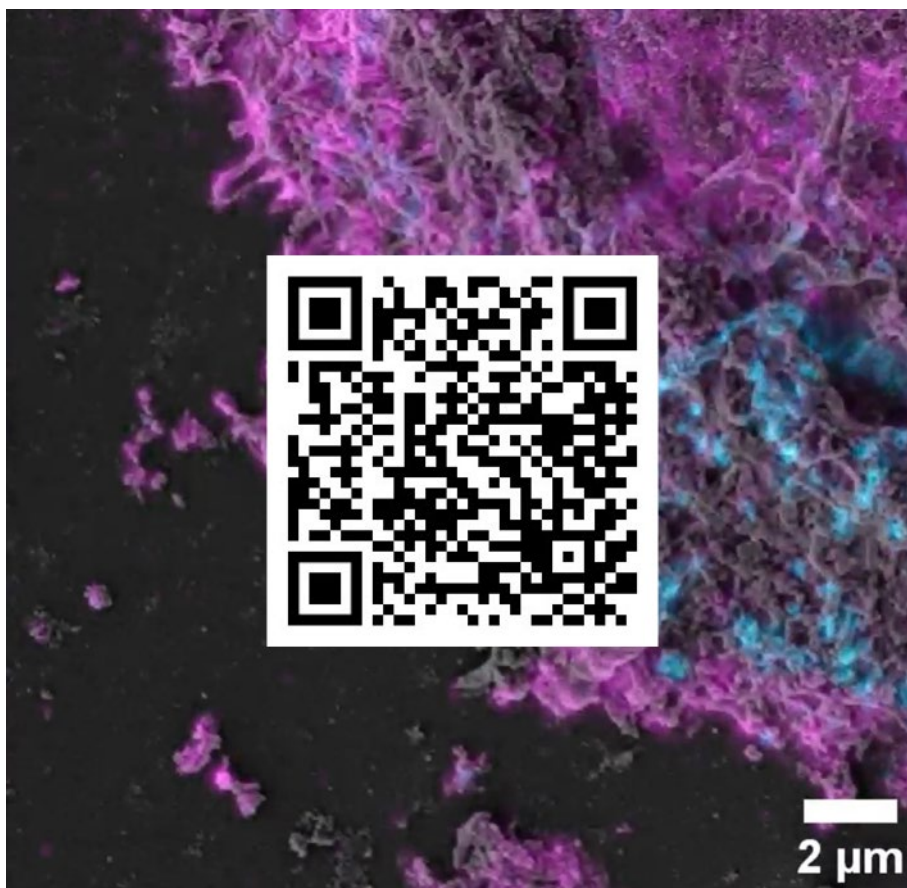
*Supplementary Video V5. **FFPE CLEM imaging over large fields of view.***

References – Supplementary Information

21. Helle, Ø. I. *et al.* Nanoscopy on-a-chip: super-resolution imaging on the millimeter scale. *Optics express* **27**, 6700-6710 (2019).

25. Diekmann, R. *et al.* Chip-based wide field-of-view nanoscopy. *Nature Photonics* **11**, 322-328 (2017).

27. Opstad, I. S. *et al.* A waveguide imaging platform for live‐cell TIRF imaging of neurons over large fields of view. *Journal of Biophotonics* **13**, e201960222 (2020).

29. Opstad, I. S. *et al.* Fluorescence fluctuation-based super-resolution microscopy using multimodal waveguided illumination. *Optics Express* **29**, 23368-23380 (2021).

30. Villegas-Hernández, L. E. *et al.* Chip-based multimodal super-resolution microscopy for histological investigations of cryopreserved tissue sections. *Light: Science & Applications* **11**, 1-17 (2022).

44. Martin‐Fernandez, M., Tynan, C. & Webb, S. A 'pocket guide' to total internal reflection fluorescence. *Journal of microscopy* **252**, 16-22 (2013).

56. Helle, Ø. I. *et al.* Structured illumination microscopy using a photonic chip. *Nature photonics* **14**, 431-438 (2020).

64. Descloux, A., Grußmayer, K. S. & Radenovic, A. Parameter-free image resolution estimation based on decorrelation analysis. *Nature methods* **16**, 918-924 (2019).

71. Tinguely, J.-C. *et al.* Photonic-chip assisted correlative light and electron microscopy. *Communications biology* **3**, 739 (2020).

74. Archetti, A. *et al.* Waveguide-PAINT offers an open platform for large field-of-view super-resolution imaging. *Nature communications* **10**, 1267 (2019).

82. Bradshaw, J. T., Mendes, S. B. & Saavedra, S. S. Planar integrated optical waveguide spectroscopy. *Analytical Chemistry* **77**, 28A-36A (2005).

83. Shen, H. *et al.* TIRF microscopy with ultra-short penetration depth. *Optics express* **22**, 10728-10734 (2014).

84. Sompuram, S. R. *et al.* A water-stable protected isocyanate glass array substrate. *Analytical biochemistry* **326**, 55-68 (2004).

Appendix D. Authorship statement

Statement describing the nature of the Ph.D. candidate's contributions for the included papers in this thesis

This thesis is comprised of three original research articles, referred to as *Papers*, produced by *the Ph.D. candidate*, namely Luis E. Villegas-Hernández, in collaboration with other researchers during his doctoral studies. The complete list of papers and specific contributions of the PhD candidate are presented below:

Paper I

Title:	*Visualizing ultrastructural details of placental tissue with super-resolution structured illumination microscopy.*
DOI:	https://doi.org/10.1016/j.placenta.2020.06.007
Authors:	<u>Luis E. Villegas-Hernández</u>, Mona Nystad, Florian Ströhl, Purusotam Basnet, Ganesh Acharya, Balpreet S. Ahluwalia.
Contribution:	LEVH prepared the tissue samples, performed the imaging experiments and subsequent image analysis. LEVH wrote the first draft of the manuscript and finished the paper. All authors contributed to writing and revising selected sections of the article.

Paper II

Title:	*Chip-based multimodal super-resolution microscopy for histological investigations of cryopreserved tissue sections.*
DOI:	https://doi.org/10.1038/s41377-022-00731-w
Authors:	<u>Luis E. Villegas-Hernández</u>*, Vishesh Dubey*, Mona Nystad, Jean-Claude Tinguely, David A. Coucheron, Firehun T. Dullo, Anish Priyadarshi, Sebastian Acuña, Azeem Ahmad, José M. Mateos, Gery Barmettler, Urs Ziegler, Åsa Birna Birgisdottir, Aud-Malin Karlsson Hovd, Kristin Andreassen Fenton, Ganesh Acharya, Krishna Agarwal, Balpreet Singh Ahluwalia.
Contribution:	LEVH planned and coordinated the experiments, performed sample preparation, image acquisition, and subsequent image analysis. LEVH wrote the first draft of the manuscript and finished the paper. All authors contributed to writing and revising selected sections of the article. *These two authors contributed equally to this work.

Paper III

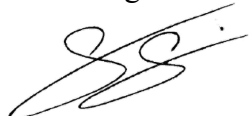|	
Title:	*Super-resolution histology of paraffin-embedded samples via photonic chip-based microscopy.*
DOI:	https://doi.org/10.1101/2023.06.14.544765
Authors:	<u>Luis E. Villegas-Hernández</u>, Vishesh K. Dubey, Hong Mao, Manohar Pradhan, Jean-Claude Tinguely, Daniel H. Hansen, Sebastián Acuña, Bartłomiej Zapotoczny, Krishna Agarwal, Mona Nystad, Ganesh Acharya, Kristin A. Fenton, Håvard E. Danielsen, Balpreet Singh Ahluwalia.
Contribution:	LEVH planned and coordinated the experiments, performed sample preparation, image acquisition, and subsequent image analysis. LEVH wrote the first draft of the manuscript and finished the paper. All authors contributed to writing and revising selected sections of the article.

Ph.D. candidate

Luis E. Villegas-Hernández

_____

Main supervisor:

Balpreet Singh Ahluwalia

_____